Technische Universität München
TUM School of Natural Sciences

Formation and Deformation of Functional (Bio)hybrid Films Revealed by Advanced Scattering Methods

Julian Eliah Heger, M.Sc.

Vollständiger Abdruck der von der TUM School of Natural Sciences der Technischen Universität München zur Erlangung eines

Doktors der Naturwissenschaften (Dr. rer. nat.)

genehmigten Dissertation.

Vorsitz: Prof. Dr. Martin Zacharias

Prüfer*innen der Dissertation:

1. Prof. Dr. Peter Müller-Buschbaum
2. Prof. Dr. Friedrich C. Simmel

Die Dissertation wurde am 29.11.2023 bei der Technischen Universität München eingereicht und durch die TUM School of Natural Sciences am 10.01.2024 angenommen.

Für meine Eltern Markus Johannes Heger
und Monika Edeltraud Lechner.

Unsere Erinnerungen sind das Gepäck,
mit dem wir in die Zukunft reisen. Für immer.

Abstract

This thesis investigates films with advanced scattering methods to determine their morphology on the nanoscale. The main aspect is to study the functional properties of organic-inorganic hybrid interfaces and their structure-function relationship. The thesis is divided into two projects: The first projet focuses on the water-based synthesis of metal oxide films at potentially low temperatures with the aim of promoting a more sustainable fabrication. Here, biohybrid interfaces made of whey protein and titania precursors form a structure directing composite. The second project investigates the isotropy in a deforming thin-film quantum dot superlattice and relates it to the inter-dot energy transfer using photoluminescence. Here, the hybrid interfaces between compressible ligands and solid quantum dots play a determining role in the observed phase transition.

Diese Arbeit untersucht Beschichtungen mit modernen Streumethoden, um deren Morphologie auf der Nanoskala zu bestimmen. Der Schwerpunkt liegt auf der Untersuchung der funktionellen Eigenschaften von organisch-anorganischen Hybridgrenzflächen und deren Struktur-Funktion-Beziehung. Die Arbeit gliedert sich in zwei Projekte: Das erste Projekt konzentriert sich auf die wasserbasierte Synthese von Metalloxidfilmen bei potenziell niedrigen Temperaturen mit dem Ziel, eine nachhaltigere Herstellung zu fördern. Dabei bilden biohybride Grenzflächen aus Molkenprotein und Titanoxid-Präkursoren einen strukturgebenden Verbund. Das zweite Projekt untersucht die Isotropie in einem sich verformenden Dünnschicht-Quantenpunkt-Übergitter und bringt diese und den Energietransfer zwischen den Quantenpunkten mit Hilfe der Photolumineszenz in Beziehung. Dabei spielen die hybriden Grenzflächen zwischen kompressiblen Liganden und festen Quantenpunkten eine entscheidende Rolle für den beobachteten Phasenübergang.

Contents

List of Abbreviations

β-lg	β-lactoglobulin
BCC	body-centered cubic
BCT	body-centered tetragonal
CNC	computer numerical control
DWBA	distorted wave Born approximation
FCC	face-centered cubic
FRET	Förster resonance energy transfer
FTIR	Fourier transform infrared
FWHM	full width at half maximum
GISANS	grazing-incidence small-angle neutron scattering
GISAXS	grazing-incidence small-angle X-ray scattering
GIWAXS	grazing-incidence wide-angle X-ray scattering
HRTEM	high-resolution transmission electron microscopy
OA	oleic acid
PDMS	poly(dimethylsiloxane)
PL	photoluminescence
PTFE	poly(tetrafluoroethylene)
QD	quantum dot

SLD ..... scattering length density

TiBALDh ..... titanium(IV) bis(ammonium lactate) dihydroxide

TTIP ..... titanium(IV) isopropoxide

List of Figures

Chapter 1

Introduction

Thin-film technology is based on coatings and thin layers of various materials and covers applications in a broad spectrum, such as optoelectronic and electronic devices, photocatalytic interfaces, sensors responsive to external stimuli, protective coatings, flexible electronics, and electrochemical cells. [1], [2] This versatile technology has the advantage that it entails potentially low material usage and affords light-weight devices with high performance-to-weight ratio. With the development of more and more advanced materials, new design strategies, e.g., optoelectronic devices on flexible foils, can be developed and implemented in every-day scenarios. [3], [4] An important branch in the field of energy-related thin-film technology are coatings based on porous and nanostructured metal oxides, such as titania. [5]–[8] With their high surface-to-volume ratio and tailored morphology, they are widely applicable, especially in photovoltaic devices, photocatalytic synthesis, and batteries. [9]–[12] To achieve desired nanostructures, wet-chemistry approaches combined with polymer templates such as beads, diblock micelles or lamellar structures are typically chosen. [13] The wet-chemical approach avoids additional and complex fabrication steps that would be necessary for, e.g., electron beam litography, and enables solution-processible coating methods such as spin coating, printing and spray coating. Besides nanostructured titania, another promising branch in the field of optoelectronic thin-film technology are films based on colloidal PbS quantum dots (QDs). [14], [15] PbS QD films provide high charger carrier mobilities, tunable bandgaps and high absorption in the infrared regime. Surface-attached ligands introduce solution processibility, making PbS QDs promising for large-scale fabrication of photodetectors and solar cells. The versatile prospects and potential of colloidal QDs in general is highlighted by the awarding of the Nobel Prize in Chemistry 2023 to Moungi G. Bawendi, Louis E. Brus, and Aleksey Yekimov for the discovery and synthesis of QDs. [16]

In both cases, hybrid interfaces between organic and inorganic materials play a fundamental role. In the first case of polymer directed metal oxide synthesis, the hybrid

interfaces between the polymer template and the metal oxide define the resulting film morphology after template removal. In the second case of QD film formation, the interfaces between organic ligands and QDs define the resulting degree of inter-dot coupling, which influences charge carrier mobility and energy transfer. The structure-function-relationship in these functional hybrid films is hence of high interest, the determination of which is accessible via experiments based on advanced scattering methods. These methods include *in-situ* grazing-incidence small-angle and wide-angle X-ray scattering (GISAXS/GIWAXS) and grazing-incidence neutron scattering (GISANS). GISAXS/GIWAXS and GISANS probe large sample volumes and thus are statistically highly relevant compared to real-space microscopy methods, which typically scan the sample locally at the surface. The scattering methods probe the inner morphology along the penetration path in a non-destructive way. Together with the high flux, especially for X-rays at synchrotron facilities, time-resolved experiments on short time-scales can be realized. Furthermore, thanks to varying contrast conditions between X-rays and neutrons, combined measurements enable the complementary investigation of the nanostructure in composite materials. The probed information on the morphology covers the crystallinity (GIWAXS) and domains on the nanoscale (GISAXS/GISANS), which fundamentally influence the functional properties of thin films in applications.

This thesis explores the structure-function-relationship of (bio)hybrid interfaces in functional films with advanced scattering methods and is divided into two main projects. The first project particularly addresses the question of how do biohybrid interfaces between a protein and titania precursors dictate the formation of the titania film morphology in the background of a more sustainable synthesis of foam-like titania films. For this, spray-deposited biohybrid films are investigated, which are made of the whey protein β-lactoglobulin (β-lg) and different titania precursors and result in foam-like morphologies. The structure-function-relationship between biohybrid interfaces and the final titania nanostructure is important to understand the structure directing properties of β-lg as a water-based biotemplate with the aim to replace synthetic polymers and the typically involved organic solvents. The focus is on the formation of the biohybrid interfaces during spray deposition revealed by *in-situ* GISAXS/GIWAXS (Figure 1.1a). Furthermore, GISAXS, GIWAXS, and GISANS probe the formation of biohybrid interfaces as a function of pH (Figure 1.1b).

The second project particularly addresses the question of how does external strain introduce deformation in superlattices built up by hybrid interfaces and change the inter-dot coupling in QD films on flexible substrates. For this, the superlattice deformation of PbS QDs capped with oleic acid (OA) ligands is examined with *in-situ* GISAXS during uniaxial elongation of the flexible substrate (Figure 1.1c). *In-situ* photoluminescence (PL)

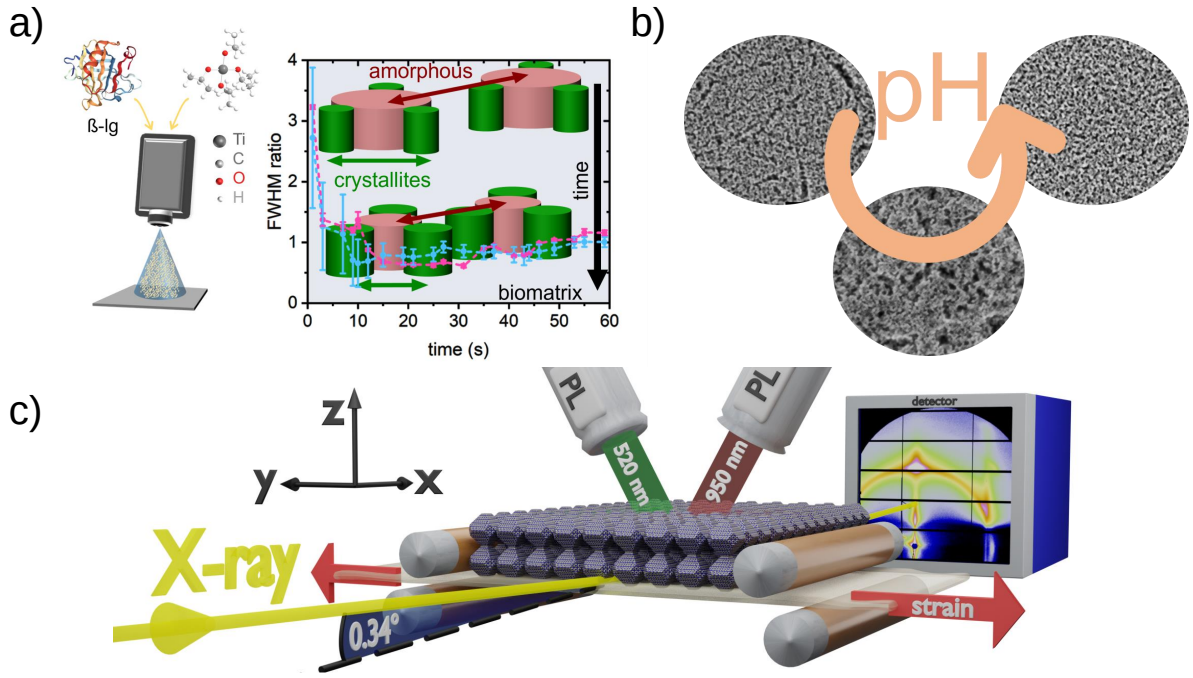

Figure 1.1.: Thesis Overview. The objects of this thesis are the investigation of (bio)hybrid interfaces and their structure-function-relationship in functional films with respect to a) low-temperature crystallization and film formation of β-lg:titania films during water-based spray deposition (Chapter 5), b) influence of pH on the morphology of biotemplated titania films (Chapter 6), and c) superlattice deformation upon uniaxial strain in PbS QD films (Chapter 7). Adapted from Ref. [17] with permission from Wiley, Copyright 2022, and from Ref. [18] with permission from the Royal Society of Chemistry, Copyright 2023.

during the elongation probes the optoelectronic coupling between the PbS QDs, which is related to the deforming superlattice.

The structure of this thesis aims to firstly introduce the reader into the theoretical background in Chapter 2. This covers the concept of sol-gel synthesis of titania nanostructures via hydrolization and polycondensation reactions, an overview of the structure of β-lg and its conformational changes upon denaturation, as well as principles on colloidal QDs and the solid structure they form. In this context, I highlight the pioneering literature, which inspired the scientific questions addressed in this thesis. Furthermore, the principles of X-ray and neutron scattering methods are described, which are applied to answer these questions. After that, I continue with experimental details on the sample fabrication and the involved materials in Chapter 3. This covers the substrates used as support for film deposition, the spray deposition of biotemplated titania films, and the synthesis PbS QDs for the deposition on flexible substrates. The characterization methods applied on the samples to probe their surface, molecular, and electronic structure are

described in Chapter 4, together with the experimental setups and sample environments at the synchrotron and neutron facilities.

Chapter 5 discusses the results of the formation of biohybrid interfaces in biotemplated titania nanostructures, with the focus on the film formation during spray deposition and is based on the publication *"Low-Temperature and Water-Based Biotemplating of Nanostructured Foam-Like Titania Films Using β-lactoglobulin"* in Advanced Functional Materials. [17]

Chapter 6 presents results and discussion on the formation of biohybrid interfaces and their tailoring properties for foam-like titania films as a function of pH. Here, by use of a water-based titania precursor and different supramolecular structures of β-lg, different porous nanostructures are introduced into foam-like titania films.

Chapter 7 discusses the results of the deformation of hybrid interfaces and the relation of photoluminescence and unit cell isotropy in PbS quantum dot superlattices under application of uniaxial strain. This chapter presents a pioneering *in-situ* GISAXS experiment on the investigation of structural changes in thin films on flexible substrates under applied strain and is based on the publication *"Superlattice Deformation in Quantum Dot Films on Flexible Substrates via Uniaxial Strain"*, which is published in Nanoscale Horizons. [18]

The summary of this thesis is given in Chapter 8, together with a outlook on future perspectives of the structure-function-relationship in functional (bio)hybrid films during formation and deformation. The summary and outlook is followed by the appendix on the index matching of QD superlattice reflexes on 2D GISAXS data utilizing the software GIXSGUI in Appendix A and on the custom-modified spray coater based on commercially available engraving machines in Appendix B. The references are listed in the Bibliography and are followed by a list of first and coauthor publications, as well as scientific contributions to conferences in the form of invited or contributed talks and posters. Lastly, I express my gratefulness to people who provided support during the time of this doctorate in the Acknowledgments.

Chapter 2

Theoretical Background

The following chapter gives a basic introduction to the relevant theoretical background for this thesis concerning titania nanostructures and their synthesis, the biopolymer β-lg and its structure, the principles of QD solids, and the applied X-ray and neutron scattering methods. Further, the scientific questions addressed in this thesis with respect to the structure-function-relationship of (bio)hybrid interfaces in functional film during formation and deformation is put in context to the existing literature, which inspired the performed experiments.

2.1. Sol-Gel Synthesis of Titania Nanostructures

Fundamental Properties of Titania

Titania is a polymorph metal oxide that primarily occurs in three distinct crystal phases: anatase, rutile, and brookite. The three polymorphs are built up by distorted TiO_6 octahedrons (Figure 2.1). These octahedrons are packed along adjacent edges for anatase, which leads to a triangular arrangement of the octahedrons in the tetragonal unit cell. In rutile, the octahedrons are packed at opposite corners, yielding a linear arrangement in the tetragonal unit cell. In contrast, the octahedrons build up an orthorombhic unit cell in brookite. All polymorphs are indirect semiconductors resulting from p-d hybridization of Ti-3d states with Ti-3p and O-2p states forming the conduction bands and O-2p states with Ti-3d forming the valence bands, the different degree of distortion and the changing atomic distances between Ti leads to a denser packing and higher thermodynamic stability for rutile and different polymorph band gap energies: anatase 3.2 eV, rutile 3.0 eV, and brookite 3.3 eV. [19]–[21] Accordingly, each titania polymorph absorbs light in the UV-range. The optoelectronic properties differ when going from bulk to mesoporous phases and changing the crystal sizes, as sizes smaller than the exciton Bohr radius lead to

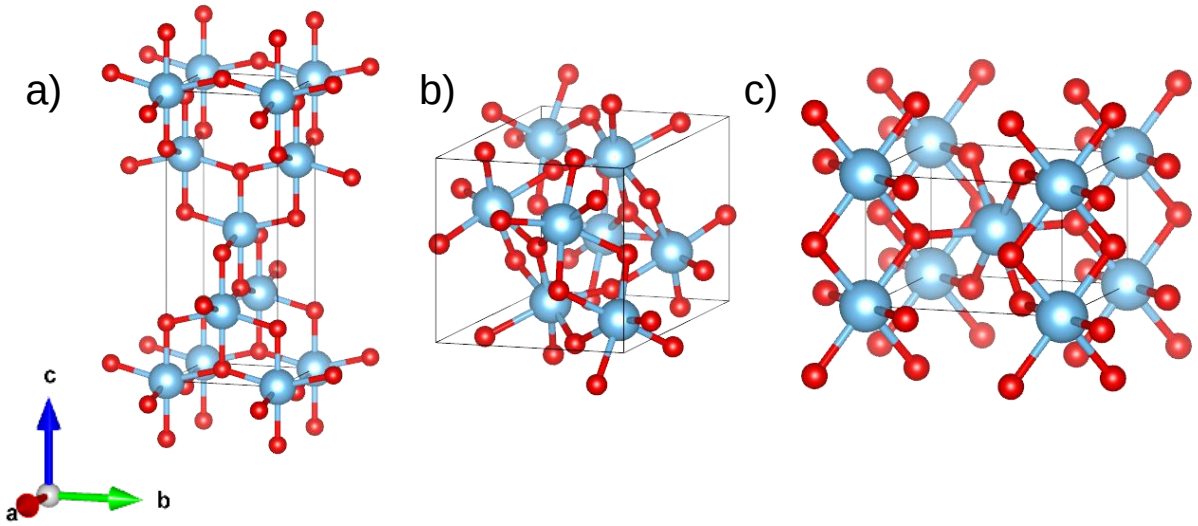

Figure 2.1.: Crystal structure of the three titania polymorphs. The crystal structure is shown in the same perspective for a) anatase, b) brookite, and c) rutile.

increased band gaps via quantum confinement effects. Also, the high surface-to-volume ratio of mesoporous titana films is beneficial for application as photoanodes in solar cells, in lithium-ion batteries, or in photocatalytic generation of hydrogen. Hence, a controlled nanostructure becomes essential for device performance.

Sol-gel Synthesis of Titania

The fabrication of nanostructured titania films in this thesis is based on the wet chemical approach of sol-gel synthesis. Sol-gel synthesis is a well-established protocol for the preparation of, e.g., metal oxides or ceramic materials from precursor materials to colloids and integrated networks of the respective material in a bottom-up routine. Advantages include the comparatively low synthesis effort and the possibility of solution-based processing for inorganic materials. The resulting sol-gels have the potential to be used as ink in industrially-scalable deposition methods such as printing or spray coating. Furthermore, the introduction of polymers into the sol-gel synthesis forms hybrid materials that can tune the resulting morphology at the nanoscale and allows for nanostructure tailoring of, e.g., metal oxides without the need for more complex lithography and high vacuum processes. Typical precursors for titania sol-gel synthesis are based on a Ti-alkoxide. A prominent example is titanium(IV) isopropoxide (TTIP) in Figure 2.2a. The pure precursor, or if stabilized in a homogeneous solution based on organic solvents such

as isopropanol or ethanol, hydrolyzes upon addition of water. Here, the OR groups are replaced by hydroxyl groups during the reaction with H_2O molecules:

$$Ti\,(RO)_4 + H_2O \rightleftarrows (HO) - Ti\,(OR)_3 + R - OH \tag{2.1}$$

Complete hydrolysis is achieved when all OR groups are replaced. If this is not the case, the partially hydrolyzed precursor monomers can continue to condensate and form a network via cross-linking and oxygen bridges along the Ti-O-Ti bonds and release H_2O or ROH upon reaction:

$$(RO)_3 - Ti - OH + (RO)_3 - Ti - OH \rightleftarrows (RO)_3 - Ti - O - Ti - (OR)_3 + H_2O \tag{2.2}$$

$$(RO)_4 - Ti + (RO)_3 - Ti - OH \rightleftarrows (RO)_3 - Ti - O - Ti - (OR)_3 + R - OH \tag{2.3}$$

The hydrolysis and condensation reactions are at the heart of sol-gel synthesis and are sensitive to various chemical parameters such as temperature, pH, amount of water, type of precursor and hydrolysis catalysts. For example, the introduction of HCl as a hydrolysis catalyst promotes hydrolysis over condensation reactions, and thus tends to increase the number of end-chain reactions rather than crosslinking at the monomer cores. As a result, more elongated networks are formed, which is favorable for the formation of foam-like and nanostructured titania films. Without HCl as a hydrolysis catalyst, there is a tendency for more bulky and compact titania clusters. While slow hydrolysis reaction and fast condensation tends to form amorphous titania networks, fast hydrolysis over condensation has the potential to form nanocrystalline titania precipitates and crystal seeds. [22] Besides TTIP, another titania precursor based on water-soluble Ti-lactate

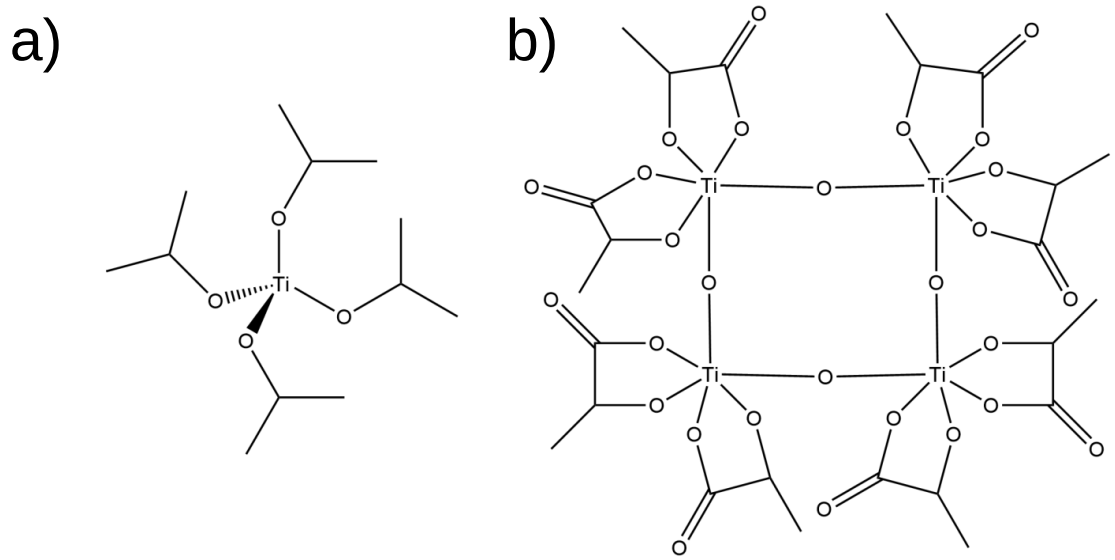

Figure 2.2.: Chemical structure of the titania precursors: a) TTIP, b) TiBALDh.

complexes, titanium(IV) bis(ammonium lactate) dihydroxide (TiBALDh), is investigated in this thesis (Figure 2.2b). TiBALDh has a chemical equilibrium with water and crystalline anatase-TiO_2 nanoparticles, which is described by the following expression: [23], [24]

$$3\left[Ti_4O_4\left(lactate\right)_8\right]^{8-} + 8NH_4^+ \rightleftarrows 8\left[Ti\left(lactate\right)_3\right]^{-2} + 4TiO_2 + 8NH_3 + 4H_2O \quad (2.4)$$

Polymer Directed Templating of Mesoporous Titania Films

Sol-gel synthesis of titania im combination with polymers is an established and powerful method to prepare titania films with a defined mesoporous nanostructure. Typically, diblock copolymers are employed, such as polysterene-b-polyethylene oxide (PS-b-PEO), which form various kind of nanostrucutures due to microphase separation in accordance with their phase diagramm. [25], [26] These nanostructures, such as micelles, cylinders, lamellae, and vesicles, are able to bind via hydrogen interactions to the titania precursor (Figure 2.3a,b). The obtained organic-inorganic hybrid solutions based on titania pre-

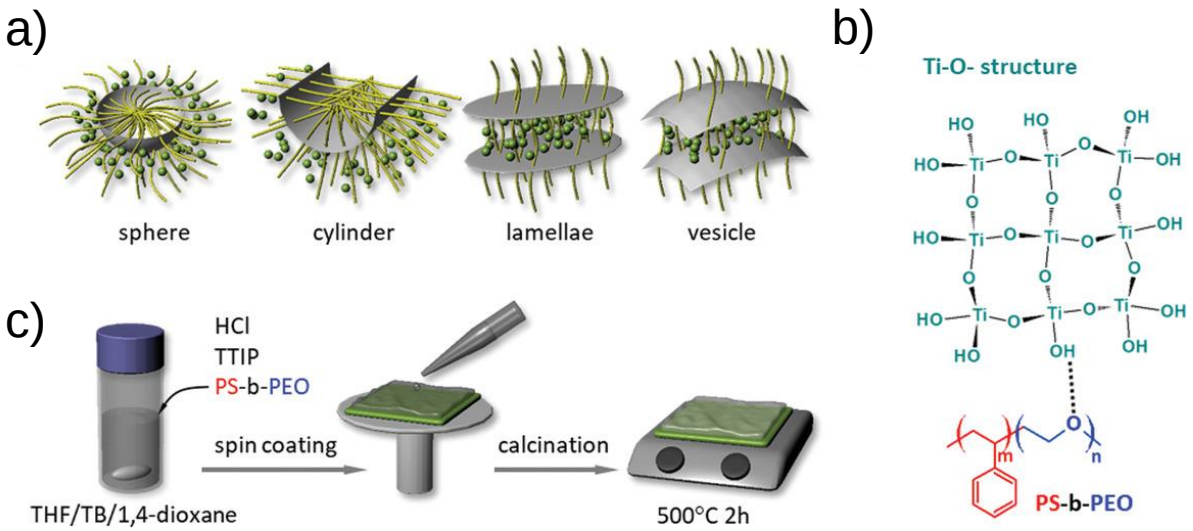

Figure 2.3.: Illustration of polymer templating in sol-gel synthesis of titania films. a) Different morphologies accessible by controlling the polymer's phase. b) The polymer template binds to the titania precursor via hydrogen interactions. c) Mesoporous and crystalline titania films are commonly prepared by spin coating out of hybrid polymer-titania solutions based on organic solvents and calcination. Reprinted from Ref. [25] with permission from Wiley, Copyright 2020.

cursor and diblock copolymer are feasible to be deposited by industrial relevant methods such as spin coating, printing, and spray coating. For example, the choose of different

kind of solvent sets as good and bad solvents for the respective blocks are straight forward methods to precisley tune the final film nanostructure. However, typically rather harmful organic solvents are involved in the film fabrication (Figure 2.3c), which limit the potential in a green and sustainable fabrication on large industrial scale. Also, high temperatures of about 500 °C are usually needed to combust the polymer template and introduce crystallinity into the amorphous titania films.

A water-based sol-gel synthesis of nanostructured titania films with potentially low-temperature crystallization is feasible by replacing synthetic polymers with biopolymers. Due to the ability to form crystalline titania upon hydrolysis, TTIP and TiBALDh are examined in this thesis for water-based routes towards foam-like and nanostructured titania films. In order to direct the titania morphology on the nanoscale, the water-based biopolymer β-lg is introduced to the sol-gel synthesis and further described in the next section.

2.2. Native and Denatured Structure of β-lg

Biopolymers are naturally occurring polymers with a defined structure and functionality. In the case of proteins, this structure is built hierarchically by a specific sequence of covalently linked amino acids. This primary structure gives rise to special conformations with helical (α-helices) or zigzag (β-sheets) symmetries, the secondary structures, via hydrogen bonds. After further complex folding, proteins exhibit a three-dimensional conformation with a monodispersive and unique shape. This tertiary structure allows proteins to function as motors, pumps, and transporters in biological systems. Some proteins form higher order quaternary structures via oligomerization.

In this thesis, I focus on the major bovine whey protein β-lg as a foaming agent for the synthesis of water-based and nanostructured biohybrid titania foams. The primary structure of β-lg consists of 162 amino acids with a total molecular weight of about 18.3 kDa and is shown in Figure 2.4. [27] There are two disulfide bridges between amino acids Cys-106 and Cys-119, and between Cys-66 and Cys-160, and a free thiol group at Cys-121. [28]

The secondary structure consists of an eight-stranded antiparallel β-sheet wrapped to form a cavity, a so-called β-barrel or calyx. [29] The β-sheet is followed by a three-turn α-helix, which gives the tertiary structure the shape of a cup with a handle (Figure 2.5), and is followed by a ninth β-strand. In its physiological state, the quaternary structure of bovine β-lg is given by a non-covalent dimer, which is a couple of two monomeric subunits linked by hydrogen bonds and electrostatic interactions. The ratio of monomer to dimer can change depending on the chemical and physical environment, e.g., at low pH the

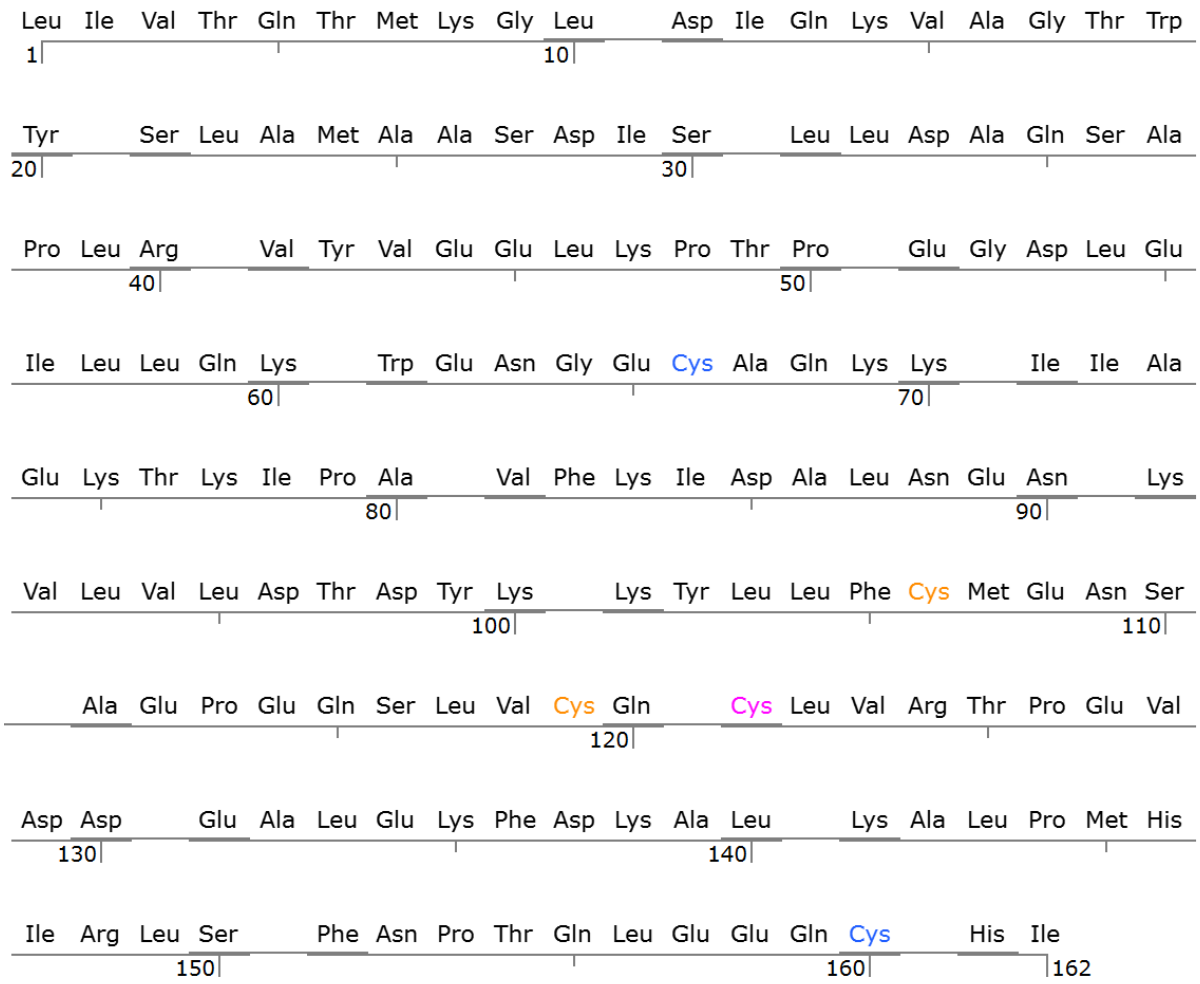

Figure 2.4.: Primary structure of β-lg. 162 amino acids form the primary structure of β-lg. The disulfide bridges are highlighted from Cys-106 to Cys-119 (orange) and from Cys-66 to Cys-160 (blue), as well as the free thiol group at Cys-121 (magenta).

dimer dissociates into monomers. The secondary structure of β-lg classifies the protein as a lipocalin. [27] The cavity nature of lipocalins reflects their common function as ligand-binding and transport proteins. Although β-lg is one of the most intensively studied representatives, its physiological function is not definitely clarified, but it is believed to bind and transport fatty acids and vitamins such as retinol from the mother's milk to the offspring. [29] The barrel structure opens at a pH value of around 6.2 to 7.1, leaving the hydrophobic core inside accessible for hydrophobic binding to ligands. [30] This reversible transition is known as the Tanford transition and reveals the suggested transport character of β-lg. In the food industry, however, β-lg is known as a foaming and texturing agent, as well as a cause of allergic reactions, motivating parts of the research on its nature. [31]

Besides the Tanford transition, there are several more conformational changes possible

Figure 2.5.: Tertiary structure of β-lg. The tertiary structure consists of β-sheets (yellow), which are forming a cavity, and a three-turn α helix (pink). The graphic is downloaded from the protein data bank RCSB PDB (https://www.rcsb.org/3d-view/1BEB/1) [27], [32]

for β-lg. For instance, when exposed to heat, the quaternary and tertiary structure unfold and the protein denatures. Depending on various parameters, such as temperature, concentration, ionic strength, and pH value, the denaturation is an irreversible process with the potential to form distinct supramolecular agglomerates. Here, β-lg is known for its capability to form amyloid-like fibrils, that are hierarchically built up by ribbons of twisted protofilaments which consists of stacked β-sheets along the protofilament's axis. [33] In general, denatured β-lg can build up various forms of aggregates. For instance, combined SAXS and SANS studies performed by *Jung et al.* and the Mezzenga group showed that the form factor changes from rod-like at pH 2 to sphere-like at pH 5.8 and to worm-like at pH 7 (Figure 2.6). [34] The amount of heat-denatured β-lg and the conversion rate k from the native state to non-native monomers and aggregates can be described within the following kinetic model:[35]

$$\ln \frac{C_t}{C_0} = \frac{1}{1-n} \ln \left(1 + (n-1)\, kt\right) \tag{2.5}$$

where C_t and C_0 are the native protein concentration at time t and the initial native protein concentration. For a concentration of 90 gL^{-1} this kinetic equation is of first order with $n = 1$ after 30 min at 78 °C and pH 7. Within these conditions, the protein is fully denatured. [35] The conformational changes upon denaturation are one of the reasons why β-lg is used for giving texture to edibles in food industry, but this idea can be also translated to non-edibles and functional materials in nanoscience. The pioneering

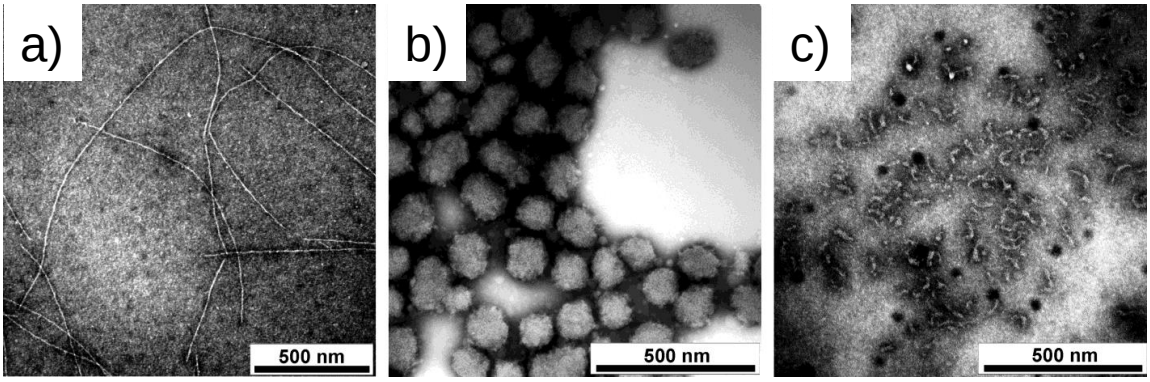

Figure 2.6.: Different shapes of β-lg aggregates after controlled denaturation: a) Amyloid-like fibrils, b) spherical aggregates, c) worm-like aggregates. Reprinted with permission from Ref. [34]. Copyright 2008 American Chemical Society.

work using β-lg amyloid fibrils as a biotemplate for the synthesis of titania nanowires was performed by *Bolisetty et al.* and the Mezzenga group with the idea to fabricate hybrid organic-inorganic photovoltaic devices. [36] This inspired the use of β-lg aggregates with varying supramolecular shape obtained by denaturation to tailor nanostructured titana films and investigate the strucutre-function-relationship in the formation of biohyrid interfaces, which is object of this thesis and discussed in Chapter 5 and Chapter 6.

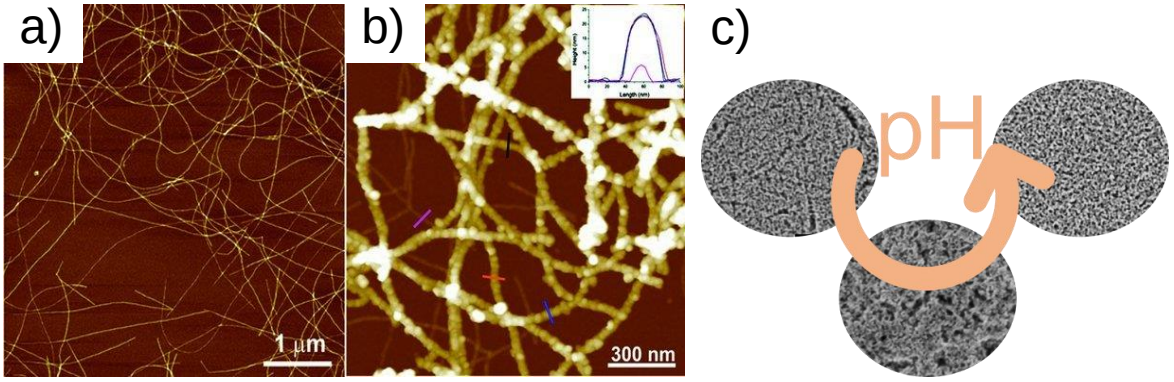

Figure 2.7.: β-lg as biotemplate. a) Network of amyloid-like fibrils based on denatured β-lg. b) Titania nanowires based on decorated β-lg fibrils. c) Schematic of biotemplated titania films with different nanostructure based on the formation of varying biohybrid interfaces as discussed in Chapter 5 and Chapter 6. Adapted from Ref. [36] with permission from Wiley, Copyright 2012.

2.3. Quantum Dot Thin Films

Semiconducting colloidal quantum dots (QDs) are a special class of nanoparticles that show unique optoelectronic properties due to full quantum confinement that is a consequence of their small sizes, typically in the range of 2-20 nm (Figure 2.8a). The following

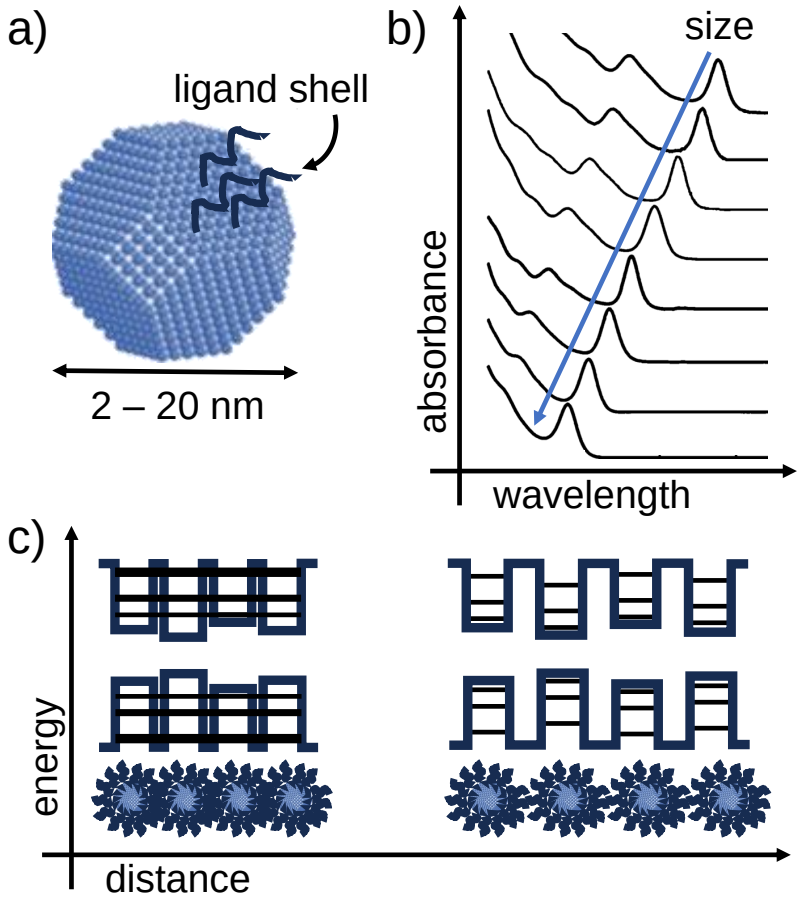

Figure 2.8.: Structure properties of PbS QD solids. a) Illustration of a truncated octahedron QD, which typically has a size between 2-20 nm and is crafted by a ligand shell. Adapted from Ref. [37] with permission from the American Chemical Society, Copyright 2020. b) QDs have a size-dependent bandgap which is relfected in the shift of the first excitonic peak in the absorbance spectra. Adapted from Ref. [38] with permission from Wiley, Copyright 2019. c) The energy levels in the potential wells are slightly different for individual QDs in an uncoupled assembly with narrow size distribution. By reducing the inter-dot distance towards an arrangement of coupled QD, their wavefunctions overlap and band formation of the electronic states occurs. Adapted from Ref. [39] with permission from Springer Nature, Copyright 2015.

section introduces the theoretical background of colloidal QDs, which are the focus of Chapter 7. Throughout the thesis, semiconducting colloidal QDs will be referred to briefly as QDs. Upon reducing the radius of a bulk semiconductor radius smaller than

the electron Bohr radius, quantum confinement effects come into play, which increases the bandgap energy. In contrast to 2D quantum wells and 1D quantum wires, QDs are 0D and fully confined materials. The quantum confinement leads to discrete energy levels, hence, QDs are often referred to as artificial atoms. The tunability of the QD bandgap energy as function of size makes the material versatile and highly promising for optoelectronic applications (Figure 2.8b). The size-bandgap dependency is mathematically described by the Brus equation: [40]

$$E_g^{QD} = E_g^{bulk} + \frac{h^2}{8m_0r^2}\left(\frac{1}{m_e^*} + \frac{1}{m_h^*}\right) - \frac{1.8e^2}{4\pi\epsilon\epsilon_0 r} \tag{2.6}$$

Here, E_g^{QD} and E_g^{bulk} are the bandgap energies of the QD and the bulk material, respectively. The product $m_0 m_{e,h}^*$ is the effective electron or hole mass, r is the effective QD radius, and h the Planck constant.

Chapter 7 focuses on QDs made of PbS, which are typically capped by an organic ligand shell. These organic ligands act as surface passivation layer and introduce higher stability of the QD surfaces against chemical degradation of the surfaces, increase solubility in common organic solvents and enable solution procession via large scale techniques such as spray coating or printing. Furthermore, the ligands act as a spacer in closed packed QD solids, leading to a superlattice structure. Replacing the ligand shell via ligand-exchange engineering is a versatile method to functionalize the QDs for various purposes. By tuning the ratio of QD precursor and ligands during the synthesis, a controlled size and size dispersion can be achieved. Depending on the PbS QD size, the individual QD shape varies from octahedron to truncated octahedron and cubooctahedron. Size, shape, and ligand shell have strong influence on the self-assembly of QDs into closed-packed solids. In these solids, the wave-function of adjacent QDs overlap, forming a strongly-coupled configuration that is beneficial for most optoelectronic applications (Figure 2.8c). The QD solid's energetic landscape formed by the closed-packed QDs is crucially dependent on the spatial disorder. Variation from a mean inter-dot distance can lead to suppressed charge-carrier transport and impact the performance in applications.

The dependency of the electronic structure in QD solids upon their coupling and hence on their inter-dot distance requires an understanding of the influence of mechanical stress on the QD solids, especially with respect to the application in optoelectronic devices on flexible substrates. *Gong et al.* investigated the PL emission of perovskite QDs embedded in a flexible polymer matrix as function of strain and discovered PL enhancement with elongation (Figure 2.9a). [41] The authors suggest changing inter-dot distances d as explanation for these novel findings, by comparing different loading concentrations of QDs inside the polymer matrix. A true understanding of morphology and inter-dot distances within different QD solids are precisely accessible with GISAXS, as, for instance,

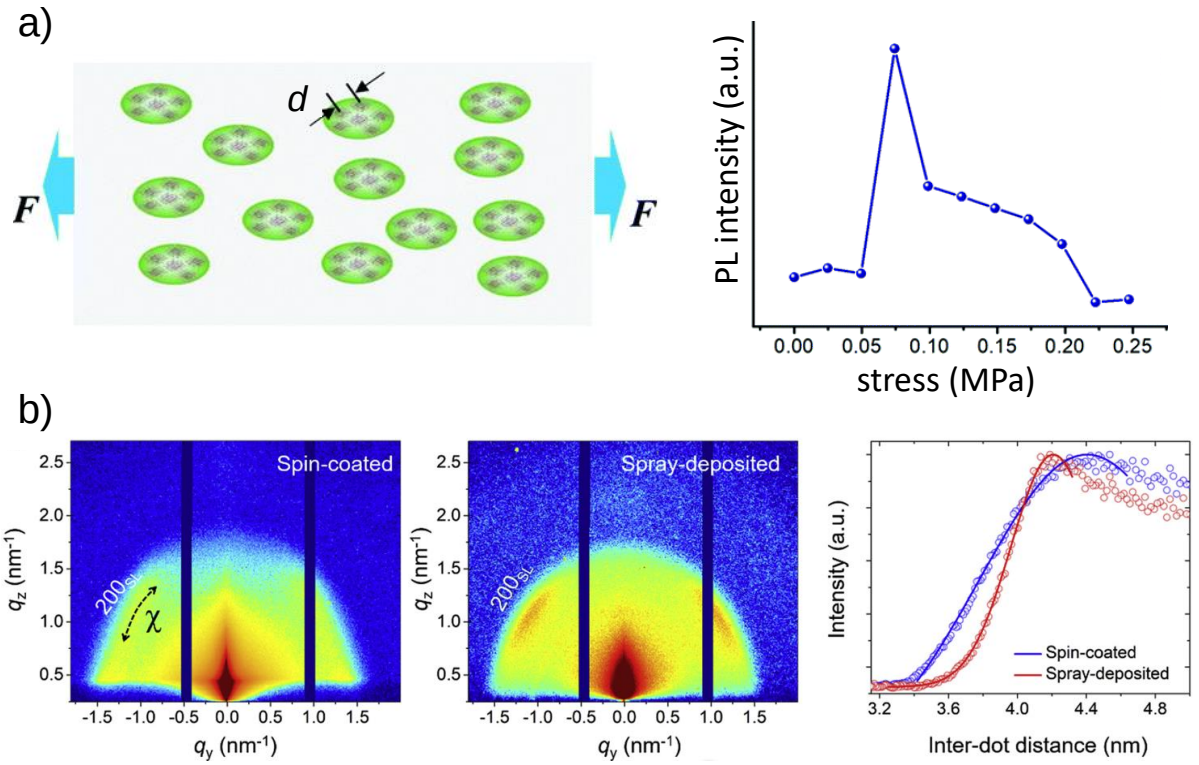

Figure 2.9.: Varying inter-dot distances in QD solids. a) Elongation of perovskite QDs in a polymer matrix changes the PL emission with a maximum intensity at a certain level of stress. Adapted from Ref. [41] with permission from the Royal Society of Chemistry, Copyright 2020. b) GISAXS provides precise insights to varying inter-dot distances between spin coated and spray coated PbS QD solids. Adapted from Ref. [42] with permission from Elsevier, Copyright 2020.

is shown by *Chen et al.* on PbS QD solids, which are prepared by spin coating and spray coating (Figure 2.9b). [42] Thus, *in-situ* GISAXS has the strong potential to uncover the structure-function-relationship upon deformation in QD solids and to complement the inspiring work of *Gong et al.*, as presented in Chapter 7.

2.4. X-ray and Neutron Scattering Fundamentals

With the high brilliance and time-resolution of a synchrotron, advanced scattering experiments, such as *in-situ* investigation of film formation and deformation, can be performed. [43] X-ray and neutron scattering experiments are highly complementary, thanks to different contrast sensitivity. This section deals with the theoretical principals of the scattering methods used in this thesis.

The X-ray scattering methods used in this thesis are all based on the concept of electro-

magnetic waves that interact and penetrate matter. This is described by the Helmholtz Equation as follows:

$$\nabla^2 \vec{E}\left(\vec{r}\right) + k^2 n^2\left(\vec{r}\right) \vec{E}\left(\vec{r}\right) = 0 \tag{2.7}$$

where $\vec{E}$ is the wave function, k the wave number, and $n\left(\vec{r}\right)$ the refractive index. The concept of refractive index is at the heart of light-matter interactions, as it brings the electromagnetic wave's wavelength and the electron density of matter into relation:

$$n\left(\vec{r},\lambda\right) = 1 - \delta\left(\vec{r},\lambda\right) + i\beta\left(\vec{r},\lambda\right) \tag{2.8}$$

The dispersion $\delta\left(\vec{r},\lambda\right)$ is a function of the specific electron density $\rho_r\left(\vec{r}\right)$, the classical electron radius $r_e = \frac{e^2}{4\pi\epsilon_0\mu_0 c^2}$, and the atomic form factor $f_j\left(\lambda\right) = f_j^0 + f_j'\left(\lambda\right) + if_j''\left(\lambda\right)$. Summing the real part of the atomic form factor over each chemical element j of the material, weighted by the stoichiometric fraction c_j and divided by the sum over the electron number Z_j, yields:

$$\delta\left(\vec{r},\lambda\right) = \frac{\lambda^2}{2\pi}\rho_e\left(\vec{r}\right) r_e \frac{\sum_j c_j \left(f_j^0 + f_j'\left(\lambda\right)\right)}{\sum_j Z_j} = \frac{\lambda^2}{2\pi}\mathfrak{Re}\left(SLD\right) \approx \frac{\lambda^2}{2\pi}\rho_e\left(\vec{r}\right) r_e \tag{2.9}$$

Here, SLD denotes the scattering length density. For the absorption $\beta\left(\vec{r},\lambda\right)$, the sum over the real part of the atomic form factor is replaced by its imaginary part:

$$\beta\left(\vec{r},\lambda\right) = \frac{\lambda^2}{2\pi}\rho_e\left(\vec{r}\right) r_e \frac{\sum_j c_j f_j''\left(\lambda\right)}{\sum_j Z_j} = \frac{\lambda^2}{2\pi}\mathfrak{Im}\left(SLD\right) \approx \frac{\lambda}{4\pi}\mu\left(\vec{r}\right) \tag{2.10}$$

For monochromatic light ($\lambda = const.$), both terms can be further simplified using the approximations $f_j^0 \approx Z_j$ and $f_j' \ll f_j^0$. Dispersion and absorption are in the order of 10^{-6} and 10^{-7}, respectively. Hence, in contrast to visible light, the refractive index is below 1. In order to probe interfaces with scattering methods, the incoming X-ray needs to experience a change in refractive index. Hence, a detectable interface consists of two domains with distinct SLD. A measure of the scattering strength is the scattering contrast of two interfaces with refractive indices $n_1 \neq n_2$, as defined as:

$$\left|\Delta\right|^2 = \left(\delta_1 - \delta_2\right)^2 + \left(\beta_1 - \beta_2\right)^2 \tag{2.11}$$

According to Babinet's principle, it is hereby only this scattering contrast, which is detectable, and it is not possible to distinguish either of the both domains with respective refractive index (Figure 2.10). This principle is important to keep in mind when analyzing scattering data. A typical example is nanoparticles embedded in a matrix, where obtained domain sizes could either originate from the nanoparticle diameter or the separating domain walls. Complementary measurements of, e.g., reference samples, real-space microscopy, combined X-ray and neutron scattering, or diffraction are suitable ways to identify how individual domains contribute to the scattering.

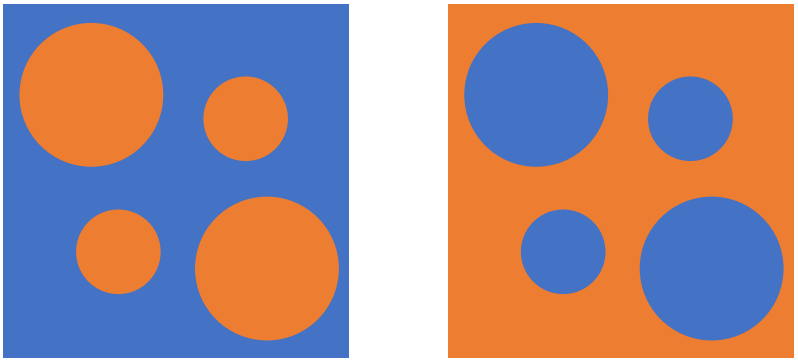

Figure 2.10.: Illustration of scattering contrast. X-ray and neutron scattering detects interfaces arising from a contrast variation $|\Delta|^2$ and do not directly relate domains to a certain SLD. According to Babinet's principle, scattering from an 'orange' domain in a 'blue' matrix yields the same intensity pattern as scattering from a 'blue' domain in an 'orange' matrix.

2.5. Grazing-Incidence Small-Angle X-ray Scattering

Switching from transmission scattering geometry to reflection scattering geometry provides morphology information of films and surfaces with high statistical validity that is representative of the average film structure (Figure 2.11). Typically, transmission measurements of thin films suffer from strong background and absorption from the substrate. Compared to transmission mode, reflection mode provides a strong signal from thin films

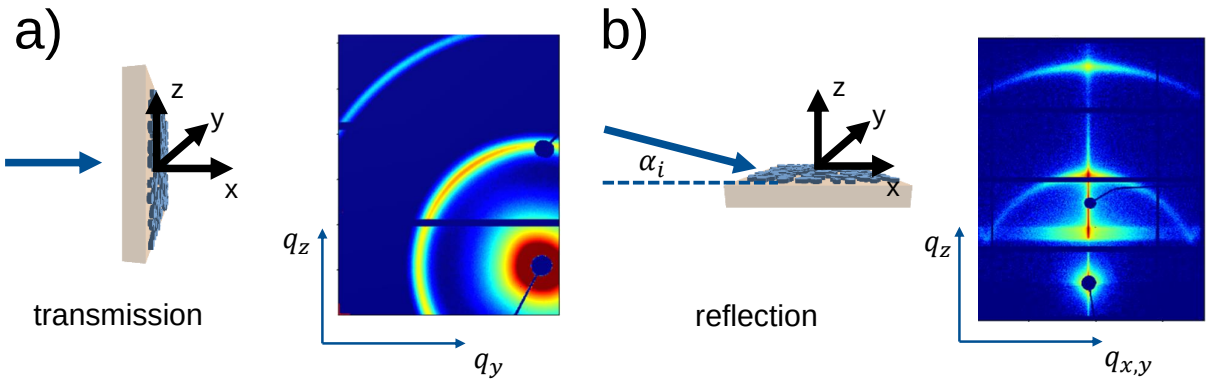

Figure 2.11.: From transmission scattering geometry to reflection. Illustration of the sample arrangement of silver behenate (AgBeh) calibration samples with the respective scattering signal in a) transmission and b) reflection measurements.

due to the footprint effect of the grazing beam scanning a large sample volume. Also, a full 3D information of the sample on the nanoscale is obtained, i.e., in-plane lateral morphology and vertical morphology along the film thickness. Hence, surface and buried structures inaccessible to surface-SEM are examined. GISAXS effectively combines dif-

fuse scattering, grazing-incidence diffraction, and small-angle scattering on a single 2D detector. [44] The non-destructive nature of the X-ray penetration compared to, e.g., cross-sectional SEM and the high temporal resolution at a synchrotron make GISAXS an optimal tool for advanced studies of *in-situ* kinetics and structure changes upon external stimulation, especially in thin films and coatings. However, higher order refractive terms add complexity to the data processing.

Thin Film Scattering Geometry

The scattering geometry is defined by the sample surface, i.e., the (x,y)-plane, and the scattering plane, i.e., the (x,z)-plane (Figure 2.12). The incident beam hits the sample surface under a shallow angle α_i, that is typically well below 1°. The scattered photons are measured as intensity on a 2D detector, where characteristic GISAXS regions can be denoted as follows: the specular beam position at $\alpha_i = \alpha_f$, diffuse scattering rod when $\alpha_i \neq \alpha_f$, out-of-plane diffuse scattering when $\Psi \neq 0$. A rotation along z probes the radial anisotropy of the sample. As most films based on polymer hybrids are isotropic, the rotation along z does not change the measured scattering pattern. Under consideration of the incoming monochromatic beam with the wave number $k_i = \frac{2\pi}{\lambda} = const.$, where λ is the wavelength, the momentum transfer $\vec{q}$ between the elastically scattered and the incoming beam is given by:

$$\vec{q} = \begin{pmatrix} q_x \\ q_y \\ q_z \end{pmatrix} = \vec{k}_f - \vec{k}_i = \frac{2\pi}{\lambda} \begin{pmatrix} \cos\alpha_f \cos\Psi - \cos\alpha_i \\ \cos\alpha_f \sin\Psi \\ \sin\alpha_f + \sin\alpha_i \end{pmatrix} \tag{2.12}$$

With the condition for elastic scattering:

$$|\vec{k}_i| = |\vec{k}_f| = \frac{2\pi}{\lambda} \tag{2.13}$$

The relation between refractive index n and the critical angle of total reflection α_c is obtained from Snell's law:

$$n = \sin(90° - \alpha_c) = \cos\alpha_c \approx 1 - \frac{\alpha_c^2}{2} \tag{2.14}$$

Hence, when neglecting small contributions from absoprtion, α_c is approximated by the real part of the SLD:

$$\alpha_c \approx \sqrt{2\delta} = \lambda\sqrt{\frac{\mathfrak{Re}\,(SLD)}{\pi}} \tag{2.15}$$

Considering the vertical component of the wavevector for the incoming beam $k_{i,z}$ and the beam transmitted through the sample $k_{t,z}$, the Fresnel transmission coefficient t has a maximum at the critical angle of total reflection with $k_{t,z} = 0$, which leads to the material dependent Yoneda peak located at $\alpha_f = \alpha_c$: [45]

$$t = \frac{2k_{i,z}}{k_{i,z} + k_{t,z}} \tag{2.16}$$

Depending on the absorption along the vertical profile of the probed volume, the penetration depth Λ probing the morphology information from the bulk is given by the vertical component of the transmitted wavevector's imaginary part:

$$\Lambda = \frac{1}{|\mathfrak{Im}(k_{t,z})|} \tag{2.17}$$

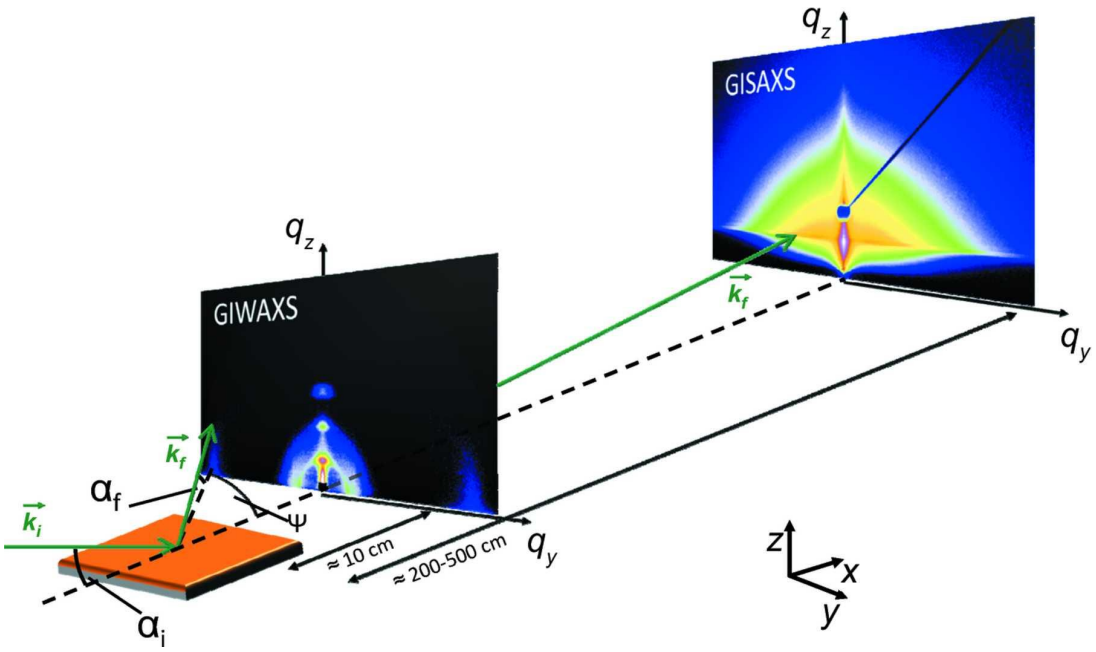

Figure 2.12.: Grazing-incidence scattering geometry. Scattered and reflected X-rays are detected at a fixed distance to the sample, which is adjusted to the incident angle α_i with respect to the incoming beam. Depending on the sample-detector distance from hundreds of mm to several m, different q-ranges and hence length scales are probed. Reprinted from Ref. [43] with permission from the International Union of Crystallography, Copyright 2015.

Distorted Wave Born Approximation

At grazing-incidence, multiple reflection and refraction events within the probed film and the substrate interface need to be taken into account. In order to adequately describe the scattering data, the so-called distorted wave Born approximation (DWBA) is used. [46] This is a first-order perturbation theory that treats, e.g., roughness as a small perturbation, $\delta V(\vec{r})$, to the smooth surface with potential $V(\vec{r})$:

$$V(\vec{r}) + \delta V(\vec{r}) \tag{2.18}$$

The obtained potential, as a function of $\vec{r}$, which is related to the surrounding electron density and the refractive index $n(\vec{r})$ in Equation 2.8, accounts for roughness and in-plane structures. The incident plane wave $\Phi_i(\vec{r}) = Ce^{i\vec{k}_1\vec{r}}$, the scattered wave $\Psi_1(\vec{r})$, and its time-reversed state $\tilde{\Psi}_2(\vec{r})$ are eigenstates of $V(r)$ according to the Helmholtz equation 2.7, where C is a normalization constant. The differential cross section of diffuse scattering, which defines the number of scattered photons within an infinitesimal solid angle, is then measured as intensity on the 2D detector and is given by Fermi's Golden Rule as a function of the perturbed potential: [46]

$$\frac{d\sigma}{d\Omega} = \frac{\left|\left\langle \tilde{\Psi}_2 \left| V \right| \Phi_i \right\rangle + \left\langle \tilde{\Psi}_2 | \delta V | \Psi_1 \right\rangle\right|^2}{16\pi^2 |C|^4} \tag{2.19}$$

The presence of δV in the second term gives rise to diffuse scattering, from which the inner nanostructure of the samples investigated with GISAXS can be deduced. For small products $q_z\sigma_z \ll 1$ of the vertical momentum transfer q_z and the standard deviation σ_z from the mean interface height z, the diffuse scattering cross section from buried structures in a matrix with scattering contrast $|\Delta|^2$ can be approximated as resulting from one effective interface: [46]

$$\frac{d\sigma}{d\Omega} = \frac{A\pi^2}{\lambda^4} |\Delta|^2 |T_i|^2 |T_f|^2 \mathfrak{P}(\vec{q}) \tag{2.20}$$

Here, A represents the surface area, which is illuminated by the beam of wavelength λ. The Fresnel transmission functions T_i and T_f have a maximum at the material specific critical angle and are constant for a fixed set of $\alpha_{i,f}$. Hence, the diffuse scattering solely depends on the diffuse scattering factor $\mathfrak{P}(\vec{q})$: [47], [48]

$$\mathfrak{P}(\vec{q}) \propto NF(\vec{q}) S(\vec{q}) \tag{2.21}$$

This allows for directly probing the amount, N, of the scattering domains, their shape and size as the Fourier transform of their electron density (form factor $F(\vec{q})$), and their arrangement (structure factor $S(\vec{q})$).

2.6. Grazing-Incidence Wide-Angle X-ray Scattering

Grazing-incidence wide-angle X-ray scattering (GIWAXS) is performed using the same scattering geometry as in GISAXS, but with a reduced sample-to-detector distance in the range of hundreds of mm (Figure 2.12). With this setup, larger momentum transfers are captured on the detector, and thus smaller distances on the atomic and molecular level are accessible. According to the Laue condition, the reciprocal lattice of crystals and molecules is probed via constructive interference of X-rays passing a set of lattice planes with the Miller indices $\{hkl\}$, when the momentum transfer $\vec{q}$ matches the reciprocal lattice vector $\vec{G}$:

$$\vec{q} = ha^* + kb^* + lc^* = \vec{G} \tag{2.22}$$

For the elastically scattered X-rays, the possible set of momentum transfer $\vec{q}$ forms the

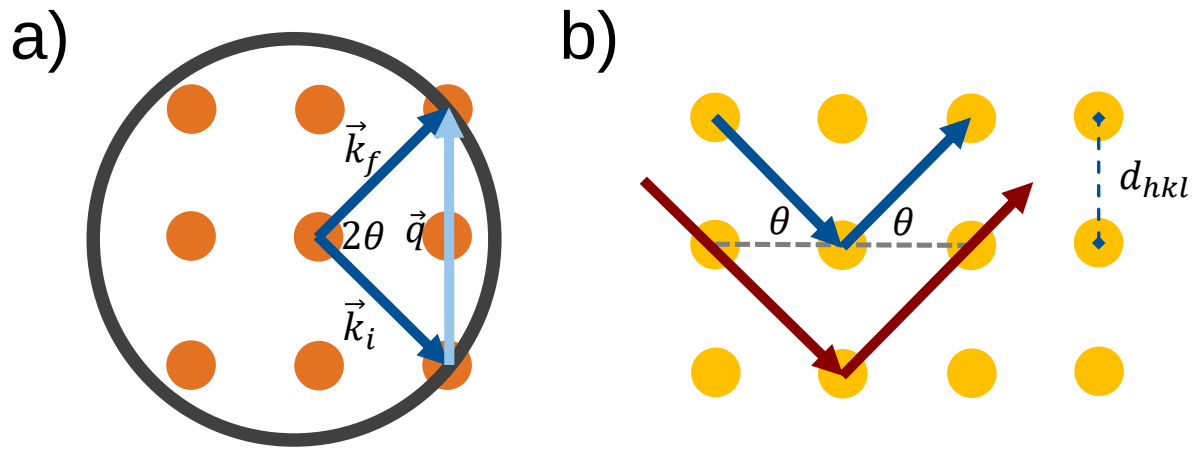

Figure 2.13.: Illustration of Laue and Bragg conditions. a) Laue: Constructive interference in reciprocal space occurs when the Ewald's sphere intersects with the reciprocal lattice. b) Bragg: Constructive interference in real space occurs when the path difference of the blue and red X-ray becomes a multiple of the wavelength λ.

surface of the so-called Ewald's sphere (Figure 2.13a). The sphere's intersections with the reciprocal lattice points are measured as a reflex on the detector. Hence, the reciprocal lattice is directly probed with GIWAXS. The Laue condition is the reciprocal equivalent to the Bragg condition in real space (Figure 2.13b), where the lattice spacing d_{hkl} is probed via constructive interference, when the path difference between interfering X-rays becomes a multiple of the wavelength λ at a certain angle θ:

$$m\lambda = 2d_{hkl} \sin(\theta) \tag{2.23}$$

When the 2D GIWAXS data is transformed from pixel space, as it is measured on the detector (Figure 2.14a), to q-space, the scattering intensity is represented as a function of $(q_z,\ q_r)$ with $q_r = \sqrt{q_x^2 + q_y^2}$. This leads to a reshaped detector image, with a missing wedge of no scattering information, as the surface of the Ewald's sphere is sliced onto a 2D map (Figure 2.14b). Another useful representation is the sector plot (Figure 2.14c), where the scattering intensity is presented as a function of $(q = |\vec{q}|, \chi)$. Also here, a missing

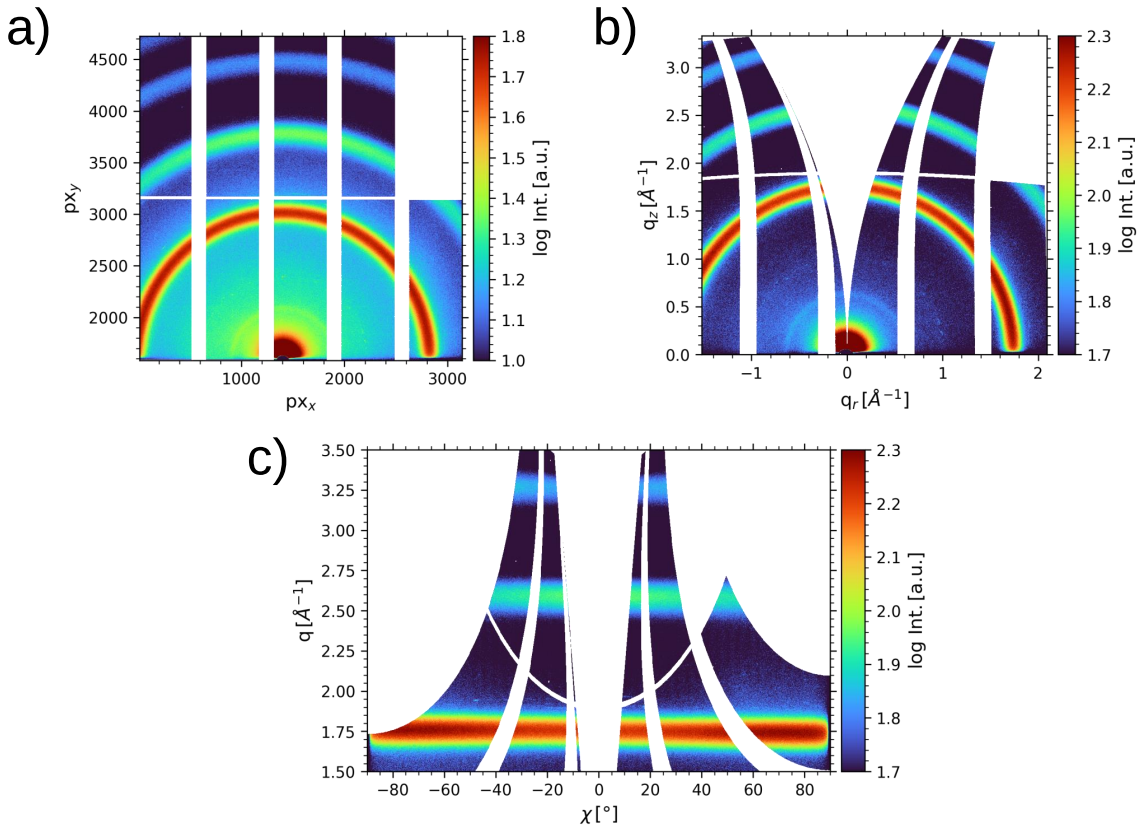

Figure 2.14.: Representation of 2D GIWAXS data a) As-measured data in pixel space. b) Reshaped data in q-space. c) Data as function of $(q,\ \chi)$ represented in a sector plot. The 2D GIWAXS data is plotted by use of the software INSIGHT (M. A. Reus, L. K. Reb, P. Müller-Buschbaum; INSIGHT: The in situ GIXS heuristic tool for efficient reduction of grazing-incidence scattering data; https://www.ph.nat.tum.de/functmat/forschung-research/insight/).

wedge of inaccessible data is centered in the intensity map. Azimuthal integration along the horizontal direction of the sector plot leads to 1D diffraction patterns as function of q, whereas radial integration of a reflex along the vertical direction of the sector plot yields information on the respective lattice planes' orientation with respect to the substrate.

To analyze 2D GIWAXS data, the data is integrated along the azimuthal angle χ to obtain 1D diffraction patterns as function of q, also called pseudo-XRD cuts. The

profiles are fitted with Gaussian functions to extract peak center values, from which lattice constant and spacing can be extracted:

$$\frac{q_{hkl}}{2\pi} = \frac{1}{d_{hkl}} = \sqrt{\left(\frac{h}{a}\right)^2 + \left(\frac{k}{b}\right)^2 + \left(\frac{l}{c}\right)^2} \tag{2.24}$$

The peak broadening of a reflex is described by the full width at half maximum (FWHM) obtained from the Gaussian fits and consists of contributions from the sample morphology as well as from instrumental broadening, which add up quadratically:

$$\Delta_{meas}^2 = \Delta_{samp}^2 + \Delta_{inst}^2 \tag{2.25}$$

Here, Δ_{meas} is the full width at half maximum as obtained from the Gaussian fits as measured, Δ_{samp} and Δ_{inst} the broadening introduced by the sample and the instrumental setup, respectively. The instrumental broadening is typically determined from calibration standards such as silver behenate (AgBeh) and lanthanum hexaboride (LaB_6).

According to the Williamson-Hall theory, the sample's peak broadening arises from the crystallite size D and microstrain ε affecting the lattice spacing: [49]

$$\Delta_{samp} = \sqrt{\Delta_{meas}^2 - \Delta_{inst}^2} = \frac{2\pi K}{D} + \varepsilon \frac{q_{hkl}}{2\pi} \tag{2.26}$$

Here, K is the Scherrer factor, which depends on the measure of peak broadening, e.g., FWHM or integral breadth, the crystallite shape, which can be different from its unit cell, and the crystallite size distribution. [50], [51] For the case of titania crystallite sizes obtained from the FWHM of a reflex, the factor K is typically set to 0.9. By plotting the corrected FWHM as function of the respective q-reflexes, D and ε can be calculated from the intercept and slope, respectively, of a linear fit. This Williamson-Hall method to separate crystallite size and microstrain from peak broadening requires a reasonable number of q-reflexes for good quality of the linear fit and the outcomes should be interpreted rather qualitatively, e.g, in comparison to a set of samples with varying synthesis conditions. Since peak broadening of titania crystallites mostly stem from the finite crystallite size, the evaluation of microstrain contribution is neglected in this thesis. Hence, the second term in Equation 2.26 is omitted, which yields the Scherrer equation: [51]

$$L_{hkl} = \frac{2\pi K}{\Delta_{samp}} \tag{2.27}$$

Here, L_{hkl} is the coherence length along a certain direction [hkl], which serves as an estimation for the lower limit of the crystallite size along the respective direction.

2.7. Grazing-Incidence Small-Angle Neutron Scattering

While the concept of grazing-incidence small-angle neutron scattering (GISANS) is the same like GISAXS, unique properties arise from the substitution of X-rays with neutrons. [52] Neutrons are massive particles with spin and no elemental charge, meaning they do not interact with the electron density of materials but with the atomic nucleus. This fundamental difference to X-rays allows for probing magnetic interfaces, hard and soft-matter materials with characteristic contrast conditions and domain sensitivity. The scattering potential is described by the Fermi pseudo-potential within the Born approximation, and following theoretical aspects are based on the references in [53], [54]:

$$V_F = \left(\frac{2\pi\hbar}{m}\right)\delta\left(\vec{r}\right)b \tag{2.28}$$

Here, $\hbar$ is the reduced Planck constant, m the neutron's mass, $\delta\left(\vec{r}\right)$ the neutron position with respect to the atomic nucleus, and the complex number $b = \mathfrak{Re}\left(b\right) + i\mathfrak{Im}\left(b\right)$, describing the scattering length of a bound nucleus. The bound scattering length b is in general a sum of the coherent scattering length b_c and the incoherent scattering length b_i, and takes interaction between the neutron spin $\vec{s}$ and the nuclear spin $\vec{I}$ into account:

$$b = b_c + \frac{b_i}{\sqrt{I\left(I+1\right)}}\vec{s}\cdot\vec{I} \tag{2.29}$$

For a given nuclear spin quantum number I, the scattering length is written for neutrons with the two states spin-up $(+)$ and spin-down $(-)$ as $b^{\pm}$:

$$b^{\pm} = b_c \pm \sqrt{\left(\frac{I}{I+1}\right)^{\pm}}b_i \tag{2.30}$$

It follows for the coherent and incoherent scattering length b_c and b_i, respectively:

$$b_c = g^+b^+ + g^-b^-, \qquad b_i = \sqrt{g^+g^-}\left(b^+ - b^-\right) \tag{2.31}$$

Here, $g^{\pm}$ are weighting factors, which satisfy $g^+ + g^- = 1$:

$$g^+ = \frac{I+1}{2I+1}, \qquad g^- = \frac{I}{2I+1} \tag{2.32}$$

The neutron scattering cross section σ_s is the sum of the coherent and incoherent scattering cross sections σ_c and σ_i, respectively. For the case of unpolarized neutrons or neuclei, the neutron scattering cross section is:

$$\sigma_s = \sigma_c + \sigma_i = 4\pi|b_c|^2 + 4\pi|b_i|^2 \tag{2.33}$$

The imaginary part of the scattering length gives rise to absorption of neutrons in the sample, which is described by the absorption cross section σ_a:

$$\sigma_a = \frac{4\pi}{k_0}\mathfrak{Im}\left(b\right) = \frac{4\pi}{k_0}\left(g^{+}\mathfrak{Im}\left(b^{+}\right) + g^{-}\mathfrak{Im}\left(b^{-}\right)\right) \tag{2.34}$$

Multiplication of the scattering length b and the absorption cross section σ_a with the atomic number density N yields the neutron dispersion and absorption, respectively: [55]

$$\delta\left(\vec{r},\lambda\right) = \frac{\lambda^2}{2\pi}\frac{\rho N_A \sum_{j=1}^{N} n_j b_j}{\sum_{j=1}^{N} M_j} = \frac{\lambda^2}{2\pi}Nb = \frac{\lambda^2}{2\pi}\mathfrak{Re}\left(SLD\right) \tag{2.35}$$

$$\beta\left(\vec{r},\lambda\right) = \frac{\lambda}{4\pi}N\sigma_a = \frac{\lambda}{4\pi}\mathfrak{Im}\left(SLD\right) \tag{2.36}$$

Here, N_A is the Avogadro number, ρ the material density, M the molar mass, and n the For a given compound based on j elements, the scattering length and atomic number densities are summed up, where the sum over b_c yields the coherent neutron SLD and the sum over b_i the incoherent neutron SLD. In analogy to GISAXS, the critical angle of total reflection for neutrons is approximated by neglecting the typically small absorption as:

$$\alpha_c \approx \lambda\sqrt{\frac{Nb}{\pi}} \tag{2.37}$$

Especially light elements, which have a low SLD for X-rays may benefit from high neutron SLD as the magnitude of the bound atom's scattering length b in Equation 2.29 is strongly fluctuating and is irregular of the electron number Z.

2.8. Analysis of GISAXS and GISANS Data

The 2D GISAXS and 2D GISANS data is reduced to 1D intensity profiles vertically along q_z at $q_y = 0$ and horizontally along q_y at the Yoneda peak, $q_z\left(\alpha_c\right)$ (Figure 2.15). With this approach, the effective interface approximation becomes valid and one obtains material specific information about the lateral morphology from $I\left(q_y\right)$ with a strong signal due to the maximum of T_f in Equation 2.20. To extract domain sizes with radius R and their size distributions as well as mean center-to-center distances D, the intensity profile of the integrated horizontal line cuts is modeled with a customized, python-based software according to the following expression: [56]

$$I\left(q\right) \propto \sum_i N_i \left\langle \left|F\left(q,R_i\right)\right|^2 \right\rangle S\left(q,D_i\right) \tag{2.38}$$

Here, the diffuse scattering factor is given in the local monodisperse approximation, where it is described by the sum over i domains. The domains, assumed to be monodisperse within the beam's coherence length, have an average form factor weighted by their Gaussian standard deviation σ_i: [56]

$$\left\langle \left| F\left(q, R_i\right) \right|^2 \right\rangle = \frac{\int \sigma_i\left(R\right) \left| F\left(q, R\right) \right|^2 dR}{\int \sigma_i\left(R\right) dR} \tag{2.39}$$

Cylindrical form factors are applied since the scattering signal consists of rotation sym-

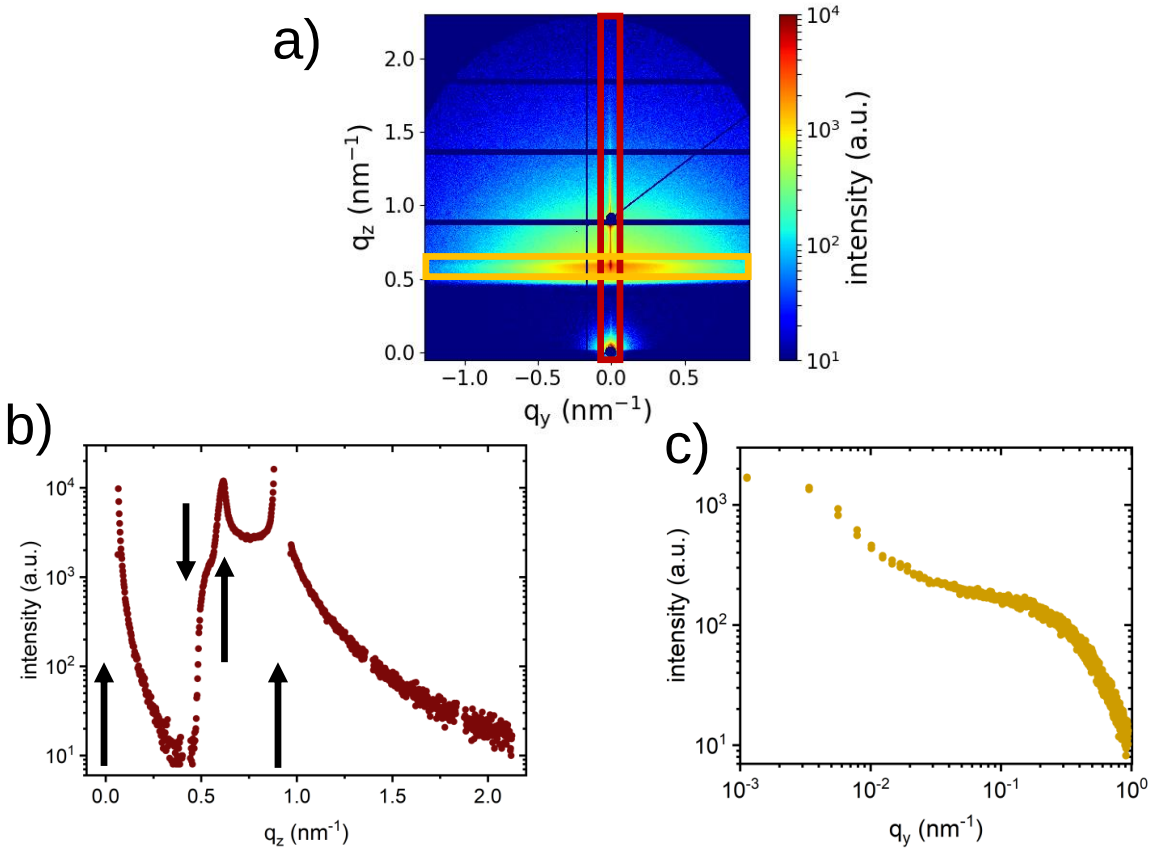

Figure 2.15.: Vertical and horizontal line cuts taken from 2D GISAXS. a) The 2D GISAXS data is reduced to vertical line cuts by integration of about 3 pixels (red box) and to horizontal line cuts by integreation of about 5 pixels (yellow box). b) Vertical line cuts with the typical GISAXS features, indicated by arrows from left to right: direct beam position at $q_z\left(\alpha_f = 0\right)$, sample horizon position at $q_z\left(\alpha_f = \alpha_i\right)$, Yoneda peak position at $q_z\left(\alpha_f = \alpha_c + \alpha_i\right)$, which is a consequence of the maximum in the Fresnel coefficient function, and the specular beam position at $q_z\left(\alpha_f = 2\alpha_i\right)$. c) Horizontal line cuts taken at the Yoneda peak position are used for the data modeling as explained in this section. The same data reduction is performed for 2D GISANS data.

metric averages of scattering centers within the probed sample volume, with the vertical

axis defined by the film-substrate and film-air interfaces. With $q_{z,c} \approx 0$, the cylindrical form factor is approximated by:

$$|F_{cyl}(q_y)|^2 = \left(R\frac{J_1(q_y, R)}{q_y}\right)^2 \tag{2.40}$$

Here, J_1 is the Bessel function of first kind. The Hosemann interference function is applied as a structure factor to model the center-to-center domain distances on a 1D paractystal lattice with $q_{z,c} \approx 0$: [57], [58]

$$S(q_y) = -\frac{1 - \exp\left(\pi\sigma_D^2 D^2 q_y^2\right)^2}{1 + \exp\left(\pi\sigma_D^2 D^2 q_y^2\right)^2 - 2\exp\left(\pi\sigma_D^2 D^2 q_y^2\right)\cos(q_y D)} \tag{2.41}$$

Both the size distribution of a single domain type and the degree of long-range order of the domain type's lateral arrangement are given as the standard deviation σ_x from a mean domain radius $x = R$ and mean center-to-center domain distance $x = D$, respectively, and expressed by a Gaussian distribution:

$$p(x) = \frac{1}{\sqrt{2\pi}\sigma_x}\exp\left(-\frac{(x - \langle x\rangle)^2}{2\sigma_x}\right) \tag{2.42}$$

Depending on the respective film morphology, a sum of up to three distinct domain types is applied in the model. In case no structural correlation between the domains is found, the structure factor S is set to 1.

Chapter 3

Sample Preparation

Parts of this chapter are based on the publications *Low-Temperature and Water-Based Biotemplating of Nanostructured Foam-Like Titania Films Using β-Lactoglobulin* (J. E. Heger, W. Chen, S. Yin, N. Li, V. Körstgens, C. J. Brett, W. Ohm, S. V. Roth, P. Müller-Buschbaum, *Advanced Functional Materials*, **32**, 2113080 (2022)) and *Superlattice Deformation in Quantum Dot Films on Flexible Substrates via Uniaxial Strain* (J. E. Heger, W. Chen, H. Zhong, T. Xiao, C. Harder, F. A. C. Apfelbeck, A. F. Weinzierl, R. Boldt, L. Schraa, E. Euchler, A. K. Sambale, K. Schneider, M. Schwartzkopf, S. V. Roth, P. Müller-Buschbaum, *Nanoscale Horizons*, **8**, 383-395 (2023)). [17], [18] Reprinted from [17] with permission from Wiley, Copyright 2022 and reproduced from [18] with permission from the Royal Society of Chemistry.

3.1. Substrates

Silicon Substrates

Silicon substrates (Silicon Materials, Kaufering, Germany) are used as substrates for the biohybrid film deposition and as a reference substrate to the flexible susbtrates for QD superlattice films. The substrates have a thickness of 0.525 mm and are polished on the surface with a (100) crystal orientation. P-doped Si substrates are used for SEM surface imaging, X-ray and neutron scattering, and undoped Si substrates for FTIR spectroscopy.

An adjusted piranha acid bath is used to clean the Si substrates prior to film deposition and install a defined surface potential for increased wettability of the films. First, 54 mL Milli-Q water (18.2 $M\Omega cm^{-1}$) is filled in a glass beaker, second 84 mL of hydrogen peroxide (Carl Roth, Germany), and lastly 198 mL of sulfuric acid (Carl Roth, Germany) are carefully and slowly added to the water. The beaker containing the acid bath is heated in a water bath set to 80 °C. After that, the cut Si wafer are fixed on a poly(tetrafluoroethylene)

(PTFE) sample holder and put inside the acid bath for 15 min. Subsqeuent flushing of the samples in three different beakers filled with 500 ml Milli-Q water, followed by rinsing the sample with a Milli-Q water from a spray bottle, washes the remaining acid bath from the substrates.

To ensure an increased wettability of the spray deposited film from aqueous solution, the Si substrates are surface treated in a controlled oxygen plasma (Nano Plasma Cleaner, Diener Electronic, Ebhausen, Germany). After putting the substrates into the plasma chamber and pumping vacuum to 0.1 mbar, oxygen atmosphere at a pressure of 0.4 mbar is introduced. The oxygen plasma is initiated by applying a frequency of 40 kHz at 250 W. As consequence, polar hydroxyl groups are forming on the Si surface, which yields a sufficient hydrophilicity of the substrate surfaces after 10 min. Film deposition is performed in direct sequence to the oxygen plasma treatment, as the effect is only of relatively short permanence.

PDMS Substrates

Poly(dimethylsiloxane) (PDMS) substrates are used as a flexible support for the deformation of QD superlattices upon strain elongation. The PDMS substrates are synthesized by mixing base and curing agent of SYLGARD 184 in a ratio of 7 : 1. The mixture is poured into a rectangular mold and stored in a vacuumed desiccator for outgassing of remaining air. Subsequently, the resulting PDMS slides are cut into substrates with dimensions of 10 mm $\times$ 60 mm and a thickness of 1 mm. Commercially available PDMS susbtrates (Goodfellow GmbH, Hamburg, Germany) with same dimensions are used as a flexible reference substrate for QD superlattice films.

Optical microscopy images reveal a smooth and homogeneous surface of the custom-made PDMS substrate, compared to a heterogeneous surface of the commercial PDMS substrate (Figure 3.1a). To evaluate the influence of the different PDMS surfaces on the superlattice morphology, PbS QD films on custom-made and commercial PDMS substrates are compared with GISAXS. The scattering intensity shows Bragg reflexes related to a nested FCC/BCT superlattice on the custom-made PDMS substrate (Figure 3.1b) and a single reflex with strong azimuthal and radial broadening on the commercial PDMS substrate, indicating weak long-range order and poor superlattice formation (Figure 3.1c). The substrate's surface influences the PbS QD film's adhesion and hence influences grain boundary formation during spin-coating and stretching. However, grain boundaries play a minor role in the observed strain distribution as discussed in Chapter 7. Since the heterogeneous surface does not provide superlattices with defined unit cells and long-range order, a homogeneous surface is necessary to form regular superlattices. Further, the reference PL spectrum of PbS QDs spin-coated on a silicon substrate shows good agreement

with the PL spectrum on custom-made PDMS (Figure 3.1d). Thus, custom-made PDMS is used as flexible substrate for the *in-situ* GISAXS, *in-situ* PL, and *in-situ* absorbance measurements during PbS QD superlattice deformation in Chapter 7.

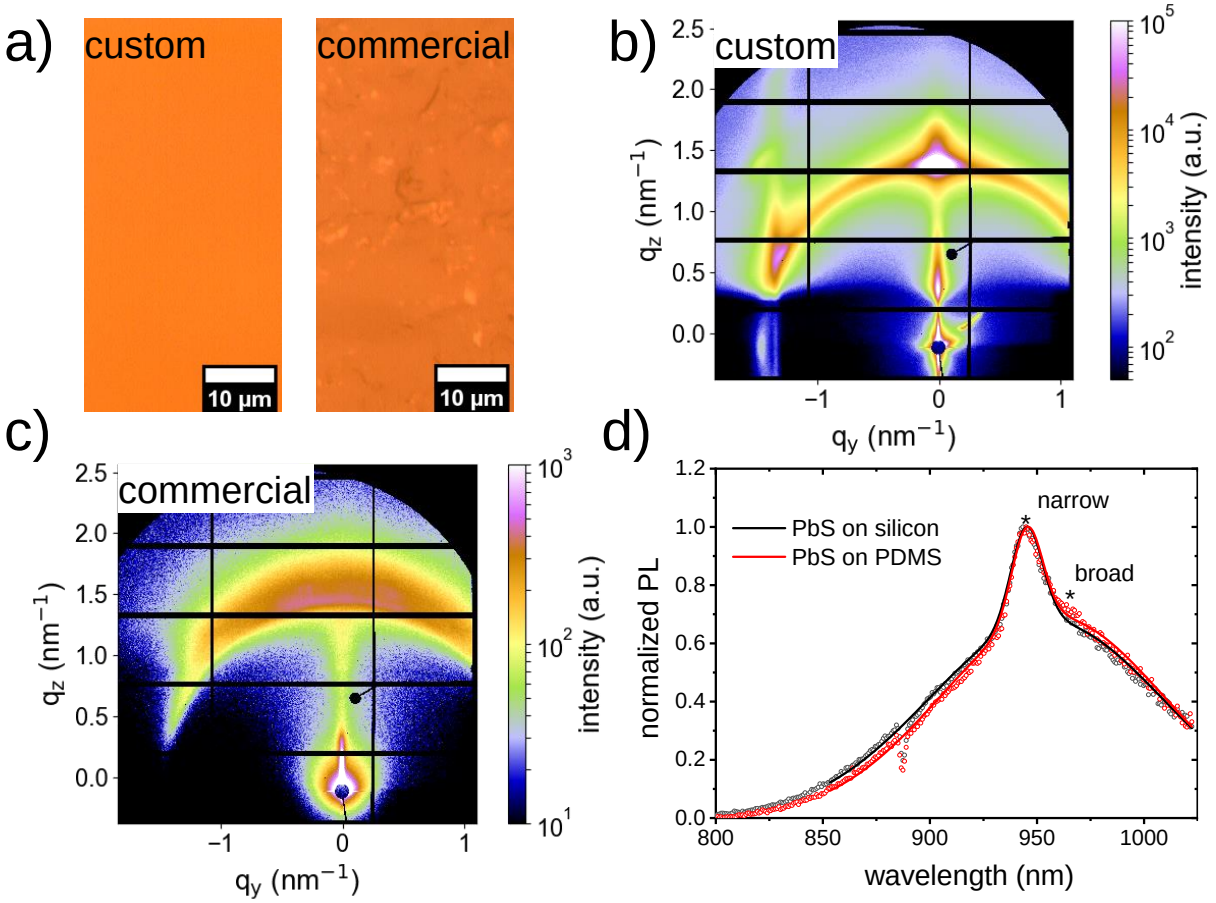

Figure 3.1.: Influence of the substrate on the PbS QD superlattice. a) Surfaces of the custom-made and commercial PDMS substrate obtained from optical microscopy. b) 2D GISAXS data of PbS QDs spin-coated on the commercial and c) on the custom-made PDMS substrate, respectively. d) PL spectra of PbS QD films on the custom-made PDMS substrate and on a silicon substrate as reference.

3.2. Spray Deposition of β-lg-templated Titania Films

The biopolymer β-lg, lyophilized powder, 90 % PAGE) and the titania precursor TTIP (97 %) and TiBALDh (50 wt. % in H_2O) are purchased from Sigma-Aldrich, Germany, and used without any further purification. Hydrochloric acid (37 %) is purchased from Carl Roth, Germany. The aqueous solutions are based on deionized water (Milli-Q, 18.2 MΩcm^{-1}).

The sample solutions under investigation in Chapter 5 are prepared as follows: 12 M HCl are diluted to 10×10^{-3} M HCl with deionized water and used as a host solvent. First, 4 mL of 10×10^{-3} M HCl are mixed with 148 µL TTIP. Second, 20 mg of β-lg are added and kept stirring for 30 min at room temperature to form a biohybrid sol–gel. After that, the β-lg:TTIP sol–gel is kept stirring in a sand bath at a temperature of 90 °C for 22 h, to promote the hydrothermal synthesis of titania nanoparticles. Also, the heating under acidic conditions leads to denaturation and unfolding of β-lg to fibrillar aggregates. [34], [59] These aggregates electrostatically bind to the titania nanoparticles and act as a templating network. The sol–gel is eventually immersed and quenched in a water bath at the temperature of 4 °C. Pure β-lg and pristine titania reference solutions are fabricated the same way without addition of the counterpart.

The sample solutions under investigation in Chapter 6 are prepared as follows: Solutions of 10 mg mL^{-1} β-lg in distilled water are adjusted to pH 5 ± 0.5 and pH 2 ± 0.5 by addition of 1 µL and 10 µL 12 M HCl, respectively. Without addition of HCl, the solutions remain at pH 7 ± 0.5. Denaturation of β-lg is introduced via thermal treatment at 90 °C for 5 hours at pH 2 and for 30 min at pH 5 and pH 7. [34] After quenching the heated solutions in an ice bath, 2.5 mL of the respective solutions are mixed with 79.2 µL TiBALDh (50 wt. % in H_2O) to obtain the biohybrid solutions. TiBALDh reference solutions are prepared by diluting the precursor with 2.5 mL distilled water and addition of 0 µL, 1 µL, and 10 µL HCl (12 M), respectively.

In-situ and *ex-situ* samples in Chapter 5 are prepared by spray deposition of the resulting β-lg:titania hybrid dispersions with an air atomizing nozzle of type JAUCO D555000 (Spraying Systems Co., Hamburg, Germany). The nozzle provides a cone-shaped spray coat with an opening angle of 10°, which results in a circular film of the biohybrid composite. The radius of the covered area depended on the sample-substrate distance as well as the opening angle of the spray cone. Precleaned and surface-treated silicon substrates are placed at a distance of 20 cm to the nozzle and heated to 120 °C. Pulsed spray deposition based on 0.5-1 mL of β-lg:titania solution is performed in intervals of 0.2 s spraying and 2.8 s drying, followed by 10 s of annealing. Hence, a single spray cycle lasts 3 s in total. A nitrogen flow set to 1 bar is used as carrier gas with a flow rate of 125 µL s^{-1}. The pulsed deposition is controlled by the magnetic valve MEBH-5/2-1/8-B, purchased from Festo SE & Co KG. More details on the spray setup used for *ex-situ* samples are given in Appendix B.

The samples under investigation in Chapter 6 are spray coated in a commercial spray chamber (PVA 350, Werner Wirth GmbH, Hamburg, Germany), located at the laboratories of the Zentrum für Energie und Information (ZEI, TU Munich, Garching), with a spray nozzle for general purpose (781S, Nordson, USA). Precleaned and surface-treated

silicon substrates with a dimension of 7x7 cm are coated by moving the spray nozzle with a speed of 150 mm s^{-1} in a grid with 5 mm spacing and a distance to the sample of 3.5 cm. The atomizing pressure of the oil-free nitrogen carrier gas is set to 0.5 bar. The samples are heated to 80 °C during deposition and annealed at 140 °C for 10 min after deposition. The wafers are used for GISANS measurements as deposited and are cut down to about 2x2 cm for GISAXS and GIWAXS measurements. FTIR samples are drop-casted from 100 µL of the respective solutions on 1x1 cm undoped silicon wafers and dried at 140 °C for 10 min.

The as-deposited biohybrid samples in Chapter 5 are irradiated with UV-light (HTC 400-241, Osram AG) for 24 h, to remove the biomatrix and to obtain the biotemplated, nanostructured titania films. The pure β-lg and pristine titania reference sample are not treated with UV-light.

To achieve nanostructured and crystalline titania films, the as-deposited biohybrid samples in Chapter 6 are calcined for 2 hours at 500 °C with a heating ramp of 1 °C min^{-1} to remove the template β-lg and the organic parts of the Ti(IV) lactate complexes. The same calcination protocol is performed for the pure TiBALDh samples as reference.

3.3. PbS QD Superlattices on Flexible Substrates

Stock solutions of PbS QDs in octane with a concentration of 80 mg mL^{-1} are supplied from Shenzhen Technology University (SZTU, China) and synthesized according to the protocol described in this section.

The QDs were synthesized following the recipe by *Chen et al.* with slight modifications as follows. [60] 1.20 g lead oxide (PbO) are dissolved in 3 mL oleic acid (OA) and 10 mL octadecene (ODE) as Pb-precursor. 0.5 mL bis(trimethylsilyl)sulfide ((TMS)2S) are diluted in 2 mL ODE as S-precursor. After the purification of the Pb-precursor solvent at 100 °C under vacuum conditions for 6 hours, the solvent is further shifted to an argon atmosphere. The S-precursor is injected into the Pb-precursor swiftly and the temperature of the mixture remains at 95 °C for 3 min for the QD crystallization reaction. Afterwards, the reaction is terminated by cooling in an ice bath. The resulting PbS QD solution is washed twice with a solvent mixture of acetone and methanol (volume ratio 2 : 1), in which the QDs are precipitated by centrifugation at 5000 rpm and dried with nitrogen to obtain a powder. For further use, the powder is redispersed in octane with a concentration of 80 mg mL^{-1}.

Two PbS QD batches are synthesized according to the same protocol. The first is used for the *in-situ* GISAXS and *in-situ* PL measurements. The second batch is used for HRTEM and *in-situ* absorbance measurements (Figure 7.10). All QD batches have

an OA ligand capping that is synthesized according to the literature and have a relaxed chain length l_0^{lig} of about 2.5 nm. [61]

The films for the *in-situ* GISAXS and PL measurements are deposited from 50 mL of the final solution on the PDMS substrates by spin-coating at 3000 rpm. It is noteworthy that the PDMS surface quality affects the degree of long-range order so that smooth and homogenous surfaces are beneficial to form PbS QD superlattices. The influence of different substrates on morphology and PL is discussed briefly in Figure 3.1 in the beginning of this section.

Chapter 4

Sample Characterization

Parts of this chapter are based on the publications *Low-Temperature and Water-Based Biotemplating of Nanostructured Foam-Like Titania Films Using β-Lactoglobulin* (J. E. Heger, W. Chen, S. Yin, N. Li, V. Körstgens, C. J. Brett, W. Ohm, S. V. Roth, P. Müller-Buschbaum, *Advanced Functional Materials*, **32**, 2113080 (2022)) and *Superlattice Deformation in Quantum Dot Films on Flexible Substrates via Uniaxial Strain* (J. E. Heger, W. Chen, H. Zhong, T. Xiao, C. Harder, F. A. C. Apfelbeck, A. F. Weinzierl, R. Boldt, L. Schraa, E. Euchler, A. K. Sambale, K. Schneider, M. Schwartzkopf, S. V. Roth, P. Müller-Buschbaum, *Nanoscale Horizons*, **8**, 383-395 (2023)). [17], [18] Reprinted from [17] with permission from Wiley, Copyright 2022 and reproduced from [18] with permission from the Royal Society of Chemistry.

4.1. Scanning Electron Microscopy

Scanning electron microscopy (SEM) probes the surface of a sample with higher resolution on the nanoscale as compared to conventional optical microscopy, since electron wavelengths are much shorter than photon wavelengths in the visual spectrum. The electron wavelength λ_e is derived from the de Broglie equation using the Planck's constant h and the electron momentum p_e, which is a function of the acceleration Voltage U_{acc}:

$$\lambda_e = \frac{h}{p_e\left(U_{acc}\right)} \tag{4.1}$$

A field emission electrode produces electrons which are focused by electromagnetic lenses. The sample is positioned at the focal point and at the working distance of the detector, which is typically around 3-5 mm. Line-by-line raster scans with the electron beam generate secondary electrons by inelastic scattering, which are then detected by an InLense detector to capture the surface morphology. By plotting the number of secondary electrons

against the scanned pixel, it is possible to visualize the surface morphology as a gray scale image. It is worth to mention that the gray scale of pixels depend among others on the specific material, height and geometry. These influences are challenging to avoid and lead to a restricted analysis of the surface topography. In order to analyze SEM images, the open source software ImageJ was used. Domain sizes and porosity can be extracted from binary images which are converted from gray scale images via the Otsu threshold algorithm. Further applying combinations of pixel erosion and dilation algorithms is helpful to reduce influence of isolated pixels and overexposed edges. For the domain sizes, the *analyze particle* algorithm in ImageJ is used. The local surface porosity is estimated by the area ratio of the black area to total pixel area. SEM measurements are performed at a 3.5 mm working distance and an accelerating voltage of 5 kV (Zeiss NVision 40, Figure 4.1). SEM measurements complement the GISAXS data with a real-space surface characterization of the as-deposited β-lg:titania sample after spray coating, the nanostructured titania sample after biopolymer removal, and the pristine titania as a reference.

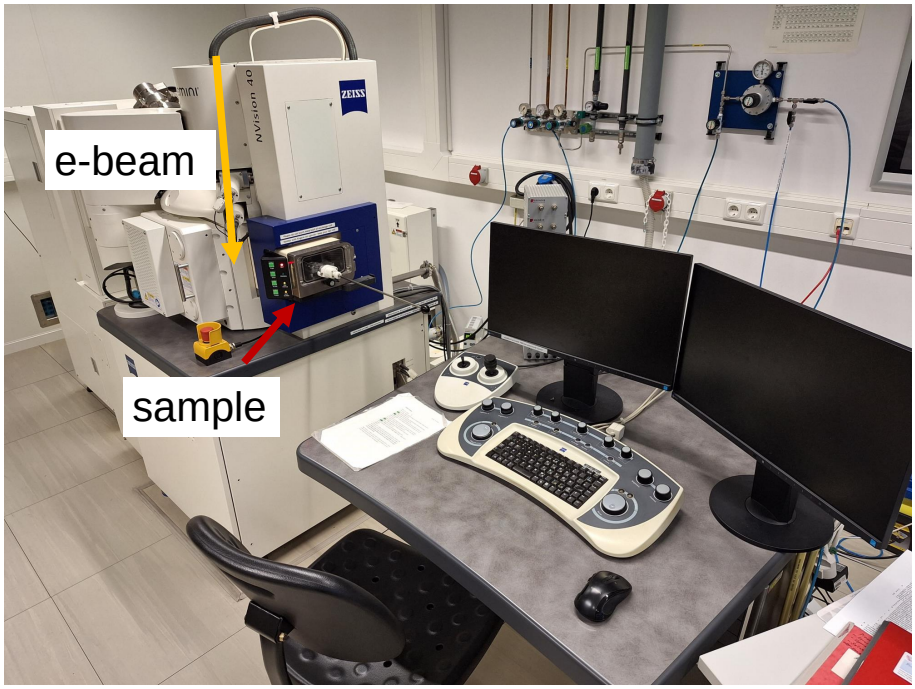

Figure 4.1.: Photograph of the SEM instrument.

Closely related to SEM, high-resolution transmission electron microscopy (HRTEM) applies electrons to study the nanostructure of materials. Due to vertical arrangement of the transmission geometry, the electron can be focused by additional electromagnetic lenses, thus achieving higher resolution. In this thesis, HRTEM measurements (Tecnai G2 F30) are used to investigate the (111) plane of PbS QD superlattices. The long-range

order, inter-dot distance, average size, and size distribution (Figure 7.1e-g) are confirmed by HRTEM and based on the second batch of PbS QDs. The average size obtained from HRTEM is (2.8 ± 0.1) nm with a standard deviation of 21 % and agrees with the results from absorbance measurements in Figure 7.10 and 4.4.

4.2. Photoluminescence

Photoluminescence (PL) is a way of probing the optoelectronic structure of materials and quantifying light emission by radiative recombination in a material exposed to light irradiation. Photon energy from a light source is absorbed by the sample and excites electrons from a lower state to a higher state. The excited electron relaxes through various mechanisms within the excited level until it relaxes to the ground state by emitting a photon of energy equal to the difference between the respective levels. The emitted photon is then detected by a photodiode. This emission of light is called fluorescence when it occurs quasi-instantaneously on short timescales. In the case of metastable excited states, light emission can still occur after the external photon pump has been switched off. This delayed emission is called phosphorescence. The time scales of PL are important to consider for optoelectronic applications, as they are directly related to the performance of LEDs and the lifetime of excitons in OPVs. A more detailed understanding of charge carrier dynamics can be obtained with time-resolved PL. In Chapter 7, the focus is placed on steady-state PL to extract the PL energy and intensity from QD in thin films *in-situ* as a function of applied strain. The PL spectra of an inorganic semiconductor depends on the absorptivity $A(\hbar\omega)$ and the chemical potential μ, which relates to the quasi-Fermi energy splitting of the electron-hole pairs forming after excitation: [62]

$$\mathrm{PL}(\hbar\omega) = A(\hbar\omega) \cdot \frac{(\hbar\omega)^2}{4\pi^2\hbar^3 c_0^2} \cdot \left(\exp\left(\frac{\hbar\omega - \Delta\mu}{k_B T}\right) - 1\right)^{-1} d\hbar\omega \tag{4.2}$$

Here, $\hbar$ is the reduced Planck's constant, ω the frequency of the emitted photon, c_0 the speed of light in vacuum, k_B the Boltzman's constant, and T the absolute sample temperature. In QD solids, energy gained, e.g., by absorbing photons, can be transferred via dipole-dipole interactions to neighboring QDs. In this case, the energy is transferred from an excited donor level to a resonant acceptor level. As the acceptor typically has a smaller bandgap energy, the energy transfer is accompanied by a redshifted PL emission. This energy transfer is known as Förster resonance energy transfer (FRET) and is graphically depicted in Figure 4.3. An important condition for FRET to take place is a sufficient spectral overlap of the donor's emission and the acceptor's absorption, which is given by the integral J:

$$J = \int I_D \varepsilon_A \lambda^4 d\lambda \tag{4.3}$$

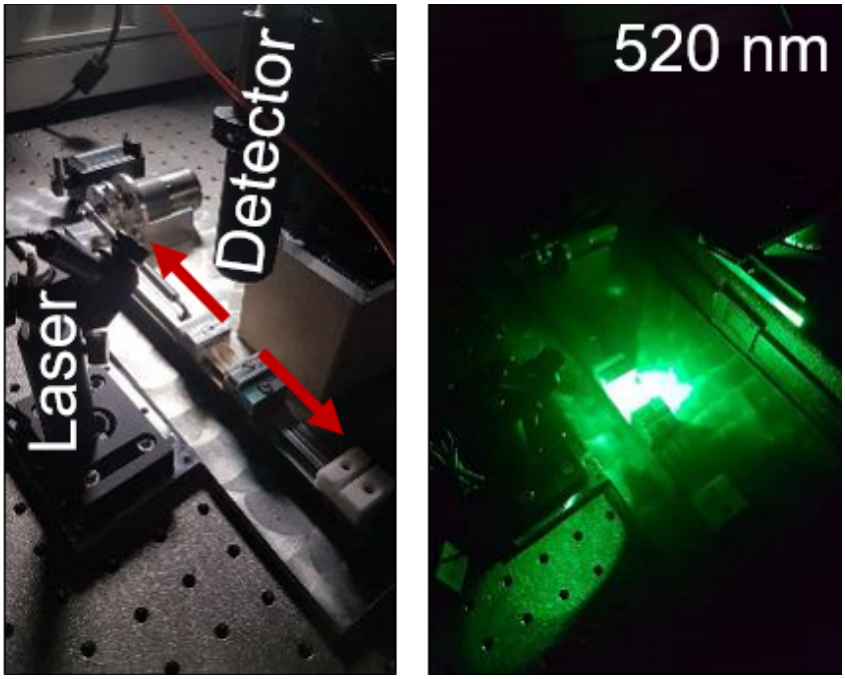

Figure 4.2.: *In-situ* PL setup. The flexible QD films were mounted in clamps that are able to uniaxial elongate the sample. At the same time, PL is measured at a detector in reflection geometry with a 520 nm laser.

Here, I_D is the donor's PL intensity, ε_A the accpetor's exctinction coefficient, and λ the photon wavelength. The FRET efficiency depends on the transfer rate k_{FRET}, which is defined by the donor's PL lifetime τ_D, the distance R between donor and acceptor, and their Förster distance R_0:

$$k_{FRET} = \frac{1}{\tau_D}\left(\frac{R_0}{R}\right)^6 \tag{4.4}$$

The Förster distance R_0 is a characteristic measure of the FRET coupling strength between donor and acceptor, and depends on the spectral overlap J, an orientation factor κ between the donor's and acceptor's dipole moments, the donor's PL quantum yield Φ_D, the donor's the refractive index n, and the Avogadro number N_A:

$$R_0^6 = \frac{9\ln(10)\kappa^2\Phi_D J}{128\pi^5 n^4 N_A} \tag{4.5}$$

At the Förster distance $R = R_0$, the FRET efficiency E_{FRET} is 50 %:

$$E_{FRET} = \left(1 + \left(\frac{R}{R_0}\right)^6\right)^{-1} \tag{4.6}$$

The power-to-six dependence on the distance R in Equation 4.4 and 4.6 makes FRET very sensitive to changing inter-dot distances in QD superlattices and plays a key role in the structure-function relationship during deformation of the QD superlattice by uniaxial strain, which is investigated in Chapter 7.

In-situ PL measurements are performed in reflection mode during uniaxial stretching (Figure 4.2. For this, a laser diode with 520 nm wavelength (CPS520, Thorlabs, typical power output 4.5 mW) and a spot size of 4.6 × 1.7 mm^2 is aligned on the sample. A finger detector made up of a long-pass filter (Thorlabs FEL0600, cut-on wavelength 600 nm), an achromatic doublet (Thorlabs AC254-075-A, focus 75 mm), and a collimator (Thorlabs F240SMA-780) captures the PL emission. The signal is read out with the software environment SpecWin Pro (Instrument Systems) via a spectrometer with 1000 ms integration time (CAS140CT-154, Instrument Systems).

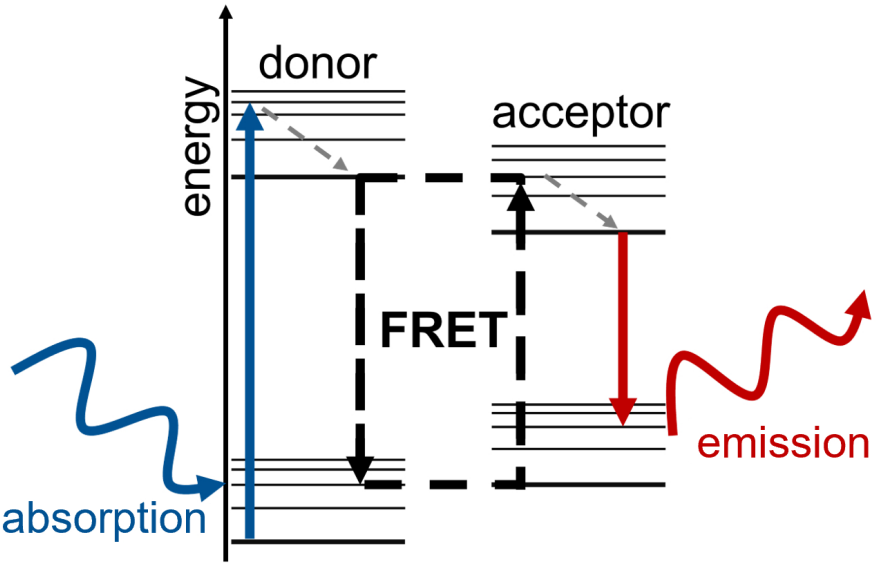

Figure 4.3.: Förster Resonance energy transfer schematic. Light energy absorbed by a donor is resonantly transferred via dipole-dipole interactions to an acceptor with a lower bandgap energy. In this case, the characteristic PL signal is redshifted

4.3. UV-Vis Spectroscopy

The optical path typically appearing in UV-Vis measurements consists of three main components: the light sources for visible light (halogen lamp) and ultraviolet light (deuterium lamp), a monochromator based on an optical grating that defines the spectral width, and a beam splitter that divides the beam into a sample and a reference beam. The emitted light travels along the optical path via mirrors and slits. After passing through the sample, the intensity of the transmitted light, $I_t(\lambda)$, is measured by a photodetector

and compared with the intensity of the reference light, $I_0(\lambda)$. The wavelength-dependent absorbance $A(\lambda)$ of the sample is given by the Lambert-Beer law:

$$A(\lambda) = -\log_{10}\left(\frac{I_t(\lambda)}{I_0(\lambda)}\right) = d\alpha(\lambda)\log_{10}(e) \tag{4.7}$$

Here, d and $\alpha(\lambda)$ are the thickness and the wavelength-dependent absorption coefficient of the sample, respectively. Therefore, by including the transparent substrate of the sample in the reference beam, its contributions can be eliminated by logarithmic subtraction. For semiconducting materials, one of the conditions for light absorption is that the photon energy E_{ph} is greater than the bandgap energy E_g. In turn, the bandgap energy of a semiconducting sample can be evaluated from UV-Vis transmission spectroscopy using the Tauc equation: [63]

$$(\alpha h\nu)^n = B\,(h\nu - E_g) \tag{4.8}$$

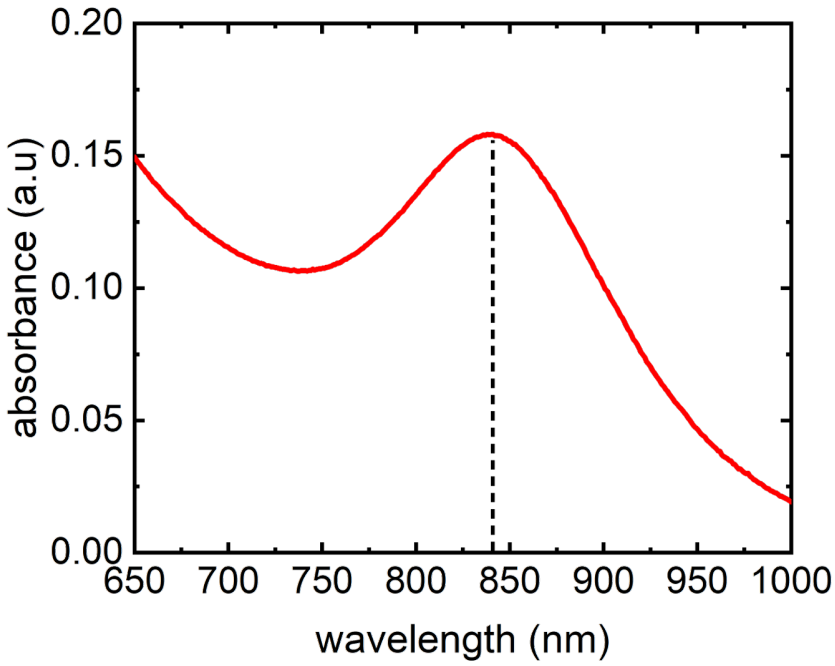

Figure 4.4.: PbS QDs absorbance spectrum. The absorbance spectrum is taken from solid films from the same batch used for *in-situ* GISAXS and *in-situ* PL experiments. I use the Weidman model to calculate the size from the absorption spectra. [64] The average QD size of (2.70 ± 0.02) nm is obtained from the absorbance center and agrees with the HRTEM result obtained from the second batch of PbS, which is prepared according to the same protocol. Reproduced from [18] with permission from the Royal Society of Chemistry.

By plotting $(\alpha h\nu)^n$ as a function of photon energy $h\nu$, the bandgap energy can be read directly from the intersection on the x-axis after linear extrapolation. Here, B is

a constant, h is the Planck's constant and $\nu = c/\lambda$ the photon frequency given by the wavelength and the speed of light c. The exponent n reflects the type of semiconductor, e.g. $n = 2$ for a direct bandgap semiconductor and $n = 0.5$ for an indirect bandgap semiconductor. In accordance with the Brus equation 2.6, empirical formulae are used to relate the size of semiconductor QDs to the bandgap energy: [64]

$$E_g = c + \frac{1}{ad^2 + bd} \tag{4.9}$$

where c is the bulk semiconductor bandgap, a and b are constants, and d is the average diameter of the studied QDs. For the PbS QDs in this work, it holds that $c = 0.41$, $a = 0.0392$, and $b = 0.114$. [64] The average QD size of the first batch is obtained by optical absorption measurements with a UV-vis-IR spectrometer (Lambda 35, PerkinElmer), with a wavelength range of 190–1100 nm and an interval of 1 nm. The average size of (2.70 ± 0.02) nm of the first PbS QD batch used in the stretching GISAXS and PL experiments is obtained from the absorbance spectrum in Figure 4.4.

4.4. Fourier-Transform Infrared Spectroscopy

Fourier-transform infrared spectroscopy (FTIR) is a powerful tool to probe the chemical structure of materials. Absorption of infrared light causes the chemical bonds of functional groups to vibrate, if the absorption is associated with a change in the dipole moment. Several vibration modes are potentially IR active, including stretching and bending of the respective bonds. Some examples of these vibrational modes are shown in Figure 4.5a.

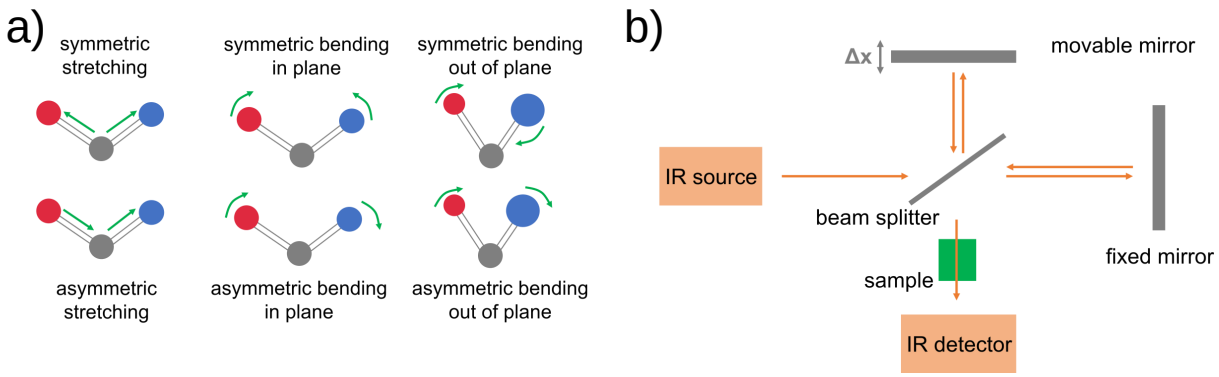

Figure 4.5.: Principles of FTIR spectroscopy: a) Examples of different vibration modes, b) Typical FTIR experimental setup.

The FTIR signal of a specific vibration mode is located at a characteristic wavenumber

$\tilde{\nu}$, given by the following formula with the speed of light c, the spring constant k, and the reduced mass μ:

$$\tilde{\nu} = \frac{1}{2\pi c}\sqrt{\frac{k}{\mu}} \tag{4.10}$$

This formula indicates that for lighter atoms or stronger bonds the FTIR signal is shifted to higher wavenumbers. It is worth mentioning that there is no direct proportionality between the peak area of the FTIR signal and the concentration of the corresponding functional group. Instead, the peak area is affected by the type of vibration and the difference in electronegativity of the involved atoms. A typical FTIR setup in transmission geometry consists of a light source with infrared spectrum and a Michelson interferometer as depicted in Figure 4.5b. Here, the IR light gets split at a beam splitter. A moving mirror adjusts the optical path difference between the split beams and lead to constructive or destructive interference, returning an interferogram as a function of mirror position $I(x)$. The IR spectrum $I(\tilde{\nu})$ is obtained by taking the Fourier transformation from the interferogram.

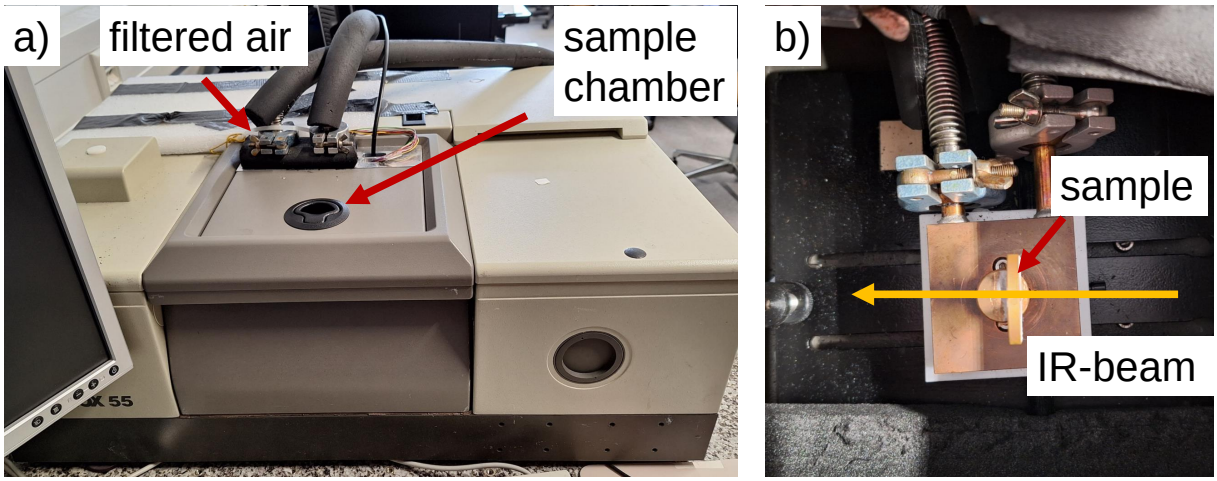

Figure 4.6.: Photographs of the FTIR instrument. a) FTIR instrument with gas inlets to reduce signal from atmosphere. b) Sample environment inside the FTIR instrument.

The FTIR samples in this thesis are placed in an Equinox 55 (Bruker) FTIR system in transmission mode, which is purged with CO_2-free and dry air (Figure 4.6). The FTIR measurements are conducted with a resolution of 2 cm^{-1} and 125 scans per measurement. Baseline correction is performed with a silicon reference sample and atmospheric compensation is taken into account.

4.5. Experimental Setups for X-ray and Neutron Scattering

This section describes the experimental setups, which are used to determine the structure-function relation in biotemplated titania films during spray coating (Chapter 5), as function of pH value (Chapter 6), and in PbS QD superlattices during deformation (Chapter 7).

In-Situ GISAXS/GIWAXS During Spray Coating

In-situ GISAXS/GIWAXS measurements are performed at the beamline P03 MiNaXS of the storage ring PETRA III (DESY, Hamburg, Germany). [65] Nozzle and substrate are mounted in a spray chamber, which is mounted into the beamline (Figure 4.7). Spray deposition is carried out with the spray protocol described above. The X-ray wavelength is 0.984 Å, corresponding to a photon energy of 12.6 keV. Dectris Ltd. Pilatus 1M detector and Dectris Ltd. Pilatus 300K detector are placed in 4871 mm and 326 mm distance to the sample position, to simultaneously record the 2D GISAXS and GIWAXS signals, respectively. Both detectors have a pixel size of (172 × 172) µm^2. 2D *in-situ* GISAXS

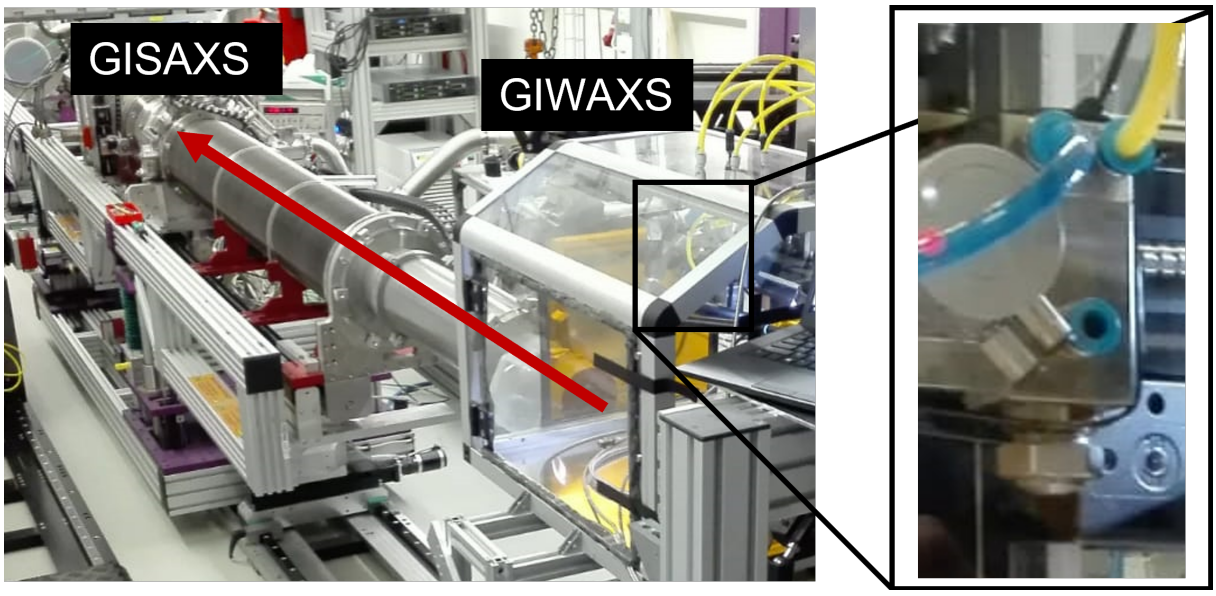

Figure 4.7.: *In-situ* spray deposition GISAXS/GIWAXS. Experimental setup at DESY beamline P03. The position of GISAXS and GIWAXS detectors is labeled along the pathway in the X-ray direction (red arrow). The air atomizing nozzle (shown in the detail) is mounted above a heating stage inside a custom-built spray chamber. Reproduced from [17] with permission from Wiley, Copyright 2022.

and GIWAXS images are taken with an exposure time chosen to be 0.1 s to ensure a high time resolution. The Si substrate is aligned to an incident angle of $\alpha_i = 0.425°$, which ensures a proper separation of the material characteristic scattering signal called Yoneda peak and the signal from specular reflection. The whole setup is periodically sweeping with 0.5 mm s^{-1} in a range of 8 mm perpendicular to the beam direction, to protect the sample from radiation damages by the high brilliance X-ray illumination (Figure 4.8).

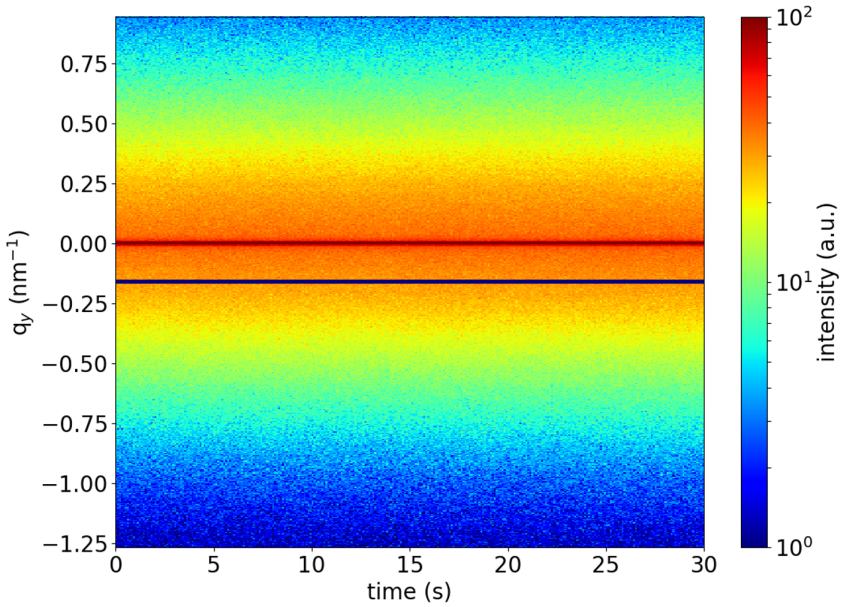

Figure 4.8.: Stability against X-ray irradiation. 2D plot showing the temporal evolution of the horizontal Yoneda line cuts during long-time exposure of 30 sat a fixed sample position. The scattering intensity remains constant and the morphology does not show any changes. The effective exposure time per spot for the *in-situ* measurements is below 0.5 s, so that any radiation damage to the sample is ruled out. Reproduced from [17] with permission from Wiley, Copyright 2022.

This also probes the film formation for different positions in the spray cone within the scanning area defined by the turning points A and B as sketched in Figure 5.1d. Optical microscope images are taken during spray deposition by a camera mounted into the spray chamber. Figure 4.9 shows the film evolution and the scanned area between the turning points A and B, together with the position C close to the center of the spray cone.

The 2D GISAXS images are reduced to 1D intensity distributions as a function of the scattering vector q_y (nm^{-1}) by use of the software DPDAK. [66] These horizontal line cuts provide lateral information about the morphology and are taken at the Yoneda peak position of the β-lg:titania biohybrid material (at $q_z = 0.6$ nm^{-1}), which corresponded to a critical angle of $\alpha_c = 0.13°$. To extract the lateral information, the horizontal line cuts are modeled by applying cylindrical form factors on a 1D paracrystal in the framework of the

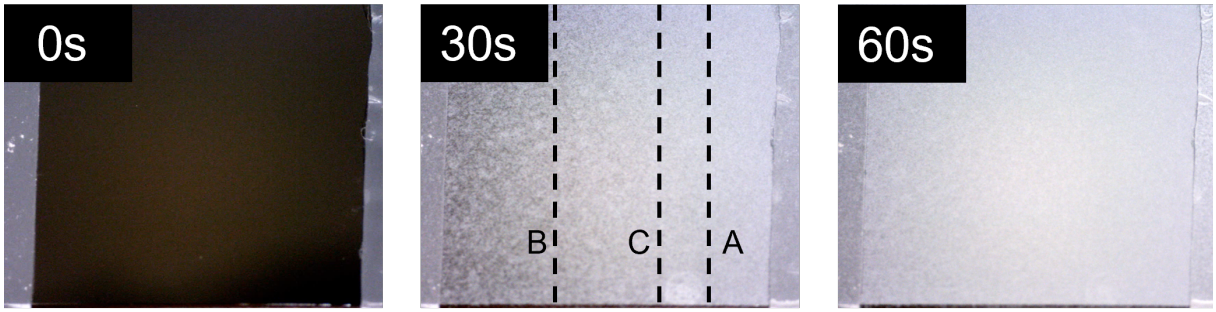

Figure 4.9.: Photographs of film formation. Photographs show the film deposition from the bare silicon substrate (0 s) and intermediate stages (30 s) to the final film (60 s). The scanning area probing the film gradient induced by the spray cone between the motor turning points A and B and the selected position C is indicated by dashed lines. Reproduced from [17] with permission from Wiley, Copyright 2022.

distorted wave Born approximation (DWBA), using the effective interface approximation in combination with the local monodisperse approximation. [67] This lateral information is modeled in terms of form factors (structure sizes) and structure factors (center-to-center distances). 2D GIWAXS images are reshaped with the MATLAB-based software package GIXSGUI and 1D intensity distributions as functions of q ($Å^{-1}$) are obtained by azimuthal integration. [68] These intensity distributions contain information about the crystalline phase evolution during spray deposition. The data is fitted with Gaussian functions to extract q-spacings, distribution widths at half maximum, and intensities of the crystalline phases.

Influnce of pH on biohybrid and biotemplated titania morphology

GISAXS and GIWAXS are performed at the beamline P03 MiNaXS of the storage ring PETRA III (DESY, Hamburg, Germany). [65] The wavelength is set to 1.05 Å, corresponding to 11.8 keV photon energy and the sample placed in 4085 mm to the GISAXS detector (Pilatus 2M, Dectris, pixel size 172 × 172 $µm^2$) and in 260 mm to the GIWAXS detector (Lambda 9M, X-Spectrum, pixel size 55 × 55 $µm^2$).

GISANS is performed at the instrument MARIA (Heinz Meier-Leibnitz Zentrum MLZ, Garching, Germany), provided by the Jülich Centre for Neutron Science (JCNS). [69] To ensure a controlled relative humidity, the samples are placed in a 3D printed spherical environmental chamber for GISANS experiments (Figure 4.10). [70] A constant flow of H_2O saturated nitrogen and dry nitrogen establishes a relative humidity of 50 %. The incident angle is set to 0.7° and the scattered neutrons with a wavelength of 10 Å are detected in a distance of 1910 mm to the sample. The 2D GISANS data is normalized

by the detector sensitivty and reduced to horizontal 1D line cuts as function of q_y (nm^{-1}) based on a python code provided by A. Koutsioumpas (JCNS, Garching).

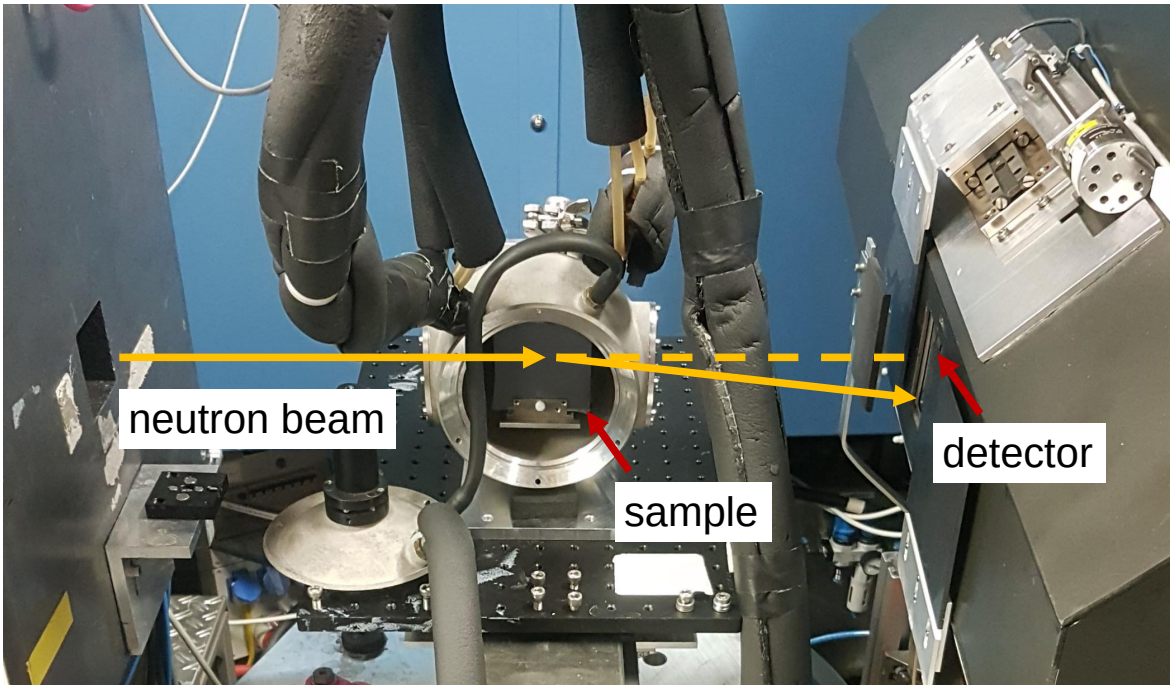

Figure 4.10.: Photograph of the GISANS setup at the MARIA instrument.

In-Situ GISAXS During Uniaxial Strain

In-situ GISAXS measurements are performed at the beamline P03 at DESY. [65] A sample-to-detector distance of 3.8 m is chosen to probe the PbS QD superlattice scattering signal. The signal is captured with a Pilatus 2M detector (Dectris, pixel size 172 × 172 μm^2). The wavelength is set to 1.05 Å, corresponding to 11.8 keV photon energy. The incidence angle was adjusted to 0.341°. During the *in-situ* experiments, the sample is moved perpendicular to the incident X-rays to probe a larger sample volume and avoid radiation damage by the highly brilliant beam.

The PDMS substrate supporting the PbS QD film is mounted in a custom-built stretching apparatus by clamping the sample edges along the strain axis (Figure 4.11a). [71], [72] The clamps are connected to two stepping motors for controlled elongation of Δl^{sub} from the initial sample length l_0^{sub}. The ratio $\Delta l^{sub}/l_0^{sub}$ measures the value of the applied strain to the substrate. Four cylindrical rolls guide the sample during the *in-situ* GISAXS experiments to prevent deformation-induced sagging and twisting of the sample (Figure 4.11b). This setup ensures controlled sample alignment with respect to the incident X-ray beam. The QD superlattice Bragg reflexes are indexed in the 2D GISAXS data with the

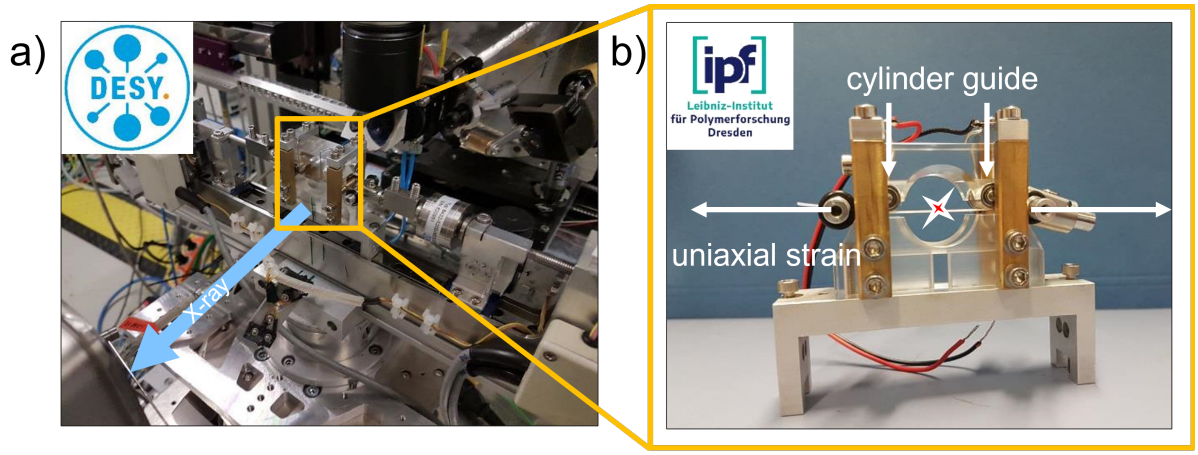

Figure 4.11.: Photographs of the *in-situ* GISAXS setup for uniaxial deformation. a) Stretching apparatus mounted at the DESY beamline P03. b) Sample holder designed by K. Schneider, A. K. Sambale, E. Euchler (IPF, Dresden) for *in-situ* GISAXS on freestanding, flexible substrates. A red star indicates the X-ray beam position on the thin QD film. Reproduced from [18] with permission from the Royal Society of Chemistry.

software GIXSGUI. [68] A detailed step-by-step guide using GIXSGUI for index matching is provided in Figure A.1–A.6 of the Appendix A.

The $(011)_{bct}$, $(110)_{bct}$, and $(111)_{fcc}$ reflexes are reduced to 1D intensity cuts by azimuthal integration with the software environment DPDAK and fitted with Gaussian functions. [66] From the extracted q_{011}, q_{110}, and q_{111} values, the superlattice spacing d_{011}, d_{110}, and d_{111} and consequently the unit cell axes a_{bct}, c_{bct}, and a_{fcc} are obtained.

Chapter 5

Low-Temperature and Water-Based Biotemplating of Nanostructured Foam-Like Titania Films Using β-Lactoglobulin

This chapter is based on the publication *Low-Temperature and Water-Based Biotemplating of Nanostructured Foam-Like Titania Films Using β-Lactoglobulin* (J. E. Heger, W. Chen, S. Yin, N. Li, V. Körstgens, C. J. Brett, W. Ohm, S. V. Roth, P. Müller-Buschbaum, *Advanced Functional Materials*, **32**, 2113080 (2022)) [17]. Reprinted from [17] with permission from Wiley, Copyright 2022.

Given the broad use of nanostructured crystalline titania films, an environmentally friendly and more sustainable synthesis route is highly desirable. Here, a water-based, low-temperature route is presented to synthesize nanostructured foam-like crystalline titania films. A pearl necklace-like nanostructure is introduced as tailored titania morphology via biotemplating with the use of the major bovine whey protein β-lactoglobulin (β-lg). It is shown that titania crystallization in a brookite-anatase mixed phase is promoted via spray deposition at a comparatively low temperature of 120 °C. The obtained crystallites have an average grain size of (4.2 $\pm$ 0.3) nm. *In-situ* grazing-incidence small-angle and wide-angle X-ray scattering (GISAXS/GIWAXS) are simultaneously performed to understand the kinetics of film formation and the templating role of β-lg during spray coating. In the β-lg:titania biohybrid composites, the crystal growth in semicrystalline titania clusters is sterically directed by the condensing β-lg biomatrix. Due to using spray coating, the green chemistry approach to titania-based functional films can be scaled up on a large scale, which can potentially be used in photocatalytic processes or systems related to energy application.

5.1. Preface

Nanostructured titania has emerged to an important research topic in the field of functional materials, due to its versatile applications. For instance, the nontoxic and photoactive semiconductor is used as a photocatalyst in self-cleaning coatings, [73], [74] molecule sensors, [75] photocatalytic production of hydrogen, [9], [76] and as an anode material in lithium-ion batteries, [10], [77]–[79] dye-sensitized solar cells, [11], [80]–[82] hybrid solar cells, [83], [84] and perovskite solar cells. [12], [85] In several of these applications, e.g., photovoltaics, a tailored morphology in terms of porosity, surface-to-volume ratio, and size distribution is beneficial for the device performance. [86] In particular, foam-like structures are of high interest due to their mechanical advantages and robustness. Among the different approaches of templating titania nanostructures, copolymer-assisted sol–gel synthesis has been shown to provide a facile way toward a controlled morphology also for films. [25], [87]–[90] Furthermore, solution processing based on copolymer-assisted sol–gel synthesis has shown high promise for economically producing nanostructured titania films via large-scale deposition techniques, such as slot-die coating [91]–[93] and spray deposition. [94]–[96] However, the synthetic copolymer templating routine comes along with comparatively toxic, harmful, or flammable organic solvents as well as a low sustainability. For an improved environmentally friendly and more sustainable scenario, water-based templating of the mesoscopic titania morphology is desirable in combination with using water-soluble biopolymers, which substitute the synthetic copolymers. [97]–[100] Besides the structural properties on the mesoscopic length scale, also the crystal phase and the crystallinity affect the performance of titania-based films in applications. The polymorph titania can be found in three different phases, namely tetragonal rutile, tetragonal anatase, and orthorhombic brookite. Rutile is known to be the thermodynamic most stable crystal form, however, showing lower photocatalytic activity compared to anatase and brookite. [101] Brookite is more laborious to obtain in a pure phase, but offers also a more promising performance in photocatalytic applications, compared to anatase and rutile. [102]–[104] Moreover, it was observed that copolymer templating of titania nanostructures from an amorphous precursor such as titanium-(IV)-isopropoxide (TTIP) in a nonaqueous media showed first crystallization starting at temperatures in the range from 250 to 500 °C. [105]–[107] To enhance low-temperature crystallization, alternative precursors such as ethylene-glycol-modified titanite (EGMT) were successfully introduced to copolymer-based titania sol–gel synthesis to enable a low-temperature crystallization. [108], [109] However, the synthesis of tailored precursor molecules like EGMT can become comparatively laborious. [110] Alternatively, anatase-brookite mixed crystalline titania phases were readily produced by the precipitation of titania precursors upon hydrolyzation in aqueous media. [111]–[113] Besides this, in anatase-brookite

mixed systems, smaller crystallite sizes are shown to be more beneficial for photocatalytic performance, in contrast to pure anatase phase materials, in which large crystallite sizes showed improved photocatalytic performance. [101], [114] However, synthetic copolymers are less sustainable compared with biopolymers and biopolymers typically also match well with aqueous processing. Among the numerous biopolymers, the bovine whey protein β-lactoglobulin (β-lg) attracted interest in this direction because it forms different supramolecular structures such as amyloid fibrils upon denaturation,[34], [59], [115]–[118] that can act as a template material in titania-based applications. [36] Hence, substituting synthetic copolymers with water-based biopolymers has the potential to combine low-temperature crystallization in aqueous media with a compatible templating route and to further promote the environmentally friendly synthesis of titania nanostructures. This work presents a facile and water-based sol–gel route to achieve crystalline titania films with a mixed anatase-brookite phase and a foam-like nanostructure at low temperatures. Our approach is based on the well-established titania precursor TTIP. As described in more detail in Section 3.2, TTIP is mixed with β-lg in acidic water to form a fibrillar biohybrid sol–gel, which is spray deposited on a heated silicon substrate (Figure 5.1).

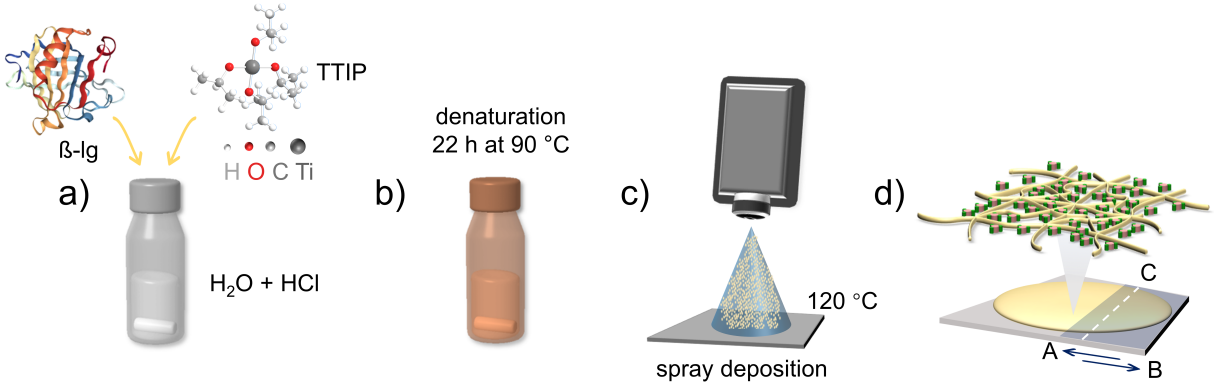

Figure 5.1.: Fabrication of β-lg:titania films. a) β-lg is mixed with the titania precursor TTIP in aqueous solution. b) Hydrothermal synthesis of titania nanoparticles at 90 °C for 22 h. The protein unfolds into a fibrillar network during denaturation by heating in the acidic environment and acts as a template for the titania nanoparticles. c) The resulting β-lg:titania film is spray deposited on a silicon substrate at 120 °C out of the resulting dispersion. d) The scanning area of the *in-situ* GISAXS/GIWAXS measurements is sketched between the turning points A and B with respect to the gradient in material induced by the spray cone. The selected data for 1, 19, 35, and 53 s were taken at position C. Reproduced from [17] with permission from Wiley, Copyright 2022.

Spray deposition allows kinetic rearrangements of the biohybrid film morphology during drying on short time scales. Furthermore, spray deposition matches the sustainable synthesis route presented in this work, due to comparatively low material wastage. The

deposited biohybrid films consist of a pearl neck-lace-like titania nanostructure that is embedded in a fibrillar β-lg biomatrix and revealed upon biopolymer extraction by ultraviolet (UV) irradiation. To reveal the kinetics of morphology formation and crystal growth during the spray deposition process, simultaneous *in-situ* grazing-incidence small-angle and wide-angle X-ray scattering (GISAXS/GIWAXS) is applied as an advanced investigation method. [43], [95], [119]–[121] Experimtal details on the *in-situ* setup are given in Section 4.5. The morphology information of the biohybrid film is complemented by *ex-situ* scanning electron microscopy (SEM) and *ex-situ* GISAXS measurements. Based on this fundamental understanding of the film formation process of the biohybrid film, the knowledge is gained to control the spray deposition and achieve low-temperature and water-based biotemplating of nanostructured foam-like titania films. Such environmentally friendly and more sustainable synthesis route will be highly desirable for multiple applications in the fields of sensors, energy conversion and energy storage.

5.2. Influence of β-lg on the Film Morphology

Surface Morphology

The sample surfaces of pristine titania, biotemplated titania after UV irradiation, and the biohybrid β-lg:titania composite films are probed with SEM (Figure 5.2).

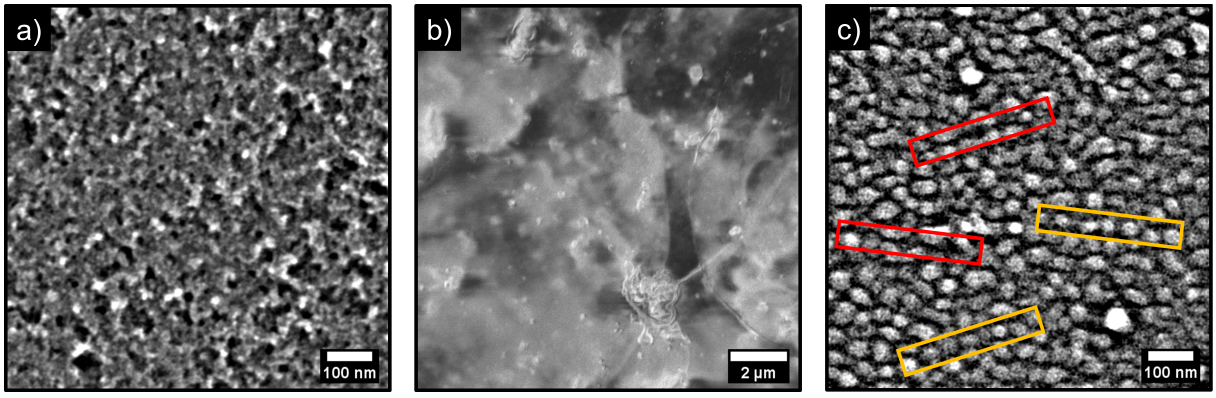

Figure 5.2.: SEM surface morphology. a) The pristine titania reference sample shows irregular porosity. b) The as-deposited biohybrid sample shows the β-lg biomatrix embedding the titania phase. c) The biotemplated sample after UV irradiation shows a nanostructured titania scaffold. Yellow boxes highlight the pearl necklace-like arrangement of titania. Red boxes highlight the fibrillar-shaped porous matrix in which the titania domains are embedded. Reproduced from [17] with permission from Wiley, Copyright 2022.

The surface of the pristine titania film shows a typical irregular foam-like structure with widely distributed pore sizes (Figure 5.2a). The surface of the biohybrid film obtained by

SEM before UV irradiation (Figure 5.2b) shows a homogenous coverage on the macroscale but provides only limited contrast for the nonconductive biopolymer matrix for an analysis on the nanoscale. The remaining biotemplated titania film has an improved contrast in SEM after UV irradiation so that the biotemplated titania nanostructure becomes apparent. The biotemplated titania film exhibits a foam-like nanostructure with a pearl necklace-like arrangement of titania structures (highlighted with yellow rectangular boxes in Figure 5.2c), separated by pores with a fibril shape (highlighted with red rectangular boxes). This finding suggests that the titania pearl necklace-like nanostructure is present in the biohybrid sample and is sterically aligned within the voids by the surrounding β-lg fibril network, as sketched in Figure 5.1d. The variation of surface morphology for the biohybrid sample with different UV exposure times is shown in Figure 5.3.

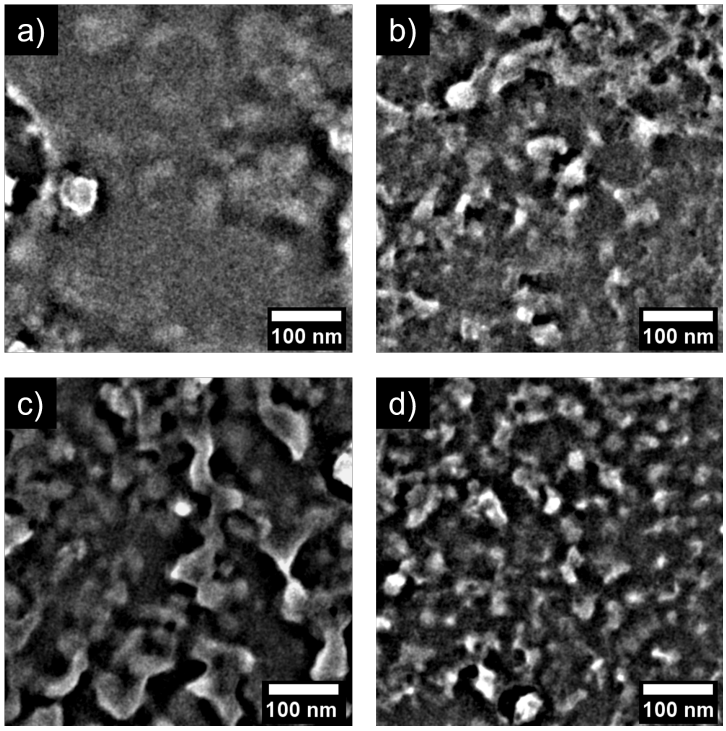

Figure 5.3.: UV light biopolymer extraction. Surface morphology obtained from SEM of the biohybrid samples after a) 5, b) 9, c) 17 and d) 22 h UV irradiation. The buried titania nanostructure gradually becomes more apparent due to the enhanced contrast in SEM upon longer UV irradiation and resulting higher degree of biopolymer extraction. Reproduced from [17] with permission from Wiley, Copyright 2022.

Inner Morphology

To understand the role of the β-lg matrix in templating of the titania nanostructure and extend the accessible information from surface to bulk morphology, static GISAXS

measurements are performed. These *ex-situ* GISAXS measurements probe the biohybrid film after spray deposition and the UV illuminated film. In addition to this, pristine titania and a pure β-lg film are measured as references. The horizontal line cuts are shown in Figure 5.4a. Three characteristic structures are extracted from the applied model of the biohybrid and titania samples. The related radii and distance values are presented in Figure 5.4b,c, respectively.

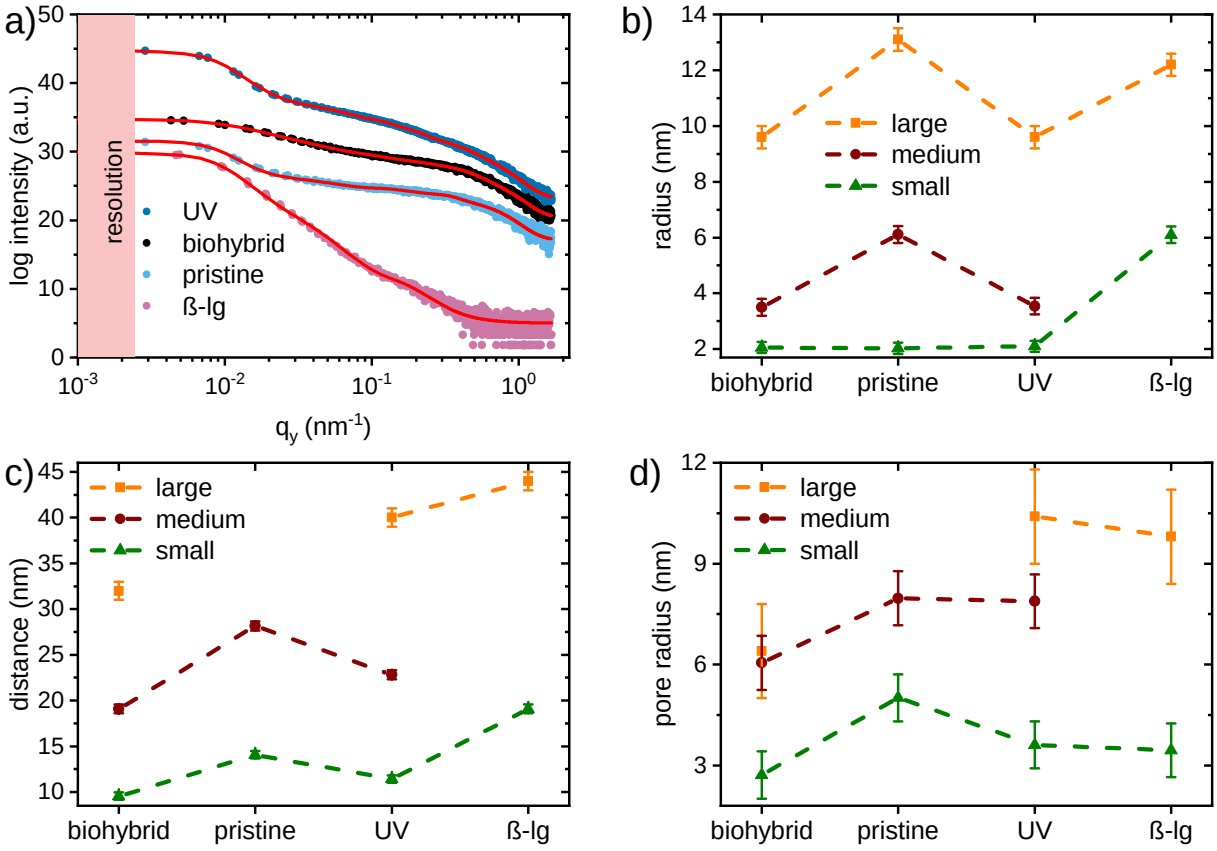

Figure 5.4.: Inner morphology. a) Horizontal line cuts from static GISAXS data of the hybrid (as-deposited biohybrid), pristine (pristine titania), UV (UV irradiated, biotemplated titania), and pure (pure β-lg) films. The modeled curves are shown with solid red lines. Corresponding b) radii as obtained from cylindrical form factors, c) center-to-center distances as obtained from the structure factors, and d) pore radii approximated by Equation 5.1. Orange squares, red circles, and green triangles represent the large, medium, and small domains, respectively. Adapted from [17] with permission from Wiley, Copyright 2022.

The biohybrid film exhibits three characteristic structures, related to a small-, medium-, and large-domain radii of (2.1 ± 0.2), (3.5 ± 0.3), and (9.6 ± 0.4) nm, respectively. These domains have a characteristic center-to-center distance of (9.6 ± 0.4), (19.1 ± 0.5), and (32 ± 1) nm, respectively. An interpretation of the morphology associated with the domain sizes is presented later in the context of the *in-situ* GISAXS/GIWAXS discus-

sion. After UV illumination, the characteristic domain radii of the biotemplated titania morphology remain unchanged compared to the biohybrid sample before UV irradiation. This indicates that mainly the titania domain form factors rather than the β-lg biomatrix contribute to the scattering intensity of the biohybrid sample, and the nanoparticle sizes of titania do not undergo obvious changes with UV irradiation. The center-to-center distances, however, slightly increase after UV irradiation, to (11.4 ± 0.4) nm (small structures), (22.8 ± 0.5) nm (medium structures), and (40 ± 1) nm (large structures), respectively. The deformation of the remaining titania scaffold that is reflected in slightly increased distances after biopolymer extraction can be seen as an inverse process to the humidity uptake in porous titania scaffolds studied in an earlier work. [122] Here, the ingress of water vapor into the pores leads to a contraction in terms of reduced center-to-center distances. For the present case of biopolymer extraction, the transition from solid to gas phase of the biomatrix during UV combustion causes isotropic expansion of the titania scaffold with slightly increasing center-to-center distances. In contrast to the biotemplated titania film, the pristine titania reference sample consists of bigger medium (radius of around (6.1 ± 0.3) nm) and large domains (radius of around (13.1 ± 0.4) nm). The small structures show the same radius ((2.1 ± 0.2) nm) as the biotemplated titania. The distances related to the small and medium domains of the pristine titania are (14.1 ± 0.4) nm and (28.2 ± 0.5) nm, respectively. For the large domains, there is no significant structural correlation in terms of center-to-center distance. The pure β-lg film consists of two characteristic structure sizes with a radius of (6.1 ± 0.3) nm for the small-sized structures and a radius of (12.2 ± 0.4) nm for the large-sized structures and the corresponding center-to-center distances of (19.1 ± 0.5) and (44 ± 1) nm, respectively. The obtained values of the small and large β-lg domains are in good agreement with expected values for bundles of about 2 (small structures) and 4 (large structures) β-lg amyloid fibrils with 6 nm in diameter. [115], [116] With the obtained radii and distances, an estimation of pore sizes in the respective sample can be given by the following expression: [67]

$$R_{pores} = \frac{1}{2} D_{domains} - R_{domains} \tag{5.1}$$

Here, R_{pores} and $R_{domains}$ refer to the radii of the pores and the respective domains with the related distances $D_{domains}$. By comparing the pores' radii (Figure 5.4d), it is found that the biotemplated titania scaffold consists of a slightly higher hierarchy in pore radii ((3.6 ± 0.7), (7.9 ± 0.8), and (10.4 ± 1.4) nm) compared to the pristine sample ((5.0 ± 0.7) and (8.0 ± 0.8) nm), respectively. It is further noticeable, that the pore radii obtained for the pure β-lg sample (Figure 5.4d, (3.5 ± 0.7) and (9.8 ± 0.8) nm) coincide with the radii of the medium and large titania domains in the biohybrid sample (Figure 5.4b, (3.5 ± 0.3) and (9.8 ± 0.4)). Vice versa, the pores related to the distances of the medium

and large titania domains inside the biohybrid sample (Figure 5.4d, (6.1 ± 0.8) and (6.4 ± 1.4) nm) coincide with the small β-lg domain radius (Figure 5.4b, (6.1 ± 0.3) nm). These observations are summarized as:

$$P_{\beta-lg,small} \approx R_{hybrid,medium} \tag{5.2}$$

$$P_{\beta-lg,large} \approx R_{hybrid,large} \tag{5.3}$$

$$P_{hybrid,medium} \approx P_{hybrid,large} \approx R_{\beta-lg,small} \tag{5.4}$$

Here, R is the domain radius of the small, medium, or large structures of the pure β-lg and the biohybrid sample, respectively. The corresponding pore radius is denoted with P. This claims that the structure factor of the biohybrid sample representing the titania domain distances can be attributed to the surrounding β-lg biomatrix, which is further supported by the increased titania domain distances after removal of the biopolymer by UV illumination. In conclusion the biohybrid morphology can be interpreted as voids inside the β-lg biomatrix, which are filled with titania and as consequence, that the β-lg domains separate the titania domains from each other.

5.3. Lateral Film Formation on the Crystalline Length Scale

To understand the temporal evolution of the overall morphology in the biohybrid film and its crystal structure during the spray deposition process, *in-situ* GIWAXS measurements are performed simultaneously to *in-situ* GISAXS during the spray deposition. In Figure 5.5 the 2D GIWAXS data at four selected times is presented. From this 2D GIWAXS data, 1D intensity curves are taken by azimuthal integration and plotted against the scattering vector q (Figure 5.6a). It shows the rise of three distinct peaks from 1 to 53 s during spray deposition. At these given four time stages a position on the film close to the inner part of the spray cone is probed (marked as position C in Figure 4.9 and Figure 5.1d). With fits of the intensity curves using Gaussian functions, the temporal evolution of the peak intensities, the q-values, and the distribution full width at half maximum (FWHM) is determined during film formation. The three peaks are assigned to the (121) brookite phase at (2.143 ± 0.002) Å^{-1}, to the (004) anatase phase at (2.650 ± 0.001) Å^{-1}, and to the (200) anatase phase at (3.318 ± 0.001) Å^{-1} of titania, respectively. These peaks are in good agreement with the reported brookite phase (PCPDS #29-1360) and anatase phase (PCPDS #21-1272). An estimation for the lower limit of the corresponding crystal sizes is calculated from the FWHM according to the Scherrer Equation 2.27. [67] The results from the Gaussian fits are presented in Figure 5.6b–e and show the film formation

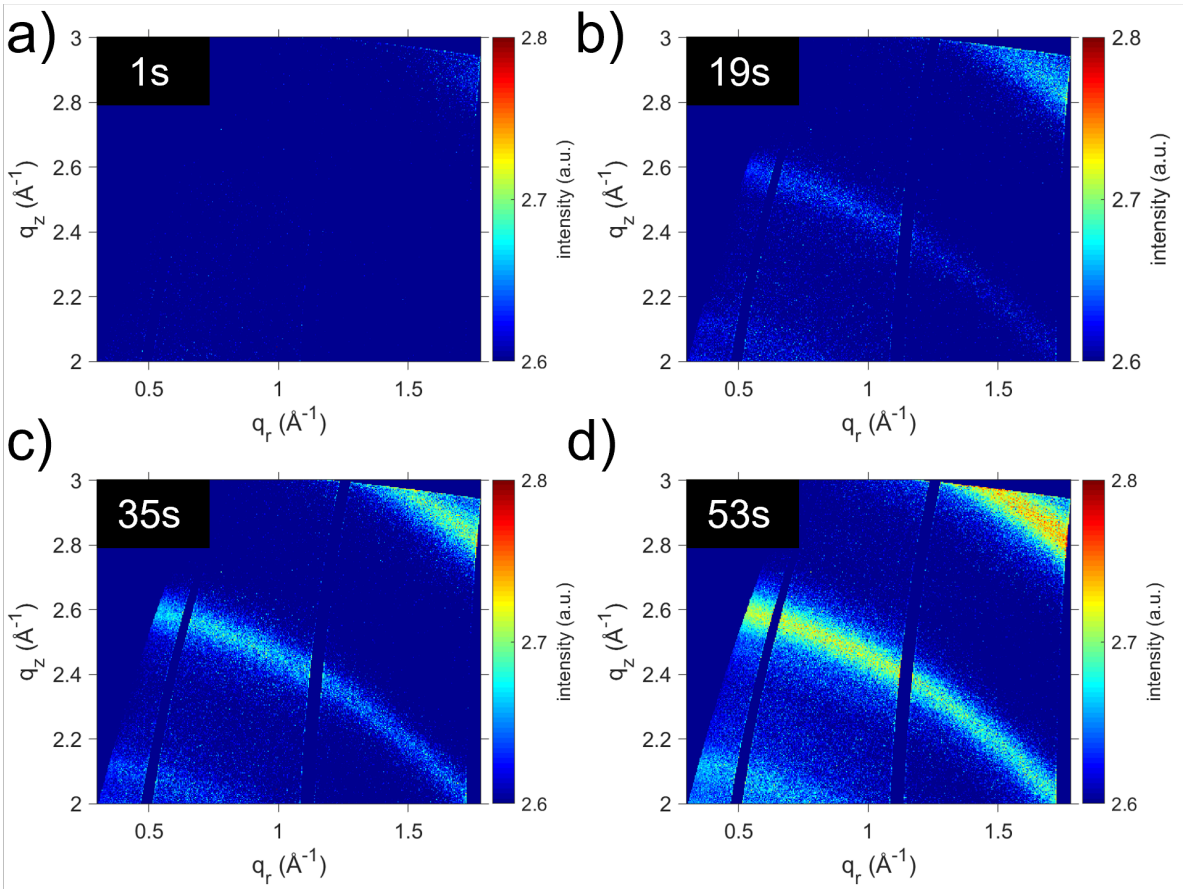

Figure 5.5.: 2D GIWAXS data. Evolution of 2D GIWAXS data shown for the selected position C at a) 1 s, b) 19 s, c) 35 s and d) 53 s. Reproduced from [17] with permission from Wiley, Copyright 2022.

on the crystalline length scale between the turning points A and B (Figure 4.9 and 5.1d) of the scanning area during the entire spray experiment. In more detail, the data shows the inner, central, and outer regions of the spray cone. The temporal evolution of the Gaussian fits suggests that only the signal intensity (Figure 5.6b) depends on the position with respect to the spray cone, whereas q-value, FWHM, and hence crystallite sizes evolve independently of the position. Thus, the inner region of the spray cone provides a larger material deposition and hence a higher signal as compared to the central and outer regions with respect to the scanned area. The local maxima at 27 s and the local minima at 43 s correspond to the turning points A and B of the sweeping motor, respectively, and hence to the positions of highest (27 s) and lowest (11 s, 43 s) deposited material amount within the measured region of the spray cone. For the fixed position C, however, the intensity shows a linear increase as a consequence of the linear growth of the film thickness and

hence the linear growth of the number of crystallites, which is characteristic of pulsed spray deposited layer-by-layer growth. [123]–[125]

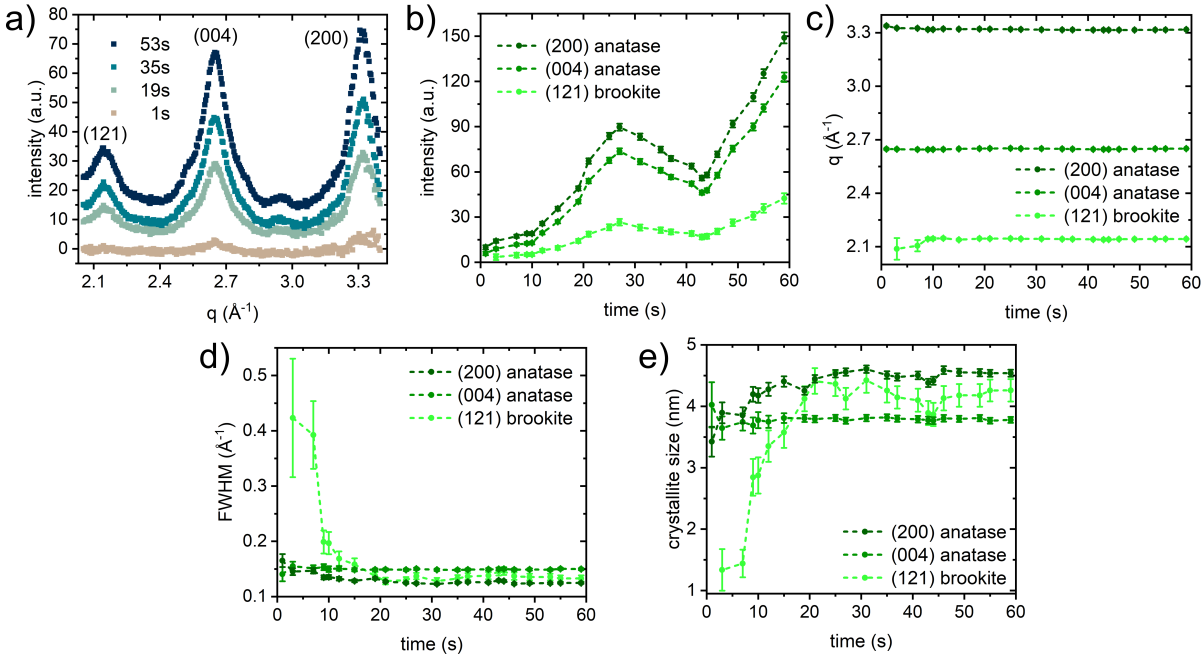

Figure 5.6.: Film formation on the crystalline length scale. a) 1D GIWAXS data after azimuthal integration of 2D GIWAXS data show the evolution of the crystal phases during spray deposition at a fixed position. Temporal evaluation of the b) intensity, c) q-position, d) FWHM, and e) crystallite size for the characteristic Bragg peaks as indicated. Reproduced from [17] with permission from Wiley, Copyright 2022.

The q-values defining the inverse lattice spacing and their respective FWHM are given in Figure 5.6c,d. The temporal evolution differs for the anatase and brookite phases. The anatase peaks indexed with (004) at (2.650 ± 0.001) Å^{-1} and (200) at (3.318 ± 0.001) Å^{-1} remain constant during the entire spray deposition. The brookite (121) peak shifts from (2.09 ± 0.06) to (2.143 ± 0.002) Å^{-1} within the first 9 s and remains constant afterward. Also, the FWHM of the brookite (121) peak shows a pronounced decay compared to the anatase crystallites from (0.4 ± 0.1) to (0.133 ± 0.006) Å^{-1} and remains constant within the error bars after approximately 30 s. At the same time, anatase (200) FWHM slightly decreases from (0.17 ± 0.01) to (0.125 ± 0.002) Å^{-1}, whereas the FWHM of the anatase (004) peak remains constant at (0.149 ± 0.002) Å^{-1}. Estimating the brookite crystal size by the Scherrer Equation 2.27 shows nucleation centers of around (1.3 ± 0.3) nm in the early stage at 3 s, growing to crystallites of (4.3 ± 0.2) nm in diameter (Figure 5.6e). I suggest, that these brookite nucleation centers are formed from the amorphous phase by the rapid solvent evaporation and temperature jump from room temperature of around 25 to 120 °C, introduced by the spray deposition on the heated substrate. [126]

The small nucleation centers have a high surface-to-volume ratio and hence high surface energy, which is lowered upon further crystal growth and consumption of the surrounding amorphous phase. [105], [127] In contrast, the estimated crystal size from the anatase (004) peak remains constant at (3.8 ± 0.1) nm after slight rearrangement within the error bars from 0 to 15 s (Figure 5.6e). The crystal size of anatase (200) shows a slight increase from (3.4 ± 0.2) to (4.5 ± 0.1) nm and remains constant after that (Figure 5.6e). These results indicate that the anatase crystallites are already formed during the hydrothermal sol–gel process and slightly grow preferentially toward the (200) direction, whereas the brookite crystallites form and grow as a consequence of spray coating on the heated substrate.

5.4. Lateral Film Formation on the Mesoscopic Length Scale

Simultaneous *in-situ* GISAXS is performed to link the lateral film formation on the mesoscopic length scale to the crystal growth evolution described before. With this, complementary information to the crystallite formation in the film on a hierarchical scale can be deduced. The chosen spray parameters cause the atomization process to be in the diluted regime when arriving at the substrate. Here, the solvent has not evaporated completely and the β-lg:titania phase is still dispersed in tiny droplets. [128] This enables drying kinetics on the substrate and hence morphological rearrangements that can be revealed by GISAXS. [129] Figure 5.7 shows the 2D GISAXS data at the selected position C close to the center of the spray cone, from which the horizontal line cuts are taken (Figure 5.8a).

The obtained radii for the small, medium, and large structures are presented in Figure 5.8b. The small structures (green triangles) grow in radius from (1.6 ± 0.2) to (2.1 ± 0.2) nm within the first 30 s of spray deposition and remain constant afterward. The medium structures (red circles) decrease from (4.4 ± 0.3) nm to (3.4 ± 0.3) nm during the first 30 s of film formation and remain constant afterward. A symmetric correlation between the shrinking medium and the growing small structure sizes is noticeable. The small structures are associated with the crystalline phase as they are in good agreement with the values for the brookite and anatase crystallite sizes obtained from GIWAXS. Hence, I conclude that the medium structures can be associated with the amorphous phase that is consumed during crystallite growth. The particle size distributions of small and medium structures both narrow with time (Figure 5.8d). This effect is more pronounced for the crystalline phase than for the amorphous phase and reflects the growing brookite crystallite size, which is approaching the constant size of anatase crystallites.

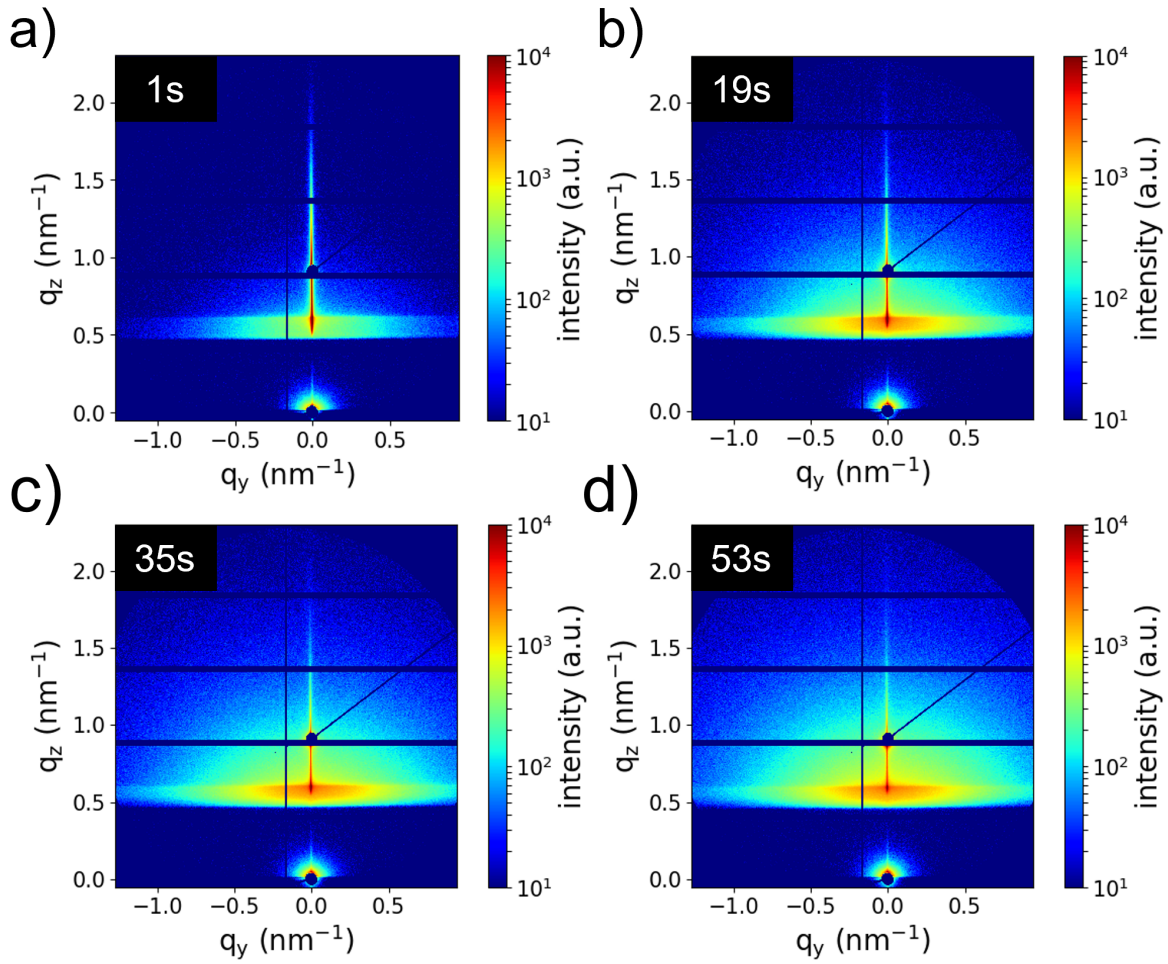

Figure 5.7.: 2D GISAXS data. Evolution of 2D GISAXS data shown for the selected position C at a) 1 s, b) 19 s, c) 35 s and d) 53 s. Reproduced from [17] with permission from Wiley, Copyright 2022.

Furthermore, the intensity related to the crystalline phase is 80 % higher than the amorphous phase intensity. Besides the structure sizes, also the center-to-center distances vary for the crystalline and the amorphous domains during film formation (Figure 5.8c).

The distance related to the titania crystallites (green circles) decreases from (10.2 ± 0.4) to (9.4 ± 0.4) nm. The distance between the amorphous domains (red squares) decreases from (20.5 ± 0.5) to (18.9 ± 0.5) nm. The distributions of the shrinking crystalline and amorphous center-to-center distances show also narrowing in the FWHM (Figure 5.8e). As discussed earlier, the distances of titania domains are related to separating β-lg domains. Hence, I conclude the driving force for the observed changes in the titania domain distances and their distribution widths to be the condensation of the surrounding biomatrix upon drying on the heated substrate. By comparing the temporal evolution

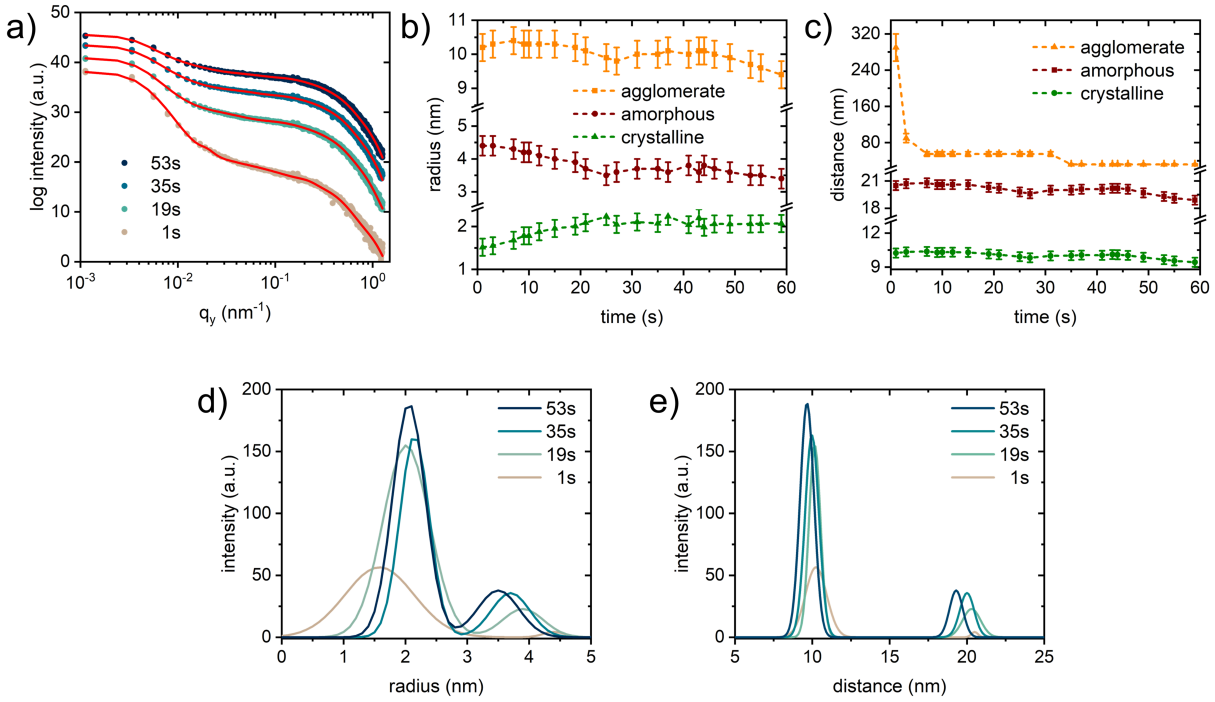

Figure 5.8.: Film formation on the mesoscopic length scale. a) Four selected horizontal line cuts at 1, 19, 35, and 53 s shown together with the modeled curves (red lines). Corresponding b) radii and c) distances of the crystalline phase (green), the amorphous phase (red) and the agglomerates (orange). d) Radius and e) distance distributions of the crystalline and amorphous phases. Reproduced from [17] with permission from Wiley, Copyright 2022.

of crystalline domain distance with the radius of the crystalline and amorphous phase, a common relation turns out, that can be described by

$$R_{amorphous} = \frac{D_{crystalline}}{\sqrt{3}} - R_{crystalline} \tag{5.5}$$

Here, $R_{amorphous}$ is the radius of the amorphous domain. $D_{crystalline}$ and $R_{crystalline}$ are the distance and the radius of the crystallites, respectively. The term $\frac{D_{crystalline}}{\sqrt{3}}$ describes the radius of an isosceles triangle. This link between amorphous and crystalline phases suggests that the titania morphology consists of semicrystalline clusters, built by an amorphous domain being centered within surrounding growing crystallites that are arranged in an isosceles triangle. In addition to the small structures (crystallites) and medium structures (amorphous phase), the large structures extracted from the horizontal line cuts decrease in radius from (10.2 ± 0.4) to (9.4 ± 0.4) nm during the time of spray deposition (Figure 5.8b) and in distance from (290 ± 30) to (32 ± 1) nm (Figure 5.8c). The evolution of the large structures equals the center-to-center distances of amorphous phase and

crystalline phase in the following way, suggesting the large structures to be agglomerates of adjacent semicrystalline clusters:

$$R_{agglomerates} = D_{crystalline} \approx \frac{1}{2} D_{amorphous} \tag{5.6}$$

Here, $R_{agglomerates}$ is the domain radius of the large structures built up by the semicrystalline clusters. $D_{amorphous}$ and $D_{crystalline}$ are the distances of the amorphous and the crystalline domain, respectively. Hence, I explain the resulting film morphology as semicrystalline titania clusters, formed by amorphous domains (medium structures) inside an isosceles triangular way arranged crystalline domains (small structures), that form agglomerates (large structures) with the adjacent semicrystalline clusters, inside the pores of the surrounding β-lg biomatrix. Besides the lateral film formation, the biohybrid film shows a uniform distribution along the vertical direction without the presence of any enrichment layers, which can be seen in the vertical line cuts taken at $q_y = 0$ nm^{-1} in Figure 5.9. This indicates also the absence of any roughness correlation between the interfaces.

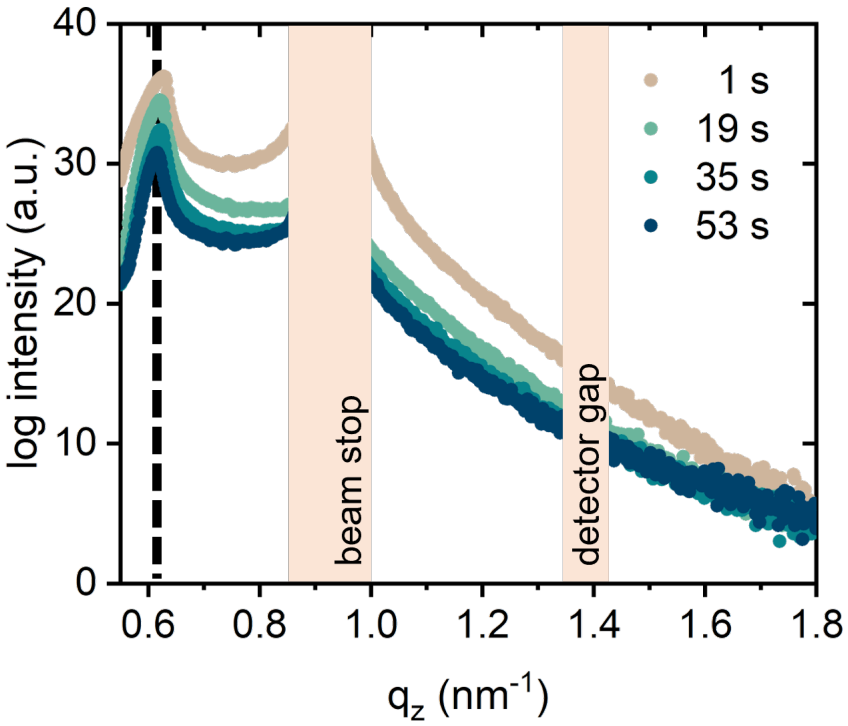

Figure 5.9.: Vertical film morphology. Vertical line cuts taken from selected GISAXS data at 1, 19, 25 and 53 s at $q_y = 0\ nm^{-1}$ provide information about vertical correlations. The absence of intensity modulations indicates a homogeneous vertical distribution without correlated roughness or enrichment layers at the interfaces. The material characteristic Yoneda peak labeled with a dashed line. The high specular intensity was blocked by a circular beam stop. Reproduced from [17] with permission from Wiley, Copyright 2022.

5.5. Steric Templating of Titania by β-lg

To further investigate the dependence of the film formation on the condensing β-lg biomatrix and to link it with the crystal growth obtained from GIWAXS, a Kratky-like analysis is performed (Figure 5.10a).

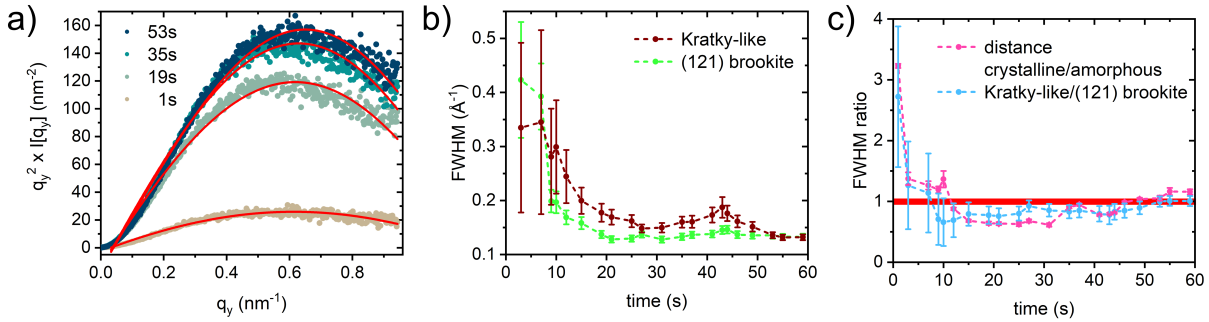

Figure 5.10.: Steric templating by the condensing biomatrix. a) Kratky-like representation of horizontal GISAXS line cuts fitted with Gaussian functions (solid red lines). b) FWHM of Kratky-like intensity bells (red circles) compared to the brookite (121) FWHM (green circles) obtained from GIWAXS. c) Ratio of Kratky-like intensity bell FWHM and brookite (121) FWHM (blue circles) converges to 1 and correlates with the ratio of the crystalline and amorphous distances' FWHM (pink circles). Reproduced from [17] with permission from Wiley, Copyright 2022.

The rise of an intensity maximum is noticeable during the film formation. These bell-shaped intensities are fitted with Gaussian functions to extract the respective center values for $q_{y,c}$ with the corresponding FWHM and hence to obtain information about the overall morphology formation, including the contributions of the crystalline, amorphous, and agglomerated domains. The evolution of the obtained $q_{y,c}$ shows an inverse correlation with the center-to-center distance associated with the crystalline phase and according to Equation 5.6 with the radius of the agglomerates

$$D_{crystalline} = R_{agglomerates} \propto \frac{1}{q_{y,c}} \tag{5.7}$$

This result further confirms that the morphology inside the biomatrix mainly consists of the semicrystalline clusters and their agglomerates. The corresponding FWHM of the Kratky-like intensity bell narrows during film formation, indicating a rearrangement into a more ordered assembly of the overall morphology. Interestingly, the Kratky-like FWHM shows the same trend in temporal evolution when compared to the brookite (121) FWHM evolution in Figure 5.10b. The ratio of the Kratky-like FWHM and brookite (121) FWHM converges to 1 and follows the evolution of the ratio obtained by dividing the crystalline phase distance's FWHM by the amorphous phase distance's FWHM (Figure 5.10c). The

convergence to 1 indicates that the film formation has finished since no changes appear anymore in the size distribution on the crystalline length scale (brookite (121) FWHM) and the overall morphology (Kratky-like intensity bell FWHM). Moreover, Figure 5.10c reflects, that the brookite crystallization and the overall morphological formation toward a more ordered spatial assembly are directly linked to the same mechanism. The temporal evolution of the morphology can be interpreted as the coalescence of the structures that is driven by the shrinking of the center-to-center distances as seen from the interdependence of radii and distances in Equations 5.5–5.7. As the semicrystalline clusters and their agglomerates are embedded in and separated by the biomatrix made up of the β-lg fibrillar network (Equations 5.1–5.4), the shrinking center-to-center distances can be related to the condensation of the β-lg biomatrix. Thus, the common mechanism for film formation is given by the fibrillar β-lg network, which acts as a steric template for the semicrystalline clusters and their agglomerates, building up the pearl necklace-like titania morphology.

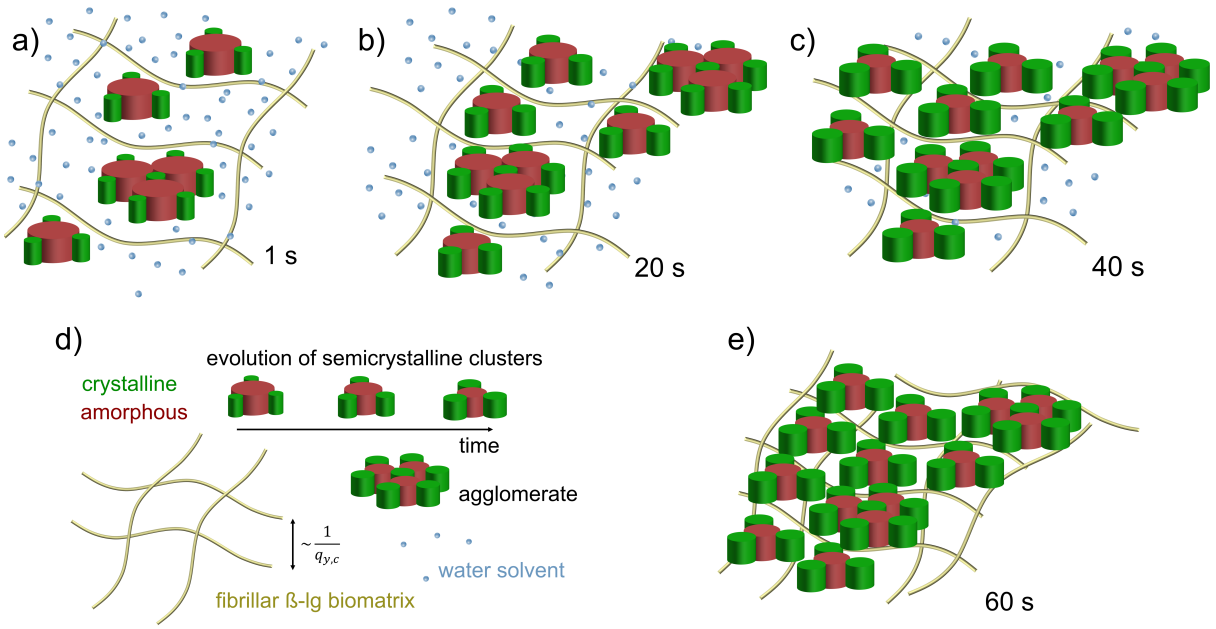

Figure 5.11.: Illustration of biotemplated film formation. The schematic illustrates the coalescence of the semicrystalline clusters and their agglomerates within the condensing fibrillar β-lg biomatrix during spray deposition on the heated substrate. The crystallites grow upon consumption of the amorphous phase. After the spray deposition and the subsequent annealing, the biohybrid film has fully dried and remains in a state of increased structural order as compared to the swollen state. Reproduced from [17] with permission from Wiley, Copyright 2022.

Since not all water evaporates during spray deposition, the biohybrid film is deposited in a swollen state of the biomatrix. The condensation mechanism takes place as the biomatrix gradually shrinks upon drying on the heated substrate, allowing for kinetic rearrangements toward higher spatial order, and eventually stops after the film has fully

dried. The mechanism of steric β-lg biotemplating is illustrated in Figure 5.11. It is further notable that the correlation of distribution widths obtained by Kratky-like analysis may serve as a tool for future evaluation of simultaneous GISAXS/GIWAXS data.

5.6. Conclusion

In the present study, I investigate the film formation of biohybrid titania:β-lg composites with respect to the influence of β-lg on the titania morphology during spray deposition on a heated substrate. For this, *in-situ* GISAXS and GIWAXS techniques are combined and complemented with static GISAXS and SEM imaging to understand the formation process on the crystalline and nanometer length scale. The titania nanostructure consists of agglomerates of semicrystalline clusters with a mixed brookite-anatase crystal phase of around (4.2 ± 0.3) nm crystal grain size. In these semicrystalline clusters, the amorphous phase is consumed by the growing crystalline phase. I show that the distribution widths obtained from a Kratky-like representation serve as a good tool to link the analysis of GISAXS to GIWAXS. As a result, there is a correlation of the brookite distribution width extracted from GIWAXS with both, the amorphous and crystalline domain distance distribution widths obtained from GISAXS. The shrinking distances of the titania domains are attributed to the condensing β-lg biomatrix, in which semicrystalline titania clusters are agglomerating. This interpretation is further supported by the findings from *ex-situ* SEM and GISAXS measurements. In SEM, the biotemplated titania exposed to UV irradiation shows a foam-like nanostructure provided by a pearl necklace-like titania scaffold, introduced by the fibrillar β-lg biomatrix. *Ex-situ* GISAXS measurements reveal, that the pore size of a pure β-lg reference agrees with the domain radii of the biohybrid titania morphology and vice versa. These results lead to the conclusion that the β-lg biomatrix acts as a promising biotemplate for the creation of foam-like titania nanostructure with a pearl necklace-like order by sterically directing the morphology formation. Therefore, this work presents an approach to a water-based, low-temperature route for the synthesis of nanostructured foam-like brookite-anatase mixed titania films by spray deposition. It is promoting an environmentally friendly and more sustainable fabrication of titania-based functional films with the possibility to an upscaling on large scale being of interest for multiple applications from the fields of sensors, energy conversion and energy storage.

Chapter 6

Tuning the Morphology of Biohybrid β-lg:titania Films with pH for Water-Based Nanostructured Titania Synthesis

The supramolecular structure of the whey protein β-lg varies when denatured at different pH values and is used as a biotemplate for the water-based synthesis of nanostructured and foam-like titania films. The water-soluble titania precursor TiBALDh is in chemical equilibrium with anatase titania nanoparticles and Ti(IV)-lactate complexes, and this equilibrium shifts with varying pH. When β-lg is mixed with TiBALDh to promote biotemplated titania precipitation, the influence of the pH value on the final film morphology becomes essential. This work investigates this influence for three pH values: pH 7, pH 5, i.e., close to the isoelectric point of β-lg, and pH 2. Spray deposition, a method of industrial relevance, is used to fabricate biohybrid β-lg:titania foam-like films. The obtained films are calcined to combust the biotemplate β-lg and achieve nanostructured titania films. To understand the influence of pH on the film morphology, GISAXS/GISANS and GIWAXS, in combination with SEM, are applied on both the biohybrid and biotemplated films. With these techniques, information about domain sizes, porosity, and crystallinity is obtained with high statistical significance. FTIR probes the interaction of TiBALDh and β-lg on the molecular level as function of pH. The results underline pH as a suitable tool for tuning the morphology in biotemplated titania films.

6.1. Preface

The omnipresent role of nanostructured titania in various applications, such as ecological and energy-related fields, indicates titania's versatile potential to contribute to environ-

mental sustainability. Nanostructured titania is used as a photocatalyst to decompose CO_2 and produce hydrogen by water-splitting, in protective and self-cleaning coatings, and as electrodes in next-generation solar cells and batteries. [130] A tailored morphology and crystallinity of the nanostructured titania is essential to benefit the overall device performance in applications. [26], [80], [131], [132] For instance, the porosity and its size distribution control the interfacial area in applications and, hence, the functionality. Sol-gel synthesis under the direction of copolymer templates is a proven strategy to introduce a controlled morphology to nanostructured titania. Moreover, the obtained solutions and dispersions are feasible for deposition via large-scale industrial methods, such as printing and spray coating. To further increase sustainability, water-based biotemplating of titania using biopolymers becomes increasingly attractive. [97], [99] In this context, the whey protein β-lg has shown its potential in the substitution of synthetic copolymers. [17], [36] The biomatrix is built up by the supramolecular structures of heat-denatured β-lg, which sterically directs the formation of titania domains within the pores of the biomatrix. The supramolecular structure and, thereby, the biomatrix depend on the pH value at which β-lg is denatured and ranges from amyloid fibrils to spherical and worm-like aggregates. [34] The water-based titania precursor TiBALDh is used in the biomineralization of titania due to its biocompatibility. Ti(IV) ammonium lactate complexes improve the water-solubility of titania. The precursor is in chemical equilibrium in water with anatase-TiO_2 and promotes the precipitation of crystalline titania at room temperature: [23], [24]

$$3\left[Ti_4O_4\left(lactate\right)_8\right]^{8-} + 8NH_4^+ \leftrightarrows 8\left[Ti\left(lactate\right)_3\right]^{2-} + 4TiO_2 + 8NH_3 + 4H_2O \quad (6.1)$$

Besides concentration and ionic strength, the chemical equilibrium depends on the pH value, which influences the amount of water-soluble Ti(IV) complexes. Hence, the pH value becomes essential to be considered for the water-based synthesis of nanostructured titania fabricated from β-lg and TiBALDh. In this chapter, the film morphology of foam-like biohybrid β-lg:TiBALDh films, which are deposited by spray coating, is investigated. Here, spray coating aligns with economic interests as it is a deposition method with low material usage and the possibility of being upscaled to industrial levels. The surface morphology of the pristine and biotemplated titania films is investigated with SEM. The information about the surface is extended to the bulk morphology of the biotemplated titania films with GISAXS and GIWAXS, where domain sizes, porosity, and crystallinity are extracted with a high statistical significance, and compared to the biohybrid and pure β-lg films. The results are complemented by neutron scattering (GISANS), which provides a different contrast sensitivity than GISAXS. The influence of pH on the domain sizes, size distribution, and crystallinity in the foam-like biohybrid films and the nanostructured, foam-like titania films after biopolymer removal is revealed. The molecular

interaction between TiBALDh and β-lg is probed with FTIR. Consequently, the results contribute to the understanding of nanostructured, foam-like, biotemplated titania films, which meet ecological and economic interests and promote sustainable material synthesis that is relevant to energy research.

6.2. Influence of the pH Value on the Foam-Like Nanostructure

To reveal the role of β-lg as a template for titania nanostructure while varying the pH value, samples of pure β-lg films, the foam-like biohybrid composite film of β-lg:TiBALDh, the biotemplated titania after β-lg removal via calcination, and pristine titania via calcination of the pure TiBALDh films are fabricated. Each sample is prepared at three different pH values under otherwise constant conditions. The pH value is adjusted to a neutral level of 7, to 5 which is close to the isoelectric point of β-lg, and to an acidic level of 2. At these values, heat denaturation of β-lg is known to introduce worm-like structures, spherical agglomerates, and amyloid fibrils, respectively. [34] Experimental details on sample preparation and characterization are given in Section 3.2 and in Section 4.5, respectively.

A direct comparison of the surface morphology with SEM after calcination of the biotemplated titania and the pristine titania, as reference, is given in Figure 6.1. The pristine titania consists of a dense surface, that is built up by nanometer-sized titania particles. With increasing pH value from 2 to 5 to 7 (Figure 6.1a, b, c), hardly any changes on the surface are recognizable. Upon higher magnification (Figure 6.1d, e, f), the titania nanoparticles become apparent. The biotemplated foam-like titania films, however, consist of nanoporous surfaces, that are built up by larger titania domains compared to the pristine domains. The underlying porous structure has a worm-like shape, that are of comparable size at the different pH, but are embedded in a changing superstructure with increasing pH (Figure 6.1g-l). This superstructure consists of titania agglomerates with sizes between 50 nm and 250 nm at pH 7. Close to the isoelectric point of β-lg at pH 5, the superstructure is characterized by spherical pores. At the acidic pH 2, where β-lg forms amyloid fibrils, the superstructure is formed by a fibrillar network of micrometer elongated pores. The surface morphology demonstrates the pH-dependent influence of β-lg as a foaming agent on the titania nanostructure. In order to quantify size distributions in a statistical relevant matter and to extend the morphology information from surface to bulk and from nano- to atomic scale, GISAXS, GIWAXS, and GISANS are performed on the different sets of samples.

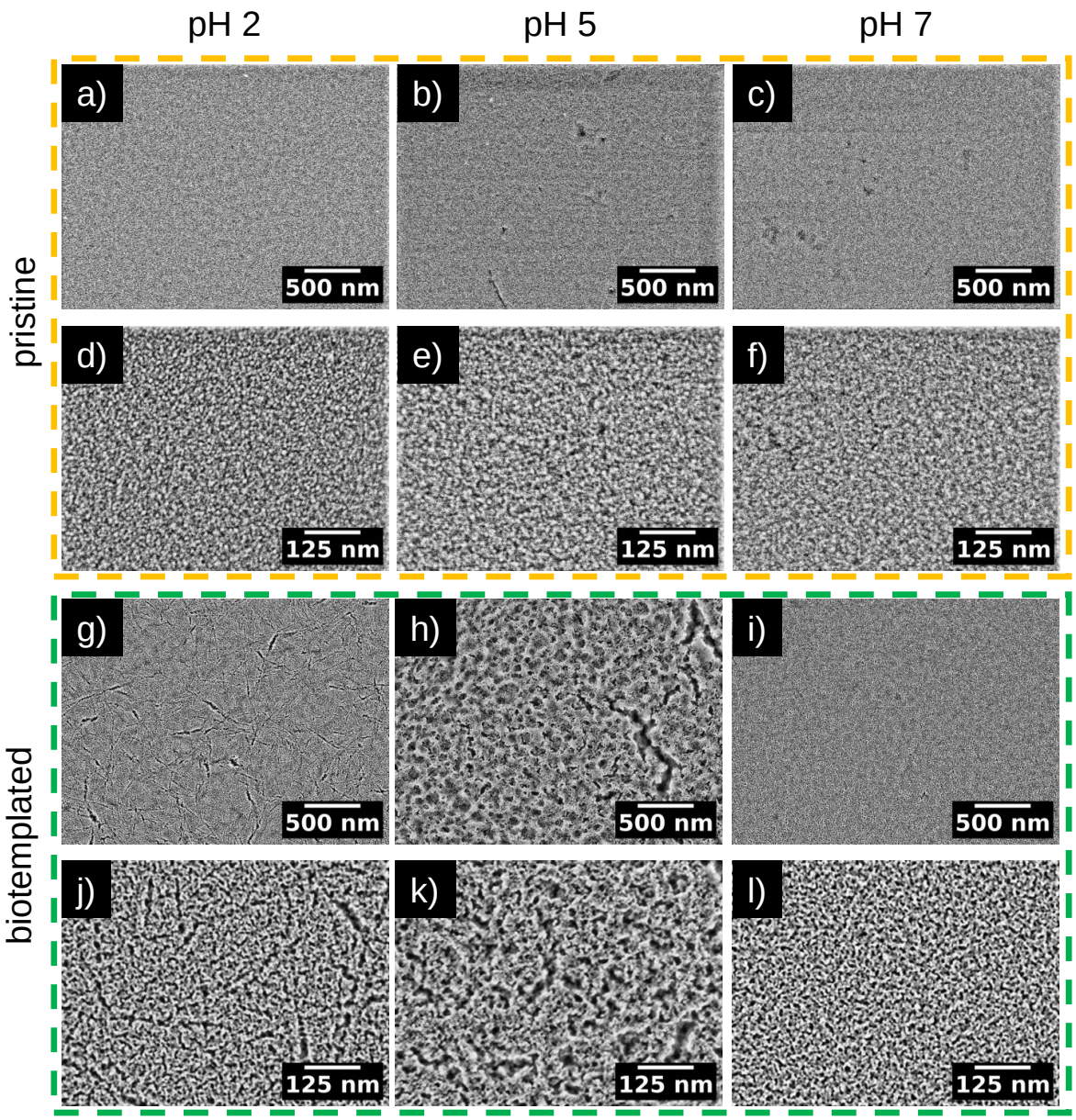

Figure 6.1.: SEM surface morphology of titania. a)-f) Surface of the pristine titania films after calcination at two different magnifications for the three different pH values. g)-l) Surface of the biotemplated titania films after calcination at two different magnifications for the three different pH values.

Figure 6.2 shows the GISAXS results and the obtained domain sizes for the biohybrid samples. To extract quantitative values, material characteristic horizontal 1D intensity line cuts taken from the 2D GISAXS data are modeled with cylindrical form factors distributed on a 1D paracrystal (Figure 6.2a). From this model, average domain sizes (Figure 6.2b) and their dispersions (Figure 6.2c) are extracted. The results show that

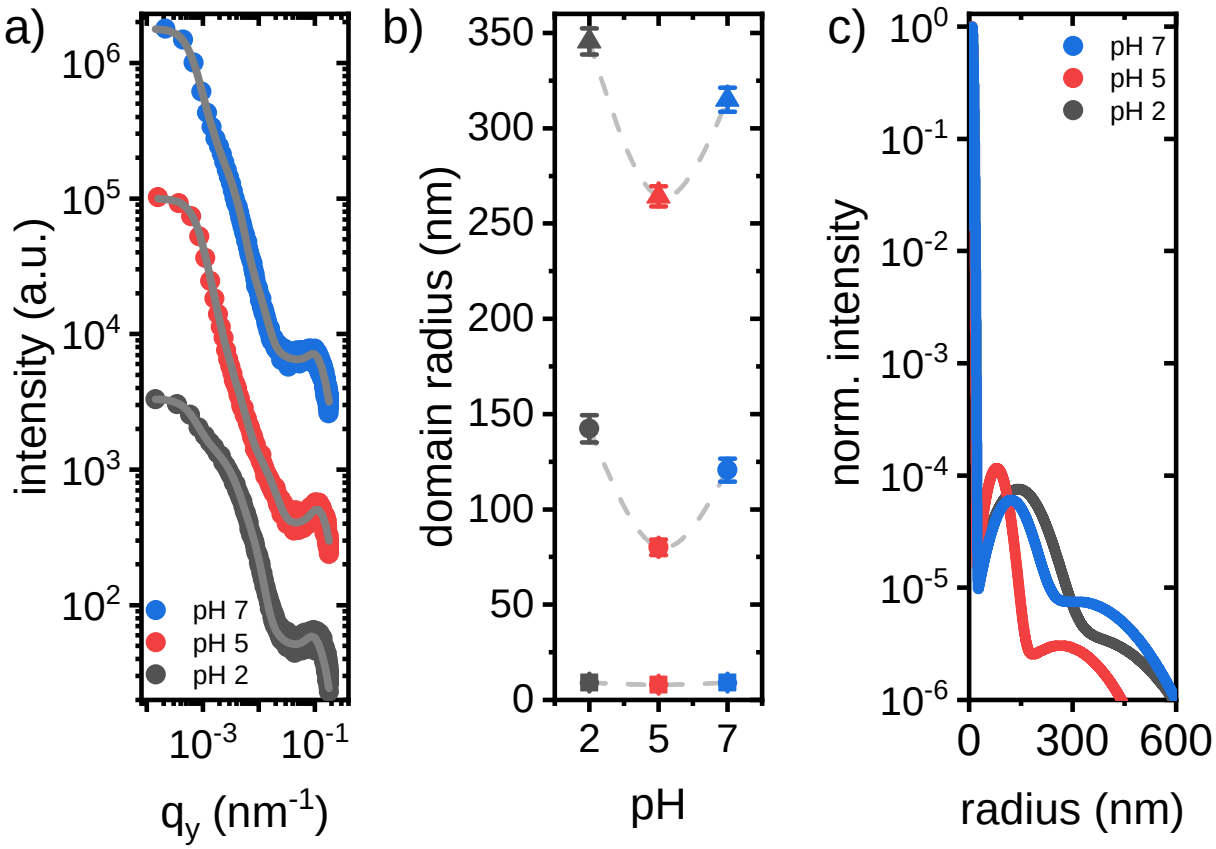

Figure 6.2.: GISAXS result from biohybrid foam-like films. a) Material characteristic horizontal 1D GISAXS line cuts of biohybrid films synthesized at three different pH values. Gray lines show the corresponding model calculations from which the domain radii are obtained. b) Domain radii as function of pH, categorized in small domains (square), medium-sized (circle), and large domains (triangle). c) Normalized size distributions of the domains in the biohybrid films at different pH values.

the biohybrid domains have a trimodular size distribution, which is built up by small, medium-sized, and large domains. The small domains remain nearly unaffected by pH with a radius of (9.0 ± 0.5) nm at pH 2, (8.0 ± 0.4) nm at pH 5, and (9.0 ± 0.5) nm at pH 7. The medium-sized domains show strong dependence on pH with a minimum radius of (80 ± 4) nm at pH 5, compared to (142 ± 7) nm at pH 2 and (121 ± 6) nm at pH 7. Also, the average radius of the large domains varies from (315 ± 6) nm at pH 7 to (264 ± 5) nm at pH 5, and to (345 ± 7) nm at pH 2. The size distribution of the medium-sized domains has the narrowest dispersion ($\sigma_m = 35$ %) and highest number at pH 5 compared to pH 2 ($\sigma_m = 40$ %) and pH 7 ($\sigma_m = 45$ %). For the small and large domains, the size distributions remain constant at $\sigma_s = 35$ % and $\sigma_l = 45$ %, respectively. To extend the information on the biohybrid film morphologies, GISANS is performed in addition to GISAXS. Neutron scattering contrast differs from X-ray and

hence complements morphology investigations by detection of additional domains. Figure 6.3a shows line cuts from 2D GISANS data of the biohybrid foam-like films synthesized at pH 7 and a pure β-lg reference. Here, the scattering signal from the biohybrid domains

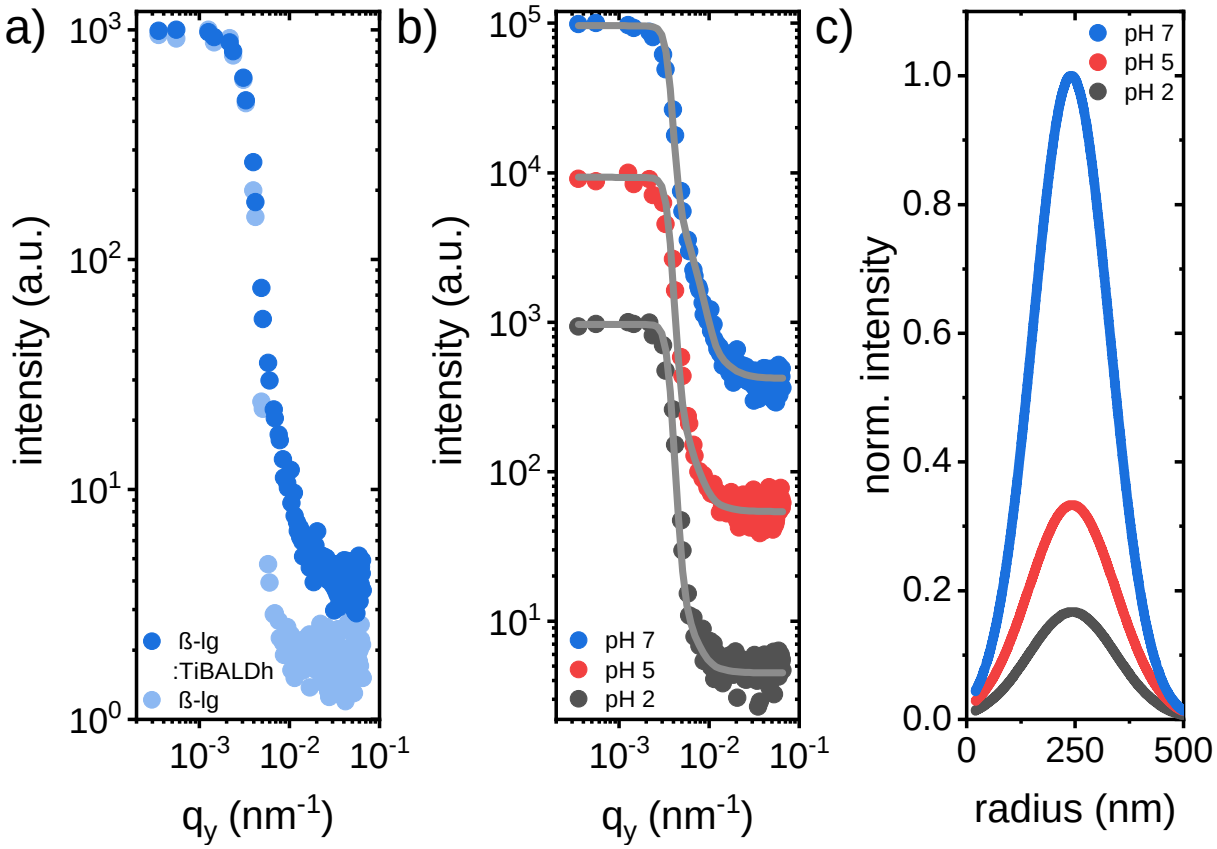

Figure 6.3.: GISANS result from biohybrid foam-like films. a) Material characteristic horizontal 1D GISANS line cuts of the biohybrid film and the pure β-lg film synthesized at pH 7. b) Material characteristic horizontal 1D GISANS line cuts of biohybrid foams synthesized at three different pH values. Gray lines show the corresponding model calculations from which the domain radii are obtained. c) Normalized size distribution of the domain radius decreases in intensity with decreasing pH value.

is higher. Stronger background at higher q_y-values in the biohybrid foam compared to the reference results from incoherent scattering of the hydrogen-rich TiBALDh domains. Figure 6.3b shows the line cuts taken of the biohybrid samples synthesized at the three different pH values. Utilizing the same model as for GISAXS, the GISANS domain radii are extracted. A single domain size of about 250 nm is sufficient to describe the data. With decreasing pH, the average size remains constant but the overall number of domains diminishes. (Figure 6.3c).

The GISAXS line cuts of the biotemplated titania foams after calcination at 500 °C are presented in Figure 6.4a, from which domain sizes are extracted (Figure 6.4b). The small

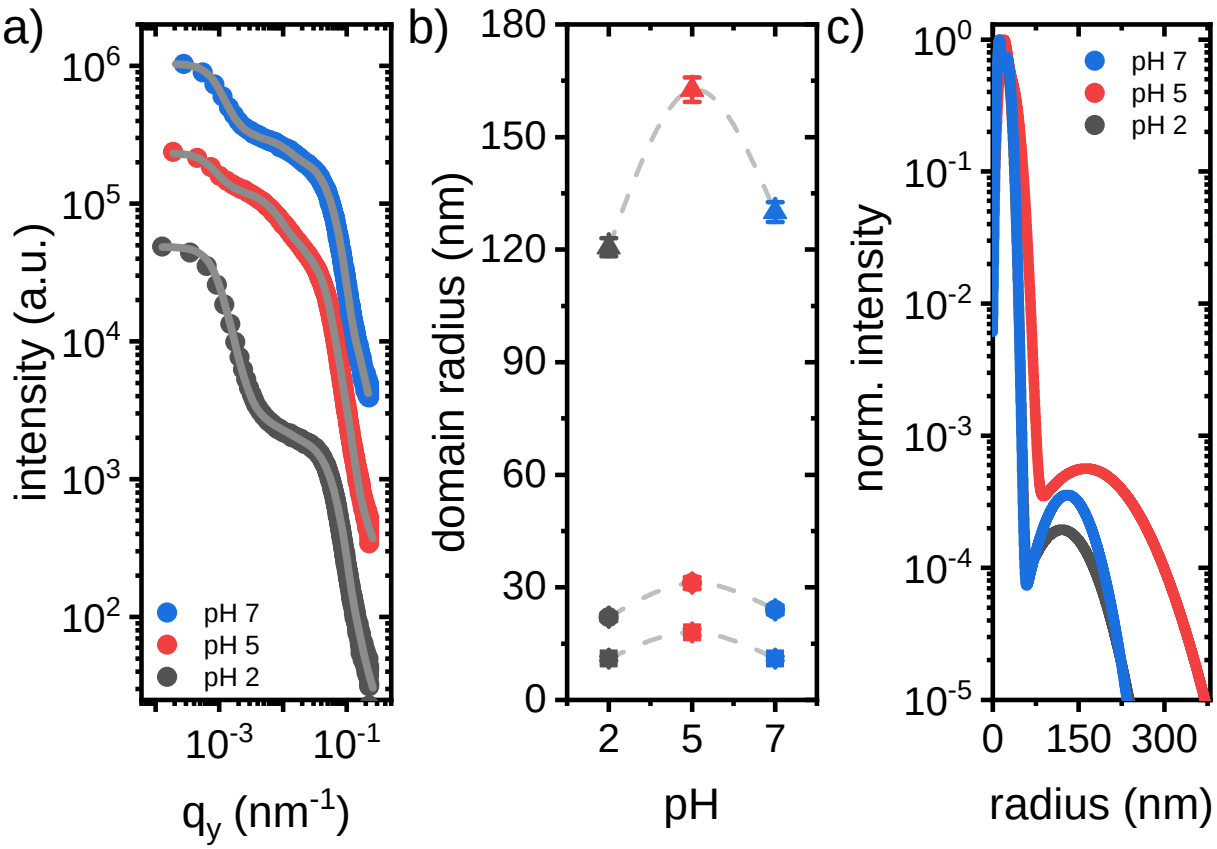

Figure 6.4.: GISAXS result from nanostructured, foam-like titania films. a) Material characteristic horizontal 1D GISAXS line cuts of the nanostructured titania films after calcination at 500 °C. Gray lines show the corresponding model calculations from which the domain radii are obtained. b) Domain radii as function of pH, categorized in small domains (square), medium-sized (circle), and large domains (triangle). c) Normalized size distributions of the domains in the nanostructured titania films after calcination at 500 °C.

domains are of same size at pH 2 and pH 7 with (11.0 ± 0.6) nm in radius. The radius of the medium-sized and large domains are with (24 ± 1) nm and (130 ± 3) nm slightly larger at pH 7 than at pH 2 with (22 ± 1) nm and (121 ± 2) nm, respectively. The largest domains are found in the pH 5 sample for all three domain types. The radii of small, medium-sized, and large domains at pH 5 are (18 ± 1) nm, (31 ± 2) nm, (163 ± 3) nm, respectively. This trend is opposite to the biohybrid foams before calcination. Whereas small domains in the nanostructured titania foams are more than twice as large, the medium-sized and large domain are smaller in comparison to the respective domains in the biohybrid foams. Furthermore, the distributions of the small and medium-sized domains tend to overlap at pH 2 ($\sigma_s = 35$ %, $\sigma_m = 36$ %), at pH 5 ($\sigma_s = 35$ %, $\sigma_m = 40$ %), and at pH 7 ($\sigma_s = 30$ %, $\sigma_m = 30$ %) (Figure 6.4c). The large domains have the broadest

distribution at pH 5 (σ_l = 45 %), followed by pH 2 (σ_l 40 %), and are the smallest at pH 7 (σ_l = 30 %).

To connect the morphology from biohybrid samples and biotemplated titania, the information about the pure β-lg films, presented in Figure 6.5, is essential. The small,

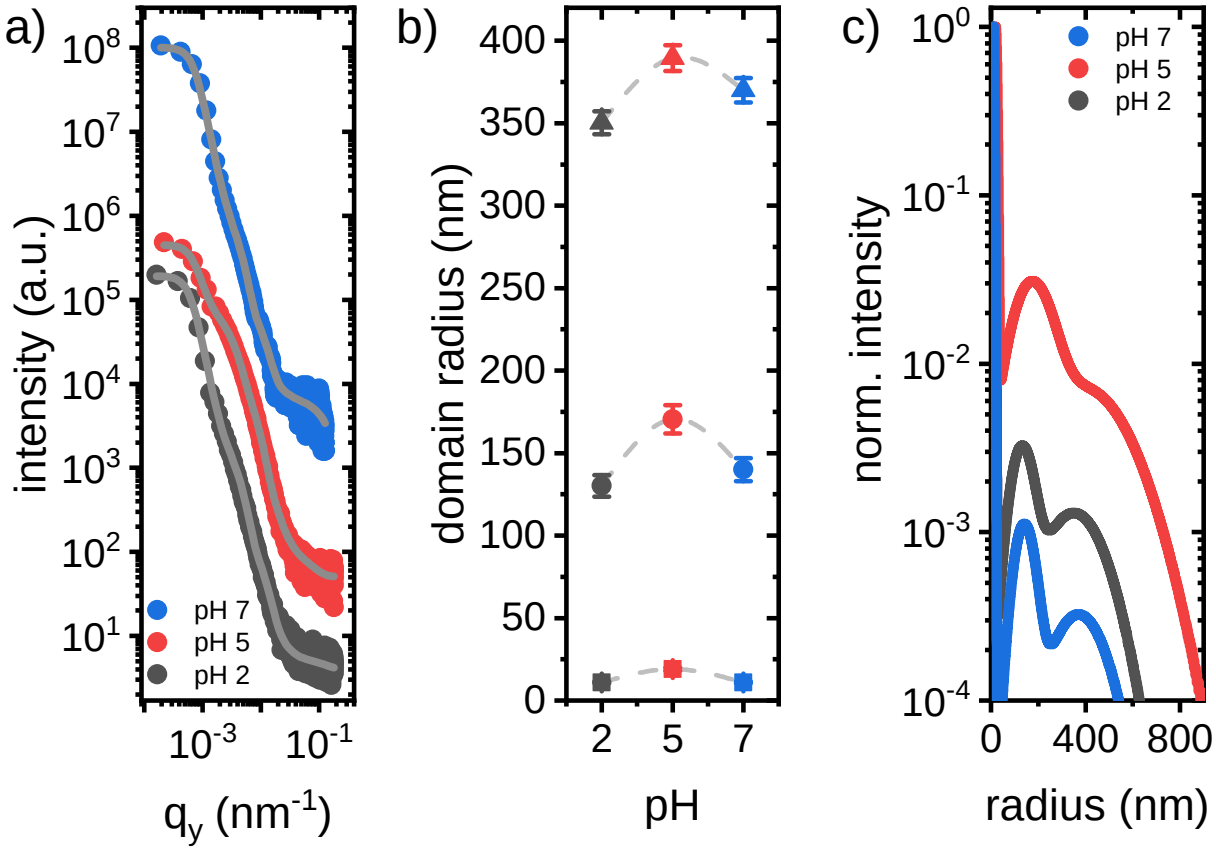

Figure 6.5.: GISAXS result from β-lg foam-like films. a) Material characteristic horizontal 1D GISAXS line cuts of β-lg films synthesized at three different pH values. Gray lines show the corresponding model calculations from which the domain radii are obtained. b) Domain radii as function of pH, categorized in small domains (square), medium-sized (circle), and large domains (triangle). c) Normalized size distributions of the domains in the pure β-lg films at different pH values.

medium-sized, and large domains have each a maximum size at pH 5 with (19 ± 1) nm, (171 ± 9) nm, and (390 ± 8) nm, respectively. At pH 2, the respective domain radii are (11 ± 1) nm, (130 ± 7) nm, (350 ± 7) nm, and at pH 7, (11 ± 1) nm, (140 ± 7) nm, (370 ± 7) nm. The size distributions for the small domains are $\sigma_s = 35$ % at pH 2, $\sigma_s = 30$ % at pH 5, and $\sigma_s = 30$ % at pH 7, for the medium-sized domains $\sigma_m = 35$ % at pH 2, $\sigma_m = 45$ % at pH 5, and $\sigma_m = 30$ % at pH 7, and for the large domains $\sigma_l = 35$ % at pH 2, $\sigma_l = 44$ % at pH 5, and $\sigma_l = 30$ % at pH 7. When comparing the biotemplated films to the pure β-lg films, the domain sizes for both sets of films show the same trend with

changing pH. The large and small domains of biotemplated titania match the medium-sized and small domains of the pure β-lg films, respectively. This result indicates that the biotemplated domains in Figure 6.4b represent the pores inside the foam-like titania films, which are formed by the β-lg-template.

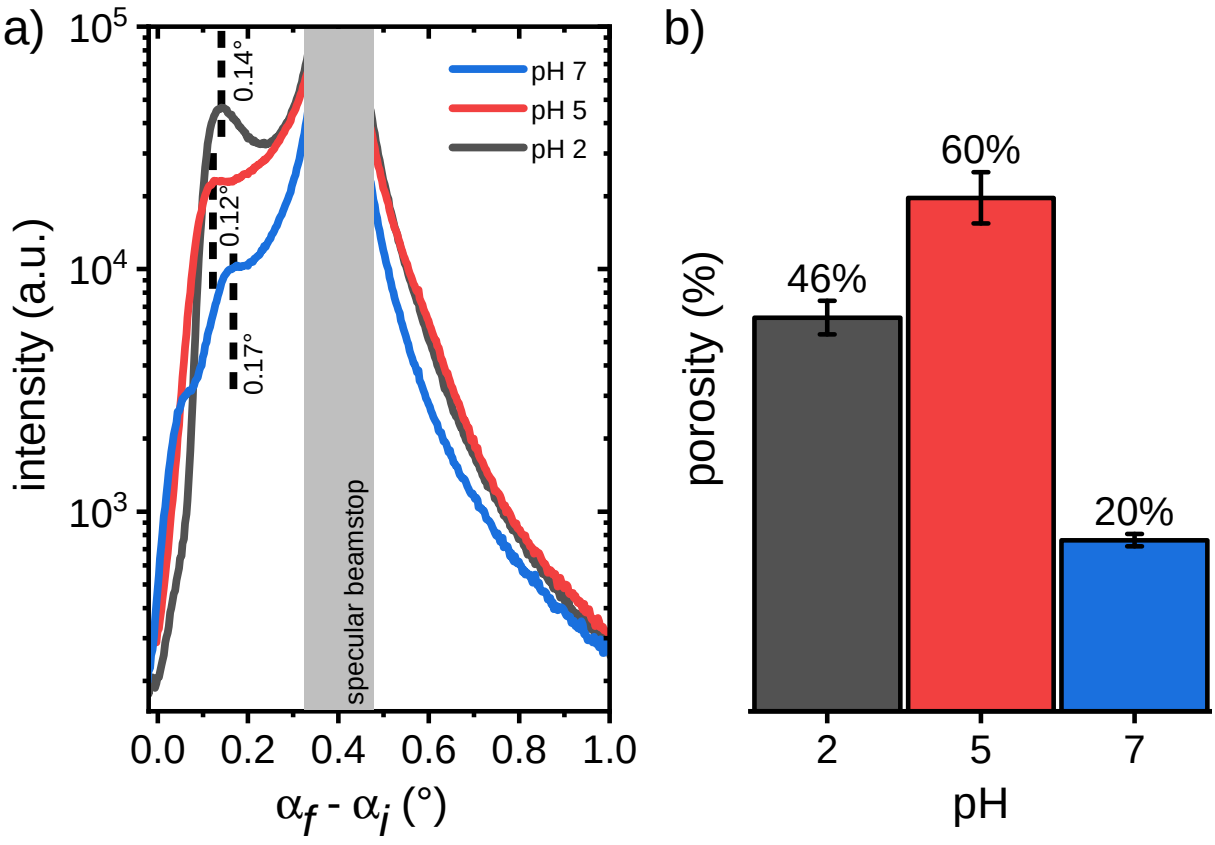

Figure 6.6.: Vertical GISAXS line cuts of biotemplated titania as function of pH. a) The vertical line cuts show a shift in the critical angle α_c, which is related to the electron density of the calcined titana films. b) The porosity of the biotemplated films after calcination at 500 °C for the different pH, as obtained from the varying electron density.

The relative degree of porosity Φ is estimated by the comparison of the varying SLD that is obtained from vertical GISAXS line cuts of the nanostructured titania after calcination (Figure 6.6a). The experimental SLD_{exp} and hence the electron density is taken from the Yoneda peak position at the critical angle $\alpha_{c,exp}$, following Equation 2.15, as explained in Section 2.5, and compared to the theoretical $\alpha_{c,bulk} = 0.19°$ calculated for bulk anatase titania with a material density of 3.9 g cm^{-3} at a wavelength of 1.05 Å. The porosity Φ is then estimated by the following equation: [109]

$$\Phi = 1 - \left(\frac{\alpha_{c,exp}}{\alpha_{c,bulk}} \right)^2 \tag{6.2}$$

The biotemplated titania films have the highest porosity of 60 % at pH 5, followed by 46 % porosity at pH 2, and 20 % porosity at pH 7 (Figure 6.6b).

Figure 6.7 shows azimuthally integrated, pseudo-XRD cuts obtained from 2D GIWAXS data of the biohybrid (Figure 6.7a) films and the calcined biotemplated titania (Figure 6.7b) films. The 1D cuts contain information about the films' crystal phase and are

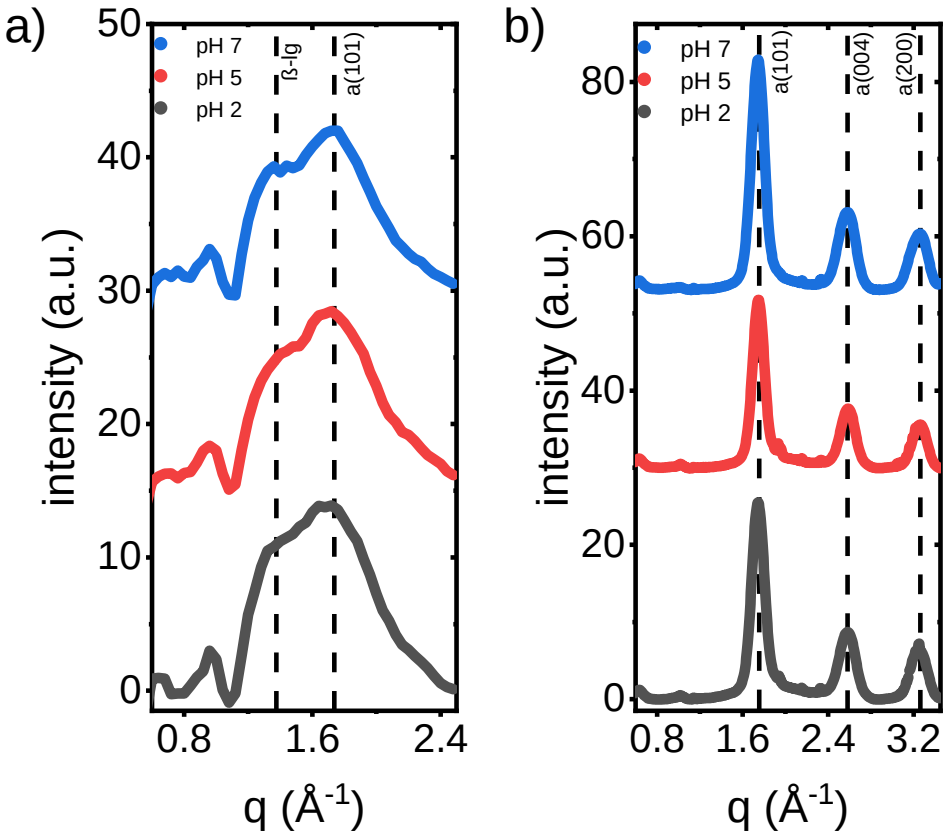

Figure 6.7.: GIWAXS result on the crystal phase. Pseudo-XRD cuts, which give information on the crystal phase of the a) foam-like biohybrid films and b) nanostructured, foam-like titania films after calcination.

analogous to powder-like X-ray diffraction. In the biohybrid films, a fingerprint of anatase can be detected with a rather broad peak at $q = 1.75$ Å^{-1}, which corresponds to the (101) anatase reflex. Furthermore, the peak at $q = 1.35$ Å^{-1} is related to β-lg and the spacing of its β-strands within a β-sheet. In the biotemplated films after calcination, the peaks centered at $q = 1.75$ Å^{-1}, $q = 2.58$ Å^{-1}, $q = 3.25$ Å^{-1} are related to the (101), (004), and (200) reflexes of anatase and do not show obvious influence of pH.

6.3. Influence of the pH Value on the Molecular Level

Drop-casted films of TiBALDh, β-lg, and the biohybrid composite are investigated with FTIR to analyze changes on the molecular level as function of pH and to also identify possible interactions between the biopolymer and the titania precursor. Figure 6.8a shows the FTIR absorbance spectra of TiBALDh at different pH. The spectra consist of rela-

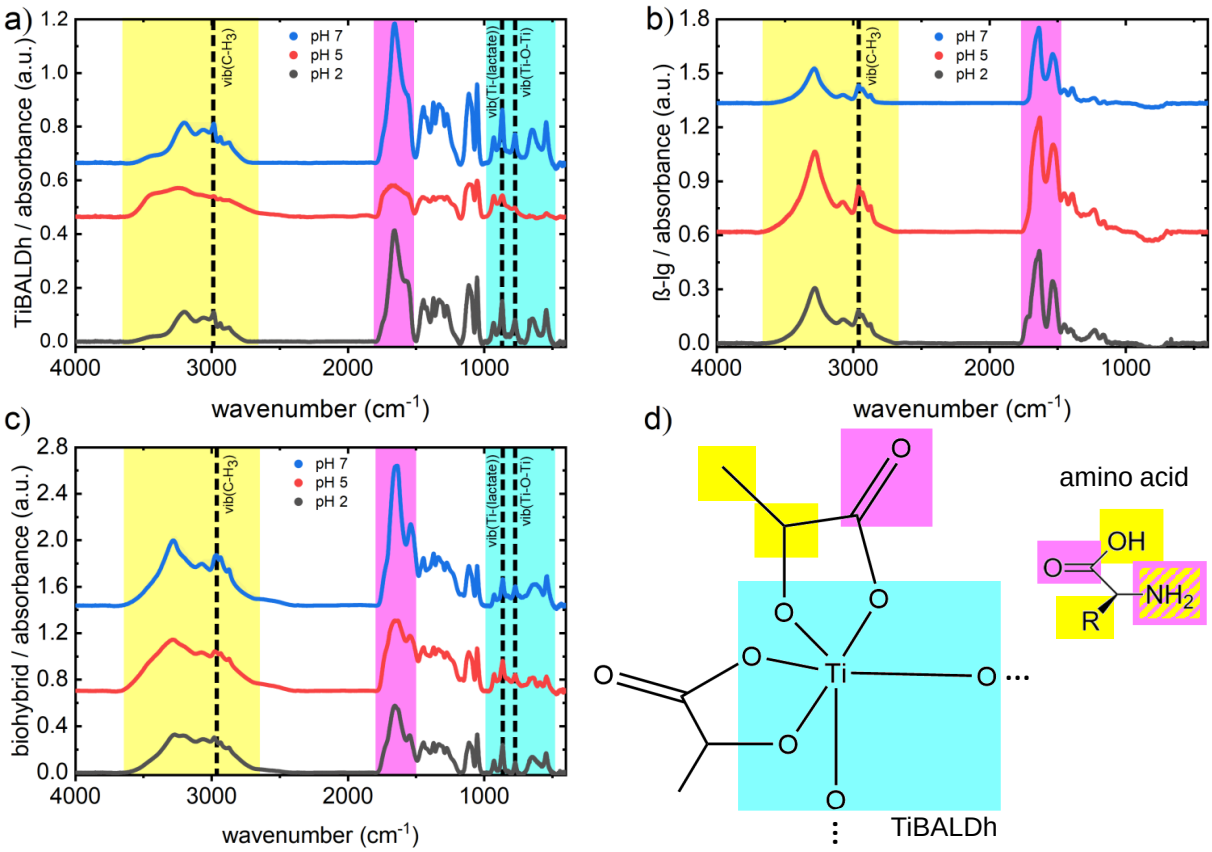

Figure 6.8.: FTIR absorbance spectra. Influence of different pH values on the a) TiBALDh films', b) β-lg films', and c) biohybrid films' absorbance spectra. d) Illustration of the molecular sites of TiBALDh and the amino acids in β-lg that are involved in the absorbance spectra.

tively complex absorbance signals that overlap strongly in the regime from 2400 cm^{-1} to 3700 cm^{-1}. Absorption peaks in this regime originate from O-H, N-H, C-H_2, and C-H_3 stretching vibrations. Also, the signal rising from carbonyl groups, i.e., C=O stretching from 1500 cm^{-1} to 1800 cm^{-1}, as well as the fingerprint region from 1500 cm^{-1} to 1200 cm^{-1}, show overlapping signals. Towards smaller wavenumbers, from 1000 cm^{-1} to 400 cm^{-1}, the absorbance peaks become more distinct and are partially related to Ti-O vibrations. Whereas the pH 7 and pH 2 films do not show major difference beside slight intensity variations in the O-H and C=O band, the pH 5 sample shows a strong deviation

with loss in intensity and peak broadening over the entire spectra. Furthermore, peak shifts of several signals, strong changes in the intensity especially in the N-H and O-H regime, and the development of an additional shoulder at 2625 cm^{-1} suggest the formation of different molecular interactions or even changes on a constitutional level of the precursor.

The absorbance spectra of the pure β-lg samples at the respective pH values is presented in Figure 6.8b. The signal at about 3280 cm^{-1}, which is assigned to the O-H stretching vibration, is decreasing in intensity with increasing pH. A smaller peak at 3072 cm^{-1} shows increasing intensity and is related to N-H stretching. The region from 1475 cm^{-1} to 1775 cm^{-1} shows two main features. The first feature around 1600 cm^{-1} to 1700 cm^{-1} is related to the amide I band, which is characteristic for proteins and includes overlapping signals from α-helices, β-sheets, and random coil segments. The second peak at about 1530 cm^{-1} is called the amide II signal, which is a contribution of several vibrations derived from amide groups. One of the main contributing vibrations is the N-H bending vibration of the amide functional group. With decreasing pH, a small shoulder evolves at 1720 cm^{-1}, which indicates that inter- or intramolecular interactions in the protein are changed at the polar group. The contributions from both the TiBALDh and β-lg spectra are recognizable along with their respective pH dependencies in the absorbance spectra of the biohybrid composite at different pH (Figure 6.8c). To evaluate the possible interactions in the biohybrid films more thoroughly, specific peaks are chosen and analyzed with respect to their peak center position.

Figure 6.9a shows the absorbance peak which is originating from the asymmetric C-H stretching vibration of the methyl groups. [133] For the pure TiBALDh samples, this peak is located at around 2985 cm^{-1} and does not change with varying pH. In the pure β-lg samples, the peak is originating from the methyl groups in the residuals of amino acids and is located at around 2060 cm^{-1}. Also this β-lg peak position does not shift with varying pH. Interestingly, in the biohybrid composite sample, the signal does shift to higher wavenumbers from about 2967 cm^{-1} at pH 7 to about 2976 cm^{-1} at pH 5 to about 2981 cm^{-1} at pH 2. This result indicates that due to interactions between TiBALDh and the protein, the system becomes pH sensitive at the molecular level. Figure 6.9b shows the absorbance peaks stemming from the Ti-(lactate) vibrations at around 868 cm^{-1} and from the Ti-O-Ti vibrations at around 775 cm^{-1}. [133], [134] In the pure TiBALDh samples, the Ti-(lactate) vibrations slightly shift towards higher wavenumbers from 867 cm^{-1} at pH 7 to 868 cm^{-1} at pH 5 to 869 cm^{-1} at pH 2, and the Ti-O-Ti vibrations remains constant at 774 cm^{-1} for pH 7 and pH 2, while it shifts to the higher wavenumber at 777 cm^{-1} for pH 5. Remarkably, this further highlights the deviating behaviour on the molecular level of TiBALDh at pH 5 when compared to pH 2 and pH 7 and might be

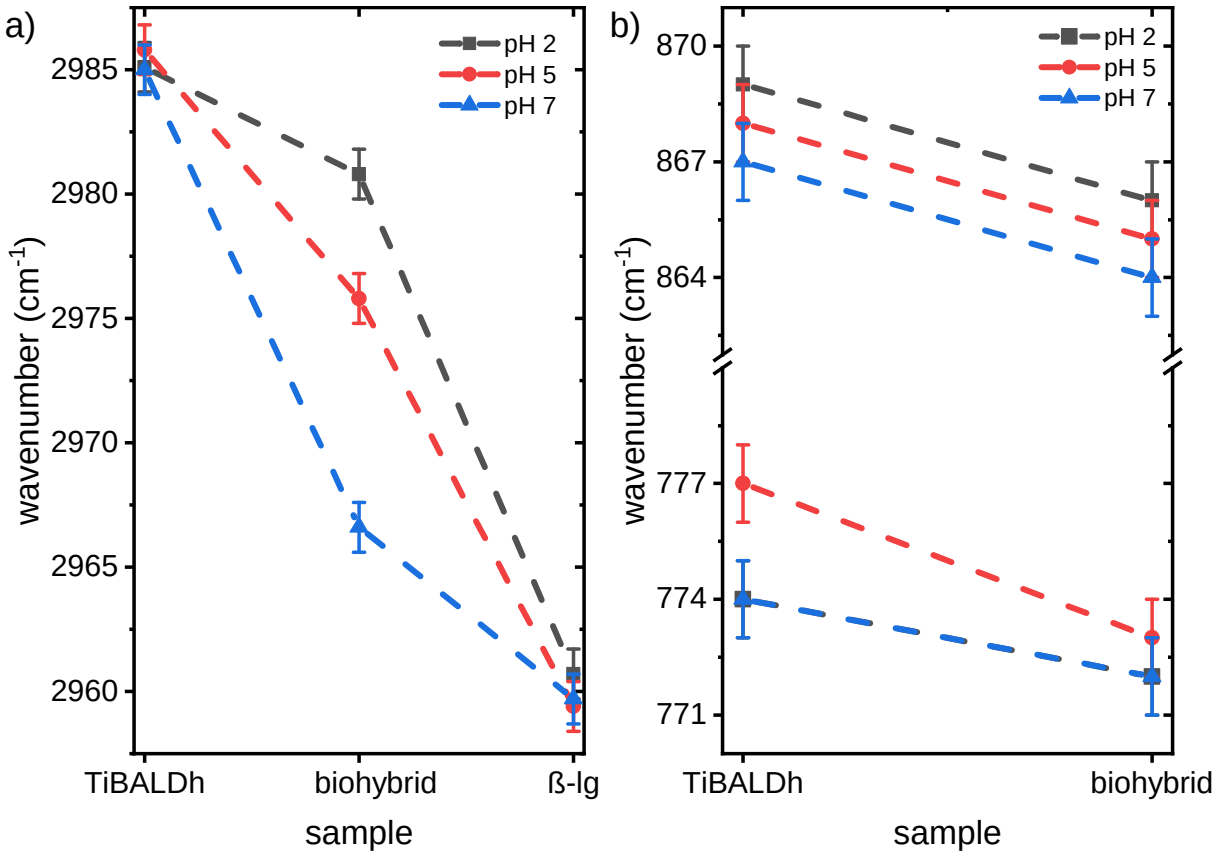

Figure 6.9.: FTIR absorbance peak shifts. a) In contrast to the pure precursor and pure protein samples, there is a pH-dependent shift of the peak center related to the asymmetric stretching vibration of C-H at the methyl groups in the biohybrid sample. b) Ti-(lactate) and Ti-O-Ti vibrations show a constant and lower pH dependency in the biohybrid composite, respectively, than compared to the pure precursor.

related to the isoelectric point of TiBALDh in the vicinity of pH 5. [24] In the biohybrid composite, the Ti-(lactate) vibrations shift to lower wavenumbers, while keeping the same pH dependency. The Ti-O-Ti vibrations remain constant in the biohybrid composite for pH 7 and pH 2, while they shift to the lower wavenumber at 773 cm^{-1} at pH 5, which is close to the values at pH 7 and pH 2, making the Ti-O-Ti vibrations less affected by varying pH in the biohybrid sample than in the pure TiBALDh sample.

6.4. Conclusion

All biohybrid domains show a minimum in their radii at pH 5 compared to pH 2 and pH 7, which hints at the influence of the isoelectric point of β-lg on the overall film morphology. The linearly decreasing domain number obtained from GISANS with an average radius of 250 nm seems to be unaffected by the isoelectric point of β-lg and may be

attributed to the decreasing amount of $Ti(lactate)_3$ domains as the chemical equilibrium shifts towards $Ti_4O_4(lactate)_8$, as shown in Expression 6.1. [23] Remarkably, the trend observed in the biohybrid samples with GISAXS inverses after calcination at 500 °C, with the nanostructured titania films having the largest domain sizes at pH 5. This fact suggests that these domains actually represent the voids of foam-like titania nanostructures, which form upon biopolymer combustion and coarsening of the amorphous phase and anatase nanoparticles into the crystalline and porous anatase phase, especially since the protein agglomerates show the same trend in domain sizes as the nanostructured titania with a maximum at pH 5. This interpretation is further reflected in the highest degree of porosity of 60 % at pH 5 for the calcined, biotemplated titania film.

The strongly deviating FTIR absorbance spectra of TiBALDh at pH 5 may originate from a pronounced formation of carboxylic acids from the ester groups via hydrolysis and may be another influence on the deviating morphology at pH 5 compared to pH 2 and pH 7. The complex TiBALDh absorbance pattern is attributed to a superposition of the lactate ligands, titania nanoparticles, and the $Ti_4O_4(lactate)_8$ complexes in the precursor. Mixing with β-lg affects the involved methyl groups and introduces stronger pH dependency to the asymmetric C-H stretching, whereas Ti-O-Ti vibrations are less affected by pH in the biohybrid state than compared to the pure precursor. The Ti-(lactate) vibrations do not change their relative pH dependency in the biohybrid films, but shift overall to slightly lower wavenumbers, which indicates a changing environment at the biohybrid interfaces.

In conclusion, the influence of pH on the morphology of biohybrid foam-like films and titania foam-like films after calcination is a critical aspect that determines the final nanostructure and porosity. While all biotemplated titania films consist of crystalline titania in the anatase phase, the titania films synthesized at pH 5 show the largest domain radii with the broadest distributions (18 nm, 35 %; 31 nm, 40 %; 163 nm, 45 %) and the highest degree of porosity (60 %), the films synthesized at pH 2 have the smallest domains with intermediate broadening of the size distributions (11 nm, 35 %; 22 nm, 36 %; 121 nm, 40 %) and an intermediate degree of porosity (46 %), and the titania films synthesized at pH 7 have intermediate domain radii with the narrowest distribution (11 nm, 30 %; 24 nm, 30 %; 130 nm, 30 %) and the lowest porosity (20 %). The results demonstrate, that controlling the supramolecular strucutre of β-lg by pH-adjusted heat denaturation will tailor the porosity and nanostructure of titania films, when applied in water-based sol-gel synthesis.

Chapter 7

Superlattice Deformation in Quantum Dot Films on Flexible Substrates via Uniaxial Strain

This chapter is based on the publication *Superlattice Deformation in Quantum Dot Films on Flexible Substrates via Uniaxial Strain* (J. E. Heger, W. Chen, H. Zhong, T. Xiao, C. Harder, F. A. C. Apfelbeck, A. F. Weinzierl, R. Boldt, L. Schraa, E. Euchler, A. K. Sambale, K. Schneider, M. Schwartzkopf, S. V. Roth, P. Müller-Buschbaum, *Nanoscale Horizons*, **8**, 383-395 (2023)) [18]. Reproduced from [18] with permission from the Royal Society of Chemistry. Results of this chapter were obtained in close collaboration with K. Schneider, A. K. Sambale, E. Euchler (Leibniz-Institut für Polymerforschung Dresden e.V., Institut für Polymerwerkstoffe, Hohe Straße 6, 01069 Dresden, Germany) [72]

The superlattice in a quantum dot (QD) film on a flexible substrate deformed by uniaxial strain shows a phase transition in unit cell symmetry. With increasing uniaxial strain, the QD superlattice unit cell changes from tetragonal to cubic to tetragonal phase as measured with *in-situ* grazing-incidence small-angle X-ray scattering (GISAXS). The respective changes in the optoelectronic coupling are probed with photoluminescence (PL) measurements. The PL emission intensity follows the phase transition due to the resulting changing inter-dot distances. The changes in PL intensity accompany a redshift in the emission spectrum, which agrees with the Förster resonance energy transfer (FRET) theory. The results are essential for a fundamental understanding of the impact of strain on the performance of flexible devices based on QD films, such as wearable electronics and next-generation solar cells on flexible substrates.

7.1. Preface

Modern technology builds on advanced materials that fulfill three properties: smart, suitable, and sustainable. Advanced materials are smart when they respond to some external triggers of various origins. The stimuli-and-response cycle is fundamental for sensors, robotics, coatings, and electronics. Moreover, they display a certain degree of autonomy, for instance, the feasibility of self-assembling and self-powering. Advanced materials are suitable when they match the expected operating conditions and optimize performance. The race for outperforming next-generation solar cells demonstrates the urgent demand for suitability. Advanced materials are sustainable when produced from abundant precursors, with low energy costs, and with high stability upon operation to reduce the environmental impact. Ideally, they are easily fabricated on a large scale to benefit economic and ecological interests. The material class of colloidal quantum dots (QDs) features promising properties in this context. [37], [135] They consist of nanocrystals showing strong quantum confinement in all dimensions due to their small sizes of 2–20 nanometers. Hence, they are commonly referred to as artificial atoms, reflecting their high versatility. [136] For instance, when deposited into a thin film, colloidal QDs self-assemble into superlattices with long-range order, similar to atoms in a solid. [42] Accordingly, unit cells periodically build up the QD superlattice (Figure 7.1). From separated to close-packed QDs in superlattices, the wavefunctions of neighboring QDs start to overlap due to the short inter-dot distances, and the energy levels split up. The consequent formation of bands offers new possibilities for charge transport and energy transfer between the QDs. The possibility of either band-like or hopping transport is given, depending on inter-dot distance and the energetic disorder. The disorder is introduced by, e.g., size-polydisperse QDs and influences the energetic landscape by bandtail and midgap states. [39], [137] Non-radiative energy transfer, e.g., via dipole–dipole interactions sensitive to the distance between neighboring QDs becomes more efficient in superlattices. [138], [139] The distance between neighboring QDs dominates the electronic coupling within these QD superlattices and influences the optoelectronic properties. [39], [41], [140] Hence, external stimuli that change the inter-dot distance can cause a response. [141] For instance, QDs embedded in flexible polydimethylsiloxane (PDMS) matrices showed enhanced luminescence when the samples were stretched. [41] This response makes QD superlattices encouraging for smart applications. [135], [142] Moreover, the feasibility of a controlled synthesis features controlled quantum confinement and thereby controlled optoelectronic properties, e.g., a broadly tunable emission or absorbance spectrum. [143] Together with high charge carrier mobilities by state-of-the-art ligand engineering, the aspect of tunability makes QDs suitable, e.g., for next-generation solar cells. [144]–[147] The optimized synthesis of colloidal QDs has a high yield from a reasonable amount of precursor materials. [26], [148]

Surface-attached ligands result in solubility for numerous solvents,increase the environmental stability and give QDs the appearance of semi-soft materials. [149]–[151] Solution processability opens the door to industrial-scale fabrication via printing, spray-deposition, or spin-coating with low energy costs and high compatibility for use in integrated circuits. [42], [152], [153] QDs deposited into thin films dramatically reduce material usage in applications. Recent techno-economic cost analyses have shown that under consideration of synthesis yield optimization, process automatization, and solvent recycling, the fabrication costs of colloidal QD films have the potential to decrease to 3 \$ m^{-2}. These aspects make QD films also a sustainable material. [154], [155] As mentioned before, the electronic and spectral performance of QD films depends on the inter-dot distance and, hence, on the QD superlattice structure. Repeating blocks of unit cells build up the QD superlattice structure and contain information about inter-dot distance and packing density. [156] Superlattices made of QDs with different sizes and size distributions, shapes, and ligand conditions can show different kinds of unit cells. For example, spray-coated large-sized lead sulfide (PbS) QDs form superlattices based on a body-centered cubic (BCC) unit cell (Figure 7.1a). [152] In contrast, printed small-sized PbS QDs show face-centered cubic (FCC) symmetry (Figure 7.1b) in early stages, which eventually form a superposition of cubic unit cells to a nested FCC/BCC structure (Figure 7.1c) due to the ligand condition shift. [42] This nested structure also forms the QD superlattice in films of spin-coated PbS QDs. There are various strategies to tailor the inter-dot distance, e.g., polymer matrix-induced spacing and ligand engineering. [41], [157]–[159] Typically, using different-sized ligand molecules, a controlled spacing between QDs is achieved. [136], [160] Post-treatment techniques, such as ligand exchange or temperature and solvent annealing, are practical tools to change the QD arrangement in a given superlattice configuration after deposition. [161]–[163] Furthermore, *Gong et al.* suggested that external strain changes the inter-dot distance by tearing neighboring QDs apart, explaining changes in the corresponding photoluminescence (PL) emission. [41] The influence of strain on the spatial configuration of QDs becomes essential for applications on flexible substrates, such as wearable electronics and printed photovoltaic foils, since flexibility inherently allows for mechanical deformations of the related devices. However, detailed studies on the correlation between QD superlattice deformation and optoelectronic coupling in QD films upon strain are rarely reported. *Winslow et al.* recently investigated QD superlattices with grazing-incidence small-angle X-ray scattering (GISAXS) and reported a unit cell phase transition from FCC to body-centered tetragonal (BCT) (Figure 7.1d)) upon sample cooling to 100 K. [164] GISAXS is a powerful method to study the superlattice deformation in QD films during strain with X-rays. [43], [146], [152], [165], [166] It is sensitive to the desired length scales and probes a large sample volume with the grazing beam's footprint

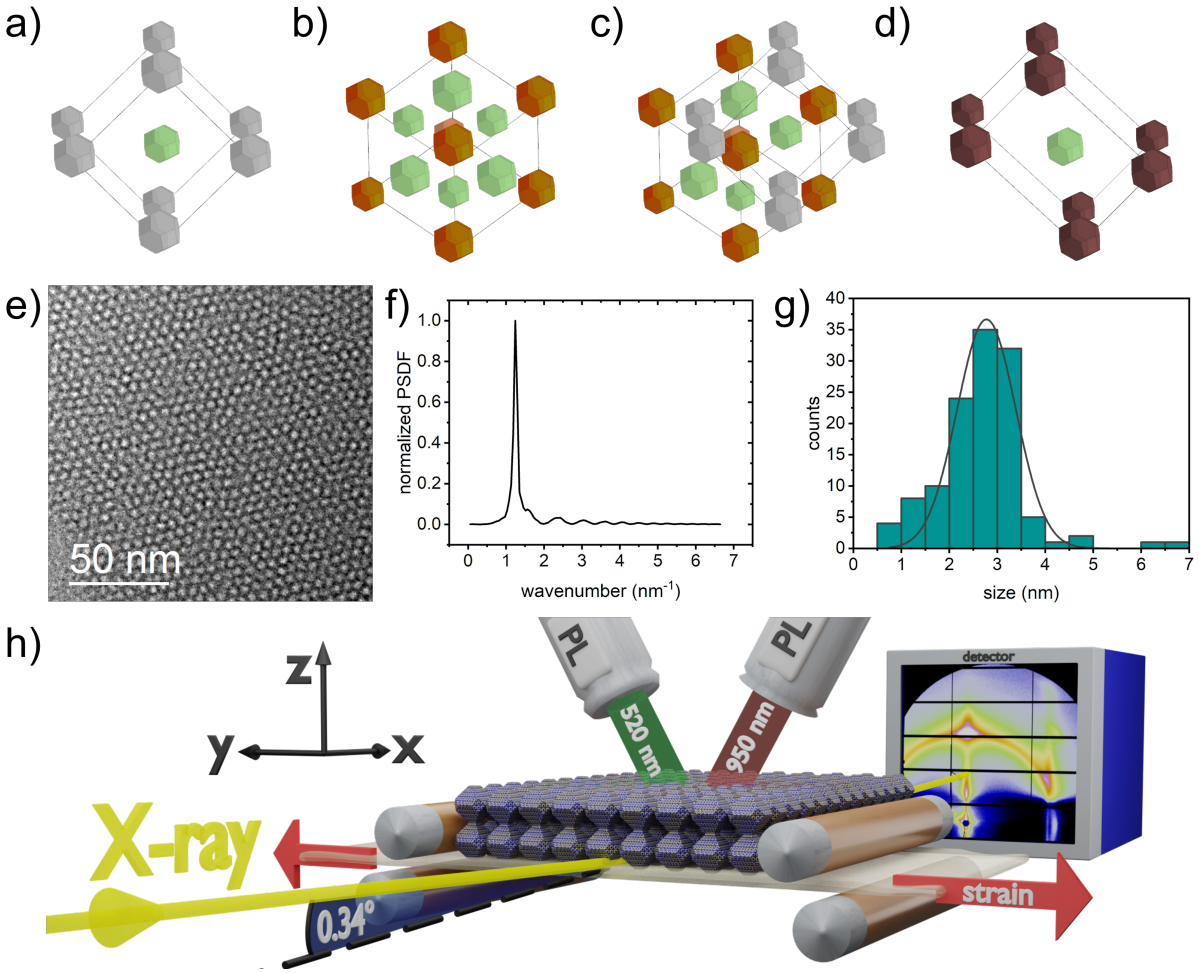

Figure 7.1.: Superlattice configuration in PbS QD films. a) BCC unit cell. b) FCC unit cell. c) Nested FCC/BCC unit cells. d) BCT unit cell. e) HRTEM surface image of the (111) close-packed PbS superlattice plane. f) The high lateral order of the superlattice is reflected in the PSDF obtained from TEM. The pronounced peak is associated with the nearest-neighbor center-to-center distance of 5 nm in the (111) plane. g) The PbS QDs have a size distribution that is obtained from HRTEM with an average size of 2.7 nm and a standard deviation of 21 %. h) Illustration of the experimental setup for *in-situ* GISAXS and *in-situ* PL that are used to determine the QD superlattice deformation and electronic coupling with increasing strain. Reproduced from [18] with permission from the Royal Society of Chemistry.

effect. In contrast, probing thin QD films with conventional small-angle X-ray scattering (SAXS) in transmission geometry typically does not yield a sufficient scattering signal. However, GISAXS requires precise sample alignment with respect to the incoming X-ray beam since it is highly surface sensitive. A bent surface could result in multiple reflection conditions and, hence, ill-defined alignment conditions. This circumstance makes the study on flexible films during uniaxial strain challenging, as the freestanding, flexible

substrate deforms under tension and thus changes the sample alignment. To overcome this challenge, a sample environment based on four cylindrical rolls is introduced. Two rolls act as support from the bottom and two as fixation from the top, acting together to guide the substrate and balance strain-induced substrate bending (Figure 4.11). This approach establishes a controlled sample alignment for successful GISAXS measurements on freestanding, flexible substrates. Given the possibility of performing GISAXS, this chapter aims to complement the understanding of QD superlattice deformation via uniaxial strain and its influence on the respective luminescence. I focus on PbS QD thin films prepared by spin-coating on flexible PDMS substrates, which exhibit a superlattice assembly. Moreover, PbS QDs have also developed into a representative role model for understanding QD superlattices. Figure 7.1e shows the transmission electron microscopy (TEM) image of the close-packed FCC (111) plane formed by the PbS QDs capped with oleic acid (OA) ligands which were used in this chapter. The high degree of spatial order and the mean inter-dot spacing are reflected in the radial power spectral density function (Figure 7.1f). The first order peak at 1.25 nm^{-1} corresponds to a mean inter-dot spacing of about 5 nm. The PbS QDs have a mean size of 2.7 nm, and a size dispersity with a standard deviation of 21 % (Figure 7.1g). Uniaxial strain applied to the sample deforms the QD superlattice. *In-situ* GISAXS probes this QD superlattice deformation, and *in-situ* PL records the optoelectronic coupling as a function of applied strain. Figure 7.1h sketches the experimental setup. Experimental details for sample fabrication and measurements are given in Section 3.1, Section 3.3, and Section 4.5.

7.2. Superlattice Deformation Upon Strain

The 2D GISAXS data in Figure 7.2 obtained from the *in-situ* uniaxial stretching experiment gives an overview of the QD superlattice deformation process with increasing substrate elongation $\Delta l^{sub}/l_0^{sub}$ from 0 % to 30 %, where Δl^{sub} is the difference to initial substrate length l_0^{sub}. The 2D data shows the direct beam blocked by a beam stop and typical GISAXS features, such as the sample horizon that separates reflected from transmitted signals and the material characteristic Yoneda peak. The GISAXS features are displayed in the vertical line cut along $q_y = 0$ nm^{-1} (Figure 7.3). Moreover, there is a change in the vertical density profile in these line cuts, first towards higher and then lower density. The scattering pattern for the relaxed sample at 0 % substrate elongation in Figure 7.2a shows prominent Bragg reflexes arranged in a bow-like intensity distribution characteristic for PbS QDs. Additional reflexes are arranged vertically along $q_y = 1.3$ nm^{-1}. I identify the unit cell by matching the indices of the respective Bragg reflexes via the routine explained in the Appendix A. It turns out that the superlattice

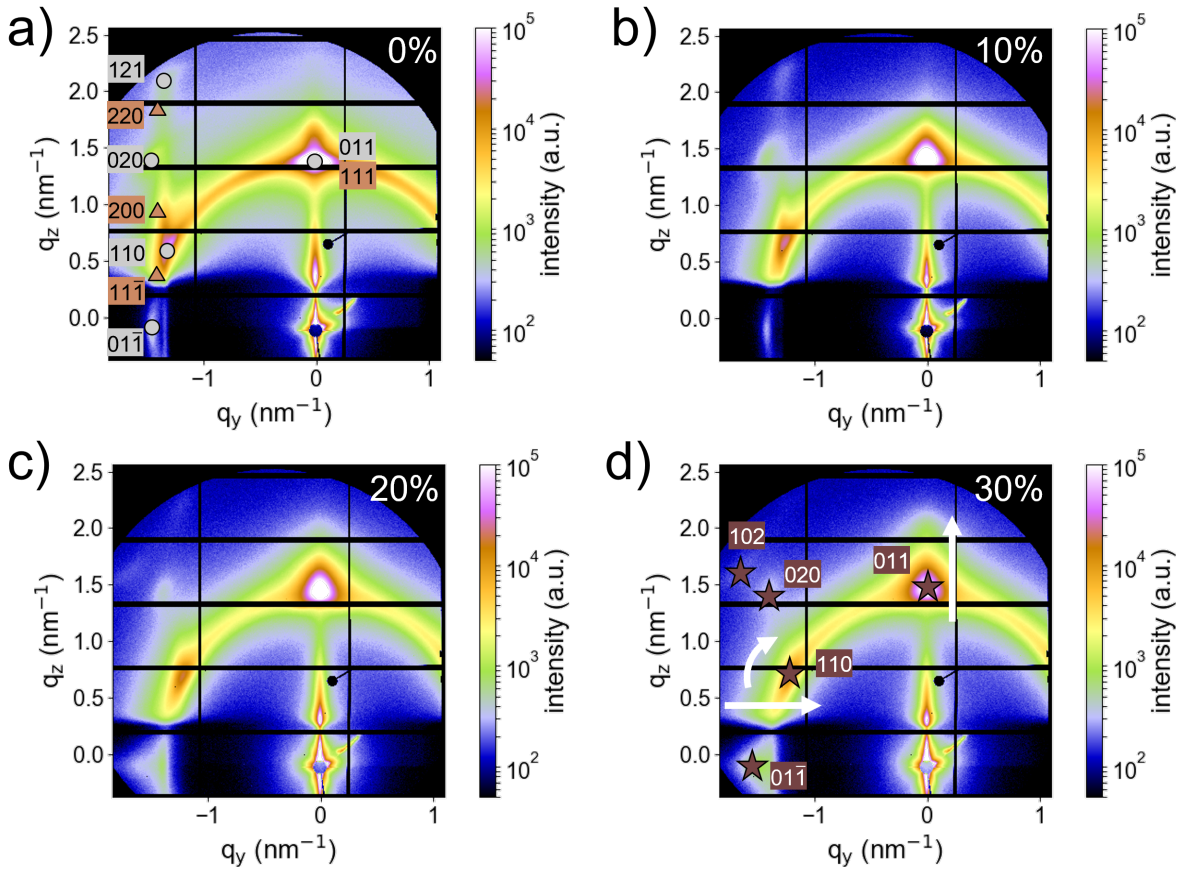

Figure 7.2.: *In-situ* 2D GISAXS data with increasing uniaxial substrate elongation. a) The relaxed state at 0 % indicates a nested FCC/BCT superlattice. Orange and grey boxes label FCC and BCT reflexes, respectively. b) At 10 %, the FCC reflexes vanish. c) With increasing substrate elongation to 20 %, the BCT (121) reflex vanishes, and the BCT (102) reflex appears. d) With increasing the substrate elongation from 0 % to the applied maximum of 30 %, the (110) reflex shifts towards lower q-values and the (011) reflex towards higher q-values, revealing an anisotropic unit cell deformation. Reproduced from [18] with permission from the Royal Society of Chemistry.

consists of FCC and BCT unit cells, forming a nested FCC/BCT structure. The (011), (01$\bar{1}$), (110), (020), and (121) superlattice planes correspond to the BCT part and are labeled with grey boxes in Figure 7.2a. The (011) reflex is aligned vertically to the direct beam position at $q_y = 0$ nm^{-1} . Hence, the BCT unit cell is in edge-on orientation with respect to the substrate plane. The (111), (11$\bar{1}$), (200), and (220) reflexes correspond to the FCC unit cell and are labeled with orange boxes in Figure 7.2a. Since the FCC's (111) reflex is located at $q_y = 0$ nm^{-1}, the FCC unit cell is present in the corner-on orientation. At 10 % substrate elongation (Figure 7.2b), the GISAXS data deviates from the relaxed state, and the (11$\bar{1}$), (200), and (220) reflexes related to the FCC phase diminish. At 20 %

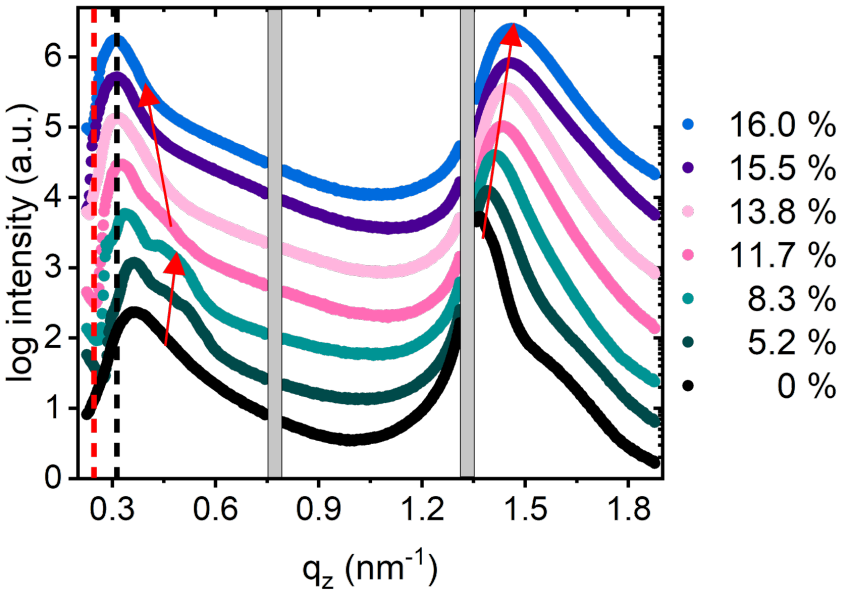

Figure 7.3.: Vertical GISAXS intensity with increasing effective strain. Vertical line cuts at $q_y = 0$ nm^{-1} are shown for the respective strain. The grey boxes mask the detector gaps. The red dashed line indicates the sample horizon. The Yoneda intensity at $q_z = 0.37$ nm^{-1} measures the sample's electron density. With increasing effective strain from 0 % to 8.3 %, an additional intensity at higher q_z values of about 0.45 nm^{-1} appears, as shown with a red arrow. This trend further confirms the increasing unit cell density along with the phase transition. The Yoneda intensities shifts towards lower q_z values from 11.7 % to 15.5 % of applied effective strain and remains constant at the black dashed line at 0.31 nm^{-1} afterward. The decreasing electron density after the phase transition reflects the increasing formation of voids with the beginning of crack propagation. The peak at $q_z = 1.4$ nm^{-1} shifting towards higher q_z corresponds to the (111) and (011) superlattice planes of the FCC and BCT unit cells, respectively. Reproduced from [18] with permission from the Royal Society of Chemistry.

substrate elongation (Figure 7.2c), the (121) reflex related to the BCT phase diminishes, and the BCT (102) reflex appears (labeled in Figure 7.2d). With increasing substrate elongation from 0 % to 30 %, the BCT (110) reflex shifts towards lower q-values and the BCT (011) reflex towards higher q-values. These shifts indicate an anisotropic deformation and, hence, suggest a change in unit cell symmetry. The shifted reflex positions and the additionally appearing reflex match the following superlattice indices of the BCT unit cell symmetry (Figure 7.2d): (011), (01$\bar{1}$), (110), (020), and (102). Interestingly, this QD superlattice deformation again relaxes when reducing the substrate elongation to 20 % and 10 %, respectively (Figure 7.4). In conclusion, the 2D GISAXS data identifies a complex unit cell evolution from nested FCC/BCT at 0 % to BCT with increasing deformation.

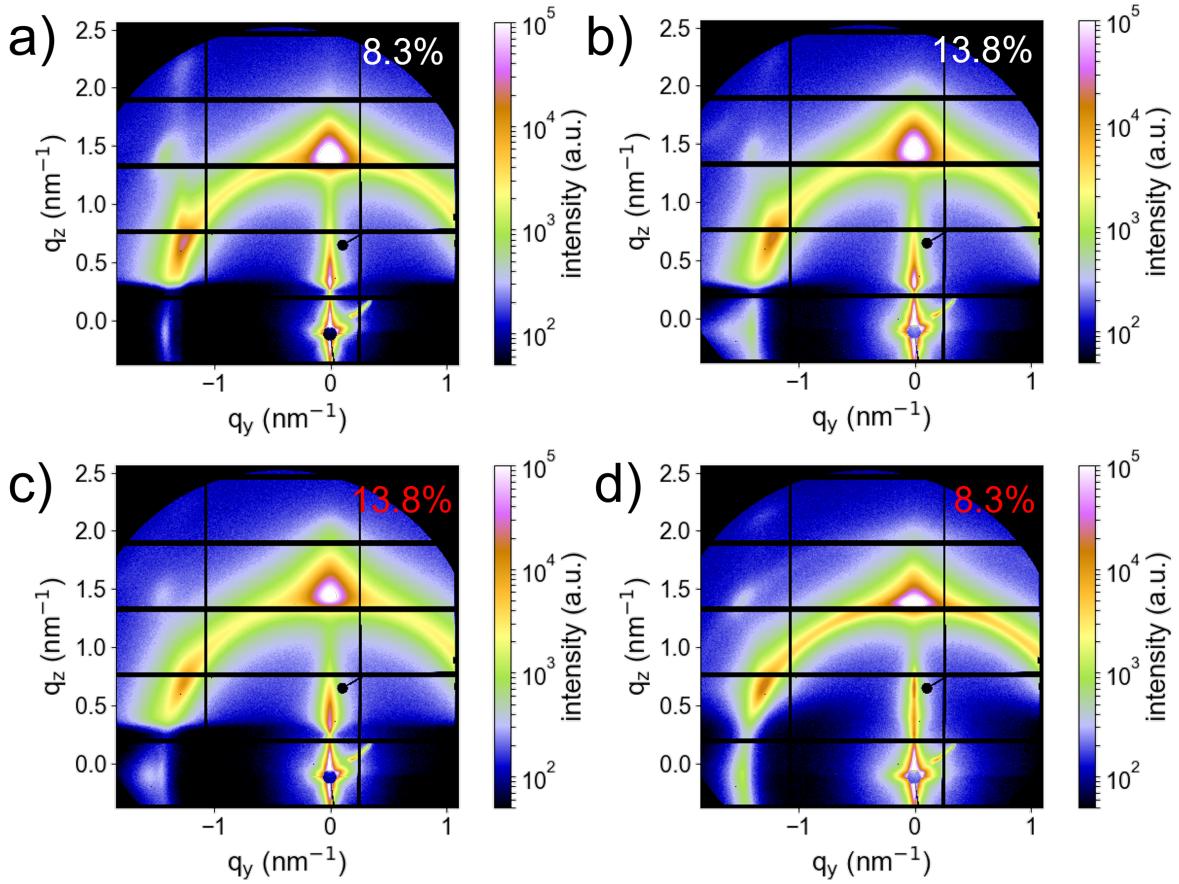

Figure 7.4.: Relaxed superlattice deformation. The superlattice deformation passing the FCC/BCT-BCC-BCT phase transition from a) 10 % of substrate elongation with the effective strain of 8.3 % to b) 20 % (the effective strain of 13.8 %), discussed in the main text, shows a relaxation of superlattice deformation in the 2D GISAXS data when releasing the substrate elongation from c) 20 % back to d) 10 %. Reproduced from [18] with permission from the Royal Society of Chemistry.

7.3. Unit Cell Evolution Upon Strain

The prominent (011) and (110) superlattice reflexes contain information about the BCT unit cell evolution upon strain, and the (111) and (200) superlattice reflexes about the FCC unit cell evolution. For analysis, the respective peaks are azimuthally integrated to one-dimensional intensity curves that are fitted with Gaussian functions (Figure 7.5a and 7.5b). From the respective center q-values, one extracts the superlattice constants a, b, and c that represent the lengths of the unit cell edges. For the tetragonal symmetry, the unit cell consists of a squared base area of side length a and a height c, with $a = b \neq c$, and for the cubic symmetry, with $a = b = c$. Hence, the aspect ratio c/a helps to understand the unit cell evolution.

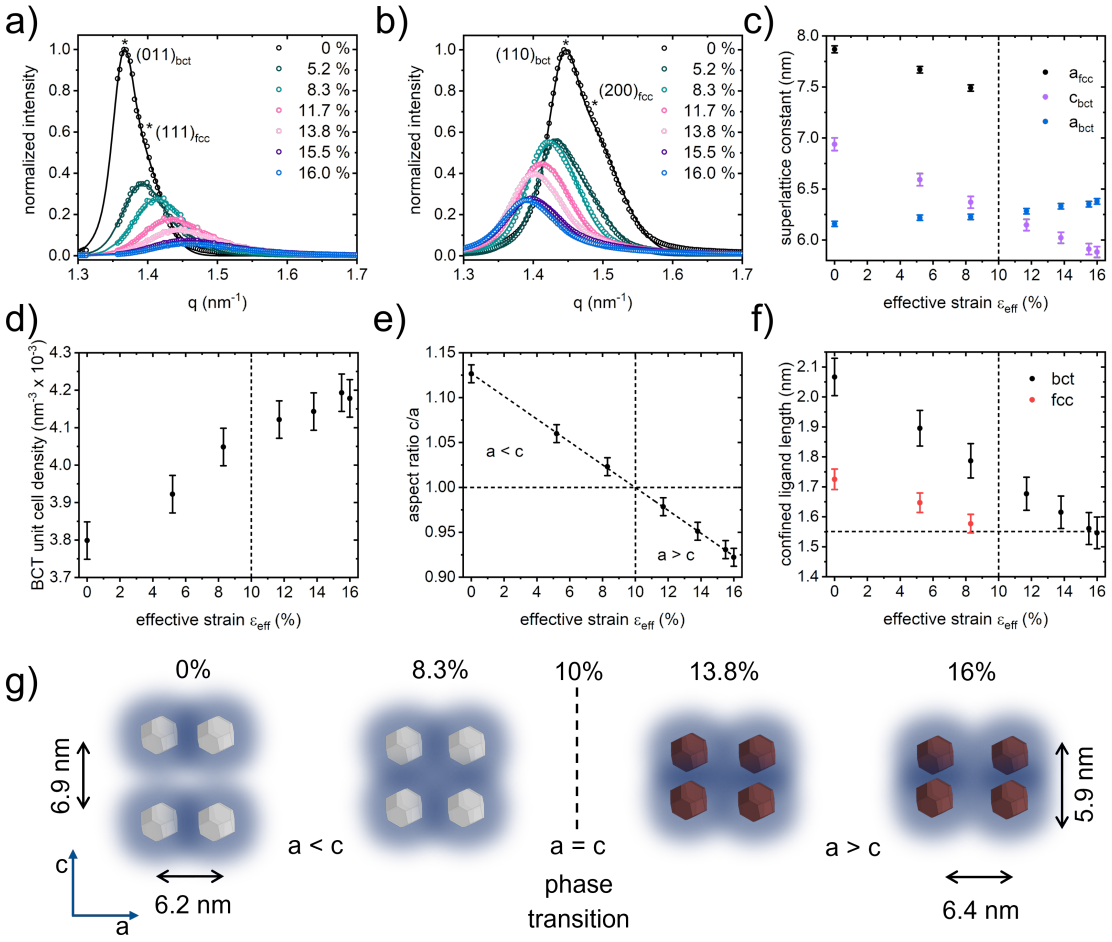

Figure 7.5.: *In-situ* unit cell evolution from the 2D GISAXS data. a) Azimuthal integrated intensity of the (011) bct and (111) fcc peaks marked with asterisks show a shift to higher q-values with increasing effective strain, indicating superlattice shrinkage. b) Azimuthal integrated intensity of the (110) bct and (200) fcc peaks marked with asterisks show a shift to lower q-values with increasing effective strain, indicating superlattice expansion. c) Evolution of superlattice constants a_{fcc}, a_{bct}, and c_{bct}. The BCT phase continuously expands and shrinks along a_{bct} and c_{bct}, respectively. The FCC phase vanishes at the unit cell phase transition when $a_{bct} = c_{bct}$. d) The BCT unit cell density increases towards the phase transition and remains constant afterwards. e) Linear dependence of the BCT unit cell's aspect ratio over the whole effective strain. At 10 %, the aspect ratio crosses the cubic phase line. Deviation of the aspect ratio from the cubic phase measure the degree of the unit cell's isotropy. f) The confined ligand length reaches the critical value of 1.55 nm at 10 %, which triggers the unit cell transition to the cubic phase. Further increase of strain also causes the BCT phase to reach the critical confinement value that eventually triggers microscopic crack propagation. g) The schematic illustrates the evolution of BCT inter-dot distance and the resulting changes in the optoelectronic coupling of adjacent QDs during phase transition from $a < c$ to $a > c$. The body-centered QDs are omitted for clarity of the visualization. Reproduced from [18] with permission from the Royal Society of Chemistry.

It is essential to highlight that the applied strain via uniaxial substrate elongation does not distribute uniformly but mainly along three different length scales of deformation on the PbS QD film: (1) 3D superlattice deformation by changing the superlattice constants $a = b$ and c on the nanoscale. (2) Grain boundary formation on the mesoscale of several tens to hundreds of nanometers. (3) Crack formation on the microscale. This chapter focuses on the superlattice deformation on the nanoscale, which is obtained directly from GISAXS analysis. To account for the inhomogeneous distribution of applied strain, I introduce an effective strain ε_{eff} with the equivalent strain magnitude: [167], [168]

$$\varepsilon_{eff} = \sqrt{\varepsilon_x^2 + \varepsilon_y^2 + \varepsilon_z^2} \tag{7.1}$$

Here, $\varepsilon_{x,y,z}$ are the principal strains $\Delta a/a_0$ and $\Delta c/c_0$ along the superlattice and the diagonal elements of the strain tensor $\hat{\boldsymbol{\varepsilon}}$:

$$\hat{\boldsymbol{\varepsilon}} = \begin{pmatrix} \Delta a/a_0 & 0 & 0 \\ 0 & \Delta a/a_0 & 0 \\ 0 & 0 & \Delta c/c_0 \end{pmatrix} \tag{7.2}$$

To qualitatively estimate the effect of grain boundary and crack formation on the distribution of the applied strain, we compare the effective strain ε_{eff}^{SL} for the superlattice and ε_{eff}^{Sub} for the substrate as a function of uniaxial substrate elongation (Figure 7.6a). Whereas the effective strain on the substrate per definition linearly follows the uniaxial elongation, the effective strain on the superlattice deviates after 10 % of substrate elongation from ε_{eff}^{Sub} with increasing magnitude until it approaches a value of $\varepsilon_{eff}^{SL} = 16$ % at $\varepsilon_{eff}^{Sub} = 30$ %. Scherrer analysis of the superlattice planes' peak broadening yields an estimation for the evolution of the average grain size (Figure 7.6b). [169] The grain size shrinks from about 165 nm to about 75 nm with increasing effective strain to 10 %. After that, the grain size decreases slightly and approaches about 62 nm at 16 % effective strain. The disintegration of larger grains to smaller grains upon strain is accompanied by the formation of grain boundaries. Since this effect is strongly suppressed after 10 %, it is suggested that the evolution of granular interfaces plays a minor role in the observed strain distribution compared to superlattice deformation and crack propagation. The increasing deviation of effective strain can be attributed to the beginning crack formation. After 30 % of substrate elongation, i.e., 16 % of effective strain on the superlattice, the applied strain fully disseminates on the cracks. Optical microscopy reveals the cracks, which are orthogonal to the direction of uniaxial strain, with a width of about 1 mm and with a distance of about 5–10 µm in the relaxed PbS QD film after the stretching experiment (Figure 7.6c). The superlattice constants a_{fcc}, a_{bct}, c_{bct} of the respective unit cells are shown against the effective strain in Figure 7.5c. The FCC unit cell shrinks along a_{fcc} from (7.87 ± 0.03) nm to (7.49 ± 0.03) nm and the FCC phase vanishes after 8.3 % of

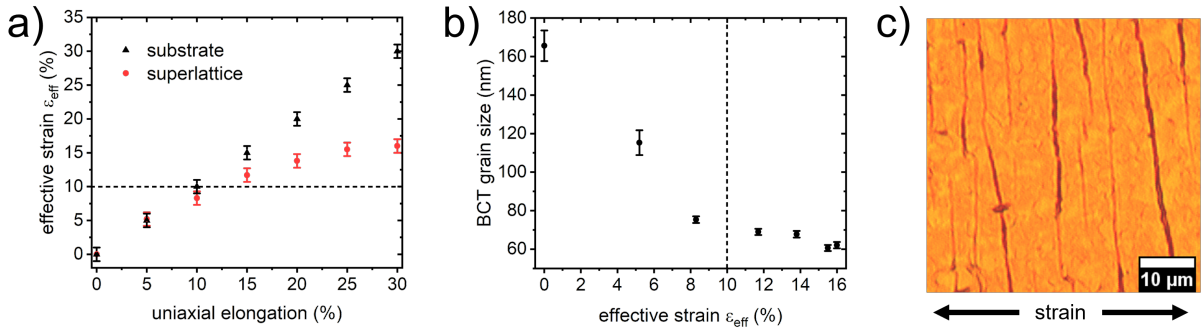

Figure 7.6.: Effective strain applied to the superlattice. a) Comparison of the effective strain applied to the superlattice and to the substrate show increasing deviation starting from 10 % of substrate elongation. The applied strain increasingly distributes on crack formation on which it is fully focused at 30 %. The maximum effective strain applied to the superlattice is 16 %. b) Besides the average superlattice domains, which are formed by the QDs around the average size of 2.7 nm, domains of larger PbS QDs pass the phase transition locally already at lower applied strain. This effect leads to peak broadening of the lattice reflexes in GISAXS and contributes to the early formation of grain boundaries towards 10 %. Average grain size obtained from Scherrer analysis. With the reduction in grain size to 10 %, grain boundaries are formed. Since only a few grain boundaries are formed after 10 %, they play a minor role in strain distribution at higher strains. c) Optical microscopy image of the PbS QD film after stretching reveals elongated cracks that are orthogonal to the direction of applied strain in a distance of 5 to 10 µm. Reproduced from [18] with permission from the Royal Society of Chemistry.

effective strain. The BCT unit cell deforms via shrinking c_{bct} from (6.94 ± 0.06) nm to (5.98 ± 0.05) nm and slightly extending a_{bct} from (6.16 ± 0.03) nm to (6.38 ± 0.03) nm (Figure 7.5c). At 10 % of effective strain the lattice constants $a_{bct} = c_{bct}$ match, indicating a cubic phase transition. The changing superlattice dimensions result in an increasing BCT unit cell density, which is given by the inverse product $a^{-2}c^{-1}$ of base area and height, respectively (Figure 7.5d). The density increases from $(3.80 \pm 0.05) \times 10^{-3}$ nm^{-3} to $(4.12 \pm 0.05) \times 10^{-3}$ nm^{-3}, which remains constant within the error bars after the phase transition. The aspect ratio provides an understanding of the BCT unit cell's symmetry evolution as a function of the effective strain (Figure 7.5e)). A horizontally dashed line at the aspect ratio of 1.00 represents the cubic phase line. With increasing effective strain from 0 % to 16 %, the aspect ratio reduces linearly from 1.13 to 0.91, passing the cubic phase line at 10 % of effective strain. The evolution of the aspect ratio reveals an FCC/BCT–BCC–BCT phase transition with $a < c$ from 0 % to 10 % and $a > c$ after 10 % to 16 %. A vertically dashed line indicates the phase transition at $a = c$ at 10 % of effective strain, separating the FCC/BCT and BCT phases. Notably, the aspect ratio changes linearly along the effective strain range, demonstrating continuous superlattice

deformation until 16 %. To further understand the phase transition and the vanishing FCC phase in the nested FCC/BCT structure with the phase transition, it is helpful to consider the spacing between the nearest PbS QD neighbors in the superlattice. The nearest-neighbor spacing $nn = D_{QD} - d_{nn}$ is given by the average QD size D_{QD} and the average nearest-neighbor center-to-center distance d_{nn}. It describes the available free space between the closest QDs, which measures the degree of intercalation and compression of the OA ligands. [170] Figure 7.7 shows the nearest-neighbor spacing of the FCC and BCT phase against effective strain for mean QD size $D_{QD} = 2.7$ nm. At 0 %, the

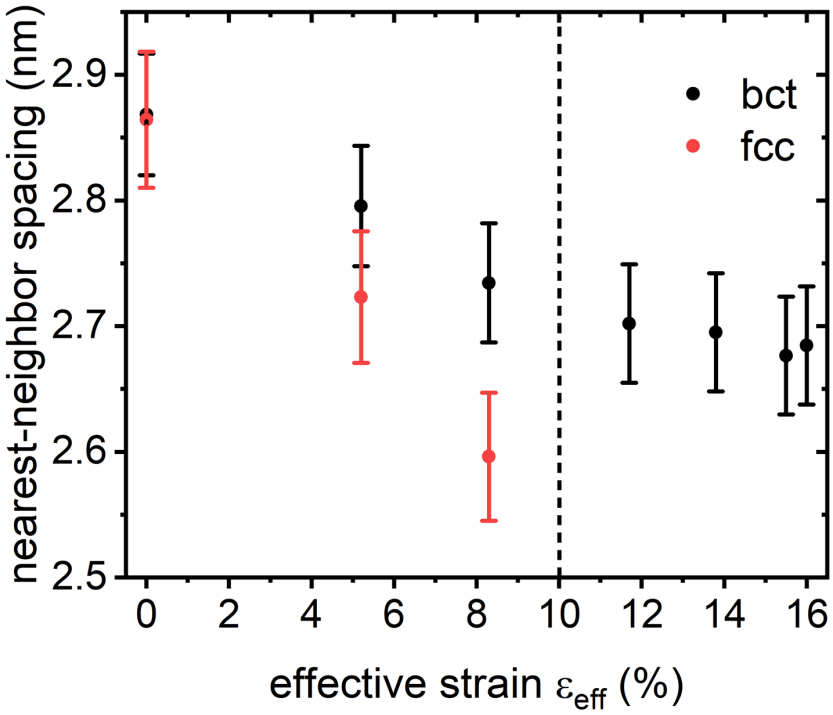

Figure 7.7.: Nearest-neighbor spacing with increasing effective strain. The edge-to-edge distance of nearest-neighbor QDs is the same for BCT and FCC in the nested unit cell configuration at 0 %. With increasing superlattice deformation, BCT and FCC nearest neighbors separate. Both spacings indicate a high degree of intercalation and compression of the ligands having a relaxed chain length of 2.5 nm. The compression level finally reaches a critical value for the FCC phase, which triggers the phase transition at 10 %. Reproduced from [18] with permission from the Royal Society of Chemistry.

two spacings of both phases $nn_{fcc} = nn_{bct} = (2.86 \pm 0.05)$ nm match because of the nested FCC/BCT structure. With increasing strain, the BCT nearest-neighbor spacing decreases to (2.68 ± 0.05) nm and remains constant within the error bars after the phase transition at 10 %. The FCC nearest-neighbor spacing, however, shows a stronger decrease to (2.60 ± 0.05) nm at 8.3 %. The reduced nearest-neighbor spacing is close to half

of the spacing of about 5 nm that two ligands would induce with relaxed chain lengths of $l_0^{lig} = 2.5$ nm. This result indicates a high degree of ligand intercalation close to the maximum, high ligand compression along the nearest- neighbor distances, and dominating repulsive interactions between the neighboring QDs. [170], [171] To quantify the ligand compression, the interface between adjacent ligand-capped QDs needs to be considered. This interface is given by the wall of the unit cell's Wigner–Seitz cell and confines the ligand length. The confined ligand length in the superlattice l_{SL}^{lig} varies from the relaxed ligand length l_0^{lig} and is given by the difference: [172]

$$l_{SL}^{lig} \;=\; R_{WS} \;-\; \frac{D_{QD}}{2} \tag{7.3}$$

of the two Wigner–Seitz cell radii $R_{WS}^{fcc} = a_{fcc}(3/16\pi)^{1/3}$ and $R_{WS}^{bct} = c_{bct}\ (3/8\pi)^{1/3}$ that limit the ligand length along the condensing superlattice constants a_{fcc} and c_{bct} for the respective unit cells. Figure 7.5f shows the evolution of l_{SL}^{lig} as a function of the effective strain. The confined ligand length reduces from (1.73 ± 0.03) nm to (1.58 ± 0.03) nm at 8.3 % for the FCC phase and from (2.07 ± 0.06) nm to (1.55 ± 0.05) nm at 16 % for the BCT phase. It is remarkable that $l_{SL}^{lig} = 1.55$ nm has the same value at the FCC/BCT–BCC–BCT phase transition at 10 % and at the transition to dominating crack propagation at 16 %. Hence, $l_{SL}^{lig} = 1.55$ nm can be seen as a critical ligand compression length promoting phase transition. The BCT unit cell deformation is depicted in Figure 7.5g. For clarity, the QD on the body-centered position is not shown. Blue clouds illustrate the electronic coupling between adjacent QDs, which changes strength and isotropy with increasing unit cell density and increasing isotropy towards the BCC phase. After the phase transition, the unit cell isotropy and the inter-dot spacing along c_{bct} decrease, while the inter-dot distance slightly increases along a_{bct}. I consider the consequences of the changing inter-dot distances and the critical confined ligand length $l_{SL}^{lig} = 1.55$ nm for the superlattice phase transition and the resulting unit cell isotropy for the optoelectronic coupling in the following sections.

7.4. Photoluminescence Upon Strain

To understand the influence of the superlattice deformation on the optoelectronic coupling upon phase transition, additional *in-situ* PL measurements are performed while increasing the effective substrate strain ε_{eff}^{Sub} from 2.5 % to 30 %. The overall PL spectrum shows an inhomogeneous broadening, which redshifts with increasing strain (Figure 7.8a). Such inhomogeneous broadening is known for polydisperse QD solids with a single mean size and becomes more pronounced with a larger QD size distribution, such as the QDs investigated in this chapter. [138] A reason for the inhomogeneous broadening in

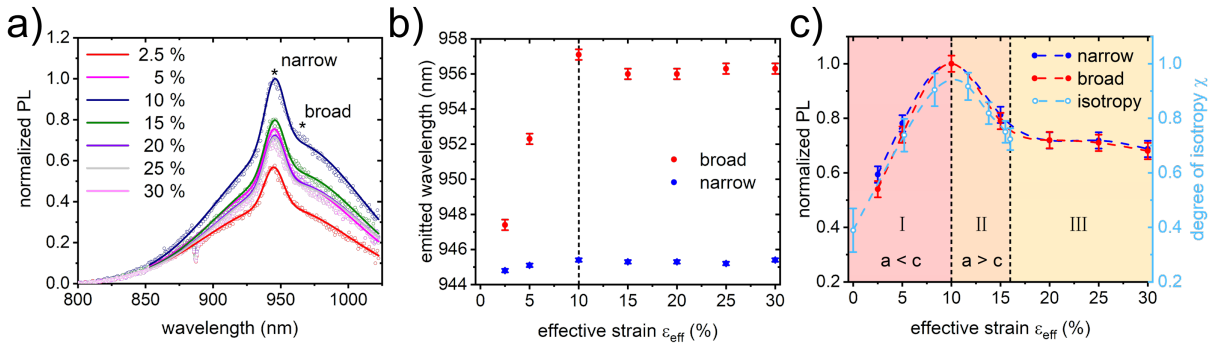

Figure 7.8.: *In-situ* PL evolution with increasing effective strain. a) The normalized PL intensity reaches a maximum in the cubic phase at 10 % and decreases afterwards. The overall profiles appear more asymmetric with higher strains. Solid lines are fits to the inhomogenously broadened spectrum based on two Gaussian functions with narrow and broad distribution, respectively. The two peak positions are marked with asterisks. b) The broad peak shows a more pronounced redshift compared to the narrow peak with changing inter-dot distances towards the phase transition, which is characteristic for FRET. c) The normalized PL intensities pass three stages with the increasing strain defined by the critical value of confined ligand length. From stage I to stage II, both PL intensities follow the varying unit cell isotropy with the maximum in the isotropic cubic phase at 10 %. Stage III shows constant PL intensities due to full strain distribution on microscopic cracks that leaves the superlattice in the state of constant deformation reached at the maximum effective strain applied to the superlattice of 16 %. Reproduced from [18] with permission from the Royal Society of Chemistry.

polydisperse assemblies is a resonant energy transfer from smaller QDs to neighboring larger QDs via dipole–dipole interactions. After radiative relaxation, the larger QDs having a smaller bandgap emit a redshifted photon compared to the donor emission from the smaller QDs. As a result, the acceptor emission intensity is enhanced. [173] The energy transfer between neighboring smaller QDs as donors and larger QDs as acceptors via dipole–dipole interactions and the characteristic redshift is described in the theory of FRET. [138], [174] The FRET efficiency is proportional to d^{-6} , where d is the inter-dot distance. Due to the power of 6 exponent, FRET efficiency is very sensitive to changing distances. [175] The influence of FRET on the PL spectrum is often observed in polydisperse QD assemblies upon varying distances, e.g., from solution to deposited film. [176], [177] Spatial sensitivity and enhanced acceptor emission intensity make FRET also essential in fluorescence-based microscopy broadly used in life sciences. [178], [179] The appearance of the PL spectra in Figure 7.8a as a function of strain strongly suggests the interpretation of the changing emission in the framework of FRET theory. Inspired by the pioneering work of *Kagan et al.*, I describe the inhomogeneously broadened PL profile as the sum of a narrow and a broad emission band. [138] By fitting the PL profiles with

two Gaussian functions, the PL intensities, the center values for the emitted wavelength, and the line broadening of the full width at half maximum (FWHM) are extracted. The normalized intensity substantially boosts to about 185 % of the initial magnitude at 2.5 % when increasing the strain towards 10 %. After the phase transition, the intensity decreases at 30 % strain to about 125 % of the initial magnitude. This PL intensity behavior is in good agreement with the findings of *Gong et al.* for perovskite QDs in bulk PDMS matrices. [41] Besides the changing intensity, the broad peak experiences a continuing redshift from (947.4 ± 0.3) nm to (957.1 ± 0.3) nm towards the phase transition. After the phase transition, the peak slightly blueshifts to (956.0 ± 0.3) nm and remains constant within the error bars (Figure 7.8b). The narrow peak only slightly redshifts from (944.8 ± 0.1) nm to (945.4 ± 0.1) nm. In addition to the redshift, the broad peak first slightly narrows in the FWHM from (124.1 ± 0.7) nm to (122.1 ± 0.7) nm and then broadens slightly to (125.6 ± 0.7) nm with respect to the phase transition (Figure 7.9). In contrast, the FWHM of the narrow peak remains constant at (16.9 ± 0.4) nm across the phase transition.

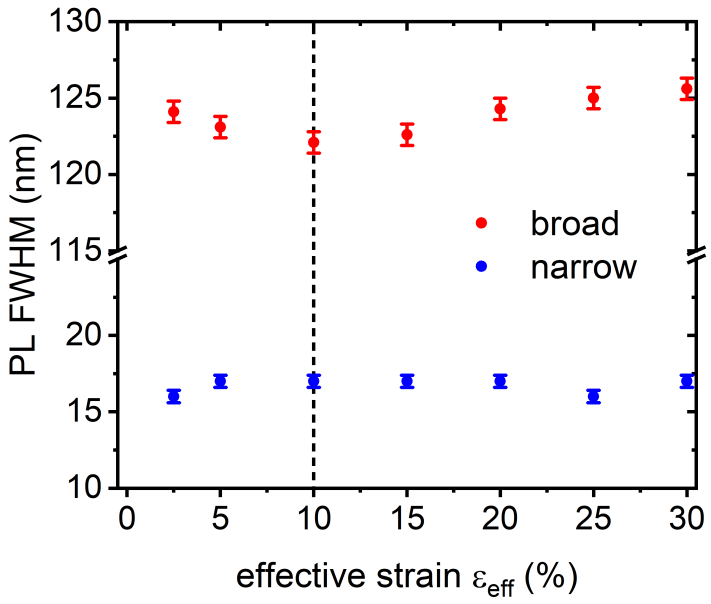

Figure 7.9.: *In-situ* PL emission broadening with effective strain. A slight decrease of PL FWHM is found for the acceptor until 10 %, followed by an increase afterwards, whereas it remains constant for the donor. With increased unit cell isotropy, donor-acceptor couples can form more uniformly with respect to their size difference. With increasing crack propagation, more donor-acceptor couples at crack interfaces rearrange, leading to an increased broadening of the acceptor emission. Reproduced from [18] with permission from the Royal Society of Chemistry.

7.5. Isotropy-Dependent FRET Efficiency

The results show that the PbS QD superlattice deforms upon sample elongation and eventually passes an FCC/BCT–BCC–BCT phase transition (Figure 7.5e). At the same time, the PL intensity and emission spectrum change with respect to the phase transition (Figure 7.8a and 7.8b; Figure 7.9). I suggest that the PL behavior observed in this chapter results from changing dipole–dipole interactions of adjacent QDs in the framework of FRET. In this context, the increasing BCT unit cell density shown in Figure 7.5d favors FRET as inter-dot distances become shorter. However, the BCT unit cell density does not increase isotropic, which affects the arrangement of adjacent QDs and needs to be considered for the dipole–dipole coupling. To quantitatively estimate the degree of isotropy upon superlattice deformation, I first introduce the anisotropy parameter $\tilde{\chi}$ as the following:

$$\tilde{\chi} \;=\; \left| 1 \;-\; \left(\frac{c}{a}\right)^4 \right| \tag{7.4}$$

Expression 7.4 reflects the unit cell anisotropy for a given aspect ratio c/a to the power of 4, considering the 4-fold rotational symmetry of the tetragonal unit cell. The degree of anisotropy becomes minimal with $\tilde{\chi} = 0$ as the aspect ratio becomes 1 in the cubic phase of maximal isotropy. The degree of isotropy χ is then given by:

$$\chi \;=\; 1 \;-\; \tilde{\chi} \tag{7.5}$$

By comparing the degree of isotropy χ with the normalized PL emission intensities of the narrow peak and the broad peak as a function of the corresponding effective strains ε_{eff}^{SL} and ε_{eff}^{Sub}, respectively, I identify three distinct stages of optoelectronic coupling with increasing uniaxial substrate elongation (Figure 7.8c)): (I) Increasing isotropy towards the cubic phase with $a < c$ that is followed by increasing PL intensity with the maximum in the isotropic cubic phase $a \;=\; c$. (II) Decreasing isotropy with $a > c$ towards the maximum $\varepsilon_{eff}^{SL} = 16$ % that is followed by decreasing PL intensity. (III) Constant PL intensity from 16 % to 30 % of substrate elongation. Besides the changes in unit cell symmetry discussed in this work, reorientations of QDs on individual superlattice sites are possible contributions to the varying optoelectronic coupling. Especially in BCC configuration, an improved facet–facet alignment of {111} and {100} QD facets, respectively, compared to the FCC is commonly observed. [156], [169], [180]–[183] I propose further investigations of QD orientation on the superlattice sites as a function of applied uniaxial strain for future studies. Alternatively, the degree of disorder in the QD film introduced by the size polydispersity and the increasing grain boundaries with strain are possible explanations for the observed redshift and the inhomogeneous broadening. [137] While disorder certainly contributes, there is a strong evidence for FRET in the perfect match of PL intensity and

unit cell isotropy based on inter-dot distances together with the characteristic redshift and FWHM narrowing of the inhomogeneously broadened peak. A more quantitative verification and analysis of strain-induced PL changes in the framework of FRET could be achieved by time-resolved photoluminescence, which is not the focus of this thesis. [176]

Stage I: Increasing PL Emission From 0 % to 10 %

In the first stage, FRET benefits from the resulting higher density of adjacent QDs and higher isotropy for dipole–dipole interactions so that it becomes more efficient and mitigates emission losses that otherwise would occur via non-radiative recombinations. [139], [184] This is reflected in the increasing PL intensity from 0 % to 10 % (Figure 7.8c).

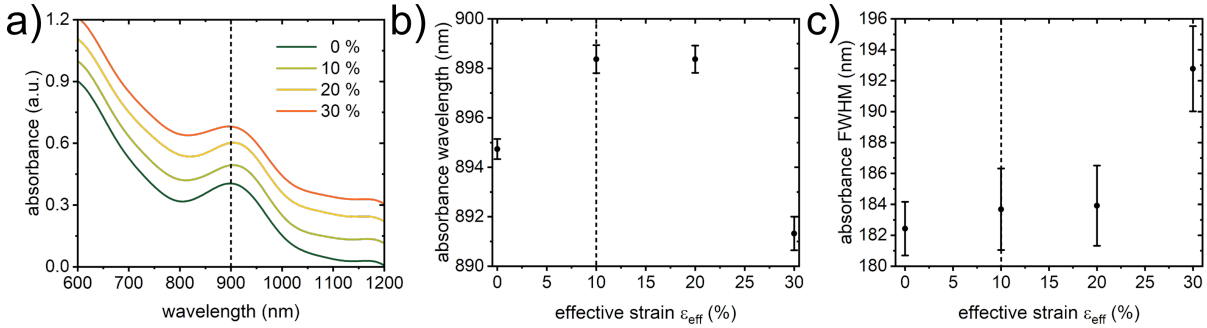

Figure 7.10.: *In-situ* absorbance spectra with increasing strain. a) First excitonic peak in the absorbance spectra of PbS QD films shows a slight shift with the increasing effective strain. The curves are fitted with Gaussian functions to extract the evolution of center wavelengths and the corresponding FWHM. b) The absorbance wavelength redshifts towards the phase transition at 10 % by about 4 nm, remains constant at 20 %, and blueshifts by about 6 nm at 30 %. The occurring redshift corresponding to about 6 meV and its correlation with the decreasing edge-to-edge distance of nearest neighbors (Figure 7.7) are in good agreement with the observed redshift via decreasing inter-dot distance upon ligand exchange in PbSe QD thin films. [185] c) The FWHM remains constant within the error bars and broadens at 30 %. The blueshift and line broadening at 30 % are attributed to the increasingly contributing interfaces at the microscopic cracks. Reproduced from [18] with permission from the Royal Society of Chemistry.

Further increase of the strain beyond 10 % would cause a compression of the confined ligand chains beyond the critical value of $l_{SL}^{lig} = 1.55$ nm, which is energetically unfavorable (Figure 7.5f). Instead, the FCC/BCT superlattice transforms into a BCC phase at 10 %. The ligands relax upon phase transition to the BCC phase, providing a longer confined ligand length of about 1.75 nm, which is in good effective strain. The FCC/BCT–BCC transition takes place via slipping in ⟨110⟩ directions on the close-packed {111} FCC planes that are in parallel alignment with the {011} BCT planes and is similar to the

Nishiyama–Wassermann path known from the martensite transition in iron. [186], [187] Consequently, neighboring QDs get locally rearranged during the FCC/BCT–BCC phase transition and with the increasing isotropy, more dipole–dipole interactions between the QDs are likely to form. This rearrangement in adjacent QD coupling is reflected in the slightly redshifted wavelengths of the inhomogeneous broadening (Figure 7.8b)) and its reduced FWHM towards the cubic phase (Figure 7.9). [138] Moreover, the decreasing nearest-neighbor spacing (Figure 7.7) agrees well with the observed redshift of the first excitonic peak in the absorbance spectra (Figure 7.10). A similar redshift in absorbance was observed by reducing nearest neighbor distances, e.g., by ligand exchange in PbSe thin films. [185]

Stage II: Decreasing PL Emission From 10 % to 16 %

Further increase of strain after the unit cell phase transition leads to the decreasing unit cell isotropy followed by decreasing PL intensity. Isotropy and emission intensity vary symmetrically with respect to the maximum at the cubic phase line. Whereas the nearest-neighbor distances in the (011) BCT plane (Figure 7.7) and the absorbance spectra remain constant (Figure 7.9), the lattice continuously shrinks along c_{bct}. The FRET efficiency, however, is reduced by the slightly increasing distance along abct since twice as many inter-dot distances along the unit cell edges are affected by a_{bct} than by c_{bct}. The reduced isotropy of QD coupling also shifts the dipole–dipole interactions, as seen from the slightly blueshifted wavelength with respect to the phase transition (Figure 7.8b). The blueshift is less pronounced than the redshift in stage I. The reason for this hysteresis is in no slipping of the densest planes being involved in stage II. At 16 %, the confined ligand length compresses to the same size that formerly caused the FCC/BCT–BCC phase transition via slipping (Figure 7.5f). In the BCT phase, however, there is no unit cell symmetry left to access via phase transition that would allow for ligand relaxation. This missing relaxation pathway causes the beginning of microscopic crack formation that conserves a constant superlattice configuration with increasing strain. Hence, the FCC/BCT–BCC–BCT phase transition is considered as a ductile-to-brittle transition.

Stage III: Constant PL Emission From 16 % to 30 %

In the final stage, the strain introduced by substrate elongation is entirely focused on the formation and widening of microscopic cracks (Figure 7.6a). The superlattice remains under tension in the configuration of isotropy, and inter-dot distances given at the maximum to the superlattice applied effective strain of 16 %. Consequently, the optoelectronic coupling remains unchanged regarding constant PL emission intensity and wavelength. I

attribute the observed slightly increasing FWHM of the inhomogeneous broadening to the loose interfaces upon crack propagation. This effect also reflects in the blueshift and the broadening at FWHM of the first excitonic peak in the absorbance spectra at 30 % of effective strain (Figure 7.9). A slight decrease of PL intensity within the error bars hints increasing contribution of the arising voids on the area illuminated by the excitation laser, causing increasing light leakage at higher strains.

7.6. Conclusion

Uniaxial strain applied to the substrate of OA-capped PbS QD thin films introduces three stages of superlattice deformation linked by the ligand shells' compression to a critical value. This critical value is about 10 % for the investigated QDs with a core-to-shell ratio of about 1.08 and corresponds to a confined ligand length of about 1.55 nm. The first two stages are linked by an FCC/BCT–BCC–BCT unit cell phase transition that relaxes the confined ligand length. The varying unit cell isotropy upon phase transition results in changed optoelectronic coupling and explains observed changes in PL emission within the framework of FRET. The third stage introduces crack propagation in the QD thin film because the critical ligand compression cannot be relaxed via unit cell phase transition. Here, the unit cell isotropy remains unchanged with increasing strain, leading to constant PL emission. Given the impact on superlattice deformation and optoelectronic coupling, the external strain on optoelectronic QD devices is necessary to account for real-world applications, e.g., on flexible substrates. Since FRET is a resonant energy transfer, its efficiency varying with strain plays a crucial role, e.g., in the figure of merit for QD solar cells. In summary, I report *in-situ* GISAXS measurements on thin films on freestanding, flexible substrates upon uniaxial strain. By comparing the results of superlattice deformation and PL, we provide a connection between strain and optoelectronic coupling. This connection is given by the variation of the unit cell isotropy upon phase transition that affects the inter-dot coupling and complements the findings from the literature on a fundamental level.

Chapter 8

Summary

This thesis explores the structure-function relationship of organic-inorganic (bio)hybrid interfaces in functional films with emphasis on the formation and deformation of these (bio)hybrid interfaces. For the analysis of the structural properties, advanced X-ray scattering methods are used, which, due to the excellent brilliance at large-scale research facilities, allow the investigation of the film nanostructure with high spatial and temporal resolution. These X-ray scattering methods are complemented by neutron scattering, SEM, and spectroscopic characterization methods. This thesis is divided into two projects, which are related to the formation and deformation of (bio)hybrid interfaces, respectively.

The first project focuses on the formation of biohybrid interfaces consisting of β-lg and titania precursors to promote a sustainable route towards nanostructured titania films. A large surface-to-volume ratio resulting from a tailored porosity in these films is of high relevance for applications, e.g., for the photocatalytic generation of hydrogen. To address the question how the the biohybrid interfaces direct the resulting inner morphology of titania films, spray deposited films are investigated with GISAXS/GISANS and GIWAXS together with SEM. Subsequently, by comparing the inner morphology obtained from GISAXS of pure β-lg films, biotemplated titania films after protein removal, and the biohybrid β-lg:titania composite films, a relationship between the titania domain distances and the β-lg domain sizes is found. This structure-function-relationship of the protein tailoring the titania film morphology manifests in the equivalence of the β-lg domain sizes, and the titania inter-domain distance, which relate to the titania pore sizes after protein removal. With this knowledge, a closer look into the film formation process during spray deposition is performed with simultaneous *in-situ* GISAXS/GIWAXS measurements. The results reveal the formation of crystalline titania in a mixed anatase-brookite phase with an average crystallite size of 4.2 nm at the set substrate temperature of 120 °C. The domain sizes and crystallite sizes obtained from GISAXS and GIWAXS, respectively, match in their temporal evolution during spray deposition. Also, the temporal evolution of the

lateral arrangement of the titania domains and the temporal evolution of the crystallite growth match. The observations reveal, that the condensing β-lg matrix sterically directs the formation of crystalline clusters, and defines the pore size after protein removal. To further investigate the potential of β-lg in establishing different titania morphologies, the influence of different β-lg aggregates on the titania film morphology is studied. This is achieved by denaturation of β-lg at pH values of 2, 5, and 7, which leads to different domain sizes. At pH 5, close to the isoelectric point of β-lg, the smallest average domain sizes are found in the biohybrid composite films and after protein removal, the largest pore radii are found at pH 5 in the biotemplated titania films. The results reveal insights into the formation of β-lg:titania biohyrid interfaces and demonstrate that the controlled aggregation of β-lg by denaturation is a suitable tool to tailor the morphology and porosity in nanostructured, foam-like titania films as a water-based alternative to conventional templating based on synthetic polymers.

Besides the formation of interfaces in functional films, also their deformation is of particular interest regarding the structure-function-relationship. The second project of this thesis explores the deformation of hybrid interfaces based on PbS QDs with oleic acid ligands that build up a QD superlattice film. As optoelectronic performance in QD superlattice devices depend on the inter-dot coupling and hence on the inter-dot arrangement, knowledge about the deformation of the superlattice arrangement is essential. The deformation of the hybrid interfaces is introduced by uniaxial strain, which is applied to a flexible substrate supporting the QD superlattice film. While GISAXS is an optimal tool to gain the required knowledge on the deforming superlattice, it is challenging to perform on flexible substrates during elongation, due to the necessary precise sample alignment with respect to the incident X-ray beam. This challenge has been overcome in close collaboration with the Leibniz-Institut für Polymerforschung Dresden (IPF) and successful *in-situ* GISAXS on flexible substrates with increasing strain is performed in a pioneering experiment. From the obtained *in-situ* GISAXS data, an equivalent strain model is obtained, which captures the 3D deformation of the supported QD superlattice on the nanoscale. The results show, that with increasing uniaxial substrate elongation, the hybrid interfaces contribute significantly to the distribution and relaxation of the induced strain. A critical compression length of about 1.55 nm of the flexible organic ligands attached to the QDs plays a crucial role. Beyond this maximum compression length, further absorption of mechanical energy is compensated via a phase transition into another crystal structure of the superlattice, where the ligand compression relaxes. This phase transition occurs from the initial nested FCC/BCT to a pure BCT lattice symmetry, passing the BCC phase. Upon further deformation, the ligands compress again to the critical value of 1.55 nm and further mechanical strain is converted into macroscopic

cracking due to lack of available crystal symmetry. Along with the phase transition in superlattice symmetry, the associated isotropy of inter-dot arrangement also varies, having a maximum in the BCC phase. The isotropy is given as a function of the aspect ratio c/a of the unit cell in the respective superlattice symmetry, which matches the emission intensity of the QD superlattice obtained from *in-situ* PL. This observation is described in the framework of FRET and connects the changing inter-dot arrangement upon deformation of the hybrid interfaces with the changing inter-dot coupling captured by PL. With this structure-function-relationship based on the deformation of hybrid interfaces in a PbS QD superlattice, significant knowledge on strain induced morphology and function changes in flexible optoelectronics based on QD superlattice is gained.

The objectives of this thesis have successfully contributed new expertise on water-based synthesis of nanostructured titania films and mechanical stability in PbS QD superlattice films by exploring their structure-function-relationship of (bio)hybrid interfaces during formation and deformation. Future studies regarding the formation of biohybrid interfaces are suggested to investigate further denaturation mechanisms of β-lg, e.g, based on alcohol additives or ionic strength. Another promising approach to nanostructured and conductive biohybrid films is offered by the use of denatured β-lg films as substrates for biotemplated sputter deposition of metals. Investigation of hydration kinetics in biohybrid films based on β-lg potentially benefit application as sustainable hydrogels. Regarding the deformation of hybrid interfaces, further research on the influence of ligand type on the morphology variation upon mechanical deformation introduced by strain, but also by compression, are able to broaden the understanding of fundamental structure-function-relationships in QD devices. The concept of studying the deformation in thin films as function of strain with *in-situ* GISAXS has great potential to be extended to other functional materials besides QD superlattices. For example, the investigation of the film formation during the deposition of conductive coatings as function of uniaxial strain applied to a flexible substrate potentially yields interesting insights into the structure-function-relationship with respect to the percolation threshold. Beyond that, there are various potential studies on the formation and deformation of (bio)hybrid interfaces in functional films inviting to be performed, for which the outcomes of this thesis aim to set a fundamental framework.

Appendix A

Superlattice Index Matching on 2D GISAXS Data With GIXSGUI

Appendix A is based on the publication *Superlattice Deformation in Quantum Dot Films on Flexible Substrates via Uniaxial Strain* (J. E. Heger, W. Chen, H. Zhong, T. Xiao, C. Harder, F. A. C. Apfelbeck, A. F. Weinzierl, R. Boldt, L. Schraa, E. Euchler, A. K. Sambale, K. Schneider, M. Schwartzkopf, S. V. Roth, P. Müller-Buschbaum, *Nanoscale Horizons*, **8**, 383-395 (2023)) [18]. Reproduced from [18] with permission from the Royal Society of Chemistry.
The MATLAB-based software GIXSGUI is used for indexing the observed superlattice reflexes on the 2D GISAXS data in Chapter 7. [68] GIXSGUI is a broadly employed application for treating raw data from grazing incidence scattering. It offers a variety of functions, such as transferring the data from the as-measured pixel space to reciprocal q-space, plotting the data in various representations, and indexing the reflexes in a scattering pattern. The graphical user interface of GIXSGUI is opened with the function gixsgui in the MATLAB Command Window, after loading the path to GIXSGUI with subfolders into the MATLAB editor (Figure A.1). For more information about the installation of GIXSGUI and the available functions, the software documentation is recommended:
https://www.aps.anl.gov/files/APS-Uploads/SECTOR8/8-ID/doc.pdf

In the following, a step-by-step guide on how to use GIXSGUI to identify the QD superlattice unit cells is presented. The routine is summed up in three main steps, with precise details listed as substeps:

1. Enter the setup parameters for scattering geometry and detector details (Figure A.2).
1.1. The setup parameters must be entered in the top right corner of the appearing

window. These parameters include the sample-detector distance, X-ray energy, incident angle, direct and specular beam positions, and detector details about, e.g., pixel size. This information is obtained by calibration measurements at the DESY P03 beamline and from the Pilatus 2M detector datasheet.

1.2. For convenience, the setup parameters are saved and exported so that they are easy to reload next time. The working directory is loaded via the path to the 2D GISAXS data. In this step-by-step guide, exemplarily GISAXS data at 0 %, 10 %, and 30 % of applied strain to the substrate is shown.

1.3. The 2D GISAXS data is loaded and plotted in q-space representation on a logarithmic intensity scale by choosing the respective plot settings and double clicking on the respective data file.

2. Calculate the superlattice reflexes for a given space group in q-space (Figure A.3-A.6).

2.1. By clicking on the Data Processing button, an additional window appears, in which the Diffraction tab is selected for calculating the superlattice reflexes.

2.2. The parameters for the unit cell's space group and superlattice constant are entered. This is an iterative process, which starts with an educated guess based on our previous work and becomes defined with the superlattice constants, which are obtained from the measured q-positions of the reflexes. [152] The q-positions are obtained by Gaussian fits of the reflexes 1D peak intensities, which are in this work azimuthally integrated by using the software DPDAK. [66] The space group #139 (I 4/mmm) is chosen with $a = b \neq c$ describing a distorted BCC unit cell to match the shifting reflexes of the BCT-BCC-BCT phase transition with increasing strain (Figure A.3, A.3, A.5). To match the remaining scattering pattern in the nested FCC/BCC symmetry before the phase transition, the space group #225 ($Fm\bar{3}m$) is selected with $a = b = c$, describing the FCC unit cell (Figure A.6).

2.3. It is necessary to enter the unit cell orientation with respect to the substrate. In this work, the (011) planes of the distorted BCC unit cell and the (111) planes of the FCC unit cell are parallel to the substrate in edge-on and corner-on orientation, respectively. After inputting the set of indices to be calculated, the calculation can be started with the respective button Start Calculation.

3. Plot selected superlattice indices on the 2D GISAXS data in q-space representation (Figure A.3-A.6).

3.1. The calculated set of indices can be plotted on the 2D GISAXS data in q-space representation when choosing the plot option Born. Spare indices of the calculated set,

which show no reflexes in the 2D GISAXS data, are deselected from the table.

3.2. Further adjustments of the intensity scale and its color code can be made in the appearing window of the combined 2D GISAXS and superlattice indices plot. When the indices match the reflex positions, the process of index matching with GIXSGUI is done.

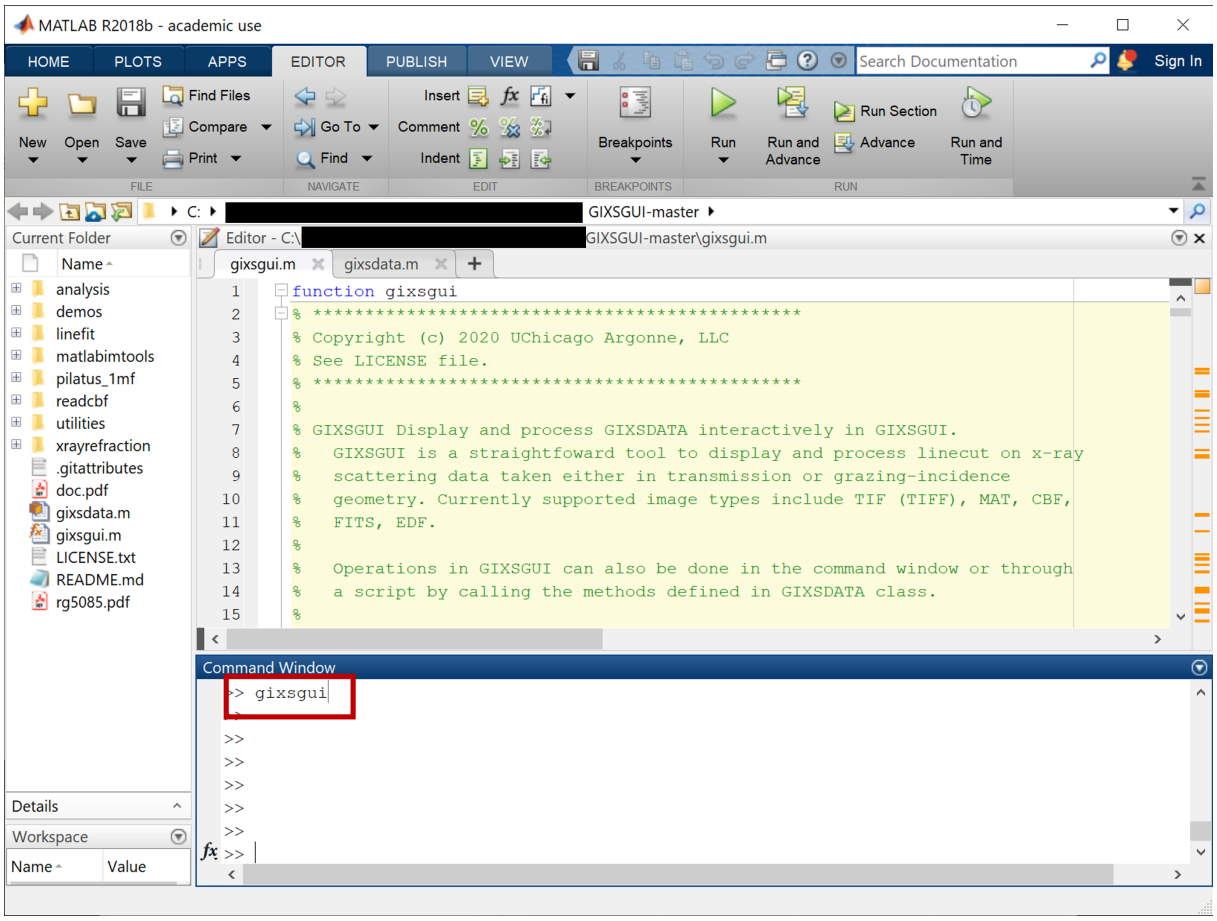

Figure A.1.: Start GIXSGUI. GIXSGUI is started by loading its path with subfolders to the editor environment of MATLAB. The function *gixsgui*, highlighted by the red box, opens the graphical user interface. Reproduced from [18] with permission from the Royal Society of Chemistry.

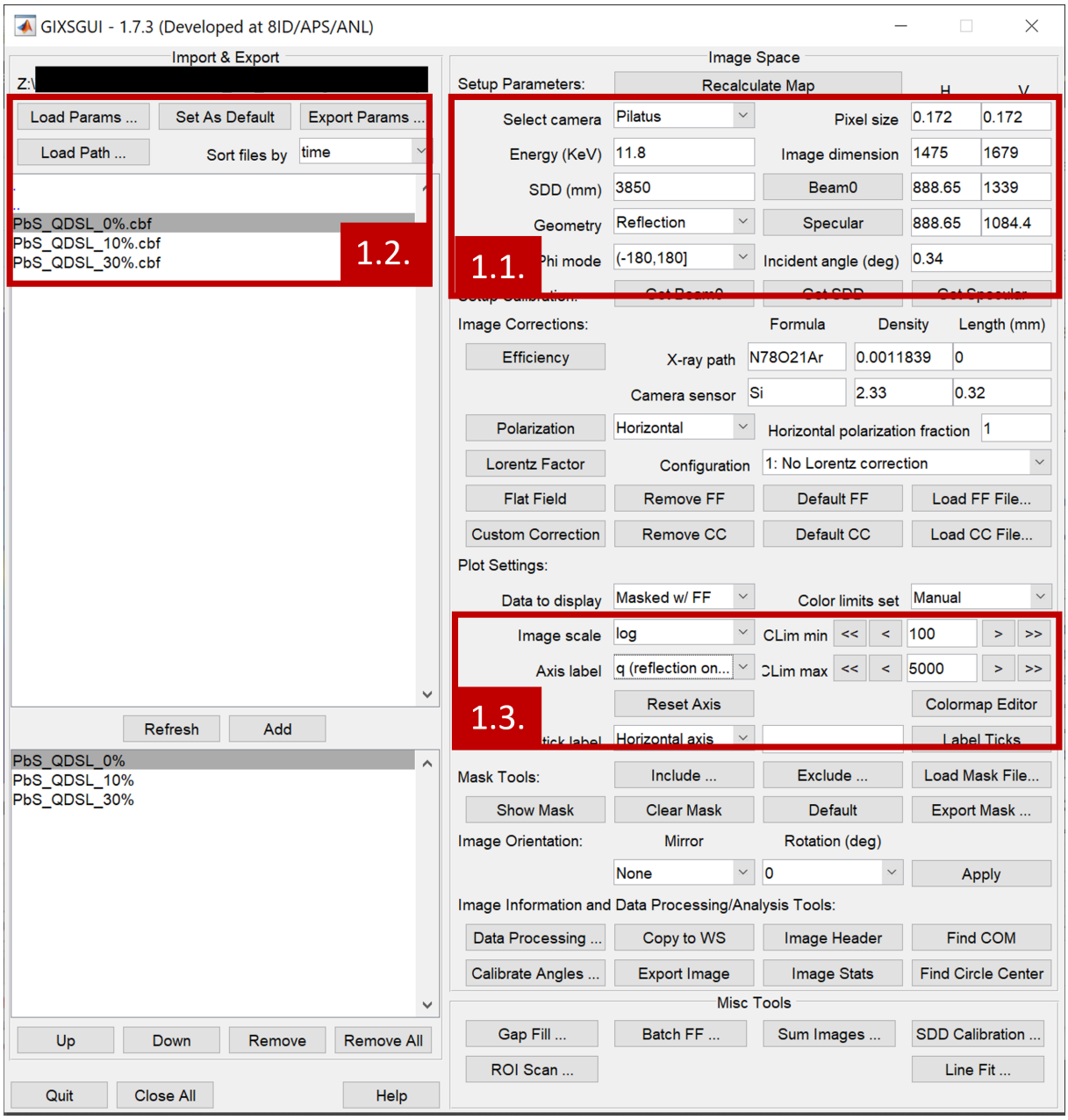

Figure A.2.: Initialize parameters. The setup parameters are entered and the working directory is opened in the main window. The 2D GISAXS data is loaded and plotted from the working directory. The button Data Processing opens a window where index calculation is done. The numbers label the steps as explained in the step-by-step guide. Reproduced from [18] with permission from the Royal Society of Chemistry.

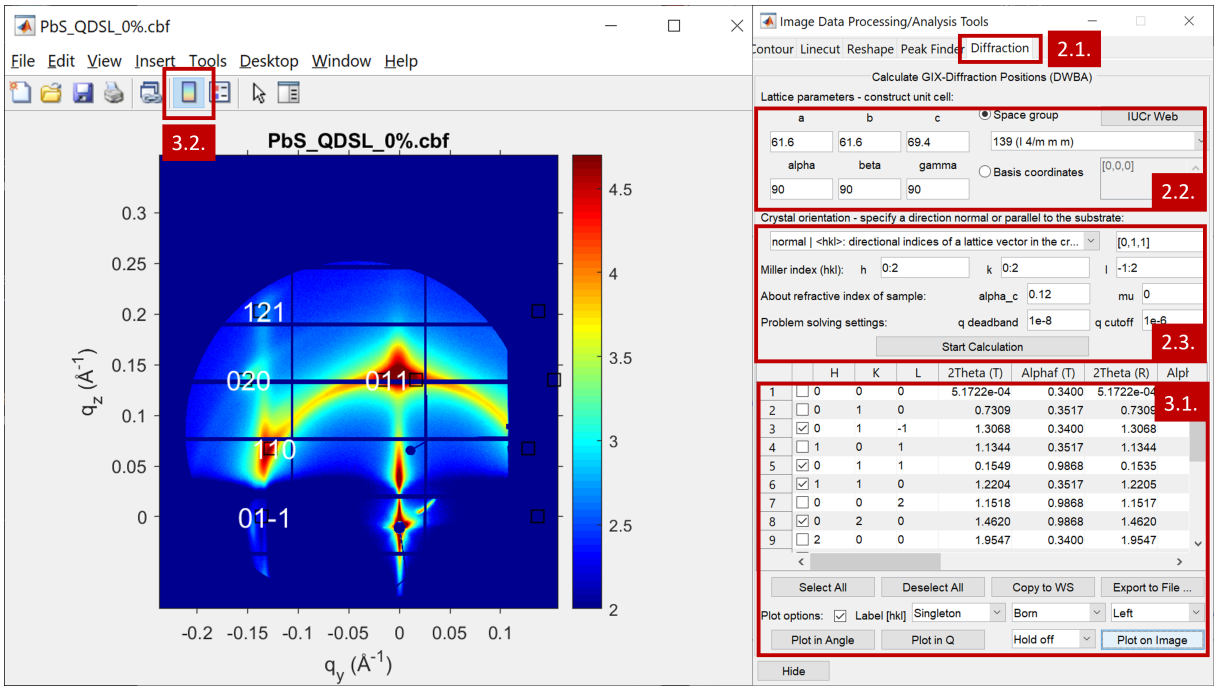

Figure A.3.: BCT at 0 %. The superlattice indices for the (121), (020), (110), (011), and (00$\bar{1}$) planes for the distorted BCC unit cell in space group #135 with edge-on orientation are matched with GIXSGUI and plotted on the 2D GISAXS data without applied strain. The superlattice constants $a = b = 61.6$ Å , and $c = 69.4$ Å are obtained from the center values of the q_{011} and q_{110} reflexes. The numbers label the steps as explained in the step-by-step guide. Reproduced from [18] with permission from the Royal Society of Chemistry.

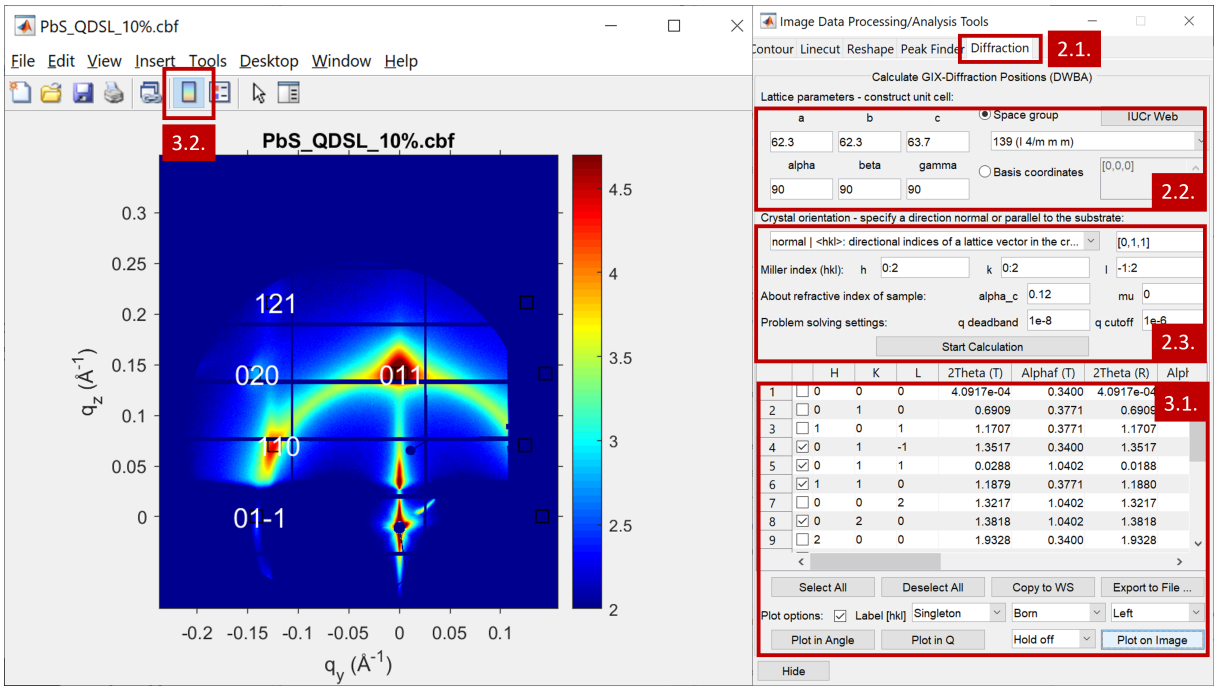

Figure A.4.: BCT at 10 %. The superlattice indices for the (121), (020), (110), (011), and (00$\bar{1}$) planes for the distorted BCC unit cell in space group #135 with edge-on orientation are matched with GIXSGUI and plotted on the 2D GISAXS data at 10 % applied strain, close to the BCT-BCC-BCT phase transition. The superlattice constants $a = b = 62.3$ Å, and $c = 63.7$ Å are obtained from the center values of the q_{011} and q_{110} reflexes. The numbers label the steps as explained in the step-by-step guide. Reproduced from [18] with permission from the Royal Society of Chemistry.

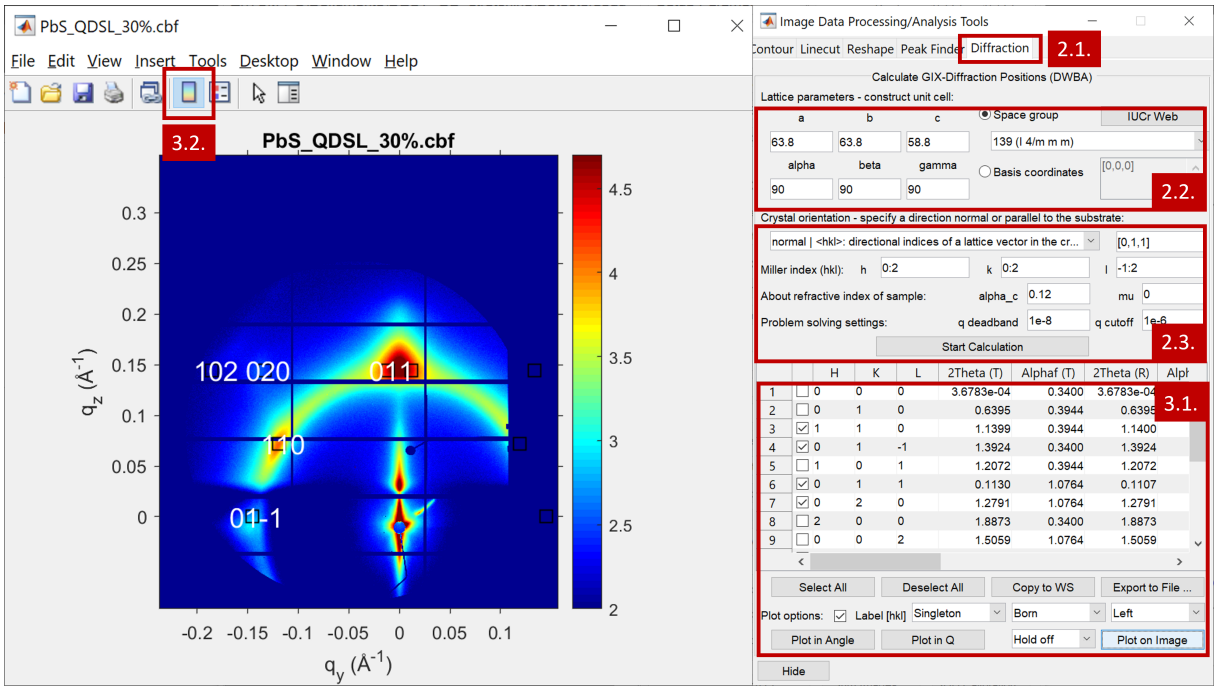

Figure A.5.: BCT at 30 %. The superlattice indices for the (121), (020), (110), (011), and (00$\bar{1}$) planes for the distorted BCC unit cell in space group #135 with edge-on orientation are matched with GIXSGUI and plotted on the 2D GISAXS data at maximum applied strain. The superlattice constants $a = b = 63.8$ Å , and $c = 58.8$ Å are obtained from the center values of the q_{011} and q_{110} reflexes. The numbers label the steps as explained in the step-by-step guide. Reproduced from [18] with permission from the Royal Society of Chemistry.

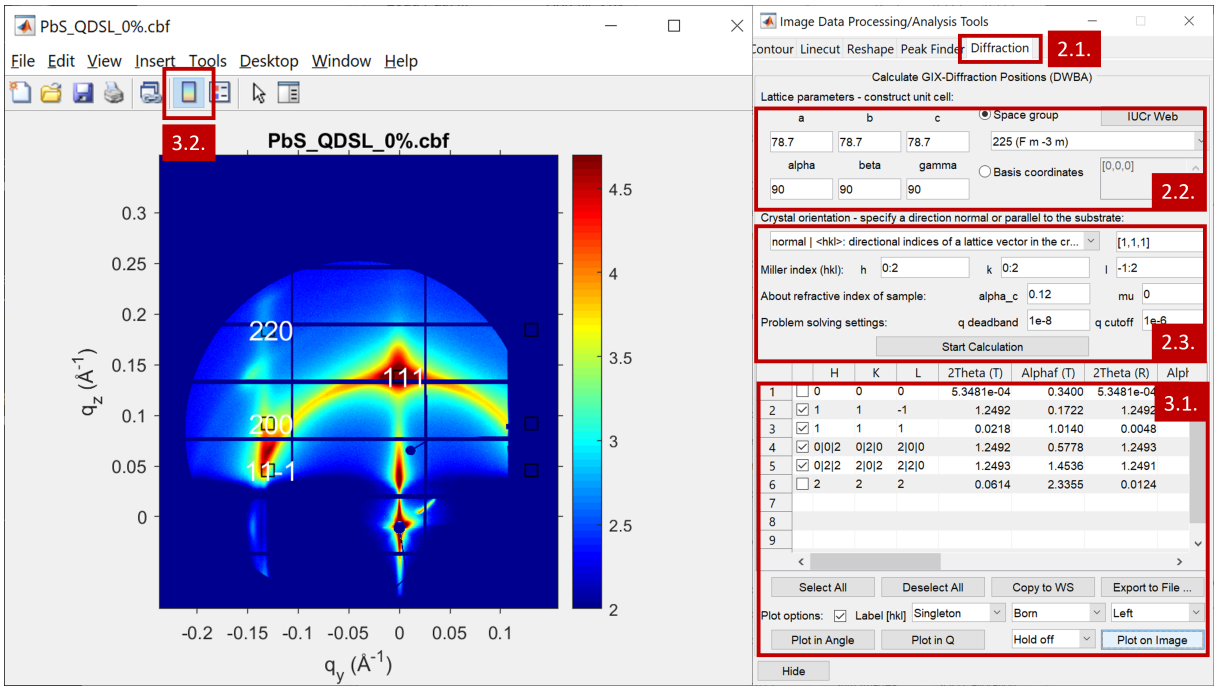

Figure A.6.: FCC at 0 %. The superlattice indices for the (220), (200), (11$\bar{1}$), and (111) planes for the FCC unit cell in space group #225 with corner-on orientation are matched with GIXSGUI and plotted on the 2D GISAXS data without applied strain. The superlattice constants $a = b = c = 78.7$ Å are obtained from the center values of the q_{111} reflex. The numbers label the steps as explained in the step-by-step guide. Reproduced from [18] with permission from the Royal Society of Chemistry.

Appendix B

Spray Coater for Controlled Area Deposition of Thin Films

Based on a computer numerical control (CNC) milling router machine kit (WindWilder), a spray coater was built for controlled area deposition (Figure B.1). Two stepper motors control the lateral movement of the spray nozzle and a single stepper motor controls the perpendicular movement. The nozzle can move freely within an effective area of 20 cm × 17 cm and is controlled via a microcontroller (Arduino Nano) and two motor drivers (A9488). The spray nozzle is easily changed to different kind of systems, such as pulsed air-atomizing nozzles or ultrasonic spray nozzles.

The pulsed spray deposition is enabled via a magnetic valve (MEBH-5/2-1/8-B, FESTO) that controls the nitrogen flow towards the nozzle and is programmed via a microcontroller (Arduino Uno R3), which is connected to the magentic valve according to the circuit diagram in Figure B.2. A MOSFET transistor (TSR-1-2450) allows for operating fast on/off cycles down to 50 ms. Once a protocol for pulsed spray deposition is load on the microcontroller, the program is started and stopped by pushing a button. The program is loaded onto the Arduino via the software Arduino IDE and the following code:

```
1 //adjust spray parameter here:
2 int cycleNumber = 10;  //number of spray cycles
3 int sprayTime = 100;  //spraying time in milliseconds
4 int dryTime = 1000;  //drying time in milliseconds
5
6 //initializing the control circuit:
7 int pushButton = 2;      //set by hardware, do not change
8 int motorControl = 9;   //set by hardware, do not change
9 int count = cycleNumber;
```

```
10
11 void setup() {
12   pinMode(pushButton, INPUT);
13   pinMode(motorControl, OUTPUT);
14   Serial.begin(9600);
15   pinMode(LED_BUILTIN, OUTPUT);
16 }
17
18 //loop controlling the magnetic valve
19 void loop() {
20 //start spray cycle by pushing the button
21   if(digitalRead(pushButton) == HIGH){
22     count = 0;
23   }
24
25 //if Arduino LED blinks, the program loaded successfully
26   digitalWrite(LED_BUILTIN, HIGH);   // turn the LED on
27   delay(500);                        // wait for half a second
28   digitalWrite(LED_BUILTIN, LOW);    // turn the LED off
29   delay(500);                        // wait for half a second
30
31 //spray cycle parameter
32   while(count < cycleNumber){
33     digitalWrite(motorControl,HIGH);
34     delay(sprayTime);
35     digitalWrite(motorControl,LOW);
36     delay(dryTime);
37     count++;
38
39 //abbort and reset spray cycle by pushing the button
40     if(digitalRead(pushButton) == HIGH){
41       count = cycleNumber;
42       delay(500);
43     }
44   }
45 }
```

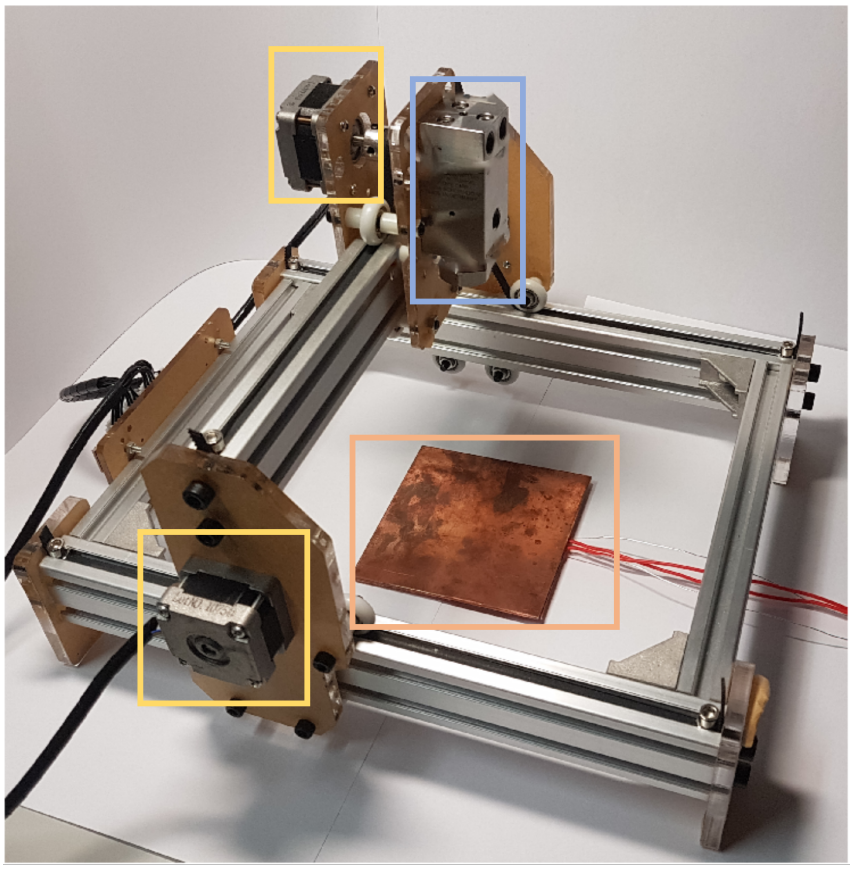

Figure B.1.: Spraycoater for area deposition. Yellow rectangles highlight the stepper motors that control the movements along x- and y-axis. The blue rectangle highlights the spray nozzle of type JAUCO D555000, which is easily attached to the spray coater. The orange rectangle represents the substrate with maximum dimensions of 20 cm $\times$ 17 cm, in this case a 10 cm $\times$ 10 cm copper hotplate for substrate heating.

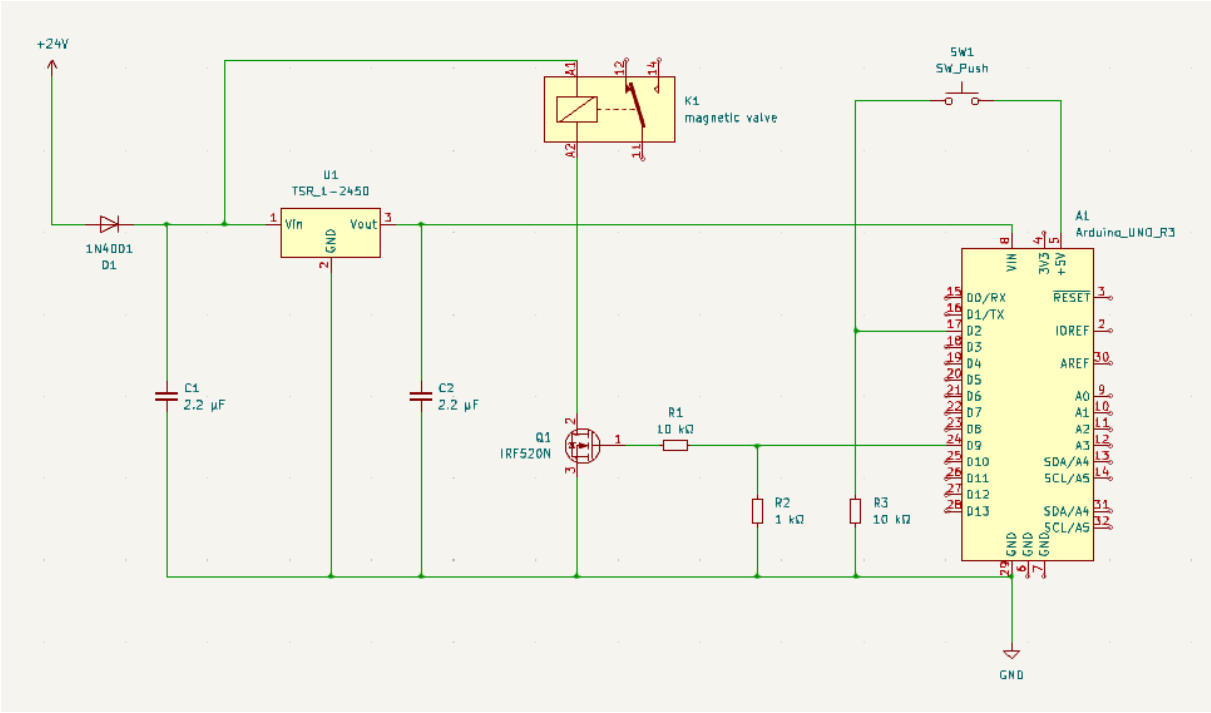

Figure B.2.: Circuit diagram for control of pulsed spray deposition.

Bibliography

[1] P. Ondrejka and M. Mikolášek, „Thin films and coatings for energy storage and conversion: From supercapacitors and batteries to hydrogen generators“, *Coatings*, vol. 13, no. 4, 742, 2023. DOI: 10.3390/coatings13040742.

[2] Q. Wang, W. Chen, W. Zhu, D. J. McClements, X. Liu, and F. Liu, „A review of multilayer and composite films and coatings for active biodegradable packaging“, *npj Sci. Food*, vol. 6, no. 1, 18, 2022. DOI: 10.1038/s41538-022-00132-8.

[3] B. Wang, W. Huang, S. Lee, L. Huang, Z. Wang, Y. Chen, Z. Chen, L.-W. Feng, G. Wang, T. Yokota, T. Someya, T. J. Marks, and A. Facchetti, „Foundry-compatible high-resolution patterning of vertically phase-separated semiconducting films for ultraflexible organic electronics“, *Nat. Commun.*, vol. 12, no. 1, 4937, 2021. DOI: 10.1038/s41467-021-25059-8.

[4] H. Zhu, Y. Shen, Y. Li, and J. Tang, „Recent advances in flexible and wearable organic optoelectronic devices“, *J. Semicond.*, vol. 39, no. 1, 011011, 2018. DOI: 10.1088/1674-4926/39/1/011011.

[5] P. Innocenzi and L. Malfatti, „Mesoporous ordered titania films: An advanced platform for photocatalysis“, *J. Photochem. Photobiol., C*, 100646, 2023. DOI: 10.1016/j.jphotochemrev.2023.100646.

[6] D. Dong, S. S. Dhanabalan, P. F. M. Elango, M. Yang, S. Walia, S. Sriram, and M. Bhaskaran, „Emerging applications of metal-oxide thin films for flexible and stretchable electronic devices“, *Appl. Phys. Rev.*, vol. 10, no. 3, 2023. DOI: 10.1063/5.0151297.

[7] I. Rodríguez-Gutiérrez, K. C. Bedin, B. Mouriño, J. B. Souza Junior, and F. L. Souza, „Advances in engineered metal oxide thin films by low-cost, solution-based techniques for green hydrogen production“, *Nanomaterials*, vol. 12, no. 12, 1957, 2022. DOI: 10.3390/nano12121957.

[8] V. Seiß, S. Thiel, and M. Eichelbaum, „Preparation and real world applications of titania composite materials for photocatalytic surface, air, and water purification: State of the art“, *Inorganics*, vol. 10, no. 9, 139, 2022. DOI: 10.3390/inorganics10090139.

[9] S. Mapukata, A. S. Hainer, A. E. Lanterna, J. C. Scaiano, and T. Nyokong, „Decorated titania fibers as photocatalysts for hydrogen generation and organic matter degradation“, *J. Photochem. Photobiol., A*, vol. 388, 112185, 2020. DOI: 10.1016/j.jphotochem.2019.112185.

[10] M. Madian, A. Eychmüller, and L. Giebeler, „Current advances in TiO_2-based nanostructure electrodes for high performance lithium ion batteries“, *Batteries*, vol. 4, no. 1, 7, 2018. DOI: 10.3390/batteries4010007.

[11] A. Mauricio Ramírez, L. Cattin, J.-C. Bernède, F. R. Díaz, M. A. Gacitúa, and M. A. del Valle, „Nanostructured TiO_2 and PEDOT electrodes with photovoltaic application“, *Nanomaterials*, vol. 11, no. 1, 107, 2021. DOI: 10.3390/nano11010107.

[12] M. Shahiduzzaman, S. Visal, M. Kuniyoshi, T. Kaneko, S. Umezu, T. Katsumata, S. Iwamori, M. Kakihana, T. Taima, M. Isomura, and K. Tomita, „Low-temperature-processed brookite-based TiO_2 heterophase junction enhances performance of planar perovskite solar cells“, *Nano Lett.*, vol. 19, no. 1, 598–604, 2019. DOI: 10.1021/acs.nanolett.8b04744.

[13] J. Gutierrez, A. Tercjak, and I. Mondragon, „Conductive behavior of high TiO_2 nanoparticle content of inorganic /organic nanostructured composites“, *J. Am. Chem. Soc.*, vol. 132, no. 2, 873–878, 2010. DOI: 10.1021/ja908359k.

[14] Y. Liu, Y. Gao, Q. Yang, G. Xu, X. Zhou, G. Shi, X. Lyu, H. Wu, J. Liu, S. Fang, M. I. Ullah, L. Song, K. Lu, M. Cao, Q. Zhang, T. Li, J. Xu, S. Wang, Z. Liu, and W. Ma, „Breaking the size limitation of directly-synthesized PbS quantum dot inks toward efficient short-wavelength infrared optoelectronic applications“, *Angew. Chem. Int. Ed.*, vol. 62, no. 17, e202300396, 2023. DOI: 10.1002/anie.202300396.

[15] S. Kumar, P. Bharti, and B. Pradhan, „Performance optimization of efficient PbS quantum dots solar cells through numerical simulation“, *Sci. Rep.*, vol. 13, no. 1, 10511, 2023. DOI: 10.1038/s41598-023-36769-y.

[16] NobelPrize.org. „The Nobel Prize in Chemistry 2023“. (2023), [Online]. Available: https://www.nobelprize.org/prizes/chemistry/2023/summary/ (visited on 11/23/2023).

[17] J. E. Heger, W. Chen, S. Yin, N. Li, V. Körstgens, C. J. Brett, W. Ohm, S. V. Roth, and P. Müller–Buschbaum, „Low–temperature and water–based biotemplating of nanostructured foam–like titania films using ß–lactoglobulin“, *Adv. Funct. Mater.*, vol. 32, no. 20, 2113080, 2022. DOI: 10.1002/adfm.202113080.

[18] J. E. Heger, W. Chen, H. Zhong, T. Xiao, C. Harder, F. A. C. Apfelbeck, A. F. Weinzierl, R. Boldt, L. Schraa, E. Euchler, A. K. Sambale, K. Schneider, M. Schwartzkopf, S. V. Roth, and P. Müller-Buschbaum, „Superlattice deformation in quantum dot films on flexible substrates via uniaxial strain“, *Nanoscale Horiz.*, vol. 8, no. 3, 383–395, 2023. DOI: 10.1039/D2NH00548D.

[19] D. Reyes-Coronado, G. Rodríguez-Gattorno, M. E. Espinosa-Pesqueira, C. Cab, R. de Coss, and G. Oskam, „Phase-pure TiO_2 nanoparticles: anatase, brookite and rutile“, *Nanotechnology*, vol. 19, no. 14, 145605, 2008. DOI: 10.1088/0957-4484/19/14/145605.

[20] H. Tang, H. Berger, P. E. Schmid, F. Lévy, and G. Burri, „Photoluminescence in TiO_2 anatase single crystals“, *Solid. State. Commun.*, vol. 87, no. 9, 847–850, 1993. DOI: 10.1016/0038-1098(93)90427-O.

[21] G. Žerjav, K. Žižek, J. Zavašnik, and A. Pintar, „Brookite vs. rutile vs. anatase: What‘s behind their various photocatalytic activities?“, *J. Environ. Chem. Eng.*, vol. 10, no. 3, 107722, 2022. DOI: 10.1016/j.jece.2022.107722.

[22] J.-P. Nikkanen, T. Kanerva, and T. Mäntylä, „The effect of acidity in low - temperature synthesis of titanium dioxide“, *J. Cryst. Growth*, vol. 304, no. 1, 179–183, 2007. DOI: 10.1016/j.jcrysgro.2007.02.012.

[23] A. Hernández-Gordillo, A. Hernández-Arana, A. Campero-Celis, and L. I. Vera-Robles, „Tibaldh as a precursor for biomimetic TiO_2 synthesis: Stability aspects in aqueous media“, *RSC Adv.*, vol. 9, no. 59, 34559–34566, 2019. DOI: 10.1039/C9RA05923G.

[24] G. A. Seisenbaeva, G. Daniel, J.-M. Nedelec, and V. G. Kessler, „Solution equilibrium behind the room-temperature synthesis of nanocrystalline titanium dioxide“, *Nanoscale*, vol. 5, no. 8, 3330–3336, 2013. DOI: 10.1039/C3NR34068F.

[25] S. Yin, L. Song, S. Xia, Y. Cheng, N. Hohn, W. Chen, K. Wang, W. Cao, S. Hou, and P. Müller–Buschbaum, „Key factors for template–oriented porous titania synthesis: Solvents and catalysts“, *Small Methods*, vol. 4, no. 3, 1900689, 2020. DOI: 10.1002/smtd.201900689.

[26] N. Li, R. Guo, W. Chen, V. Körstgens, J. E. Heger, S. Liang, C. J. Brett, M. A. Hossain, J. Zheng, P. S. Deimel, A. Buyruk, F. Allegretti, M. Schwartzkopf, J. G. C. Veinot, G. Schmitz, J. V. Barth, T. Ameri, S. V. Roth, and P. Müller–Buschbaum, „Tailoring ordered mesoporous titania films via introducing germanium nanocrystals for enhanced electron transfer photoanodes for photovoltaic applications“, *Adv. Funct. Mater.*, vol. 31, no. 34, 2102105, 2021. DOI: 10.1002/adfm.202102105.

[27] S. Brownlow, J. H. Morais Cabral, R. Cooper, D. R. Flower, S. J. Yewdall, I. Polikarpov, A. C. North, and L. Sawyer, „Bovine ß-lactoglobulin at 1.8 å resolution–still an enigmatic lipocalin“, *Structure*, vol. 5, no. 4, 481–495, 1997. DOI: 10.1016/s0969-2126(97)00205-0.

[28] H. C. Liu, W. L. Chen, and S. J. T. Mao, „Antioxidant nature of bovine milk ß-lactoglobulin“, *J. Dairy Sci.*, vol. 90, no. 2, 547–555, 2007. DOI: 10.3168/jds.S0022-0302(07)71538-2.

[29] G. Kontopidis, C. Holt, and L. Sawyer, „Invited review: Ss-lactoglobulin: Binding properties, structure, and function“, *J. Dairy Sci.*, vol. 87, no. 4, 785–796, 2004. DOI: 10.3168/jds.S0022-0302(04)73222-1.

[30] K. Sakurai and Y. Goto, „Dynamics and mechanism of the Tanford transition of bovine ß-lactoglobulin studied using heteronuclear NMR spectroscopy“, *J. Mol. Biol.*, vol. 356, no. 2, 483–496, 2006. DOI: 10.1016/j.jmb.2005.11.038.

[31] Z. Sun, M. Wang, S. Han, S. Ma, Z. Zou, F. Ding, X. Li, L. Li, B. Tang, H. Wang, N. Li, H. Che, and Y. Dai, „Production of hypoallergenic milk from DNA-free beta-lactoglobulin (BLG) gene knockout cow using zinc-finger nucleases mRNA“, *Sci. Rep.*, vol. 8, no. 1, 15430, 2018. DOI: 10.1038/s41598-018-32024-x.

[32] H. M. Berman, J. Westbrook, Z. Feng, G. Gilliland, T. N. Bhat, H. Weissig, I. N. Shindyalov, and P. E. Bourne, „The protein data bank“, *Nucleic Acids Res.*, vol. 28, no. 1, 235–242, 2000. DOI: 10.1093/nar/28.1.235.

[33] C. C. vandenAkker, M. F. M. Engel, K. P. Velikov, M. Bonn, and G. H. Koenderink, „Morphology and persistence length of amyloid fibrils are correlated to peptide molecular structure“, *J. Am. Chem. Soc.*, vol. 133, no. 45, 18030–18033, 2011. DOI: 10.1021/ja206513r.

[34] J.-M. Jung, G. Savin, M. Pouzot, C. Schmitt, and R. Mezzenga, „Structure of heat-induced ß-lactoglobulin aggregates and their complexes with sodium-dodecyl sulfate“, *Biomacromolecules*, vol. 9, no. 9, 2477–2486, 2008. DOI: 10.1021/bm800502j.

[35] J. J. Kehoe, L. Wang, E. R. Morris, and A. Brodkorb, „Formation of non-native ß-lactoglobulin during heat-induced denaturation“, *Food Biophysics*, vol. 6, no. 4, 487–496, 2011. DOI: 10.1007/s11483-011-9230-3.

[36] S. Bolisetty, J. Adamcik, J. Heier, and R. Mezzenga, „Amyloid directed synthesis of titanium dioxide nanowires and their applications in hybrid photovoltaic devices“, *Adv. Funct. Mater.*, vol. 22, no. 16, 3424–3428, 2012. DOI: 10.1002/adfm.201103054.

[37] C. R. Kagan, L. C. Bassett, C. B. Murray, and S. M. Thompson, „Colloidal quantum dots as platforms for quantum information science“, *Chem. Rev.*, vol. 121, no. 5, 3186–3233, 2021. DOI: 10.1021/acs.chemrev.0c00831.

[38] Y. Xia, S. Liu, K. Wang, X. Yang, L. Lian, Z. Zhang, J. He, G. Liang, S. Wang, M. Tan, H. Song, D. Zhang, J. Gao, J. Tang, M. C. Beard, and J. Zhang, „Cation–exchange synthesis of highly monodisperse PbS quantum dots from ZnS nanorods for efficient infrared solar cells“, *Adv. Funct. Mater.*, vol. 30, no. 4, 1907379, 2020. DOI: 10.1002/adfm.201907379.

[39] C. R. Kagan and C. B. Murray, „Charge transport in strongly coupled quantum dot solids“, *Nat. Nanotechnol.*, vol. 10, no. 12, 1013–1026, 2015. DOI: 10.1038/nnano.2015.247.

[40] L. Brus, „Electronic wave functions in semiconductor clusters: Experiment and theory“, *J. Phys. Chem.*, vol. 90, no. 12, 2555–2560, 1986. DOI: 10.1021/j100403a003.

[41] Y. Gong, J. Shen, Y. Zhu, X. Yang, L. Zhang, and C. Li, „Stretch induced photoluminescence enhanced perovskite quantum dot polymer composites“, *J. Mater. Chem. C*, vol. 8, no. 4, 1413–1420, 2020. DOI: 10.1039/C9TC05966K.

[42] W. Chen, H. Tang, Y. Chen, J. E. Heger, N. Li, L. P. Kreuzer, Y. Xie, D. Li, C. Anthony, Z. Pikramenou, K. W. Ng, X. W. Sun, K. Wang, and P. Müller-Buschbaum, „Spray-deposited PbS colloidal quantum dot solid for near-infrared photodetectors“, *Nano Energy*, vol. 78, 105254, 2020. DOI: 10.1016/j.nanoen.2020.105254.

[43] A. Hexemer and P. Müller-Buschbaum, „Advanced grazing-incidence techniques for modern soft-matter materials analysis“, *IUCrJ*, vol. 2, no. Pt 1, 106–125, 2015. DOI: 10.1107/S2052252514024178.

[44] D.-M. Smilgies, „GISAXS: A versatile tool to assess structure and self–assembly kinetics in block copolymer thin films“, *J. Polym Sci.*, vol. 60, no. 7, 1023–1041, 2022. DOI: 10.1002/pol.20210244.

[45] Y. Yoneda, „Anomalous surface reflection of x rays“, *Phys. Rev.*, vol. 131, no. 5, 2010–2013, 1963. DOI: 10.1103/PhysRev.131.2010.

[46] S. K. Sinha, E. B. Sirota, S. Garoff, and H. B. Stanley, „X-ray and neutron scattering from rough surfaces“, *Phys. Rev. B*, vol. 38, no. 4, 2297–2311, 1988. DOI: 10.1103/PhysRevB.38.2297.

[47] A. Naudon, D. Babonneau, D. Thiaudière, and S. Lequien, „Grazing-incidence small-angle X-ray scattering applied to the characterization of aggregates in surface regions“, *Physica B*, vol. 283, no. 1-3, 69–74, 2000. DOI: 10.1016/S0921-4526(99)01894-3.

[48] C. E. Williams, R. P. May, and A. Guinier, „Small–angle scattering of X–rays and neutrons“, in *X-ray characterization of materials*, E. Lifshin, Ed., Weinheim and New York: Wiley-VCH, 1999, 211–254. DOI: 10.1002/9783527613748.ch4.

[49] G. K. Williamson and W. H. Hall, „X-ray line broadening from filed aluminium and wolfram“, *Acta Metall.*, vol. 1, no. 1, 22–31, 1953. DOI: 10.1016/0001-6160(53)90006-6.

[50] J. I. Langford and A. J. C. Wilson, „Scherrer after sixty years: A survey and some new results in the determination of crystallite size“, *J. Appl. Cryst.*, vol. 11, no. 2, 102–113, 1978. DOI: 10.1107/S0021889878012844.

[51] A. R. Stokes and A. J. C. Wilson, „A method of calculating the integral breadths of Debye-Scherrer lines“, *Math. Proc. Cambridge Philos. Soc.*, vol. 38, no. 3, 313–322, 1942. DOI: 10.1017/S0305004100021988.

[52] P. Müller-Buschbaum, „Grazing incidence small-angle neutron scattering: Challenges and possibilities“, *Polym. J.*, vol. 45, no. 1, 34–42, 2013. DOI: 10.1038/pj.2012.190.

[53] V. F. Sears, „Appendix. Neutron scattering lengths and cross sections“, in *Neutron Scattering*, ser. Methods in Experimental Physics, vol. 23, Elsevier, 1986, 521–550. DOI: 10.1016/S0076-695X(08)60561-X.

[54] V. F. Sears, „Neutron scattering lengths and cross sections“, *Neutron News*, vol. 3, no. 3, 26–37, 1992. DOI: 10.1080/10448639208218770.

[55] P. Müller-Buschbaum, „GISAXS and GISANS as metrology technique for understanding the 3D morphology of block copolymer thin films“, *Eur. Polym. J.*, vol. 81, 470–493, 2016. DOI: 10.1016/j.eurpolymj.2016.04.007.

[56] R. Lazzari, „IsGISAXS : A program for grazing-incidence small-angle X-ray scattering analysis of supported islands“, *J. Appl. Cryst.*, vol. 35, no. 4, 406–421, 2002. DOI: 10.1107/S0021889802006088.

[57] R. Hosemann, „Crystalline and paracrystalline order in high polymers“, *J. Appl. Phys.*, vol. 34, no. 1, 25–41, 1963. DOI: 10.1063/1.1729085.

[58] G. Renaud, R. Lazzari, and F. Leroy, „Probing surface and interface morphology with grazing incidence small angle X-Ray scattering“, *Surf. Sci. Rep.*, vol. 64, no. 8, 255–380, 2009. DOI: 10.1016/j.surfrep.2009.07.002.

[59] W. S. Gosal, A. H. Clark, P. D. A. Pudney, and S. B. Ross-Murphy, „Novel amyloid fibrillar networks derived from a globular protein: ß-lactoglobulin“, *Langmuir*, vol. 18, no. 19, 7174–7181, 2002. DOI: 10.1021/la025531a.

[60] W. Chen, J. Zhong, J. Li, N. Saxena, L. P. Kreuzer, H. Liu, L. Song, B. Su, D. Yang, K. Wang, J. Schlipf, V. Körstgens, T. He, K. Wang, and P. Müller-Buschbaum, „Structure and charge carrier dynamics in colloidal PbS quantum dot solids“, *J. Phys. Chem. Lett.*, vol. 10, no. 9, 2058–2065, 2019. DOI: 10.1021/acs.jpclett.9b00869.

[61] W. Gong, P. Wang, D. Dai, Z. Liu, L. Zheng, and Y. Zhang, „Infrared colloidal quantum dots for photoelectric conversion devices“, *J. Mater. Chem. C*, vol. 9, no. 9, 2994–3025, 2021. DOI: 10.1039/D0TC05902A.

[62] M. Tebyetekerwa, J. Zhang, Z. Xu, T. N. Truong, Z. Yin, Y. Lu, S. Ramakrishna, D. Macdonald, and H. T. Nguyen, „Mechanisms and applications of steady-state photoluminescence spectroscopy in two-dimensional transition-metal dichalcogenides“, *ACS Nano*, vol. 14, no. 11, 14579–14604, 2020. DOI: 10.1021/acsnano.0c08668.

[63] J. Tauc, R. Grigorovici, and A. Vancu, „Optical properties and electronic structure of amorphous germanium“, *Phys. Status Solidi B*, vol. 15, no. 2, 627–637, 1966. DOI: 10.1002/pssb.19660150224.

[64] M. C. Weidman, M. E. Beck, R. S. Hoffman, F. Prins, and W. A. Tisdale, „Monodisperse, air-stable PbS nanocrystals via precursor stoichiometry control“, *ACS Nano*, vol. 8, no. 6, 6363–6371, 2014. DOI: 10.1021/nn5018654.

[65] A. Buffet, A. Rothkirch, R. Döhrmann, V. Körstgens, M. M. Abul Kashem, J. Perlich, G. Herzog, M. Schwartzkopf, R. Gehrke, P. Müller-Buschbaum, and S. V. Roth, „P03, the microfocus and nanofocus X-ray scattering (MiNaXS) beamline of the PETRA III storage ring: The microfocus endstation“, *J. Synchrotron Rad.*, vol. 19, no. Pt 4, 647–653, 2012. DOI: 10.1107/S0909049512016895.

[66] G. Benecke, W. Wagermaier, C. Li, M. Schwartzkopf, G. Flucke, R. Hoerth, I. Zizak, M. Burghammer, E. Metwalli, P. Müller-Buschbaum, M. Trebbin, S. Förster, O. Paris, S. V. Roth, and P. Fratzl, „A customizable software for fast reduction and analysis of large X-ray scattering data sets: Applications of the new DPDAK package to small-angle X-ray scattering and grazing-incidence small-angle X-ray scattering“, *J. Appl. Cryst.*, vol. 47, no. Pt 5, 1797–1803, 2014. DOI: 10.1107/S1600576714019773.

[67] F. Li, Y. Liu, G. Shi, W. Chen, R. Guo, D. Liu, Y. Zhang, Y. Wang, X. Meng, X. Zhang, Y. Lv, W. Deng, Q. Zhang, Y. Shi, Y. Chen, K. Wang, Q. Shen, Z. Liu, P. Müller–Buschbaum, and W. Ma, „Matrix manipulation of directly–synthesized PbS quantum dot inks enabled by coordination engineering“, *Adv. Funct. Mater.*, vol. 31, no. 45, 2104457, 2021. DOI: 10.1002/adfm.202104457.

[68] Z. Jiang, „GIXSGUI: A MATLAB toolbox for grazing-incidence X-ray scattering data visualization and reduction, and indexing of buried three-dimensional periodic nanostructured films“, *J. Appl. Cryst.*, vol. 48, no. 3, 917–926, 2015. DOI: 10.1107/S1600576715004434.

[69] Heinz Maier-Leibnitz Zentrum et al., „MARIA: Magnetic reflectometer with high incident angle“, *Journal of large-scale research facilities*, vol. 1, A8, 2015. DOI: 10.17815/jlsrf-1-29.

[70] T. Widmann, L. P. Kreuzer, G. Mangiapia, M. Haese, H. Frielinghaus, and P. Müller-Buschbaum, „3D printed spherical environmental chamber for neutron reflectometry and grazing-incidence small-angle neutron scattering experiments“, *Rev. Sci. Instrum.*, vol. 91, no. 11, 113903, 2020. DOI: 10.1063/5.0012652.

[71] B. Chang, K. Schneider, I. Kuehnert, and G. Heinrich, „Cavitation behavior of semi-crystalline polymers during uniaxial stretching studied by synchrotron small-angle X-ray scattering“, in *Small Angle Scattering and Diffraction*, F. Yokaichiya and M. K. K. D. Franco, Eds., London, UK: IntechOpen, 2018. DOI: 10.5772/intechopen.74224.

[72] E. Euchler, A. K. Sambale, K. Schneider, K. Uhlig, R. Boldt, M. Stommel, A. Stribeck, M. Schwartzkopf, A. Rothkirch, and S. V. Roth, „Beamline-implemented stretching devices for in situ X-ray scattering experiments“, *J. Phys.: Conf. Ser.*, vol. 2380, no. 1, 012109, 2022. DOI: 10.1088/1742-6596/2380/1/012109.

[73] M. Piispanen and L. Hupa, „Comparison of self-cleaning properties of three titania coatings on float glass“, *Appl. Surf. Sci.*, vol. 258, no. 3, 1126–1131, 2011. DOI: 10.1016/j.apsusc.2011.09.048.

[74] M. G. Salvaggio, R. Passalacqua, S. Abate, S. Perathoner, G. Centi, M. Lanza, and A. Stassi, „Functional nano-textured titania-coatings with self-cleaning and antireflective properties for photovoltaic surfaces“, *Sol. Energy*, vol. 125, 227–242, 2016. DOI: 10.1016/j.solener.2015.12.012.

[75] Y. Bai, I. Mora-Seró, F. de Angelis, J. Bisquert, and P. Wang, „Titanium dioxide nanomaterials for photovoltaic applications“, *Chem. Rev.*, vol. 114, no. 19, 10095–10130, 2014. DOI: 10.1021/cr400606n.

[76] R. Shwetharani, M. Sakar, C. A. N. Fernando, V. Binas, and R. G. Balakrishna, „Recent advances and strategies to tailor the energy levels, active sites and electron mobility in titania and its doped/composite analogues for hydrogen evolution in sunlight“, *Catal. Sci. Technol.*, vol. 9, no. 1, 12–46, 2019. DOI: 10.1039/C8CY01395K.

[77] M. G. Fischer, X. Hua, B. D. Wilts, I. Gunkel, T. M. Bennett, and U. Steiner, „Mesoporous titania microspheres with highly tunable pores as an anode material for lithium ion batteries“, *ACS Appl. Mater. Interfaces*, vol. 9, no. 27, 22388–22397, 2017. DOI: 10.1021/acsami.7b03155.

[78] A. L. Linsebigler, G. Lu, and J. T. Yates, „Photocatalysis on TiO_2 surfaces: Principles, mechanisms, and selected results“, *Chem. Rev.*, vol. 95, no. 3, 735–758, 1995. DOI: 10.1021/cr00035a013.

[79] Y. Liu and Y. Yang, „Recent progress of TiO_2-based anodes for Li ion batteries“, *J. Nanomater.*, vol. 2016, 1–15, 2016. DOI: 10.1155/2016/8123652.

[80] B. O'Regan and M. Grätzel, „A low-cost, high-efficiency solar cell based on dye-sensitized colloidal TiO_2 films“, *Nature*, vol. 353, no. 6346, 737–740, 1991. DOI: 10.1038/353737a0.

[81] A. Aboulouard, B. Gultekin, M. Can, M. Erol, A. Jouaiti, B. Elhadadi, C. Zafer, and S. Demic, „Dye sensitized solar cells based on titanium dioxide nanoparticles synthesized by flame spray pyrolysis and hydrothermal sol-gel methods: A comparative study on photovoltaic performances“, *J. Mater. Res. Technol.*, vol. 9, no. 2, 1569–1577, 2020. DOI: 10.1016/j.jmrt.2019.11.083.

[82] M. M. Byranvand, A. N. Kharat, and M. H. Bazargan, „Titania nanostructures for dye-sensitized solar cells“, *Nano Micro Lett.*, vol. 4, no. 4, 253–266, 2012. DOI: 10.1007/BF03353723.

[83] V. Körstgens, S. Pröller, T. Buchmann, D. Moseguí González, L. Song, Y. Yao, W. Wang, J. Werhahn, G. Santoro, S. V. Roth, H. Iglev, R. Kienberger, and P. Müller-Buschbaum, „Laser-ablated titania nanoparticles for aqueous processed hybrid solar cells“, *Nanoscale*, vol. 7, no. 7, 2900–2904, 2015. DOI: 10.1039/C4NR06782G.

[84] C. C. Oey, A. B. Djurišić, H. Wang, K. K. Y. Man, W. K. Chan, M. H. Xie, Y. H. Leung, A. Pandey, J.-M. Nunzi, and P. C. Chui, „Polymer–TiO_2 solar cells: TiO_2 interconnected network for improved cell performance“, *Nanotechnology*, vol. 17, no. 3, 706–713, 2006. DOI: 10.1088/0957-4484/17/3/015.

[85] J. Bai and B. Zhou, „Titanium dioxide nanomaterials for sensor applications“, *Chem. Rev.*, vol. 114, no. 19, 10131–10176, 2014. DOI: 10.1021/cr400625j.

[86] F. Iskandar, A. B. D. Nandiyanto, K. M. Yun, C. J. Hogan, K. Okuyama, and P. Biswas, „Enhanced photocatalytic performance of brookite TiO_2 macroporous particles prepared by spray drying with colloidal templating“, *Adv. Mater.*, vol. 19, no. 10, 1408–1412, 2007. DOI: 10.1002/adma.200601822.

[87] Y. Wang, Y. He, Q. Lai, and M. Fan, „Review of the progress in preparing nano TiO_2: An important environmental engineering material“, *J. Environ. Sci.*, vol. 26, no. 11, 2139–2177, 2014. DOI: 10.1016/j.jes.2014.09.023.

[88] K. Liu, H. Fu, K. Shi, F. Xiao, L. Jing, and B. Xin, „Preparation of large-pore mesoporous nanocrystalline TiO_2 thin films with tailored pore diameters“, *J. Phys. Chem. B*, vol. 109, no. 40, 18719–18722, 2005. DOI: 10.1021/jp054546p.

[89] Z. Sun, M. Wolkenhauer, G.-G. Bumbu, D. H. Kim, and J. S. Gutmann, „GISAXS investigation of nanoparticles in PS-b-PEO block-copolymer films“, *Physica B*, vol. 357, no. 1-2, 141–143, 2005. DOI: 10.1016/j.physb.2004.11.043.

[90] Q. Lian, M. Z. Mokhtar, D. Lu, M. Zhu, J. Jacobs, A. B. Foster, A. G. Thomas, B. F. Spencer, S. Wu, C. Liu, N. W. Hodson, B. Smith, A. Alkaltham, O. M. Alkhudhari, T. Watson, and B. R. Saunders, „Using soft polymer template engineering of mesoporous TiO_2 scaffolds to increase perovskite grain size and solar cell efficiency“, *ACS Appl. Mater. Interfaces*, vol. 12, no. 16, 18578–18589, 2020. DOI: 10.1021/acsami.0c02248.

[91] P. Yang, D. Zhao, D. I. Margolese, B. F. Chmelka, and G. D. Stucky, „Block copolymer templating syntheses of mesoporous metal oxides with large ordering lengths and semicrystalline framework“, *Chem. Mater.*, vol. 11, no. 10, 2813–2826, 1999. DOI: 10.1021/cm990185c.

[92] N. Li, L. Song, L. Bießmann, S. Xia, W. Ohm, C. J. Brett, E. Hadjixenophontos, G. Schmitz, S. V. Roth, and P. Müller–Buschbaum, „Morphology phase diagram of slot–die printed TiO_2 films based on sol–gel synthesis“, *Adv. Mater. Interfaces*, vol. 6, no. 12, 1900558, 2019. DOI: 10.1002/admi.201900558.

[93] A. Verma, D. Martineau, E. Hack, M. Makha, E. Turner, F. Nüesch, and J. Heier, „Towards industrialization of perovskite solar cells using slot die coating“, *J. Mater. Chem. C*, vol. 8, no. 18, 6124–6135, 2020. DOI: 10.1039/D0TC00327A.

[94] T. Dhandayuthapani, R. Sivakumar, R. Ilangovan, C. Gopalakrishnan, C. Sanjeeviraja, and K. Jeyadheepan, „Eco-friendly nebulized spray deposition of bifunctional anatase TiO_2 thin films exhibiting multicolor switching and efficient NH_3 gas sensing at room temperature“, *Mater. Res. Express*, vol. 6, no. 6, 065053, 2019. DOI: 10.1088/2053-1591/ab0e38.

[95] L. Song, W. Wang, V. Körstgens, D. Moseguí González, F. C. Löhrer, C. J. Schaffer, J. Schlipf, K. Peters, T. Bein, D. Fattakhova-Rohlfing, S. V. Roth, and P. Müller-Buschbaum, „In situ study of spray deposited titania photoanodes for scalable fabrication of solid-state dye-sensitized solar cells“, *Nano Energy*, vol. 40, 317–326, 2017. DOI: 10.1016/j.nanoen.2017.08.023.

[96] L. La Notte, L. Salamandra, A. Zampetti, F. Brunetti, T. M. Brown, A. Di Carlo, and A. Reale, „Airbrush spray coating of amorphous titanium dioxide for inverted polymer solar cells“, *Int. J. Photoenergy*, vol. 2012, 1–5, 2012. DOI: 10.1155/2012/897595.

[97] A. Ivanova, D. Fattakhova-Rohlfing, B. E. Kayaalp, J. Rathouský, and T. Bein, „Tailoring the morphology of mesoporous titania thin films through biotemplating with nanocrystalline cellulose“, *J. Am. Chem. Soc.*, vol. 136, no. 16, 5930–5937, 2014. DOI: 10.1021/ja411292u.

[98] D. Ramimoghadam, S. Bagheri, and S. B. Abd Hamid, „Biotemplated synthesis of anatase titanium dioxide nanoparticles via lignocellulosic waste material“, *Biomed Res. Int.*, vol. 2014, 205636, 2014. DOI: 10.1155/2014/205636.

[99] Q. Chen, M. Betker, C. Harder, C. J. Brett, M. Schwartzkopf, N. M. Ulrich, M. E. Toimil–Molares, C. Trautmann, L. D. Söderberg, C. L. Weindl, V. Körstgens, P. Müller–Buschbaum, M. Ma, and S. V. Roth, „Biopolymer–templated deposition of ordered and polymorph titanium dioxide thin films for improved surface–enhanced raman scattering sensitivity“, *Adv. Funct. Mater.*, vol. 32, no. 6, 2108556, 2022. DOI: 10.1002/adfm.202108556.

[100] Y.-Y. Kim, C. Neudeck, and D. Walsh, „Biopolymer templating as synthetic route to functional metal oxide nanoparticles and porous sponges“, *Polym. Chem.*, vol. 1, no. 3, 272, 2010. DOI: 10.1039/b9py00366e.

[101] N. S. Allen, N. Mahdjoub, V. Vishnyakov, P. J. Kelly, and R. J. Kriek, „The effect of crystalline phase (anatase, brookite and rutile) and size on the photocatalytic activity of calcined polymorphic titanium dioxide (TiO_2)“, *Polym. Degrad. Stab.*, vol. 150, 31–36, 2018. DOI: 10.1016/j.polymdegradstab.2018.02.008.

[102] H. T. T. Tran, H. Kosslick, M. F. Ibad, C. Fischer, U. Bentrup, T. H. Vuong, L. Q. Nguyen, and A. Schulz, „Photocatalytic performance of highly active brookite in the degradation of hazardous organic compounds compared to anatase and rutile“, *Appl. Catal., B*, vol. 200, 647–658, 2017. DOI: 10.1016/j.apcatb.2016.07.017.

[103] S. Pigeot-Rémy, D. Gregori, R. Hazime, A. Hérissan, C. Guillard, C. Ferronato, S. Cassaignon, C. Colbeau-Justin, and O. Durupthy, „Size and shape effect on the photocatalytic efficiency of TiO_2 brookite“, *J. Mater. Sci.*, vol. 54, no. 2, 1213–1225, 2019. DOI: 10.1007/s10853-018-2924-x.

[104] A. Di Paola, M. Bellardita, and L. Palmisano, „Brookite, the least known TiO_2 photocatalyst“, *Catalysts*, vol. 3, no. 1, 36–73, 2013. DOI: 10.3390/catal3010036.

[105] P. Kohn, S. Pathak, M. Stefik, C. Ducati, U. Wiesner, U. Steiner, and S. Guldin, „Low temperature crystallisation of mesoporous TiO_2“, *Nanoscale*, vol. 5, no. 21, 10518–10524, 2013. DOI: 10.1039/c3nr03009a.

[106] Y.-F. Chen, C.-Y. Lee, M.-Y. Yeng, and H.-T. Chiu, „The effect of calcination temperature on the crystallinity of TiO_2 nanopowders“, *J. Cryst. Growth*, vol. 247, no. 3-4, 363–370, 2003. DOI: 10.1016/S0022-0248(02)01938-3.

[107] I. Oja, A. Mere, M. Krunks, R. Nisumaa, C.-H. Solterbeck, and M. Es-Souni, „Structural and electrical characterization of TiO_2 films grown by spray pyrolysis“, *Thin Solid Films*, vol. 515, no. 2, 674–677, 2006. DOI: 10.1016/j.tsf.2005.12.243.

[108] L. Song, A. Abdelsamie, C. J. Schaffer, V. Körstgens, W. Wang, T. Wang, E. D. Indari, T. Fröschl, N. Hüsing, T. Haeberle, P. Lugli, S. Bernstorff, and P. Müller-Buschbaum, „A low temperature route toward hierarchically structured titania films for thin hybrid solar cells“, *Adv. Funct. Mater.*, vol. 26, no. 39, 7084–7093, 2016. DOI: 10.1002/adfm.201603867.

[109] W. Wang, T. Widmann, L. Song, T. Fröschl, N. Hüsing, G. Mo, Z. Wu, P. Zhang, S. V. Roth, H. Fan, and P. Müller-Buschbaum, „Aging of low-temperature derived highly flexible nanostructured TiO_2 /P3HT hybrid films during bending“, *J. Mater. Chem. A*, vol. 7, no. 17, 10805–10814, 2019. DOI: 10.1039/C9TA01544B.

[110] X. Jiang, T. Herricks, and Y. Xia, „Monodispersed spherical colloids of titania: Synthesis, characterization, and crystallization“, *Adv. Mater.*, vol. 15, no. 14, 1205–1209, 2003. DOI: 10.1002/adma.200305105.

[111] K. Chalastara, F. Guo, S. Elouatik, and G. P. Demopoulos, „Tunable composition aqueous-synthesized mixed-phase TiO_2 nanocrystals for photo-assisted water decontamination: Comparison of anatase, brookite and rutile photocatalysts“, *Catalysts*, vol. 10, no. 4, 407, 2020. DOI: 10.3390/catal10040407.

[112] D. A. H. Hanaor, I. Chironi, I. Karatchevtseva, G. Triani, and C. C. Sorrell, „Single and mixed phase TiO_2 powders prepared by excess hydrolysis of titanium alkoxide“, *Adv. Appl. Ceram.*, vol. 111, no. 3, 149–158, 2012. DOI: 10.1179/1743676111Y.0000000059.

[113] I. Kartini, I. Y. Khairani, Chotimah, K. Triyana, and W. Sri, „Nanostructured titanium dioxide for functional coatings“, in *Titanium Dioxide*, D. Yang, Ed., London, UK: IntechOpen, 2018. DOI: 10.5772/intechopen.74555.

[114] K. Y. Jung, S. B. Park, and S.-K. Ihm, „Linear relationship between the crystallite size and the photoactivity of non-porous titania ranging from nanometer to micrometer size“, *Appl. Catal., A*, vol. 224, no. 1-2, 229–237, 2002. DOI: 10.1016/S0926-860X(01)00784-0.

[115] J. Adamcik, J.-M. Jung, J. Flakowski, P. de Los Rios, G. Dietler, and R. Mezzenga, „Understanding amyloid aggregation by statistical analysis of atomic force microscopy images“, *Nat. Nanotechnol.*, vol. 5, no. 6, 423–428, 2010. DOI: 10.1038/nnano.2010.59.

[116] M. J. Uttinger, T. R. Heyn, U. Jandt, S. E. Wawra, B. Winzer, J. K. Keppler, and W. Peukert, „Measurement of length distribution of beta-lactoglobulin fibrils by multiwavelength analytical ultracentrifugation“, *Eur. Biophys. J.*, vol. 49, no. 8, 745–760, 2020. DOI: 10.1007/s00249-020-01421-4.

[117] J. Adamcik and R. Mezzenga, „Adjustable twisting periodic pitch of amyloid fibrils“, *Soft Matter*, vol. 7, no. 11, 5437, 2011. DOI: 10.1039/c1sm05382e.

[118] J. Adamcik and R. Mezzenga, „Proteins fibrils from a polymer physics perspective“, *Macromolecules*, vol. 45, no. 3, 1137–1150, 2012. DOI: 10.1021/ma202157h.

[119] S. V. Roth, „A deep look into the spray coating process in real-time-the crucial role of X-rays“, *J. Phys.: Condens. Matter*, vol. 28, no. 40, 403003, 2016. DOI: 10.1088/0953-8984/28/40/403003.

[120] W. Cao, S. Yin, M. Plank, A. Chumakov, M. Opel, W. Chen, L. P. Kreuzer, J. E. Heger, M. Gallei, C. J. Brett, M. Schwartzkopf, A. A. Eliseev, E. O. Anokhin, L. A. Trusov, S. V. Roth, and P. Müller-Buschbaum, „Spray-deposited anisotropic ferromagnetic hybrid polymer films of PS-b-PMMA and strontium hexaferrite magnetic nanoplatelets“, *ACS Appl. Mater. Interfaces*, vol. 13, no. 1, 1592–1602, 2021. DOI: 10.1021/acsami.0c19595.

[121] D. M. Balazs, T. A. Dunbar, D.-M. Smilgies, and T. Hanrath, „Coupled dynamics of colloidal nanoparticle spreading and self-assembly at a fluid-fluid interface“, *Langmuir*, vol. 36, no. 22, 6106–6115, 2020. DOI: 10.1021/acs.langmuir.0c00524.

[122] L. Song, M. Rawolle, N. Hohn, J. S. Gutmann, H. Frielinghaus, and P. Müller-Buschbaum, „In situ monitoring mesoscopic deformation of nanostructured porous titania films caused by water ingression“, *ACS Appl. Mater. Interfaces*, vol. 11, no. 35, 32552–32558, 2019. DOI: 10.1021/acsami.9b10750.

[123] W. Chen, R. Guo, H. Tang, K. S. Wienhold, N. Li, Z. Jiang, J. Tang, X. Jiang, L. P. Kreuzer, H. Liu, M. Schwartzkopf, X. W. Sun, S. V. Roth, K. Wang, B. Xu, and P. Müller-Buschbaum, „Operando structure degradation study of PbS quantum dot solar cells“, *Energy Environ. Sci.*, vol. 14, no. 6, 3420–3429, 2021. DOI: 10.1039/D1EE00832C.

[124] W. Ohm, A. Rothkirch, P. Pandit, V. Körstgens, P. Müller-Buschbaum, R. Rojas, S. Yu, C. J. Brett, D. L. Söderberg, and S. V. Roth, „Morphological properties of airbrush spray-deposited enzymatic cellulose thin films“, *J. Coat. Technol. Res.*, vol. 15, no. 4, 759–769, 2018. DOI: 10.1007/s11998-018-0089-9.

[125] M. Ramesh, K. M. Boopathi, T.-Y. Huang, Y.-C. Huang, C.-S. Tsao, and C.-W. Chu, „Using an airbrush pen for layer-by-layer growth of continuous perovskite thin films for hybrid solar cells“, *ACS Appl. Mater. Interfaces*, vol. 7, no. 4, 2359–2366, 2015. DOI: 10.1021/am506886d.

[126] B. L. Kirsch, E. K. Richman, A. E. Riley, and S. H. Tolbert, „In-situ X-ray diffraction study of the crystallization kinetics of mesoporous titania films“, *J. Phys. Chem. B*, vol. 108, no. 34, 12698–12706, 2004. DOI: 10.1021/jp036442p.

[127] N. Kränzlin, M. Staniuk, F. J. Heiligtag, L. Luo, H. Emerich, W. van Beek, M. Niederberger, and D. Koziej, „Rationale for the crystallization of titania polymorphs in solution“, *Nanoscale*, vol. 6, no. 24, 14716–14723, 2014. DOI: 10.1039/C4NR04346D.

[128] P. Jenny, D. Roekaerts, and N. Beishuizen, „Modeling of turbulent dilute spray combustion“, *Prog. Energy Combust. Sci.*, vol. 38, no. 6, 846–887, 2012. DOI: 10.1016/j.pecs.2012.07.001.

[129] L. Amirav and E. Lifshitz, „A spray-based technique for the production of MnS thin films“, *ChemPhysChem*, vol. 16, no. 2, 353–359, 2015. DOI: 10.1002/cphc.201402645.

[130] A. J. Haider, Z. N. Jameel, and I. H. Al-Hussaini, „Review on: Titanium dioxide applications“, *Energy Procedia*, vol. 157, 17–29, 2019. DOI: 10.1016/j.egypro.2018.11.159.

[131] C. S. Lewis, Y. R. Li, L. Wang, J. Li, E. A. Stach, K. J. Takeuchi, A. C. Marschilok, E. S. Takeuchi, and S. S. Wong, „Correlating titania nanostructured morphologies with performance as anode materials for lithium-ion batteries“, *ACS Sustainable Chem. Eng.*, vol. 4, no. 12, 6299–6312, 2016. DOI: 10.1021/acssuschemeng.6b00763.

[132] J. Perlich, M. Memesa, A. Diethert, E. Metwalli, W. Wang, S. V. Roth, A. Timmann, J. S. Gutmann, and P. Müller-Buschbaum, „Preservation of the morphology of a self-encapsulated thin titania film in a functional multilayer stack: An X-ray scattering study“, *ChemPhysChem*, vol. 10, no. 5, 799–805, 2009. DOI: 10.1002/cphc.200800800.

[133] O. V. Otieno, E. Csáki, O. Kéri, L. Simon, I. E. Lukács, K. M. Szécsényi, and I. M. Szilágyi, „Synthesis of TiO_2 nanofibers by electrospinning using water-soluble Ti-precursor“, *J. Therm. Anal. Calorim.*, vol. 139, no. 1, 57–66, 2020. DOI: 10.1007/s10973-019-08398-z.

[134] V. A. Zeitler and C. A. Brown, „The infrared spectra of some Ti-O-Si, Ti-O-Ti and Si-O-Si compounds“, *J. Phys. Chem.*, vol. 61, no. 9, 1174–1177, 1957. DOI: 10.1021/j150555a010.

[135] M. Liu, N. Yazdani, M. Yarema, M. Jansen, V. Wood, and E. H. Sargent, „Colloidal quantum dot electronics“, *Nat. Electron.*, vol. 4, no. 8, 548–558, 2021. DOI: 10.1038/s41928-021-00632-7.

[136] J. J. Choi, J. Luria, B.-R. Hyun, A. C. Bartnik, L. Sun, Y.-F. Lim, J. A. Marohn, F. W. Wise, and T. Hanrath, „Photogenerated exciton dissociation in highly coupled lead salt nanocrystal assemblies“, *Nano Lett.*, vol. 10, no. 5, 1805–1811, 2010. DOI: 10.1021/nl100498e.

[137] P. Guyot-Sionnest, „Electrical transport in colloidal quantum dot films“, *J. Phys. Chem. Lett.*, vol. 3, no. 9, 1169–1175, 2012. DOI: 10.1021/jz300048y.

[138] C. R. Kagan, C. B. Murray, and M. G. Bawendi, „Long-range resonance transfer of electronic excitations in close-packed CdSe quantum-dot solids“, *Phys. Rev. B*, vol. 54, no. 12, 8633–8643, 1996. DOI: 10.1103/PhysRevB.54.8633.

[139] M. S. Kodaimati, C. Wang, C. Chapman, G. C. Schatz, and E. A. Weiss, „Distance-dependence of interparticle energy transfer in the near-infrared within electrostatic assemblies of PbS quantum dots“, *ACS Nano*, vol. 11, no. 5, 5041–5050, 2017. DOI: 10.1021/acsnano.7b01778.

[140] A. A. Chistyakov, M. A. Zvaigzne, V. R. Nikitenko, A. R. Tameev, I. L. Martynov, and O. V. Prezhdo, „Optoelectronic properties of semiconductor quantum dot solids for photovoltaic applications“, *J. Phys. Chem. Lett.*, vol. 8, no. 17, 4129–4139, 2017. DOI: 10.1021/acs.jpclett.7b00671.

[141] P. Siffalovic, L. Chitu, K. Vegso, E. Majkova, M. Jergel, M. Weis, S. Luby, I. Capek, J. Keckes, G. A. Maier, A. Satka, J. Perlich, and S. V. Roth, „Towards strain gauges based on a self-assembled nanoparticle monolayer–SAXS study“, *Nanotechnology*, vol. 21, no. 38, 385702, 2010. DOI: 10.1088/0957-4484/21/38/385702.

[142] M. K. Choi, J. Yang, T. Hyeon, and D.-H. Kim, „Flexible quantum dot light-emitting diodes for next-generation displays“, *npj Flexible Electron.*, vol. 2, no. 1, 2018. DOI: 10.1038/s41528-018-0023-3.

[143] D. M. Kroupa, M. Vörös, N. P. Brawand, B. W. McNichols, E. M. Miller, J. Gu, A. J. Nozik, A. Sellinger, G. Galli, and M. C. Beard, „Tuning colloidal quantum dot band edge positions through solution-phase surface chemistry modification“, *Nat. Commun.*, vol. 8, no. 1, 15257, 2017. DOI: 10.1038/ncomms15257.

[144] S. Lee, M.-J. Choi, G. Sharma, M. Biondi, B. Chen, S.-W. Baek, A. M. Najarian, M. Vafaie, J. Wicks, L. K. Sagar, S. Hoogland, F. P. G. de Arquer, O. Voznyy, and E. H. Sargent, „Orthogonal colloidal quantum dot inks enable efficient multilayer optoelectronic devices“, *Nat. Commun.*, vol. 11, no. 1, 4814, 2020. DOI: 10.1038/s41467-020-18655-7.

[145] M.-J. Choi, García de Arquer, F. Pelayo, A. H. Proppe, A. Seifitokaldani, J. Choi, J. Kim, S.-W. Baek, M. Liu, B. Sun, M. Biondi, B. Scheffel, G. Walters, D.-H. Nam, J. W. Jo, O. Ouellette, O. Voznyy, S. Hoogland, S. O. Kelley, Y. S. Jung, and E. H. Sargent, „Cascade surface modification of colloidal quantum dot inks enables efficient bulk homojunction photovoltaics“, *Nat. Commun.*, vol. 11, no. 1, 103, 2020. DOI: 10.1038/s41467-019-13437-2.

[146] Q. Chen, C. J. Brett, A. Chumakov, M. Gensch, M. Schwartzkopf, V. Körstgens, L. D. Söderberg, A. Plech, P. Zhang, P. Müller-Buschbaum, and S. V. Roth, „Layer-by-layer spray-coating of cellulose nanofibrils and silver nanoparticles for hydrophilic interfaces“, *ACS Appl. Nano Mater.*, vol. 4, no. 1, 503–513, 2021. DOI: 10.1021/acsanm.0c02819.

[147] S. Zheng, J. Chen, E. M. J. Johansson, and X. Zhang, „PbS colloidal quantum dot inks for infrared solar cells“, *iScience*, vol. 23, no. 11, 101753, 2020. DOI: 10.1016/j.isci.2020.101753.

[148] J. Yang, T. Ling, W.-T. Wu, H. Liu, M.-R. Gao, C. Ling, L. Li, and X.-W. Du, „A top-down strategy towards monodisperse colloidal lead sulphide quantum dots“, *Nat. Commun.*, vol. 4, no. 1, 1695, 2013. DOI: 10.1038/ncomms2637.

[149] G. Shi, H. Wang, Y. Zhang, C. Cheng, T. Zhai, B. Chen, X. Liu, R. Jono, X. Mao, Y. Liu, X. Zhang, X. Ling, Y. Zhang, X. Meng, Y. Chen, S. Duhm, L. Zhang, T. Li, L. Wang, S. Xiong, T. Sagawa, T. Kubo, H. Segawa, Q. Shen, Z. Liu, and W. Ma, „The effect of water on colloidal quantum dot solar cells“, *Nat. Commun.*, vol. 12, no. 1, 4381, 2021. DOI: 10.1038/s41467-021-24614-7.

[150] Z. Ning, O. Voznyy, J. Pan, S. Hoogland, V. Adinolfi, J. Xu, M. Li, A. R. Kirmani, J.-P. Sun, J. Minor, K. W. Kemp, H. Dong, L. Rollny, A. Labelle, G. Carey, B. Sutherland, I. Hill, A. Amassian, H. Liu, J. Tang, O. M. Bakr, and E. H. Sargent, „Air-stable n-type colloidal quantum dot solids“, *Nat. Mater.*, vol. 13, no. 8, 822–828, 2014. DOI: 10.1038/nmat4007.

[151] J. Zhou, F. Fang, W. Chen, M. Mei, P. Liu, J. Hao, H. Tang, S. Liang, W. Lei, R. Pan, J. Cheng, P. Müller-Buschbaum, X. W. Sun, W. Cao, K. Zheng, and K. Wang, „Luminescent perovskite nanocrystal composites via in situ ligand polymerization towards display applications“, *J. Mater. Chem. C*, vol. 9, no. 41, 14740–14748, 2021. DOI: 10.1039/D1TC03775G.

[152] W. Chen, H. Tang, N. Li, M. A. Scheel, Y. Xie, D. Li, V. Körstgens, M. Schwartzkopf, S. V. Roth, K. Wang, X. W. Sun, and P. Müller-Buschbaum, „Colloidal PbS quantum dot stacking kinetics during deposition via printing“, *Nanoscale Horiz.*, vol. 5, no. 5, 880–885, 2020. DOI: 10.1039/D0NH00008F.

[153] E. Georgitzikis, P. E. Malinowski, Y. Li, J. Maes, L. M. Hagelsieb, S. Guerrieri, Z. Hens, P. Heremans, and D. Cheyns, „Integration of PbS quantum dot photodiodes on silicon for NIR imaging“, *IEEE Sens. J.*, vol. 20, no. 13, 6841–6848, 2020. DOI: 10.1109/JSEN.2019.2933741.

[154] C. J. Wrasman, C. Zhou, A. Aitbekova, E. D. Goodman, and M. Cargnello, „Recycling of solvent allows for multiple rounds of reproducible nanoparticle synthesis“, *J. Am. Chem. Soc.*, vol. 144, no. 26, 11646–11655, 2022. DOI: 10.1021/jacs.2c02837.

[155] A. R. Kirmani, M. Woodhouse, and J. M. Luther, „Technoeconomic model suggests scaling-up perovskite quantum dots for optoelectronics warrants improved synthesis yield, solvent recycling, and automation“, *ACS Energy Lett.*, vol. 7, no. 4, 1255–1259, 2022. DOI: 10.1021/acsenergylett.2c00250.

[156] R. Li, K. Bian, T. Hanrath, W. A. Bassett, and Z. Wang, „Decoding the superlattice and interface structure of truncate PbS nanocrystal-assembled supercrystal and associated interaction forces“, *J. Am. Chem. Soc.*, vol. 136, no. 34, 12047–12055, 2014. DOI: 10.1021/ja5057032.

[157] M. C. Weidman, K. G. Yager, and W. A. Tisdale, „Interparticle spacing and structural ordering in superlattice PbS nanocrystal solids undergoing ligand exchange“, *Chem. Mater.*, vol. 27, no. 2, 474–482, 2015. DOI: 10.1021/cm503626s.

[158] J. Zhou, Y. Liu, J. Tang, and W. Tang, „Surface ligands engineering of semiconductor quantum dots for chemosensory and biological applications“, *Mater. Today*, vol. 20, no. 7, 360–376, 2017. DOI: 10.1016/j.mattod.2017.02.006.

[159] J.-C. Cheng, L.-Y. Pan, X.-L. Huang, Y.-P. Huang, Y.-H. Wang, S.-P. Xu, F.-F. Li, Z.-W. Men, and T. Cui, „Interparticle spacing effect among quantum dots with high-pressure regulation“, *Nanomaterials*, vol. 11, no. 2, 325, 2021. DOI: 10.3390/nano11020325.

[160] M. C. Weidman, Q. Nguyen, D.-M. Smilgies, and W. A. Tisdale, „Impact of size dispersity, ligand coverage, and ligand length on the structure of PbS nanocrystal superlattices“, *Chem. Mater.*, vol. 30, no. 3, 807–816, 2018. DOI: 10.1021/acs.chemmater.7b04322.

[161] J. Zhang, J. Tolentino, E. R. Smith, J. Zhang, M. C. Beard, A. J. Nozik, M. Law, and J. C. Johnson, „Carrier transport in PbS and PbSe QD films measured by photoluminescence quenching“, *J. Phys. Chem. C*, vol. 118, no. 29, 16228–16235, 2014. DOI: 10.1021/jp504240u.

[162] H. Tang, J. Zhong, W. Chen, K. Shi, G. Mei, Y. Zhang, Z. Wen, P. Müller-Buschbaum, D. Wu, K. Wang, and X. W. Sun, „Lead sulfide quantum dot photodetector with enhanced responsivity through a two-step ligand-exchange method“, *ACS Appl. Nano Mater.*, vol. 2, no. 10, 6135–6143, 2019. DOI: 10.1021/acsanm.9b00889.

[163] Z. Lingley, S. Lu, and A. Madhukar, „A high quantum efficiency preserving approach to ligand exchange on lead sulfide quantum dots and interdot resonant energy transfer“, *Nano Lett.*, vol. 11, no. 7, 2887–2891, 2011. DOI: 10.1021/nl201351f.

[164] S. W. Winslow, D.-M. Smilgies, J. W. Swan, and W. A. Tisdale, „Reversible temperature-induced structural transformations in PbS nanocrystal superlattices“, *J. Phys. Chem. C*, vol. 124, no. 24, 13456–13466, 2020. DOI: 10.1021/acs.jpcc.0c02853.

[165] M. C. Weidman, D.-M. Smilgies, and W. A. Tisdale, „Kinetics of the self-assembly of nanocrystal superlattices measured by real-time in situ X-ray scattering“, *Nat. Mater.*, vol. 15, no. 7, 775–781, 2016. DOI: 10.1038/nmat4600.

[166] Y. Xia, W. Chen, P. Zhang, S. Liu, K. Wang, X. Yang, H. Tang, L. Lian, J. He, X. Liu, G. Liang, M. Tan, L. Gao, H. Liu, H. Song, D. Zhang, J. Gao, K. Wang, X. Lan, X. Zhang, P. Müller–Buschbaum, J. Tang, and J. Zhang, „Facet control for trap–state suppression in colloidal quantum dot solids“, *Adv. Funct. Mater.*, vol. 30, no. 22, 2000594, 2020. DOI: 10.1002/adfm.202000594.

[167] P. L. Rosendahl, M. Drass, J. Felger, J. Schneider, and W. Becker, „Equivalent strain failure criterion for multiaxially loaded incompressible hyperelastic elastomers“, *Int. J. Solids Struct.*, vol. 166, 32–46, 2019. DOI: 10.1016/j.ijsolstr.2019.01.030.

[168] Y. Staudt, C. Odenbreit, and J. Schneider, „Failure behaviour of silicone adhesive in bonded connections with simple geometry“, *Int. J. Adhes. Adhes.*, vol. 82, 126–138, 2018. DOI: 10.1016/j.ijadhadh.2017.12.015.

[169] J. Novák, R. Banerjee, A. Kornowski, M. Jankowski, A. André, H. Weller, F. Schreiber, and M. Scheele, „Site-specific ligand interactions favor the tetragonal distortion of PbS nanocrystal superlattices“, *ACS Appl. Mater. Interfaces*, vol. 8, no. 34, 22526–22533, 2016. DOI: 10.1021/acsami.6b06989.

[170] S. W. Winslow, W. A. Tisdale, and J. W. Swan, „Prediction of PbS nanocrystal superlattice structure with large-scale patchy particle simulations“, *J. Phys. Chem. C*, vol. 126, no. 33, 14264–14274, 2022. DOI: 10.1021/acs.jpcc.2c03348.

[171] B. A. Korgel, S. Fullam, S. Connolly, and D. Fitzmaurice, „Assembly and self-organization of silver nanocrystal superlattices: Ordered “soft spheres”“, *J. Phys. Chem. B*, vol. 102, no. 43, 8379–8388, 1998. DOI: 10.1021/jp981598o.

[172] B. W. Goodfellow, Y. Yu, C. A. Bosoy, D.-M. Smilgies, and B. A. Korgel, „The role of ligand packing frustration in body-centered cubic (bcc) superlattices of colloidal nanocrystals“, *J. Phys. Chem. Lett.*, vol. 6, no. 13, 2406–2412, 2015. DOI: 10.1021/acs.jpclett.5b00946.

[173] B. Zhang, I. Lyskov, L. J. Wilson, R. P. Sabatini, A. Manian, H. Soleimaninejad, J. M. White, T. A. Smith, G. Lakhwani, D. J. Jones, K. P. Ghiggino, S. P. Russo, and W. W. H. Wong, „FRET-enhanced photoluminescence of perylene diimides by combining molecular aggregation and insulation“, *J. Mater. Chem. C*, vol. 8, no. 26, 8953–8961, 2020. DOI: 10.1039/D0TC02108C.

[174] K. F. Chou and A. M. Dennis, „Förster resonance energy transfer between quantum dot donors and quantum dot acceptors“, *Sensors*, vol. 15, no. 6, 13288–13325, 2015. DOI: 10.3390/s150613288.

[175] A. J. Mork, M. C. Weidman, F. Prins, and W. A. Tisdale, „Magnitude of the Förster radius in colloidal quantum dot solids“, *J. Phys. Chem. C*, vol. 118, no. 25, 13920–13928, 2014. DOI: 10.1021/jp502123n.

[176] S. W. Clark, J. M. Harbold, and F. W. Wise, „Resonant energy transfer in PbS quantum dots“, *J. Phys. Chem. C*, vol. 111, no. 20, 7302–7305, 2007. DOI: 10.1021/jp0713561.

[177] K. Tai, W. Lü, I. Umezu, and A. Sugimura, „Inter-dot distance dependence of photoluminescence properties in CdSe quantum dot systems“, *Appl. Phys. Express*, vol. 3, no. 3, 035202, 2010. DOI: 10.1143/APEX.3.035202.

[178] F. Gordon, S. Elcoroaristizabal, and A. G. Ryder, „Modelling Förster resonance energy transfer (FRET) using anisotropy resolved multi-dimensional emission spectroscopy (ARMES)“, *Biochim. Biophys. Acta, Gen. Subj.*, vol. 1865, no. 2, 129770, 2021. DOI: 10.1016/j.bbagen.2020.129770.

[179] R. B. Sekar and A. Periasamy, „Fluorescence resonance energy transfer (FRET) microscopy imaging of live cell protein localizations“, *J. Cell Biol.*, vol. 160, no. 5, 629–633, 2003. DOI: 10.1083/jcb.200210140.

[180] J. J. Choi, C. R. Bealing, K. Bian, K. J. Hughes, W. Zhang, D.-M. Smilgies, R. G. Hennig, J. R. Engstrom, and T. Hanrath, „Controlling nanocrystal superlattice symmetry and shape-anisotropic interactions through variable ligand surface coverage“, *J. Am. Chem. Soc.*, vol. 133, no. 9, 3131–3138, 2011. DOI: 10.1021/ja110454b.

[181] K. Bian, Z. Wang, and T. Hanrath, „Comparing the structural stability of PbS nanocrystals assembled in fcc and bcc superlattice allotropes“, *J. Am. Chem. Soc.*, vol. 134, no. 26, 10787–10790, 2012. DOI: 10.1021/ja304259y.

[182] I. A. Zaluzhnyy, R. P. Kurta, A. André, O. Y. Gorobtsov, M. Rose, P. Skopintsev, I. Besedin, A. V. Zozulya, M. Sprung, F. Schreiber, I. A. Vartanyants, and M. Scheele, „Quantifying angular correlations between the atomic lattice and the superlattice of nanocrystals assembled with directional linking“, *Nano Lett.*, vol. 17, no. 6, 3511–3517, 2017. DOI: 10.1021/acs.nanolett.7b00584.

[183] Z. Quan, W. S. Loc, C. Lin, Z. Luo, K. Yang, Y. Wang, H. Wang, Z. Wang, and J. Fang, „Tilted face-centered-cubic supercrystals of PbS nanocubes“, *Nano Lett.*, vol. 12, no. 8, 4409–4413, 2012. DOI: 10.1021/nl302324b.

[184] N. Nakazawa, Y. Zhang, F. Liu, C. Ding, K. Hori, T. Toyoda, Y. Yao, Y. Zhou, S. Hayase, R. Wang, Z. Zou, and Q. Shen, „The interparticle distance limit for multiple exciton dissociation in PbS quantum dot solid films“, *Nanoscale Horiz.*, vol. 4, no. 2, 445–451, 2019. DOI: 10.1039/C8NH00341F.

[185] A. Wolcott, V. Doyeux, C. A. Nelson, R. Gearba, K. W. Lei, K. G. Yager, A. D. Dolocan, K. Williams, D. Nguyen, and X.-Y. Zhu, „Anomalously large polarization effect responsible for excitonic red shifts in PbSe quantum dot solids“, *J. Phys. Chem. Lett.*, vol. 2, no. 7, 795–800, 2011. DOI: 10.1021/jz200080d.

[186] L. Sandoval, H. M. Urbassek, and P. Entel, „The Bain versus Nishiyama-Wassermann path in the martensitic transformation of Fe“, *New J. Phys.*, vol. 11, no. 10, 103027, 2009. DOI: 10.1088/1367-2630/11/10/103027.

[187] L. H. Zhang, M. J. Cheng, X. H. Shi, J. W. Shuai, and Z. Z. Zhu, „Bain and Nishiyama-Wassermann transition path separation in the martensitic transitions of Fe“, *RSC Adv.*, vol. 11, no. 5, 3043–3048, 2021. DOI: 10.1039/D0RA09332G.

List of Publications

First Author Journal Articles

- **J. E. Heger** W. Chen, H. Zhong, T. Xiao, C. Harder, F. A.C. Apfelbeck, A. F. Weinzierl, R. Boldt, L. Schraa, E. Euchler, A. K. Sambale, K. Schneider, M. Schwartzkopf, S. V. Roth, P. Müller-Buschbaum. Superlattice deformation in quantum dot films on flexible substrates via uniaxial strain. *Nanoscale Horiz.* **8**, 383-395 (2023)

  (DOI: 10.1039/d2nh00548d)

- **J. E. Heger**, W. Chen, S. Yin, N. Li, V. Körstgens, C. J. Brett, W. Ohm, S. V. Roth, P. Müller-Buschbaum. Low-Temperature and Water-Based Biotemplating of Nanostructured Foam-Like Titania Films Using ß-Lactoglobulin. *Adv. Funct. Mater.* **32**, 2113080 (2022)

  (DOI: 10.1002/adfm.202113080)

Coauthor Journal Articels

- M. Hofmaier, **J. E. Heger**, S. Lentz, S. Schwarz, P. Müller-Buschbaum, T. Scheibel, A. Fery, M. Müller. Influence of the Sequence Motive Repeating Number on Protein Folding in Spider Silk Protein Films. *Biomacromolecules* (2023)

  (DOI: 10.1021/acs.biomac.3c00688)

- X. Jiang, A. J. Gillett, T. Zheng, X. Song, **J. E. Heger**, K. Sun, L. V. Spanier, R. Guo, S. Liang, S. Bernstorff, P. Müller-Buschbaum. Operando Study of the Influence of Small Molecule Acceptor on the Morphology Induced Device Degradation of Organic Solar Cells with Different π-π Stacking. *Energy Environ. Sci.* (2023)

  (DOI: 10.1039/D3EE02527F)

- Y. Zou, X. Bai, S. Kahmann, L. Dai, S. Yuan, S. Yin, **J. E. Heger**, M. Schwartzkopf, S. V. Roth, C.-C. Chen, J. Zhang, S. D. Stranks, R. H. Friend, P. Müller-Buschbaum. A Practical Approach Towards Highly Reproducible And High-Quality Perovskite Films Based on An Aging Treatment. *Adv. Mat.*, 2307024 (2023)

  (DOI: 10.1002/adma.202307024)

- M. Betker, C. Harder, E. Erbes, **J. E. Heger**, A. E. Alexakis, B. Sochor, Q. Chen, M. Schwartzkopf, V. Körstgens, P. Müller-Buschbaum, K. Schneider, S. A. Techert, L. D. Söderberg, S. V. Roth. Sprayed Hybrid Cellulose Nanofibril–Silver Nanowire Transparent Electrodes for Organic Electronic Applications. *ACS Appl. Nano Mater.* **6**, 13677–13688 (2023)

  (DOI: 10.1021/acsanm.3c02496)

- K. Sun, R. Guo, Y. Liang, **J. E. Heger**, S. Liu, S. Yin, M. A. Reus, L. V. Spanier, F. Deschler, S. Bernstorff, P. Müller-Buschbaum. Morphological Insights into the Degradation of Perovskite Solar Cells under Light and Humidity. *ACS Appl. Mater. Interfaces* **15**, 30342–30349 (2023)

  (DOI: 10.1021/acsami.3c05671)

- Y. Zou, J. Eichhorn, S. Rieger, Y. Zheng, S. Yuan, L. Wolz, L. V. Spanier, **J. E. Heger**, S. Yin, C. R. Everett, L. Dai, M. Schwartzkopf, C. Mu, S. V. Roth, I. D. Sharp, C. c. Chen, J. Feldmann, S. D. Stranks, P. Müller-Buschbaum. Ionic Liquids Tailoring Crystal Orientation and Electronic Properties for Stable Perovskite Solar Cells. *Nano Energy* **112**, 108449 (2023)

  (DOI: 10.1016/j.nanoen.2023.108449)

- Y. Li, Y. Li, **J. E. Heger**, J. Zhou, T. Guan, C. R. Everett, W. Wei, Z. Hong, Y. Wu, X. Jiang, S. Yin, X. Yang, D. Li, C. Jiang, B. Sun, P. Müller-Buschbaum. Revealing Surface and Interface Evolution of Molybdenum Nitride as Carrier-Selective Contacts for Crystalline Silicon Solar Cells. *ACS Appl. Mater. Interfaces* **15**, 13753–13760 (2023)

  (DOI: 10.1021/acsami.2c22781)

- J. Ye, A. Ren, L. Dai, T. Baikie, R. Guo, D. Pal, S. Gorgon, **J. E. Heger**, J. Huang, Y. Sun, R. Arul, G. Grimaldi, K. Zhang, J. Shamsi, Y.-T. Huang, H. Wang, J. Wu, A. F. Koenderink, L. Torrente Murciano, M. Schwartzkopf, S. V. Roth, P. Müller-Buschbaum, J. J. Baumberg, S. D. Stranks, N. C. Greenham, L. Polavarapu, W. Zhang, A. Rao, R. L.Z. Hoye. Direct Linearly-Polarised Electroluminescence from Perovskite Nanoplatelet Superlattices. *arXiv preprint arXiv:2302.03582* (2023)

(DOI: 10.48550/arXiv.2302.03582)

- S. Yin, Y. Zou, M. A. Reus, X. Jiang, S. Tu, T. Tian, R. Qi, Z. Xu, S. Liang, Y. Cheng, **J. E. Heger**, M. Schwartzkopf, S. V. Roth, P. Müller-Buschbaum. Tailored fabrication of quasi-isoporous and double layered α-Fe2O3 thin films and their application in photovoltaic devices. *Chem. Eng. J.* **455**, 140135 (2023)

  (DOI: 10.1016/j.cej.2022.140135)

- A. L. Oechsle, **J. E. Heger**, N. Li, S. Yin, S. Bernstorff, P. Müller-Buschbaum. In Situ Observation of Morphological and Oxidation Level Degradation Processes within Ionic Liquid Post-treated PEDOT:PSS Thin Films upon Operation at High Temperatures. *ACS Appl. Mater. Interfaces* **14**, 30802–30811 (2022)

  (DOI: 10.1021/acsami.2c05745)

- A. L. Oechsle, **J. E. Heger**, N. Li, S. Yin, S. Bernstorff, P. Müller-Buschbaum. Correlation of Thermoelectric Performance, Domain Morphology and Doping Level in PEDOT:PSS Thin Films Post-Treated with Ionic Liquids. *Macromol. Rapid Commun.* **42**, 2100397 (2021)

  (DOI: 10.1002/marc.202100397)

- N. Li, R. Guo, W. Chen, V. Körstgens, **J. E. Heger**, S. Liang, C. J Brett, M. A. Hossain, J. Zheng, P. S. Deimel, A. Buyruk, F. Allegretti, M. Schwartzkopf, J. G. C. Veinot, G. Schmitz, J. V. Barth, T. Ameri, S. V. Roth, P. Müller-Buschbaum. Tailoring Ordered Mesoporous Titania Films via Introducing Germanium Nanocrystals for Enhanced Electron Transfer Photoanodes for Photovoltaic Applications. *Adv. Funct. Mater.* **31**, 2102105 (2021)

  (DOI: 10.1002/adfm.202102105)

- L. P. Kreuzer, T. Widmann, C. Geiger, P. Wang, A. Vagias, **J. E. Heger**, M. Haese, V. Hildebrand, A. Laschewsky, C. M. Papadakis, P. Müller-Buschbaum. Salt-Dependent Phase Transition Behavior of Doubly Thermoresponsive Poly(sulfobetaine)-Based Diblock Copolymer Thin Films. *Langmuir* **37**, 9179–9191 (2021)

  (DOI: 10.1021/acs.langmuir.1c01342)

- P. S. Schwarz, L. Tebcharani, **J. E. Heger**, P. Müller-Buschbaum, J. Boekhoven. Chemically fueled materials with a self-immolative mechanism: transient materials with a fast on/off response. *Chem. Sci.* **12**, 9969–9976 (2021)

  (DOI: 10.1039/D1SC02561A)

- W. Cao, S. Yin, M. Plank, A. Chumakov, M. Opel, W. Chen, L. P. Kreuzer, **J. E. Heger**, M. Gallei, C. J. Brett, M. Schwartzkopf, A. A. Eliseev, E. O. Anokhin, L. A. Trusov, S. V. Roth, P. Müller-Buschbaum. Spray-Deposited Anisotropic Ferromagnetic Hybrid Polymer Films of PS-b-PMMA and Strontium Hexaferrite Magnetic Nanoplatelets. *ACS Appl. Mater. Interfaces* **13**, 1592–1602 (2020)

  (DOI: 10.1021/acsami.0c19595)

- W. Chen, H. Tang, Y. Chen, **J. E. Heger**, N. Li, L. P. Kreuzer, Y. Xie, D. Li, C. Anthony, Z. Pikramenou, K. W. Ng, X. W. Sun, K. Wang, P. Müller-Buschbaum. Spray-deposited PbS colloidal quantum dot solid for near-infrared photodetectors. *Nano Energy* **78**, 105254 (2020)

  (DOI: 10.1016/j.nanoen.2020.105254

- D. Yang, B. Cao, V. Körstgens, N. Saxena, N. Li, C. Bilko, S. Grott, W. Chen, X. Jiang, **J. E. Heger**, S. Bernstorff, P. Müller-Buschbaum. Tailoring Morphology Compatibility and Device Stability by Adding PBDTTPD-COOH as Third Component to Fullerene-Based Polymer Solar Cells. *ACS Appl. Energy Mater.* **3**, 2604–2613 (2020)

  (DOI: 10.1021/acsaem.9b02290

Conference Contributions

Invited Talk

- *Biotemplating of titania nanostructures for hybrid photon sensors.*
  Institute of Flexible Electronics at Northwestern Polytechnical University
  Xi'an Shaanxi, China, 10.10.2019.

Contributed Talks

- *Low-Temperature and Water-Based Biotemplating of Nanostructured Foam-Like Titania Films using ß-Lactoglobulin.*
  Deutsche Physikalische Gesellschaft DPG-Frühjahrstagung
  Dresden, Germany, 26.03.–31.03.2023.

- *Superlattice deformation and its impact on photoluminescence in PbS quantum dot thin films: In situ GISAXS study on the correlation of morphology and photoluminescence.*
  Deutsche Physikalische Gesellschaft DPG-Frühjahrstagung
  Regensburg, Germany, 04.09.–09.09.2022.

- *GISAXS/GISANS.*
  E13 Summer School
  Nassfeld, Austria, 12.07.–15.04.2022.

- *ß-lactoglobulin-biotemplating of crystalline TiO_2 films at low temperature.*
  6th Bioinspired Materials
  Kostenz, Germany, 21.03.–24.03.2022.

- *Superlattice deformation in PbS quantum dot thin films introduced by uniaxial strain.*
  DESY Photon Science Users' Meeting, online meeting
  Germany, 21.01.–28.01.2022.

- *In situ GIXS investigation of ß-lactoglobulin templated TiO_2 hybrid film formation during spray deposition: An approach to green synthesis of functional materials.*
  American Chemical Society ACS Spring 2021, online meeting
  USA, 05.04.–16.04.2021.

- *In situ GIXS study on the crystallization and mesoscale film formation of lead-free MBI perovskite on mesoporous titania during spray deposition from a green solvent.*
  Deutsche Physikalische Gesellschaft DPG-Frühjahrstagung, online meeting
  Germany, 27.09.–01.10.2021.

- *Nanoscale film formation and crystallization of lead-free MBI hybrid perovskite on mesoporous Titania during spray deposition.*
  10th International Workshop on Functional Nanocomposites, online meeting
  Italy, 07.09.–10.09.2021.

- *Biopolymer templated hierarchical titania films for hybrid solar cells.*
  4th internal biennial science meeting of the MLZ
  Grainau, Germany, 24.06.–27.06.2019.

- *In operando stability investigation of biotemplated photoactive layers for solar cells.*
  10th Energy Colloquium of the Munich School of Engineering, online meeting
  Germany, 30.07.2020.

- *GISAXS/GIWAXS/GISANS.*
  E13 Summer School
  Obertauern, Austria, 12.06.–15.06.2018.

Posters

- *Sustainable biohybrid interfaces: GISANS study on spray deposited whey protein and titania composite films at varying pH.*
  MLZ User Meeting, Munich
  Germany, 08.12.–09.12.2022.

- *Investigating the stability of TiO_2:P3HT hybrid photoactive layers during heating with operando GISAXS.*
  The 16th International Conference on Surface X-ray and Neutron Scattering (SXNS16), online meeting
  Sweden, 11.01.–14.01.2022.

- *GISANS study on whey protein and titania interfaces: Influence of pH on spray deposited biohybrid film morphology.*
  MLZ User Meeting, online meeting
  Germany, 07.12.–08.12.2021.

- *In situ GISAXS/GIWAXS investigation of ß-sheet mediated biotemplating in TiO_2:ß-lactoglobulin films during spray deposition.*
  DESY Photon Science Users' Meeting, online meeting
  Germany, 25.01.–09.01.2021.

- *In situ GIXS observation of spray coating lead-free perovskite on mesoporous titania.*
  11th Energy Colloquium of the Munich School of Engineering, online meeting
  Germany, 28.07.–29.07.2021.

- *Observing the role of ß-lactoglobulin in biotemplating TiOx during spray deposition with in situ GIXS techniques: A route to green sol-gel chemistry.*
  Deutsche Physikalische Gesellschaft DPG-Frühjahrstagung, online meeting
  Germany, 22.03.–24.03.2021.

- *GISANS study of bio-hybrid films: Influence of pH on spraycoated ß-lactoglobulin:TiO2 film morphology for biotemplated titania nanostructures.*
  MLZ User Meeting, online meeting
  Germany, 08.12.–09.12.2020.

- *Biohybrid thin films for templating titania nanostructures.*
  MLZ User Meeting
  München, Germany, 10.12.–11.12.2019.

- *Biopolymer templated titanium dioxide films prepared via spray coating.*
  Deutsche Physikalische Gesellschaft DPG-Frühjahrstagung
  Regensburg, Germany, 31.03.–05.04.2019.

- *Spray deposition of biotemplated titania for hybrid solar cells.*
  9th Energy Colloquium of the Munich School of Engineering
  Garching, Germany, 01.08.2019.

- *Directional, hierarchical films via spray coating.*
  German Conference for Research with Synchrotron Radiation, Neutrons and Ion Beams at Large Facilities 2018 (SNI2018)
  Garching, Germany, 17.09.–19.09.2018.

Acknowledgments

First and foremost, I thank my supervisor Peter Müller-Buschbaum for the friendly reception in his group and for his suggestions on the topic of this dissertation. His encouragement and willingness to discuss the objectives contributed greatly to the progress and success of this thesis. Peter, I highly appreciate all of your support and your full trust in me and this dissertation.

As my mentor, Christine Papadakis has been standing by my side from the first day and encouraged me with scientific discussions to successfully pass each milestone along this dissertation. Thank you for your help with your door literally always being open.

None of the X-ray and neutron data would have been possible to be acquired without the fruitful collaboration with Sigrid Bernstorff, Alexandros Koutsioumpas, Wiebke Ohm, Stephan Roth and Matthias Schwartzkopf. Thank you for your inspiration and support during so many exciting beamtimes.

The success of this dissertation and related research travels to large scale fascilities, collaborators, and conferences required a smooth coordination of administration. Carola Kappauf and Marion Waletzki, thank you for your support in the organization and all your patience with lots of paperwork.

From the first idea of a scientific question to its experimental realization, the data analysis, and the publication in journals and on conferences, my collaborators and colleagues contributed with important discussions, their knowledge and skills, and helpful support not only during beamtimes. Without the following persons, a success of this dissertations would have hardly been possible. Thank you! Pablo Alvarez Herrera, Fabian Apfelbeck, Thomas Baier, Lorenz Bießmann, Christoph Bilko, Marco Bobinger, Michael Böhmer, Regine Boldt, Calvin Brett, Altantulga Buyan-Arivijikh, Wei Cao, Wei Chen,

Lyuyang Chen, Xiaojing Ci, Mihael Čorić, Lautaro Diaz Piola, Eric Euchler, Christopher Everett, Oliver Filonik, Reinhold Funer, Christina Geiger, Sebastian Grott, Tianfu Guan, Renjun Guo, Constantin Harder, Mirjam Hofmaier, Nuri Hohn, Linus Huber, Zhaonan Jin, Xinyu Jiang, Xiongzhuo Jiang, Florian Jung, Jia-Jhen Kang, Josef Kaplonski, Chia-Hsin Ko, Volker Körstgens, David Kosbahn, Lucas Kreuzer, Jenny Lebert, Morgan Le Dû, Lixing Li, Nian Li, Yanan Li, Zerui Li, Suzhe Liang, Yuxin Liang, Christoph Lindenmeir, Franziska Löhrer, David Machenschalk, Raphael Märkl, Josef Mock, Dieter Müller, Bart-Jan Niebuur, Anna Lena Oechsle, Guangjiu Pan, Thien An Pham, Dominik Petz, Ivana Pivarnikova, Shambavi Pratap, Benjamin Predeschly Stephan Pröller, Ruoxuan Qi, Lennart Reb, Julija Reitenbach, Manuel Reus, Tobias Widmann, Anna Sambale, Nitin Saxena, Lucas Schraa, Simon Schaper, Johannes Schlipf, Konrad Schneider, Alfons Schulte, Dominik Schwaiger, Patrick Schwarz, Kaltrina Shehu, Lin Song, Lukas Spanier, Kun Sun, Ting Tian, Suo Tu, Apostolos Vagias, Peixi Wang, Weijia Wang, Simon Wegener, Christian Weindl, Alexander Weinzierl, Lea Westphal, Tobias Widmann, Kerstin Wienhold, Senlin Xia, Tianxiao Xiao, Zhuijun Xu, Dan Yan, Yingying Yan, Shanshan Yin, Jinsheng Zhang, Peiran Zhang, Feifei Zheng, Tianle Zheng, Qi Zhong, Huaying Zhong, Yuqin Zou.

The list of people who must be acknowledged is seemingly endless and impossible to be satisfied within these short lines of acknowledgments. I had the great opportunity to meet marvelous persons from around the world, who enlightened me and gave me the chance to discover other countries and cultures. Along this way, colleagues turned into friendship with a bond so strong, that it will last beyond.

My whole family is with me during high tide and low tide, and this is a great source of energy. Especially in the darkest times you have been with me waiting for the sunrise: Claus, Brigitte, Matthias, Tommi, Dani, Eva, Fab, Luki, and my wonderful wife Jianping. Thank you from the bottom of my heart.

Finally, I thank my parents Markus and Monika for their unconditional love and support. There are no words to express my gratefulness and my love to you. This dissertation is dedicated to you.